



Provided by the author(s) and University of Galway in accordance with publisher policies. Please cite the published version when available.

Title	Towards an additive manufactured macroencapsulation device for islet cell replacement therapy
Author(s)	Levey, Ruth E.
Publication Date	2020-07-28
Publisher	NUI Galway
Item record	http://hdl.handle.net/10379/16240

Downloaded 2024-04-25T10:34:17Z

Some rights reserved. For more information, please see the item record link above.





NUI Galway
OÉ Gaillimh

**Towards an additive manufactured macroencapsulation
device for islet cell replacement therapy**

By

Ruth E. Levey B.Sc.

A thesis submitted to the National University of Ireland Galway, as
fulfilment of the requirements for the Degree of Doctor of Philosophy

Discipline of Anatomy

College of Medicine, Nursing and Health Sciences

Supervisor:

Prof Garry Duffy

July 2020

Table of Contents

List of Abbreviations	7
List of Figures	10
List of Tables	13
Authors Declaration	14
Abstract.....	15
Acknowledgments.....	16
Publications & Presentations	18
Peer Reviewed Journal Articles.....	18
Conference Presentations.....	19
Chapter 1.....	21
Introduction	21
1.1 The pancreas.....	22
1.1.1 The anatomy of the pancreas	22
1.1.2 The anatomy of the islets of Langerhans.....	23
1.2 Glycemic regulation	25
1.2.1 Insulin.....	25
1.2.2 Glucagon	27
1.3 Diabetes mellitus	29
1.3.1 The global impact of diabetes mellitus.....	29
1.3.2 The pathophysiology of diabetes mellitus.....	29
1.3.3 Current Treatments	32
1.4 Transplantation.....	38
1.4.1 Whole pancreas transplantation	38
1.4.2 Pancreatic islet transplantation	39
1.5 Extravascular islet transplantation	43
1.5.1 Sources of cells for transplantation	43
1.6 Cell encapsulation technology	46
1.6.1 Microencapsulation systems	48
1.6.2 Macroencapsulation systems	49
1.6.3 Challenges	50
1.7 Advances in macroencapsulation systems for the treatment of T1DM	53
1.7.1 TheraCyte.....	53
1.7.2 Viacyte.....	55
1.7.3 β Air.....	58

1.7.4 Sernova Cell Pouch.....	60
1.7.5 MailPan	62
1.8 The DRIVE project	66
1.9 Thesis Objectives.....	69
Chapter 2.....	70
Examining the Angiogenic and Foreign Body Response of soft tissue implants with various 3D printed porous topographies.....	70
2.1 Introduction	71
2.1.1 Aims.....	72
2.2 Materials and Methods.....	73
2.2.1 Implant fabrication.....	73
2.2.2 Subdermal implantation in rats	78
2.2.3 Fixation, embedding and staining	79
2.2.4 X-ray microtomography (Micro-CT)	80
2.2.5 Scanning Electron Microscopy (SEM).....	80
2.2.6 Fibrous capsule analysis.....	80
2.2.7 Macrophage response	84
2.2.8 Angiogenesis	86
2.2.9 Statistical analysis	88
2.3 Results.....	89
2.3.1 Post-explantation imaging of implants	89
2.3.2 Fibrous capsule analysis.....	91
2.3.3 Macrophage response	96
2.3.4 Angiogenesis	100
2.4 Discussion.....	103
Chapter 3.....	106
Assessing the effects of VEGF releasing microspheres on the angiogenic and foreign body response to a multiscale porosity macroencapsulation device.....	106
3.1 Introduction	107
3.1.1 Aims.....	109
3.2 Materials and Methods.....	110
3.2.1 Macroencapsulation device and contents.....	110
3.2.2 Subdermal implantation in rats	113
3.2.3 Fixation, embedding and staining	115
3.2.4 Angiogenesis	115
3.2.5 Scanning Electron Microscopy (SEM).....	116

3.2.6 Fibrous capsule analysis.....	116
3.2.7 Macrophage response	117
3.2.8 Statistical analysis	117
3.3 Results.....	118
3.3.1 X-ray microtomography (Micro-CT)	118
3.3.2 <i>In-vivo</i> analysis of angiogenesis	118
3.3.3 Angiogenesis	121
3.3.4 Scanning Electron Microscopy (SEM).....	126
3.3.5 Fibrous capsule analysis.....	126
3.3.6 Macrophage response	132
3.4 Discussion.....	135
Chapter 4.....	139
To examine the potential of the multiscale porosity islet encapsulation device for the treatment of diabetes in STZ-induced diabetic rodents.....	139
4.1 Introduction	140
4.1.1 Aims.....	142
4.2 Materials and Methods.....	143
4.2.1 Isolation and purification of syngeneic islets.....	143
4.2.2 Induction of diabetes in rats	144
4.2.3 Macroencapsulation device and contents.....	144
4.2.4 Intra-peritoneal implantation in rats	145
4.2.5 X-ray microtomography (MicroCT)	148
4.2.6 Scanning Electron Microscopy (SEM).....	148
4.2.7 Fixation, embedding and staining.....	148
4.2.8 Polarised Light Microscopy (PLM).....	149
4.2.9 Statistical analysis	150
4.3 Results.....	151
4.3.1 Induction of diabetes in rats	151
4.3.2 Implantation of syngeneic islets within a collagen gel	151
4.3.3 Implantation of syngeneic islets encapsulated within a multiscale porosity non-sutured macroencapsulation device.....	154
4.3.4 MicroCT Analysis of the multiscale porosity non-sutured macroencapsulation device	157
4.3.5 Implantation of syngeneic islets encapsulated within a multiscale porosity macroencapsulation device sutured to the anterior abdominal wall	157
4.3.6 Analysis of blood glucose levels 2.5 weeks following explant of devices.....	159

4.3.7 Analysis of the fibrous capsule surrounding sutured macroencapsulation device	162
4.3.8 Analysis of fibrous capsule composition around sutured macroencapsulation devices using polarised light microscopy	165
4.3.9 Analysis of the angiogenesis surrounding sutured macroencapsulation devices	165
4.3.10 Analysis of the macrophage response surrounding sutured macroencapsulation devices	167
4.3.11 Comparison of histological analysis of devices sutured to the anterior abdominal wall vs submuscular implantation	167
4.4 Discussion.....	170
Chapter 5.....	172
To examine the scalability and functionality of multiscale porous islet encapsulation devices in an STZ-induced diabetic porcine model.....	172
5.1 Introduction	173
5.1.1 Aims.....	174
5.2 Materials and Methods.....	175
5.2.1 Determining the most favourable AAW site for implantation of an islet encapsulation device	175
5.2.2 Device fabrication	179
5.2.3 Porcine Studies.....	181
5.2.4 Tissue processing and histology.....	185
5.2.5 Diffusion tensor imaging and analysis	186
5.2.6 MicroCT	188
5.2.7 Pull-off testing of integrated multiscale porosity devices and smooth surfaced control.....	188
5.2.8 Scanning Electron Microscopy (SEM).....	188
5.2.9 Fixation, embedding and staining.....	189
5.2.10 Statistical analysis	189
5.3 Results.....	190
5.3.1 Determining the most favourable AAW site for implantation of a multiscale porosity macroencapsulation device	190
5.3.2 Analysing the diffusion capabilities of the multiscale porosity device	192
5.3.3 Diffusion tensor imaging of the fibrous capsule surrounding the multiscale porosity and smooth devices	193
5.3.4 Pull-off testing of integrated multiscale porosity devices and smooth surfaced control.....	196
5.3.5 MicroCT and SEM imaging of multiscale porosity and smooth devices with associated surrounding tissue	196

5.3.6 Analysis of the fibrous capsule surrounding the multiscale porosity and smooth devices	198
5.3.7 Analysis of the angiogenesis surrounding multiscale porosity and smooth devices	202
5.3.8 Analysis of the macrophage response surrounding multiscale porosity and smooth devices	207
5.4 Discussion.....	209
Chapter 6.....	213
Thesis Discussion.....	213
6.1 Overview	214
6.2 Thesis results summary.....	215
6.2.1 Determining an optimal surface topography.....	215
6.2.2 VEGF releasing microspheres as a vascularisation strategy	217
6.2.3 Determining the therapeutic efficacy of the multiscale porosity macroencapsulation device	217
6.2.4 Clinical translation study.....	218
6.3 Clinical relevance	219
6.3.1 Putting a positive spin on fibrous capsule development.....	219
6.3.2 DRIVE technology as a treatment for T1D	220
6.4 Future work.....	224
6.5 Final conclusion.....	227
Bibliography	228

List of Abbreviations

AAW	Anterior Abdominal Wall
ANOVA	Analysis of Variance
ATP	Adenosine triphosphate
ATP-K+	Adenosine triphosphate sensitive potassium channel
CGM	Continuous glucose monitoring
CO₂	Carbon Dioxide
CT	Computed Tomography
dL	Decilitre
DM	Diabetes mellitus
DRIVE	Diabetes reversing implants with enhanced viability and long- term efficacy
DTI	Diffusion Tensor Imaging
EC	European Commission
ECM	Extracellular matrix
EDC	1-Ethyl-3-(3-dimethyl-aminopropyl) carbodiimide hydrochloride
FA	Fractional Anisotropy
FBG	Fasting blood glucose
GLUT	Glucose transporter
GTMP	Gene therapy medicinal product
h	Hour
H₂O₂	Hydrogen peroxide
HA	Hyaluronic acid
HCl	Hydrochloric acid
HFPE	Hepatic First-Pass Effect
HOSu	N-Hydroxysuccinimide
HPA	3-(4-hydroxyphenyl) propionic acid
HRP	Horse radish peroxidase
IEQ	Islet equivalents
IIDP	Integrated Islet Distribution Program
IPSC	Induced Pluripotent Stem Cell
IRS	Insulin Receptor Substrate

IV	Intravenous
iPSCs	Induced pluripotent stem cells
kg	Kilogram
L	Liter
MAG	Morphomics Analytics Group
MD	Mean Diffusivity
MES	2- [N-Morpholino] ethanesulfonic acid
MicroCT	Micro Computed Tomography
Mg	Milligram
mm	Millimetre
mmol	Millimole
mM	Millimolar
mL	Millilitre
min	Minute
μL	Microlitre
μm	Micrometre
μM	Micromolar
natHA	Native HA
NSM	Non-sutured macroencapsulation devices
O₂	Oxygen
PBS	Phosphate buffered saline
PDF	Perfluorodecalin
PEG	Polyethylene Glycol
PFC	Perfluorocarbon
PFD	Perfluorodecalin
PI3K	Phosphatidylinositol 3-kinase
PLM	Polarized Light Microscopy
PP	Pancreatic protein
PPBG	Post-prandial blood glucose
PTFE	Polytetrafluorethylene
RAMP	Reference Analytics Morphomics Population

S	Sutured macroencapsulation devices
SD	Standard Deviation
SEM	Scanning Electron Microscopy
SMBG	Self-monitoring blood glucose
sec	Second [time]
STZ	Streptozotocin
TAP	Transversus Abdominus Plane
T1D	Type 1 Diabetes
T2D	Type 2 Diabetes
VEGF	Vascular endothelial growth factor
v	volume
w	weight
WHO	World Health Organisation

List of Figures

Figure 1.1: Schematic depicting the anatomical relations of the pancreas	22
Figure 1.2: Islets of Langerhans	24
Figure 1.3: Glucose stimulated insulin secretion.....	26
Figure 1.4: Glycemic regulation	28
Figure 1.5: Number of people (20-79 years) with diabetes globally defined by region	29
Figure 1.6: Pathogenesis of T1D	31
Figure 1.7: Evolution of insulin therapy devices.....	33
Figure 1.8: Components of an insulin pump therapy	35
Figure 1.9: An outline of the function of the closed loop system that makes up the artificial pancreas.....	37
Figure 1.10: Schematic outlining the process of islet isolation from the human pancreas. .	41
Figure 1.11: Overview of utilising a patient’s own somatic cells for a cell transplantation to treat T1D	46
Figure 1.12: Overview of current encapsulation processes for pancreatic islets/ β -cells.....	47
Figure 1.13: Inflammatory and healing processes that occur following the <i>in vivo</i> implantation of a biomaterial	51
Figure 1.14: TheraCyte encapsulation system.....	54
Figure 1.15: Viacyte encapsulation systems.....	57
Figure 1.16: Generation 1 and 2 of the β Air device with cross-sectional schematics of device interiors.....	59
Figure 1.17: Sernova Cell Pouch System.....	61
Figure 1.18: The MailPan (MAcroencapsulation of PANcreatic Islets) Device	63
Figure 1.19: The aim of the DRIVE project.....	66
Figure 2.1: Control of the liquid rope-coil effect	74
Figure 2.2: Microporous coating with salt nucleation	76
Figure 2.3: Manufacturing of increasingly complex 3D printed porous topographies.....	78
Figure 2.4: Micro-CT imaging of implant implantation sites within the dorsum of rat model.	79
Figure 2.5: Morphometric and stereological methods used to analyse fibrous capsule thickness	82
Figure 2.6: The physical dissector method	85
Figure 2.7: Unbiased counting frame, the principal	86
Figure 2.8: Post-explantation representative images of implants in-situ	90
Figure 2.9: Analysis of the fibrous capsule	92

Figure 2.10: Analysis of the volume fraction of myofibroblasts within the surrounding fibrous capsule.....	94
Figure 2.11: Analysis of collagen maturity and organisation at the tissue/implant interface	95
Figure 2.12: Analysis of the macrophage response at the tissue/implant interface.....	98
Figure 2.13: Analysis of the macrophage phenotype surrounding the 3D printed porous topography implants.....	99
Figure 2.14: Analysis of angiogenesis between the tissue/implant interface and the panniculus carnosus.....	101
Figure 2.15: Analysis of vessel stability and maturity at the tissue/implant interface	102
Figure 3.1: Rat sized (10 x 10 x 2 mm) macroencapsulation devices	110
Figure 3.2: Vascular Endothelial Growth Factor (VEGF) microspheres.	112
Figure 3.3: Study Design	114
Figure 3.4: Micro-CT images of devices implanted subcutaneously in the dorsal thoracic region of rats.....	119
Figure 3.5: In-vivo evaluation of angiogenesis at 4 weeks	120
Figure 3.6: Analysis of angiogenesis between the tissue-device interface and the panniculus carnosus.	122
Figure 3.7: Analysis of vessel stability and maturity at the tissue-device interface.....	123
Figure 3.8: Analysis of blood vessel diameters.....	125
Figure 3.9: Representative Scanning Electron Microscopy (SEM) images of-VEGF and +VEGF devices	127
Figure 3.10: Analysis of the fibrous capsule thickness	129
Figure 3.11: Analysis of the volume fraction of myofibroblasts within the surrounding fibrous capsule.....	130
Figure 3.12: Analysis of the fibrous capsule and collagen maturity at the tissue device interface.....	131
Figure 3.13: Analysis of the macrophage response at the tissue/device interface.....	133
Figure 3.14: Analysis of the macrophage phenotype surrounding the implanted devices.	134
Figure 4.1: Implantation process of multiscale porosity device	147
Figure 4.2: Establishing STZ-induced diabetic rats	152
Figure 4.3: Islet cell encapsulation within a collagen gel implanted intra-peritoneally.....	154
Figure 4.4: Non-sutured macroencapsulation devices containing islets implanted intra-peritoneally	155
Figure 4.5: Micro-CT imaging of non-sutured macroencapsulation devices containing islets implanted intra-peritoneally.....	156
Figure 4.6: Sutured macroencapsulation devices containing islets intra-peritoneally	158

Figure 4.7: Summary fasting blood glucose concentrations (mg/dL) for 0-8 weeks.....	159
Figure 4.8: Analysis of blood glucose levels 2.5 weeks following explant of devices & histological analysis of associated pancreatic tissue	160
Figure 4.9: SEM imaging of sutured macroencapsulation devices with associated surrounding tissue	161
Figure 4.10: Analysis of fibrous capsule formation around sutured macroencapsulation devices	163
Figure 4.11: Analysis of fibrous capsule composition around sutured macroencapsulation devices using polarised light microscopy.....	164
Figure 4.12: Analysis of angiogenesis surrounding sutured devices	166
Figure 5.1: Determining the dimensions of potential implant sites in the AAW.....	178
Figure 5.2: Upscaling of multiscale porous device	180
Figure 5.3: Establishing an STZ-induced diabetic pig model - Analysis of the first pig enrolled.....	182
Figure 5.4: Surgical placement of unscaled multiscale porous devices	184
Figure 5.5: Processing of tissue samples en bloc.....	185
Figure 5.6: Determining the dimensions of potential implant sites in the AAW.....	191
Figure 5.7: Comparing the diffusion capabilities of multiscale porosity devices to an oral biologic delivery system.....	192
Figure 5.8: DTI analysis of the fibrous capsule surrounding multiscale porosity and smooth macroencapsulation devices.....	195
Figure 5.9: Pull-off testing of tissue surrounding multiscale porous devices and smooth control after 2 weeks of submuscular implantation in pig	196
Figure 5.10: MicroCT and SEM imaging of multiscale porous and smooth devices with associated surrounding tissue	197
Figure 5.11: Analysis of fibrous capsule formation around multiscale porous and smooth macroencapsulation devices.....	200
Figure 5.12: Analysis of myofibroblast abundance around multiscale porous and smooth macroencapsulation devices.....	201
Figure 5.13: Analysis of angiogenesis around multiscale porous and smooth macroencapsulation devices.....	205
Figure 5.14: Analysis of vessel stability and maturity surrounding multiscale porous and smooth macroencapsulation devices	206
Figure 5.15: Analysis of macrophage response surrounding multiscale porous and smooth macroencapsulation devices.....	208

List of Tables

Table 1.1: Summary of Encapsulation systems in clinical trial.....	64
Table 1.2: Modifications and adaptations of the DRIVE macroencapsulation system throughout this thesis.....	68
Table 2.1: Description of features of each implant.....	77
Table 3.1: Summary of published angiogenic analysis surrounding macroencapsulation devices.....	138
Table 5.1: Design criteria for implant site.....	177
Table 6.1: Comparing current islet macroencapsulation systems with the DRIVE.....	223

Authors Declaration

I declare that all of the work presented in this thesis was carried out in accordance with the regulations of the National University of Ireland, Galway. This is original work carried out by myself, except where indicated by reference in the text. This thesis has not been submitted previously for any other academic award.

Signed:



Ruth E. Levey

Date:

Abstract

Islet encapsulation devices can induce a Foreign Body Response (FBR) and the formation of a hardened avascular fibrotic capsule. This FBR is heightened when the device features a smooth surface as fibrous tissue is unable to adhere to the device, causing friction and thus instigating a substantial immunological reaction causing implant failure. In this thesis we examine whether additive manufactured multiscale porous topographies can promote optimal tissue integration and vascularisation for the purpose of long-term functional islet macroencapsulation devices.

Devices exhibiting progressively more complex surface topographies (quantity of pores, microtexture and macrotexture) were implanted subcutaneously in a rodent model. Upon explant, analysis of the fibrous capsule, angiogenic and macrophage response were performed. To determine whether this macroencapsulation device can support syngeneic islet survival and function, intra-peritoneal delivery of islets encapsulated within multiscale porosity macroencapsulation devices was performed in an STZ-induced diabetes rodent model. To validate scalability and functionality, devices were implanted in an STZ-induced diabetes pig model for two weeks before the blood glucose levels were measured in response to the infusion of insulin through the device.

SEM and MicroCT imaging demonstrated no tissue attachment and a noticeable void between the smooth surface devices and surrounding tissue. A significant increase in capsule thickness, vessel density and maturity were associated with complex surface topographies with no difference in macrophage populations. Moreover, macroencapsulated syngeneic islets maintained glucose responsiveness and function for up to 8 weeks. Bioavailability was equal when the same dose of insulin is delivered via the device vs subcutaneously in diabetic pig model.

The additive manufactured multiscale porous topographies we developed on silicone macroencapsulation devices increased tissue integration, vascularity and supported extended islet function in vivo. Our findings demonstrated clinical scalability and large animal functionality with the ability to resolve diffusion limitations of current macroencapsulation devices. We aim to continue the translation of the multiscale porosity macroencapsulation device and improve the outcomes of people with Type 1 diabetes through the development of viable, long term implant.

Acknowledgments

There are a number of people who I would like to thank, without which I could not have completed this work.

First and foremost, I would like to thank my supervisor, Prof. Garry Duffy. I consider myself very fortunate to be able to learn from you and your research experience. I want to thank you for providing me with an invaluable mentorship filled with endless opportunities, without which I would not have met such amazing people or seen so much of the world in the last 3 years. When I constantly doubted that I could reach deadlines, stand in front of an audience or even succeed, your unwavering support and belief in me kept me going. I am so thankful for your commitment and willingness to help me grow not only as an early stage researcher, but as an individual.

As this was a hugely collaborative project, I would like to acknowledge everyone who made the DRIVE project possible, and in particular I would like to acknowledge the training, collaborative lab work, assistance and materials provided by various partners of the project. Thank you to Dr Eoin O’Cearbhaill, Dr Fergal Coulter and all from UCD who helped develop and manufacture the macroencapsulation devices for both small and large animal studies. I would like to thank Abiel srl for providing training on device explantation and for their work in running the *in vivo* rat experiments. I would like to thank the partners in EXPLORA Biotech for their work with the large animal studies. I would also like to thank the partners at RCSI Dr Helena Kelly and Dr Liam McDonough for providing training on gel encapsulation and development and production of encapsulation gels for islet studies. Thanks to Dr Eimear Dolan for all her help with DRIVE in the early days, for collaborative publication opportunities, her endless positivity, and career and life advice. And finally, a huge thank you to Dr Scott Robinson. You were an enormous help in the first 2 yrs of my project and a tremendous source of knowledge, support and straight talking. Thanks for the endless pints and laughs.

Thank you to the amazing Duffy Lab members, both past and present. I could not have met a more positive, encouraging and helpful group of people. I would especially like to thank the research assistants Ericka Maye and James Prendergast, and my PhD sister and brother Rachel Beatty and David Monahan. I could never have hoped to make better friends. James, we have been inseparable since first year of undergrad in 2012, thanks for being the greatest best friend in the world. Thank you for the many many coffee break rants and also

for the endless supply of help and advice. This PhD journey was made less painful having such funny and supportive friends around me.

Many many many thanks goes to the technical wizards both past and present; Mark Canney, Pierce Lalor, Kerry Thompson, Ian O'Brien and Emma McDermott. Thank you for your expert technical support, for rescuing me and my experiments from absolute failure from time to time, and most importantly for everything you have taught me over the years. You are collectively the most cool, calm and collected people I have ever met, despite the fact that the lab would probably be in bits without you.

I would also like to thank the anatomy department. You all have collectively invested and provided me with a wealth of knowledge over the years that has made me the scientist I am today. Thank you to Prof Peter Dockery, for all the advice and support throughout the years, and for imparting your stereological wisdom upon me. Thank you also to Researchers/Lecturers Dr Helen Dodson, Dr Kerry Thompson, Dr Alanna Stanley, Dr Janice O'Sullivan, Dr Emma McDermott, Dr Dara Cannon, Dr Siobhan McMahon and Dr Yolanda Garcia (to name a few). It has been a pleasure to have been surrounded by such intelligent, compassionate, empowering and helpful women. Thank you for your invaluable support throughout the years. I aspire to be like you.

Thank you to the talented undergraduate and masters research students who were under my supervision; Paige Hinton, Ericka Maye, Fiona Cronin, Donal O'Keefe, Alex O'Brien, Lucy Dockery and Robert Bagnall, thank you all for allowing me to hone my teaching skills, and for collectively carrying out great work to support my research.

To Mam and Dad, without any shadow of a doubt this would not have been possible without your support and encouragement. I don't always show my appreciation but know that I am eternally grateful to you both for everything. Thank you to Jennifer, Barry and Aimee for your encouragement, at times it was really needed. P.S. I promise I will find a job now.

To Darragh for his continued and unflinching love, support and encouragement for the last 6 years. I am truly thankful for having you in my life and for believing in me long after I'd lost belief in myself. I really appreciate everything you do to make me smile. Thank you to my partner in crime Baby, although you are a cat, you have been a huge source of happiness and comfort to me for the last 12 years. I hope you never die. Love you both always.

Collectively your support and guidance has helped me to make it beyond what I imagined myself capable of achieving.

Publications & Presentations

Peer Reviewed Journal Articles

Levey RE, Coulter FB, Scheiner K, Deotti S, Robinson ST, McDonough L, Wylie R, Dockery P, Kelly HM, Gherzi G, Hennink WE, Kok RJ, O’Cearbhaill E, Duffy GP. Assessing the effects of VEGF releasing microspheres on the angiogenic and foreign body response to a 3D printed silicone-based macroencapsulation device. **(In Preparation)**. *Journal of Controlled Release*.

Levey RE*, Robinson ST*, Coulter FB*, Deotti S, Paetzold R, Dockery P, Dolan EB, Lowery AJ, Bellavia G, Straino S, Cianfarani F, Duffy GP*, O’Cearbhaill E*. To examine the scalability and functionality of multiscale porous islet encapsulation devices in an STZ-induced diabetic porcine model **(In Preparation)**. *Science Translational Medicine*.

Coulter FB*, **Levey RE***, Robinson ST*, Deotti S, Paetzold R, Monaghan M, Dockery P, Dolan EB, Prendergast JJ, Lowery AJ, Beatty R, Moerman KM, Bellavia G, Straino S, Cianfarani F, Salamone M, Bruno CM, Gherzi G, Duffy GP*, O’Cearbhaill E*. Additive Manufacturing of Multi-Scale Porous Soft Tissue Implants That Encourage Vascularization and Tissue Ingrowth **(Currently in revision)**. *Science Translational Medicine*.

Robinson ST, **Levey RE**, Beatty R, Connolly D, Dolan EB, Osborne NH, Dockery P, Henke PK, Duffy GP. A Versatile Technique for High-Resolution 3D Imaging of Human Arterial Segments Using Micro-Computed Tomography **(In Press, Journal Pre-Proof)**. *Journal of Vascular Science*, 2020.

Duffy GP, Robinson ST, O’Connor R, Wylie R, Mauerhofer C, Bellavia G, Straino S, Cianfarani F, Mendez K, Beatty R, **Levey RE**, O’Sullivan J, McDonough L, Kelly H, Roche ET*, Dolan EB*. Implantable Therapeutic Reservoir Systems for Diverse Clinical Applications in Large Animal Models. *Advanced Healthcare Materials*, 2020, 9, 11.

Gallagher LB, Dolan EB, O’Sullivan J, **Levey RE**, Cavanagh BL, Kovarova L, Pravda M, Velebny V, Farrell T, O’Brien FJ, Duffy GP. Pre-culture of mesenchymal stem cells within RGD-modified hyaluronic acid hydrogel improves their resilience to ischaemic conditions. *Acta Biomaterialia* 2020, 105.

Dolan EB*, Hofmann B*, Vaal H, Bellavia G, Straino S, Kovarova L, Pravda M, Velebny V, Daro D, Braun N, Monahan DS, **Levey RE**, O’Neill H, Hinderer S, Greensmith R, Monaghan MG, Schenke Layland K, Dockery P, Murphy BP, Kelly HM, Wildhirt S, Duffy GP. A Bioresorbable Carrier and Passive Stabilization Device to Improve Heart Function Post-Myocardial Infarction. *Materials Science and Engineering C*. 2019, 103, 109751.

Dolan EB, Varela CE, Mendez K, Whyte W, **Levey RE**, Robinson ST, Maye E, O’Dwyer J, Beatty R, Rothman A, Fan Y, Hochstein J, Rothenbacher SE, Wylie R, Starr R, Monaghan M, Dockery P, Duffy GP*, Roche ET*. An actuatable soft reservoir modulates host foreign body response. *Science Robotics* 2019, 4, 33.

*co first/last author

Conference Presentations

Levey RE, Coulter FB, Robinson ST, Deotti S, Monaghan M, Dockery P, Dolan EB, Prendergast JJ, Bellavia G, Straino S, Cianfarani F, Salamone M, Bruno CM, Gherzi G, O’Cearbhaill E, Duffy GP. “Additive Manufacturing of Multi-Scale Porous Soft Tissue Implants That Encourage Vascularisation and Tissue Ingrowth” (Oral) World Biomaterials Congress (WBC), Glasgow, December 2020.

Levey RE, Coulter FB, Robinson ST, Deotti S, Monaghan M, Dockery P, Dolan EB, Prendergast JJ, Bellavia G, Straino S, Cianfarani F, Salamone M, Bruno CM, Gherzi G, O’Cearbhaill E, Duffy GP. “Assessing the effects of VEGF releasing microspheres on the angiogenic and foreign body response surrounding multi-scale porous macroencapsulation devices” (Oral) Microscopy Society Ireland Symposium (MSI), Dublin, January 2020.

Levey RE, Coulter FB, Robinson ST, Deotti S, Dockery P, Dolan EB, O’Cearbhaill E, Duffy GP. “Additive Manufactured Multiscale Porous Coatings on Macroencapsulation Devices Modulate the Host Response” (Oral) Engineers Ireland Biomedical Research Medal Presentation at Bioengineering in Ireland (BinI). Carlow, January 2020.

Levey RE, Coulter F, Robinson ST, Maye EM, Gherzi G, Dockery P, O’Cearbhaill E, Duffy GP. “Examining the host response to islet cell encapsulation devices with 3D printed multiscale porous coatings” (Poster) Advanced Technologies & Treatments for Diabetes, Madrid, February 2020.

Levey RE, Coulter F, Robinson ST, Gherzi G, Dockery P, O’Cearbhaill E, Duffy GP. “Addressing the foreign body response to implantable reservoirs” (Oral) Matrix Biology Ireland Annual Meeting (MBI), Dublin, November 2019.

Levey RE, Coulter F, Robinson ST, Maye EM, Gherzi G, Dockery P, O’Cearbhaill E, Duffy GP. “Examining the Host Response to Cell Encapsulation Devices with 3D Printed multiscale porous coatings” (Oral) Elevator pitch presentation at the International Pancreas and Islet Transplant Association (IPITA), Lyon, July 2019.

Levey RE, Coulter F, Robinson ST, Maye EM, Gherzi G, Dockery P, O’Cearbhaill E, Duffy GP. “To assess the host response to a porous polymer cell encapsulation device following subcutaneous implantation in rats” (Poster) European Society of Artificial Organs Congress, Madrid, September 2018.

Levey RE, Robinson ST, Coulter FB, Gherzi G, Burke L, Kelly HM, O’Cearbhaill E, Duffy GP. “To assess the host response to a porous polymer cell encapsulation device following subcutaneous implantation in rats” (Poster) College of Medicine, Nursing and Health Sciences Research Day, NUI Galway, May 2018.

Levey RE, Robinson ST, Beatty RB, Duffy GP “Characterisation of the foreign body response to a porous polymer macroencapsulation device containing pro-angiogenic growth factors following subcutaneous implantation in rats” (Poster) Matrix Biology Ireland, Trinity College Dublin, September 2017.

Levey RE, Chiaponni M, Butler-Hallisey C, Thompson K, Dodson H. “Analysis of the cell cycle in human cultured cells using FUCCI, a multicolour live cell imaging system” (Poster) Microscience Microscopy Congress, Manchester, July 2017.

Levey RE, Chiaponni M, Butler-Hallisey C, Thompson K, Dodson H. “Analysis of the cell cycle in human cultured cells using FUCCI, a multicolour live cell imaging system” (Poster) Anatomical Society “Anatomists on the Edge”, National University of Ireland Galway, June 2017.

Levey RE, Chiaponni M, Butler-Hallisey C, Thompson K, Dodson H. “Analysis of H2AX protein abundance in human breast cancer cells – Methods Development” (Poster) Anatomical Society Meeting, Brighton, 2016.

Within the DRIVE Consortium

As part of DRIVE, quarterly consortium meetings were held at different partner institutions. Throughout my PhD, I gave oral presentations updating the consortium partners on project progress.

Introduction

Chapter 1

Introduction

1.1 The pancreas

1.1.2 The anatomy of the pancreas

The pancreas functions as both an exocrine and endocrine organ, playing vital roles in macronutrient digestion and metabolism/energy homeostasis through the release of digestive enzymes and hormones. It is an elongated organ which lies obliquely at the level of the L1-L2 vertebral bodies. The majority of this organ lies retroperitoneal with exception of the tail. Anatomically the pancreas is divided into five parts, the head, uncinete process, neck, body and tail (*Figure 1.1*).

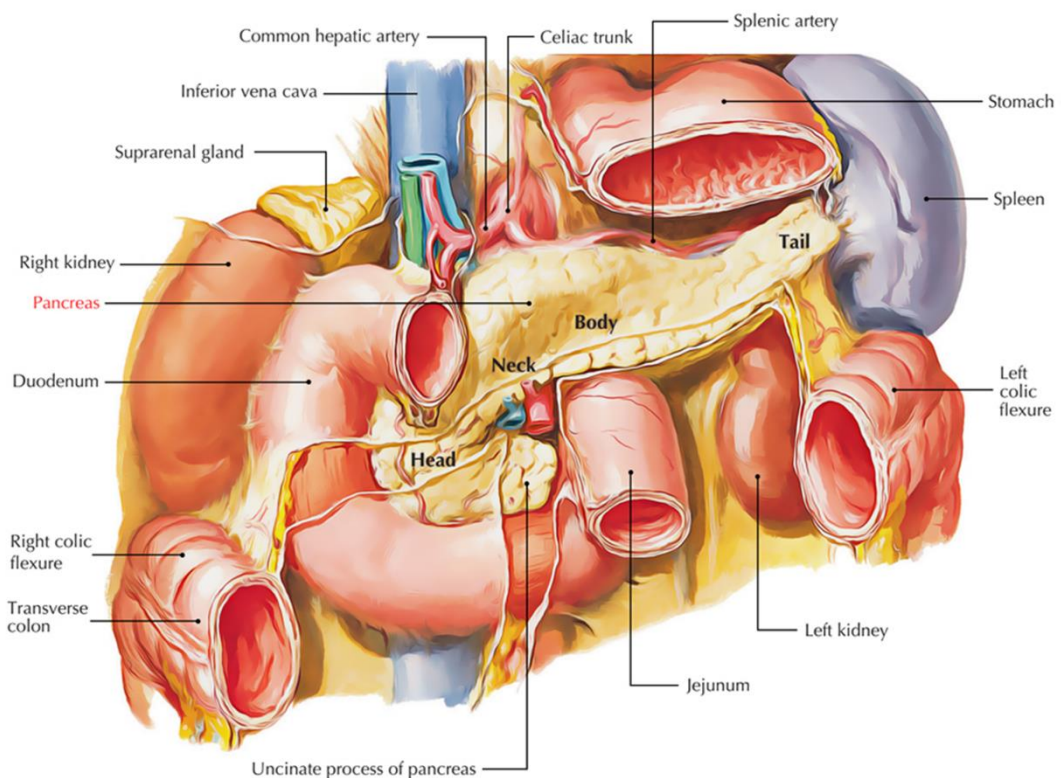


Figure 1.1: Schematic depicting the anatomical relations of the pancreas [462].

The head is the widest part of the pancreas, and lies within the descending and horizontal portions of the duodenum. The uncinete process extends medially from the inferior portion of the head, under the body of the pancreas, to lie posteriorly to the superior mesenteric vessels. The neck of the pancreas is located between the head and body. This portion lies anterior the superior mesenteric vessels and the origin of the hepatic portal vein – formed by the union of the superior mesenteric and splenic veins. The body of the pancreas is located centrally, lying posterior to the stomach and antero-laterally to the superior mesenteric vessels. Finally, the tail lies medially and in close proximity to the hilum of the spleen. It is enclosed within the splenorenal ligament alongside the splenic vessels [1].

The pancreas has an extensive arterial blood supply, from the pancreatic branches of the splenic artery and also the superior and inferior pancreaticoduodenal arteries which are branches of the coeliac trunk and superior mesenteric arteries, respectively. Venous blood drains from the head of the pancreas into the superior mesenteric branches of the portal vein and into the splenic vein from the remainder [1].

The exocrine component of the pancreas has a lobulated structure composed of clusters of cells, known as acini which are responsible for the production of digestive enzyme precursors. A series of short intercalated ducts drain adjacent lobules into a network of intralobular collecting ducts, which subsequently empty into the main pancreatic duct. The main pancreatic duct spans from the tail to the head of the pancreas where it connects with the common bile duct to form the hepatopancreatic duct, or the ampulla of Vater. This structure opens into the descending portion of the duodenum via the major duodenal papilla [1]. The endocrine component of the pancreas, responsible for metabolism/energy homeostasis is composed of clusters of endocrine cells known as the islets of Langerhans.

1.1.3 The anatomy of the islets of Langerhans

The islets of Langerhans (islets) are clusters of specialised cells located throughout the pancreas that are responsible for the production and release of hormones and peptides responsible for blood glucose homeostasis. Islets account for approximately 1–2% of the total weight of the pancreas [2] and consist of five distinct cell types; α -cells, β -cells, γ -cells, δ -cells and ϵ -cells (*Figure 1.2*). Glucagon-producing α -cells account for 15-20% of islet cells. Glucagon is a peptide hormone released in response to low blood glucose concentrations and responds by stimulating glucose production in the liver for the maintenance of adequate plasma glucose concentrations [3]. C-peptide and insulin-producing β -cells account for 65-80% of islet cells. C-peptide plays a critical role in the transformation of proinsulin, the prohormone precursor of insulin into mature insulin [4,5]. Insulin is a peptide hormone that is released in response to elevated blood glucose concentrations. It promotes the metabolism of carbohydrates, fats and protein by stimulating the absorption of glucose initiated by binding to receptors in the cell walls of liver, fat and skeletal muscle cells [6]. Somatostatin-producing δ -cells account for 3–10% of islet cells. Somatostatin is a peptide hormone responsible for inhibiting the release of both glucagon and insulin [7]. Pancreatic polypeptide-producing γ -cells account for 3–5% of islet cells. Pancreatic polypeptide is involved in the regulation of gastrointestinal motility, satiety, metabolism and the suppression of insulin and somatostatin secretion [8,9]. Ghrelin-producing ϵ -cells account for <1% of islet cells.

Ghrelin is a multifaceted gut hormone that stimulates growth hormone release, food intake and fat deposition. Ghrelin is famously known as the 'hunger hormone' [10].

Morphologically pancreatic islets are oval shaped and range from 50-500 μm in diameter [11]. The cellular organisation of human islets does not exhibit precise anatomical subdivisions, instead a more random interconnected arrangement exists between α -cells and β -cells [12,13]. However, more recent findings have proposed that the arrangement of islets is specific, with an outer layer of α - and δ -cells and a core of β -cells, similar to rodent islets [14]. Further discrepancy has arisen in relation to these cellular arrangements with emphasis on size of the islet and their location within the pancreas. Smaller sized islets are said to possess a greater proportion of β -cells, while islets located in the head of the pancreas are associated with a larger proportion of pancreatic polypeptide-producing γ -cells [14].

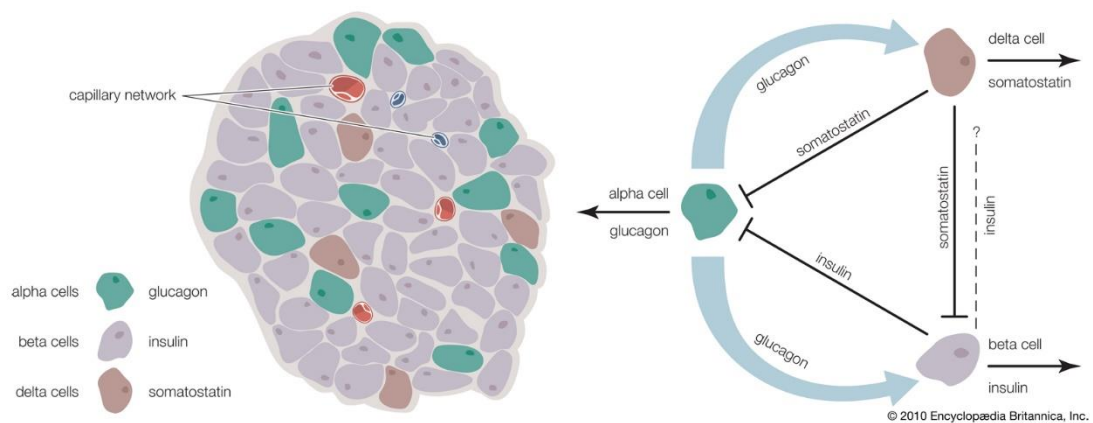


Figure 1.2: Islets of Langerhans. The islets of Langerhans contain α -cells, β -cells and δ -cells and that produce glucagon, insulin, and somatostatin, respectively. γ -cells (or PP) cells, are located at the periphery of the islets and secretes pancreatic polypeptide. These hormones regulate one another's secretion through paracrine cell-cell interactions [463].

The islets of Langerhans are a highly metabolic group of cells which require ample amounts of oxygen and glucose to function correctly. Typically they receive between 5-15 % of the pancreatic blood supply even though they account for as little as 1-2% of the healthy pancreatic mass [15–17]. These native islet cells are encompassed by a dense capillary network, with radial diffusion distances equating to $\sim 10\text{--}15 \mu\text{m}$ [18,19]. This high islet blood-flow rate guarantee that these specialised cells receive adequate oxygen and nutrient supply for survival and function [20].

1.2 Glycemic regulation

The physiological regulation of glucose metabolism is maintained via an endocrine signalling feedback loop between pancreas, liver, and glucose-consuming tissues. Through its numerous hormones, particularly glucagon and insulin, the pancreas maintains blood glucose levels within a very narrow homeostatic range of 70-110 mg/dL or 4–6 mmol/L (conversion factor: 1 mg/dL = 0.0555 mmol/L) [21].

1.2.1 Insulin

The effects of insulin include: increasing cellular uptake of glucose from the blood; promoting the cellular rate of glucose utilization as an energy source; promoting glycogenesis in liver and skeletal muscle cells; stimulating fat synthesis in hepatocytes and adipose tissue. These effects collectively cause a decrease in blood glucose levels to return to normoglycemia.

Circulating blood glucose is taken up by the facilitative glucose transporter GLUT2 located on the plasma membrane of pancreatic β -cells. Once transported inside the cell, glucose molecules undergo glycolysis (*Figure 1.3 (a)*). The free energy released in this process is used to generate the high-energy adenosine triphosphate (ATP) molecules, thus resulting in an increased ATP/ADP ratio. This causes the closure of ATP dependant potassium channels, causes an accumulation of potassium ions triggering depolarisation of the plasma membrane. This change in membrane polarisation activates voltage-dependent calcium channels. Increased intracellular calcium concentrations initiate the fusion of insulin granules with the plasma membrane and exocytosis of insulin [22]. Insulin secretion is a biphasic process (*Figure 1.3 (b)*), in which the majority of insulin is released 5-10 minutes after the glucose stimulus (phase 1), with the second slower phase of secretion occurring after 45 minutes [23–25].

Insulin circulates in the blood stream until it meets and binds to its specific receptor on insulin responsive tissues of the body namely skeletal muscle, adipose tissue and the liver which clears approximately 60% of endogenous insulin via the hepatic portal vein (*Figure 1.4*). The specific insulin receptor is a tyrosine kinase, an enzyme family contributing to the function of high-affinity cell surface receptors for many polypeptide growth factors, cytokines, and hormones. Without insulin, this receptor remains in its inactive configuration. However, once insulin binding occurs, it initiates a complex intracellular signalling network through (Insulin Receptor Substrate) IRS proteins, phosphatidylinositol 3-kinase (PI3K) and extracellular signal-regulated kinase cascades [26].

IRS1 is an important protein responsible for the recruitment and activation of enzymes to initiate the stimulation of glucose transport and more specifically the Glucose Transporter 4 (GLUT4) membrane translocation [27,28]. Insulin-stimulated glucose uptake is accomplished by insulin-sensitive GLUT4 transporters located on the plasma membrane of muscle cells, adipocyte, hepatocytes and other targeted tissues. This uptake of glucose into hepatocytes, insulin stimulates the synthesis and storage of glycogen while inhibiting glycogenolysis (*Figure 1.4*). As circulating glucose and insulin levels decrease, the GLUT4 transporters deactivate [27–29]. The insulin signalling pathway ceases with the degradation of insulin via endosomes and lysosomes and dephosphorylation of insulin receptors [27–29].

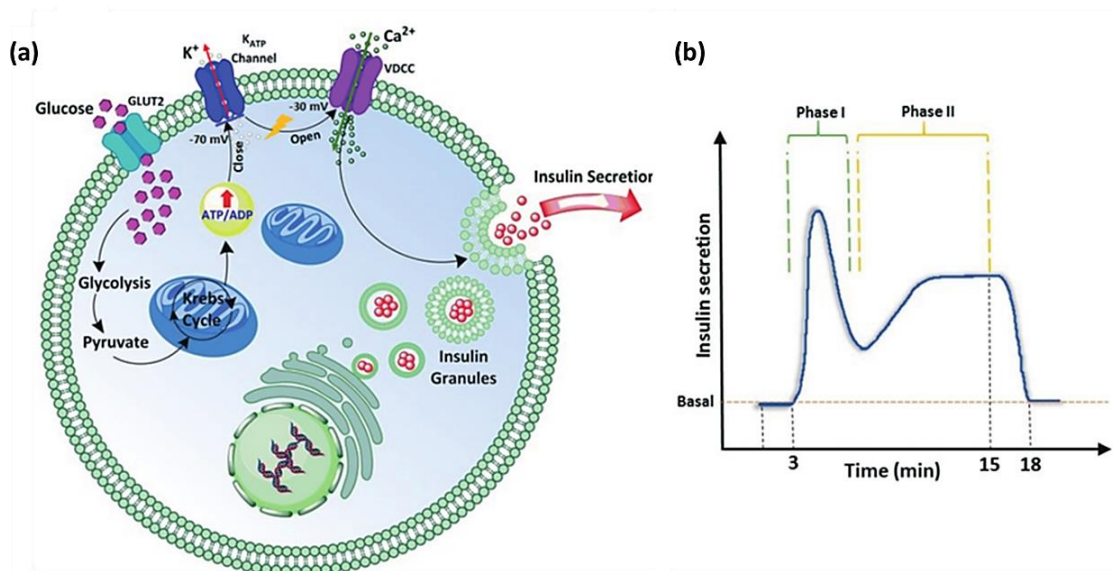


Figure 1.3: Glucose stimulated insulin secretion. **(a)** Pathway in pancreatic β -cells. **(b)** Biphasic insulin release profile [464].

1.2.2 Glucagon

Glucose homeostasis depends upon the synchronised release of glucagon and insulin from pancreatic alpha and beta cells, respectively, in a tightly regulated, multi-loop feedback system [30,31]. As described previously, elevations in blood glucose levels stimulate the release of insulin from the pancreas which promotes the uptake of glucose and use by insulin-dependent tissues, triggers glycogenesis in the liver and muscle tissue and also suppresses glucagon secretion [30–32]. As blood glucose decreases toward a hypoglycemic state, glucagon is released from the pancreas. In humans, pancreatic islets are composed of approximately 15-20% α -cells and 65-80% β -cells, hinting at the relative importance of glucagon secretion [12,33]. Various factors and hormones modulate glucagon secretion from the pancreatic alpha cell [34]. Together, these factors regulate glucagon secretion to prevent the potentially lethal state of hypoglycemia.

The cellular mechanisms governing glucagon secretion from α -cells is very similar to that which regulates insulin secretion from β -cells. At low concentrations of glucose, when the secretion of glucagon is stimulated, changes in membrane polarisation activate voltage-dependent calcium channels. Increased intracellular calcium concentrations initiate the fusion of glucagon-containing secretory granules with the plasma membrane and the exocytosis of glucagon [35].

Glucagon circulates in the blood stream until it meets and binds to its specific G-protein coupled receptors found predominantly on skeletal muscle and the liver cells which are major sites of glycogen storage. Upon entry into hepatocytes, glucagon promotes breakdown of glycogen to glucose (glycogenolysis), promotes glucose synthesis (gluconeogenesis), inhibits glycogen formation (glycogenesis), and mobilizes export of glucose into the circulation (*Figure 1.4*). Thus, glucagon provides a critical response to hypoglycemia [32]. However, glucagon acts as more than just counter-regulatory hormone to insulin. It also influences lipid metabolism, affects food intake, body weight, promotes autophagy, and has pleiotropic effects on the cardiovascular system [36–38].

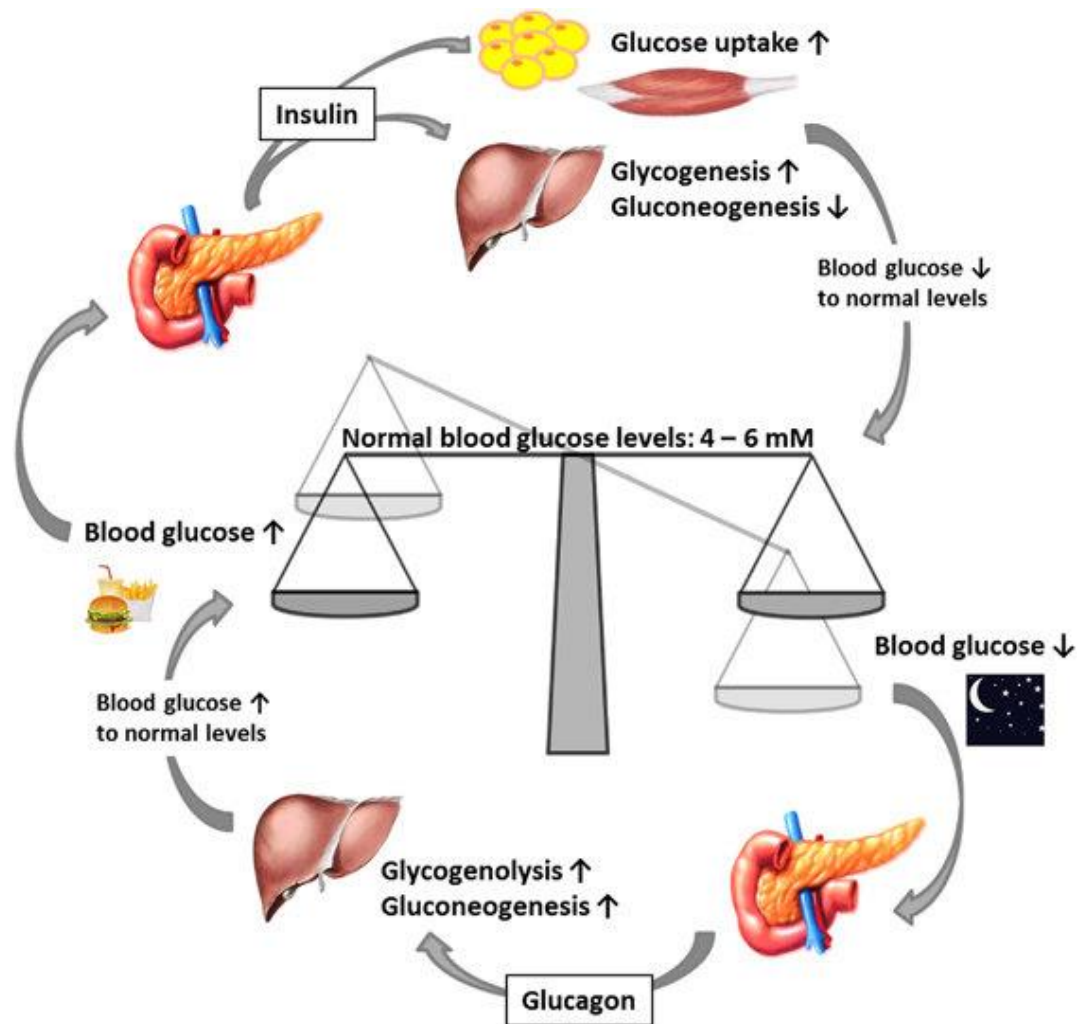


Figure 1.4: Glycemic regulation. Maintenance of blood glucose levels by glucagon and insulin. When blood glucose levels are low, the pancreas secretes glucagon, which increases endogenous blood glucose levels through glycogenolysis. After a meal, when exogenous blood glucose levels are high, insulin is released to trigger glucose uptake into insulin-dependent muscle and adipose tissues as well as to promote glycogenesis [465].

1.3 Diabetes mellitus

1.3.1 The global impact of diabetes mellitus

Diabetes mellitus (DM) is a chronic metabolic disease characterised by the dysregulation of glucose metabolism. DM is a major health problem that has reached alarming levels across the globe. In 2019, 463 million people were living with diabetes worldwide and this number is expected to rise to 578 million by the year 2030 and 700 million by the year 2045 [39] (Figure 1.5). It is estimated that 4.2 million deaths are attributed to diabetes and its related complications. The prevalence of this disease is associated with a substantial annual global health cost of approximately 760 billion USD and is estimated to rise to 845 billion USD by 2045 [39].

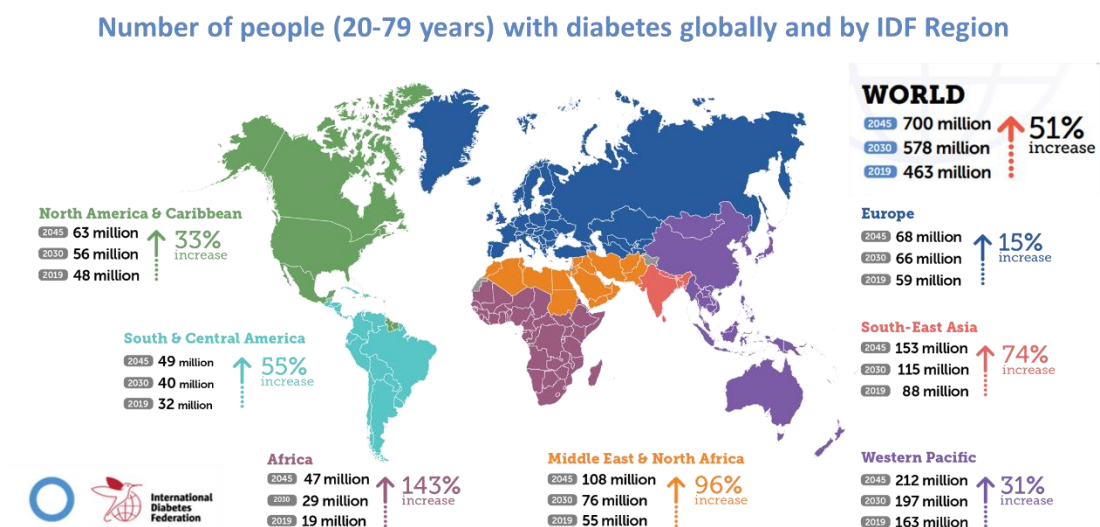


Figure 1.5: Number of people (20-79 years) with diabetes globally defined by region [39].

1.3.2 The pathophysiology of diabetes mellitus

DM is a group of metabolic diseases related to impaired insulin availability and/or efficacy within the body. As described previously, insulin is a key hormone involved in glucose homeostasis, that is released in response to elevated blood glucose concentrations. It promotes the metabolism of carbohydrates, fats and protein by stimulating the absorption of glucose initiated by binding to receptors in the cell membranes of liver, fat and skeletal muscle cells [6]. Numerous pathogenic processes are involved in the development of DM. These include autoimmune destruction of the β -cells with consequent insulin deficiency and abnormalities that result in resistance to insulin action [40]. Impairment of insulin secretion and/or defects in insulin action results in unregulated blood glucose levels which can lead to high blood glucose, hyperglycemia.

Uncontrolled hyperglycemia is the primary cause of symptoms of patients presenting with undiagnosed DM. Examples of associated symptoms include; polyuria, polydipsia, increased hunger and unexplained weight loss [41]. If left undiagnosed and/or poorly managed, hyperglycemia can lead to further complications such as; cardiovascular complications, retinopathy, nephropathy, and lower limb neuropathy [42]. A number of diagnostic criteria are used to determine the underlying mechanisms causing hyperglycemia that categorise DM into three main types: Type 1 (T1D), Type 2 (T2D) and gestational DM [43,44]. A patient presenting with any of the aforementioned symptoms can be diagnosed for T1D or T2D by:

- Random plasma glucose test ≥ 11.1 mmol/L
- A fasting plasma glucose test ≥ 7.0 mmol/L; or ≥ 5.6 mmol/L in gestational diabetes
- An oral glucose tolerance test, plasma glucose ≥ 11.1 mmol/L two hours after administering 75g anhydrous glucose orally; or ≥ 7.8 mmol/L in gestational diabetes
- Tests in the ranges above in the absence of symptoms require an additional plasma glucose test on a separate day to confirm a diagnosis

T2D, previously known as non-insulin-dependent, or adult-onset diabetes accounts for up to 90-95% of all cases of DM worldwide [45]. T2D is a progressive form of diabetes generally resulting from the body's ineffective use of insulin. The primary mechanism of T2D development is known as insulin resistance which impairs glucose uptake by target tissues, affecting normal glucose metabolism [46]. Insulin resistance is primarily caused by abnormal insulin secretion, due to prolonged instances of hyperglycemia. Increased insulin resistance increases insulin demand by causing the liver to incorrectly release glucose into the blood creating a higher demand for blood glucose regulation [47]. These increasing demands result in acute oxidative stress to the β -cells, causing progressive cell death and associated reductions in endogenous insulin production [48,49]. T2D is generally preventable, by staying a normal weight, exercising regularly, and eating properly [45]. However, the progression of T2D can be halted and even reversed with appropriate lifestyle changes [50]. If glycemic regulation remains sub optimal, an oral pharmacotherapy, metformin is used to manage insulin sensitivity and control blood glucose levels [51,52] however, disease progression may result in the need for insulin replacement therapy [53].

T1D, formerly known as juvenile diabetes, is less prevalent than T2D, accounting for 5-10% of all cases of DM worldwide [39,45]. The disease pathology is said to be caused by a complex relationship between a genetic predisposition to the disease and a number of environmental factors, triggering β -cell autoimmunity and consequent T-cell mediated destruction of β -cells in the pancreas [54,55] (*Figure 1.6*). To date, insights into the manipulation of the immune system have been increasing rapidly to search for potential therapies and treatments for T1D [56]. However, implementing treatments remain a challenge as interventions are typically administered preceding the immunological destruction peak ultimately, limiting the effect of potential treatments. A combination of pre-diagnosis combined with effective treatment strategy for autoimmunity are necessary for the prevention and/or development of T1D [56,57]. Unlike T2D, due to the functional impairment and consequent degeneration of entire β -cell mass in T1D patients, lifelong insulin therapy is required [58–61].

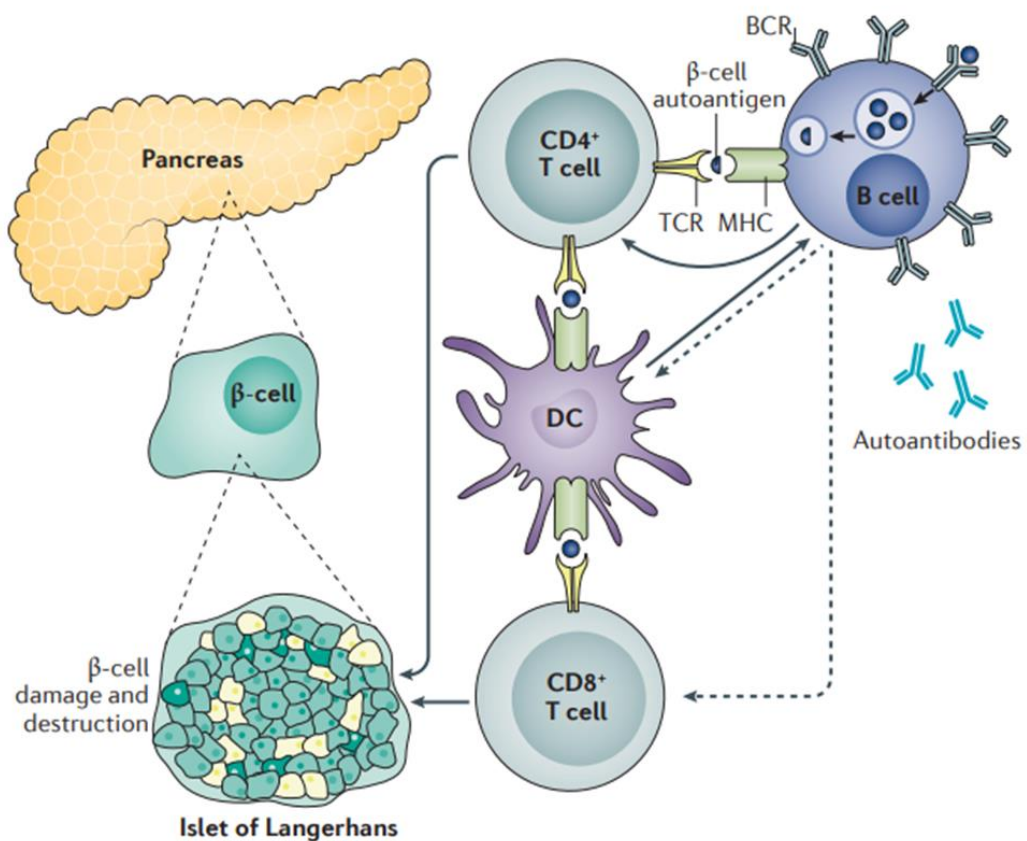


Figure 1.6: Pathogenesis of T1D. T-cells (CD4⁺ and CD8⁺) and dendritic cells (DC) interact with auto antigen presenting β -cells. This leads to the subsequent targeting of pancreatic islets by the T-cells for destruction [466].

1.3.3 Current Treatments

1.3.3.1 *Insulin therapy*

Due to the functional impairment and consequent degeneration of β -cell mass in T1D patients, T2D treatment strategies are not suitable. As a result, T1D require lifelong insulin therapy which is administered via multiple daily injections or subcutaneous infusion using an insulin pump [58–61]. Various insulin analogues with different onsets and durations of action have been developed to enable patients to maintain a tight glucose control. Optimum glycemic control calls for multiple-dose insulin regimens that mimic physiological insulin release. Analogue insulin is available in two main forms, short/rapid-acting insulin and long-acting insulin [62]. Insulin glargine is a long-acting, manmade version of human insulin. It ensures the maintenance of basal insulin for overnight and between-meal glycemic control [63]. Structural modification of this insulin molecule causes insulin glargine to precipitate within subcutaneous tissue and to form a depot that is gradually absorbed into the bloodstream [64]. Short/rapid-acting insulin, such as Lispro and Aspart are administered in conjunction with long-acting insulin, to cover ingested carbohydrate loads and treat hyperglycemia [65,66].

T1D patients have the vital responsibility of monitoring their blood glucose levels and administering exogenous insulin in response to glucose levels multiple times per day for the rest of their lives. Glucose regulation is difficult even for the most compliant patients as a variety of factors must be taken into consideration when calculating an insulin dose; plasma glucose levels, insulin/carbohydrate ratio, carbohydrate intake, intensity of physical exercise after injection, and individual insulin sensitivity. Any inaccuracy in insulin dosage can result in episodes of hypo- and hyperglycemia, which are the primary cause of diabetic complications [60,67]. Hypoglycemia occurs as a result of excess insulin and compromised glucose counter regulation and typically correspond with blood glucose levels < 70 mg/dL (3.9 mmol/L) [68]. Hypoglycemia can cause autonomic symptoms such as shaking, sweating, anxiety, palpitations and nausea and in extreme cases cognitive impairment, unconsciousness, seizures, and death [67,69,70]. Hypoglycemic unawareness occurs in approximately 40% of T1D patients and occurs as a result of prolonged exposure to low blood glucose, antecedent hypoglycemia, recurrent severe hypoglycemia and the failure of counter-regulatory hormones [71]. This is a dangerous condition that increases the incidence of unknowingly surpassing the initial autonomic symptoms and progressing to more extreme conditions, ultimately affecting a patient's safety and quality of life severely.

Hyperglycemia is associated with equally devastating complications and is characterised as blood glucose level > 180 mg/dL. Resultant complications include kidney failure, heart attack, stroke, blindness, nerve damage, and many other diseases [67]. A minority of patients suffer from a severe form of the disease known as brittle or labile diabetes. Brittle diabetics can often experience extreme fluctuations in blood glucose levels despite practising a good treatment regime, which can often result in hypo- or hyperglycemia [72,73].



Figure 1.7: Evolution of insulin therapy devices. **(a)** Insulin syringe and vial **(b)** Insulin pen **(c)** Test strips for collected blood. **(d)** Blood glucose monitor **(e)** Lancing device **(f)** Insulin pump [467].

As stated previously, self-monitoring blood glucose (SMBG) is fundamental for achieving adequate glycemic control. Traditionally a patient would monitor their blood glucose using a small blood glucose monitor device (*Figure 1.7 (d)*). A small pin-prick is used to draw blood and is then collected on a testing strip (*Figure 1.7 (c, e)*). This testing strip is inserted into the device where an electrochemical reading determines blood glucose concentration almost immediately allowing the patient to manage their blood glucose levels with insulin via syringe or food as necessary [74] (*Figure 1.7 (a)*). As this form of blood glucose monitoring only provides a blood glucose reading at a snapshot in time, it must be repeated multiple times daily to be effective.

Improvements in blood glucose monitoring led to the development of continuous glucose monitoring (CGM). This involves subcutaneous implantation of a sensor enabling glucose concentrations in the interstitial fluid to be measured. To ensure accurate functioning this must be calibrated daily by a SMBG reading. CGM devices obtain interstitial glucose data every five minutes which is then transferred to a separate recording device or a smart phone application to be viewed immediately and/or be saved for viewing later [75]. Through CGM devices (*Figure 1.8 (e)*), these phone applications can alert the patient to sudden changes in blood glucose levels allowing for quicker response times to hyper/hypoglycemic events [76]. CGMs sensor-signalling capabilities with wireless data transmission, has improved blood glucose management by providing real-time updates and recording blood glucose levels for review with a healthcare provider, and through alert systems to negate incidences of harmful glycaemic events [77].

1.3.3.1.1 Advancements in insulin administration

Technological developments in insulin administration and glucose monitoring have enabled diabetics to achieve greater glycemic control. Devices replacing the traditional vial and syringe, such as insulin pens [78,79] (*Figure 1.7 (b)*) and pumps [80] (*Figure 1.7 (f)*), have gained popularity due to their convenient and effective means of insulin administration [81]. Insulin pens offer greater convenience, discretion, and reduced pain upon administration, thus increasing patient preference, social acceptability, and treatment adherence. Furthermore, they are linked with increased dosing accuracy and safety features, to reduce the risk of inaccurate dosing and consequent hypo- and hyperglycemia [79,82–84]. Insulin pumps offer a more accurate retrospective and real-time continuous monitoring of blood glucose while simplifying patient's insulin requirements.

Insulin pumps are pocket-sized programmable battery-powered devices worn externally on the body. They contain a reservoir of insulin which is connected by tubing to an infusion set, a subcutaneous needle/cannula which is held on the skin and allows for the delivery of insulin without changing the needle or injection site for up to 3 days. Pumps are programmed to either release a low or basal rate of insulin continuously to mimic basal pancreatic rates or a bolus dose close to mealtime to control the rise in blood glucose after a meal or other hyperglycemic events.



Figure 1.8: Components of an insulin pump therapy. The image on the left shows how an insulin pump and continuous glucose monitoring (CGM) would be worn by the patient. The right images shows the **(a)** Insulin pump, **(b)** the insulin reservoir that is inserted into the pump, **(c)** the infusion set, consisting of the needle and cannula and adhesive patch to keep it in place, **(d)** the infusion set insertion device, to make it easier to place the cannula correctly and **(e)** CGM [93].

Bolus doses are managed by the patient and blood glucose monitoring is still required to ensure blood glucose is effectively controlled. The development of insulin pumps continues to cater to the specific needs of the users.

Manufacturers such as Roche, Abbott Laboratories, Medtronic (*Figure 1.9*) etc. strive to produce alternative needle sets, cannulas, tubing sizes to accommodate and customise for each patients' lifestyle and body composition. Insulin pumps remove a great deal of responsibility from T1D patients providing them with enhanced glycemic control [85] however, increased incidences of unnoticeable biochemical hypoglycemia can occur, which could potentially impair cognitive function [86].

In recent years a new form of insulin pump has been developed referred to as patch pumps [87]. Unlike traditional insulin pumps, the patch pump essentially untethers the patient, working in the absence of any tubing by attaching directly onto the skin. They attach discreetly to the infusion site where a cannula inserts directly from the device into the skin and is wirelessly controlled by a separate device or a smart phone application. They permit the delivery of basal insulin, bolus insulin, or both [87,88]. The majority of patch pumps have some disposable components while others are completely disposable. 5% of people who use insulin pumps or about 25,000 people worldwide have opted for patch pumps with most using the Omnipod by Insulet [87,89]. Like other patch pumps such as JewelPump by Debiotech [90], Solo by Roche [91], Libertas by BD [92], and Medtronic PatchPump [93], the Omnipod pump contains a reservoir, angled diffusion set automated inserter, pumping mechanism and power source, all contained within a small water tight casing. Currently the devices must be prefilled by the user however, these will be redesigned to accommodate insulin cartridges in the future.

Like traditional insulin pumps the life-span of patch pumps is limited to approximately 3 days due to stickiness of adhesive, insulin volume capacity and the foreign body response to the cannula restricting the delivery of insulin.

1.3.3.1.2 The artificial pancreas

Although the use of insulin injections and pumps are life-prolonging treatment methods, they fail to mimic real-time secretory patterns of pancreatic β -cells or prevent long-term complications [94,95]. The artificial pancreas, is a closed-loop system combining the advancements of CGM and exogenous insulin pumps with a dosing algorithm to create a new generation of medical device for glycemic regulation in T1D patients [96,97] (*Figure 1.9*).

The artificial pancreas aims to improve the quality of life and care of patients by removing the responsibility of full glycemic control from the patient apart from self-monitoring of blood glucose testing to ensure system calibration [96,97]. Weisman *et al* [98] previously demonstrated that artificial pancreas systems uniformly improved glucose control in a multi-centre systematic review and meta-analysis of out-patient randomised control trials, despite heterogeneous clinical and technical factors. The artificial pancreas is still in the early stages of development and is limited by the available algorithms. To ensure accuracy, manual inputs of self-monitored blood glucose levels twice daily to ensure system calibration, mealtime carbohydrates and current blood glucose level to provide a bolus dose of insulin. However, as companies such as Bigfoot Biomedical, Johnson & Johnson, Medtronic, etc. [99] fuel advancements of algorithms and reduce user input requirements, the artificial pancreas remains a promising future system for the treatment of T1D [100].

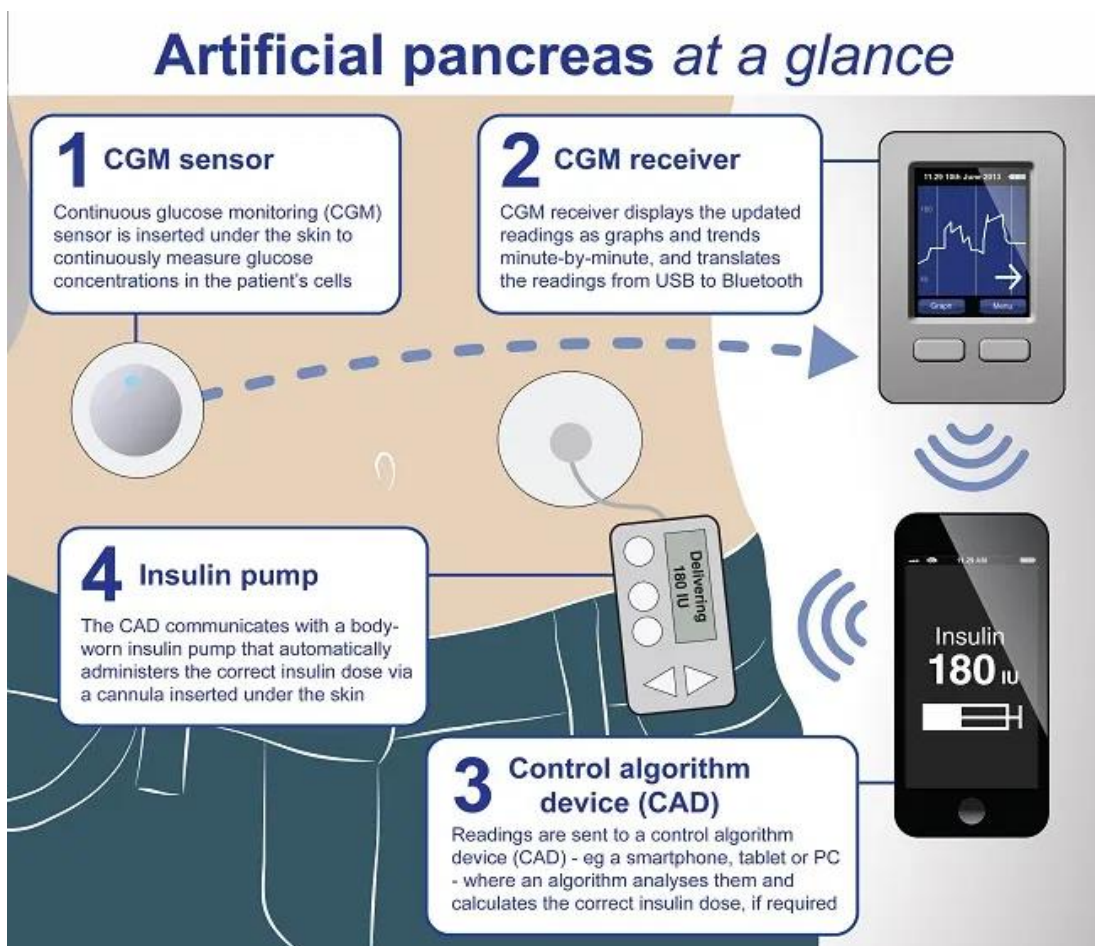


Figure 1.9: An outline of the function of the closed loop system that makes up the artificial pancreas [468].

1.4 Transplantation

Successful whole pancreas or pancreatic islet transplantation has been demonstrated to be efficacious in significantly improving the quality of life of diabetic patients. The aim of these transplantations is to restore sufficient β -cell mass, enabling patients to endogenously produce the insulin required for optimal glycemic regulation while minimising the risk of human error associated with self-administration of insulin. After several decades, insulin therapy can become inefficient increasing the risk of developing complications such as hypoglycemic unawareness, marked hyperglycemia, ketoacidosis and lifestyle degradation with loss of independence. In this instance, transplantation may be offered as a treatment to restore physiological regulation of glycemia and improve the general state of the patient [101].

1.4.1 Whole pancreas transplantation

Whole pancreas transplantation is a procedure which can be efficacious in the reversal of diabetes and is typically performed only after 20 years of established diabetes. This is a highly invasive surgical procedure requiring subsequent lifelong immunosuppression to prevent rejection of the graft and future autoimmune destruction. Immunosuppressive regimes are associated with long term risks and side effects such as opportunistic infections, an increased risk of malignancies, and bone marrow suppression and cytopenia [102]. There are also a number of specific side effects associated with specific drugs. Corticosteroids are commonly used in immunosuppression and chronic corticosteroid use is associated with side effects such as weight gain, osteoporosis, hypertension, hyperlipidaemia, and glucose intolerance [103]. Some examples of non-steroidal immunosuppressant and their long-term side effects are: calcineurin inhibitors, tacrolimus and cyclosporines, which are associated with nephrotoxicity and neurotoxicity [104]; azathioprine is associated with hepatotoxicity; and there is an increased cancer risk in patients using these agents for immunosuppression long-term [105].

The first reported whole pancreas transplantation was performed 50 years ago at the University of Minnesota, and remains the current gold standard for the restoration of β -cell mass today. Over 23,000 transplants have taken place, in both T1D and T2D patients [42]. Due to the highly invasive nature of the surgical procedure and the requirement for systemic immunosuppression to prevent graft rejection, strict patient selection criteria exist [106]. Firstly, the patient must have end stage renal disease and plan to or have had a kidney transplant. Pancreas transplantations are commonly performed as simultaneous organ transplantations with the kidney.

Diabetic nephropathy and kidney disease are a serious complication of DM, affecting 20-40% of all patients with T2D, and results in a large degree of morbidity and mortality [107]. The risk of major complications of two surgeries is minimised by performing the surgeries simultaneously; as a result, more than 80% of all pancreas transplants are as part of a simultaneous kidney-pancreas surgery [108]. Alternatively, a pancreas transplant may be necessitated without a simultaneous kidney transplant in diabetic patients with frequent wide fluctuation in glycemic levels, with a high risk of life-threatening hypoglycemia [106].

1.4.2 Pancreatic islet transplantation

Pancreatic islet transplantation has become an established approach to β -cell replacement therapy, returning endogenous insulin production to diabetic patients [72,73]. In contrast to whole pancreas transplantation, islet transplantation is a minimally invasive procedure. Advancements in techniques for islet isolation, islet culture, and peritransplant management of the islet transplant recipient has resulted in substantial improvements in metabolic and safety outcomes for patients. This form of treatment has been investigated since the 1970s, when Ballinger *et al* demonstrated glycemic regulation following islet transplantation in both syngeneic and allogeneic settings in rodents [109]. Concurrent research identified the liver as the most efficient site of engraftment following portal vein infusion [110] which was followed by validation of intrahepatic autologous islet transplantation in canines [111]. In the 1980s the first patient series of total pancreatectomy with islet autotransplantation for the treatment of chronic pancreatitis, demonstrating in some cases prevention or amelioration of postpancreatectomy diabetes [112]. Decades of research has provided proof of principle for the use of the liver for transplantation of isolated autoislets establishing the possibility for use of alloislets for treatment of humans with T1D. For patients with T1D or insulin-deficient forms of diabetes, isolation of islets from a deceased donor pancreas with intrahepatic transplantation of allogeneic islets can ameliorate problematic hypoglycemia, stabilise glycemic lability, and maintain on-target glycemic control, consequently with improved quality of life, and often without the requirement for insulin therapy [113]. However, efficacious outcomes are primarily dependent upon the numbers of islets transplanted that survive engraftment, recipients of autoislets are limited to receive the number of islets isolated from their own pancreas, whereas recipients of alloislets may receive islets isolated from more than one donor pancreas.

The development of alternative sources of islet cells for transplantation, whether from autologous, allogeneic, or xenogeneic tissues, is an active area of investigation that promises to expand access and indications for islet transplantation in the future treatment of diabetes [113]. Islet transplantation today consists of two main steps; islet isolation and transplantation of isolated islets.

1.4.2.1 Islet isolation

Islet isolation and purification from the surrounding pancreatic parenchyma was of paramount importance to ensure successful translation of islet isolations to the clinic. Research into improving the purity and viability of isolated islets for transplantation several research groups [114,115] led to the publication in 1988 of an automated method for isolation of human pancreatic islets using the Ricordi Chamber by Camillo Ricordi [116]. This process firstly involves perfusing the pancreas with a digestive enzyme. The pancreas is divided into two main halves which are cannulated individually. The pancreas is then perfused with the digestion solution; after which it is distended. The fat is removed and then the pancreas is cut into smaller pieces to facilitate transfer to the Ricordi Chamber [117]. The Ricordi Chamber consists of two stainless steel chambers separated by a 280 μ m mesh. The pancreas and glass marbles, to aid with mechanical digestion, are placed in the bottom of the chamber before additional digestive enzymes are added. The wire mesh is placed over the top and the Ricordi Chamber is fully assembled by adding the top chamber and closing [116]. This is then connected to the digestion circuit. This digestion circuit enables a solution to be circulated through the entire system to heat the pancreas, gradually dilute collagenases and collect the islets (*Figure 1.10*). The islets are then purified further using a gradient method, using specific medias of different density to isolate the islet tissue, such as a Ficoll Gradient [118]. Ficoll is a hydrophilic polysaccharide dissolved in the media to increase the density and create a gradient. Isolated pancreatic tissue is washed of collagenase solutions and then suspended in heaviest density of the gradient. Subsequently, gradually lower densities are overlaid to form the gradient. Multiple layers of Ficoll are used to separate the islets by purity. The top layer of Ficoll contains isolated fat and connective tissues. The first layer of gradient will have the purest isolation of tissue. The next layer will be less pure but is still collected, as many islets remain here. The isolated islets are then washed of Ficoll and suspended in culture media before use. This method was first applied in 1990 by Scharp *et al* to the first case of allogeneic islet transplantation for T1D resulting in a short period of insulin independence [119].

Isolated islets are measured and counted according to islet equivalents (IEQ). An IEQ is a standardised islet volume, where one IEQ is a perfectly spherical islet of 150 μ m. Islets are counted within 50 μ m ranges and correction factors are used to convert the counted islet diameters into IEQs [120,121]. On average, islet yield can range from 250,000 – 400,000 IEQ per pancreas, highlighting that the protocol is not perfect, and a large number of islets are lost throughout the process. The islet transplantation procedure needs 10,000 IEQ/kg of the recipient for successful insulin independence, with a minimum of 5,000 IEQ/kg needed to see improvement in glycemic control, and 10,000 IEQ/kg needed for insulin independence. As such, in an average 70kg patient, between two and three pancreases are required to provide sufficient IEQ for a successful procedure [122,123].

As mentioned previously the site of transplantation of pancreatic islets is imperative, for supplying oxygen and nutrients to the isolated islets; although isolated islets are functionally intact, they have lost their vascular blood supply. The hepatic portal vein was identified very early as a potential site for efficacious islet transplantation [124]. The portal vein can be accessed non-invasively through the use of a percutaneous catheter which helps to minimise the surgical risk of the procedure [81]. The vascular transplantation of the islets is highly attractive as it provides direct access to oxygenation and nutrient supply.

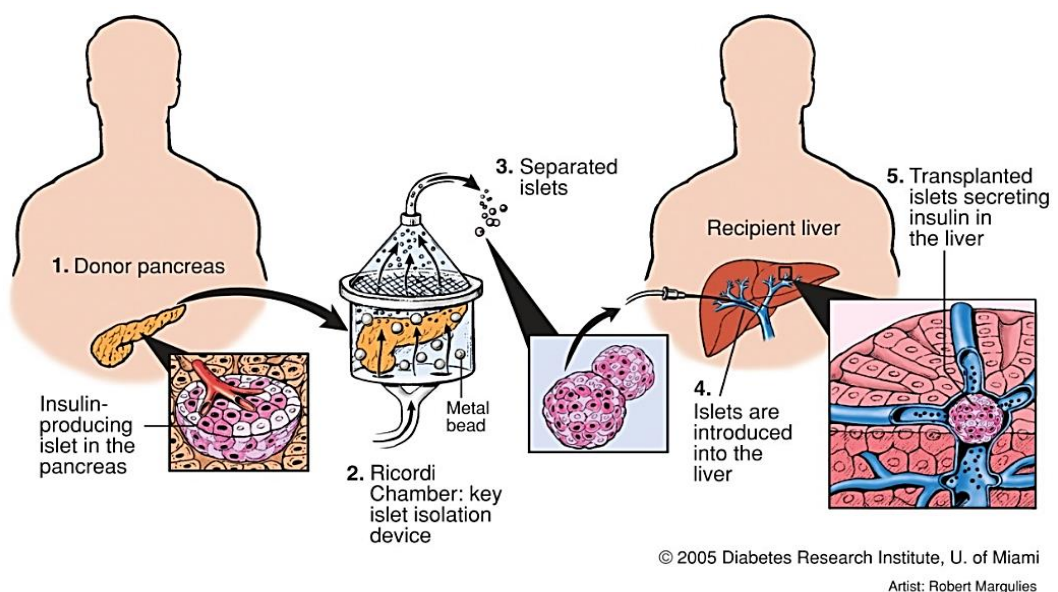


Figure 1.10: Schematic outlining the process of islet isolation from the human pancreas. The Ricordi Chamber was a key device designed to automate the separation of islets from the bulk of pancreatic acinar tissue.

1.4.2.2 Transplantation and the Edmonton protocol

The first successful islet transplantation was performed almost 30 years ago, by *Najarian et al* and *Largiadér et al* [125]. However, it was not until 2000 and the development of the Edmonton protocol, led by James Shapiro, that insulin independence was achieved [123]. This established the need for transplantation of a sufficient islet β -cell mass to attain insulin independence and near-normal glycemic control in humans with T1D. It also required the avoidance of glucocorticoid use in the immunosuppression regimen to avoid islet toxicity and insulin resistance [126]. In this study, seven T1D patients underwent an immunosuppressive regimen which allowed for a significant increase in islet viability after transplantation. Islet isolation was performed as described in the previous section and transplanted while using an immunosuppression regimen consisting of sirolimus, tacrolimus and daclizumab [123]. Over a median follow-up of 11.9 months, all patients were insulin free. The results of this study caused a dramatic increase in clinical islet transplantation activity worldwide. A successful transplantation of islets allows the patient to endogenously produce and control blood glucose, with up to 44% of treated patients being insulin free for up to three years [72].

However, Islet cell transplantation has not become the gold standard treatment for T1D due to several limitations including clinical success rates not yet comparable with whole organ transplantation, a shortage of high-quality donors for islet isolation, and the high cost of a specialized human islet cell isolation facility. The risk-benefit ratio of islet cell transplantation must be carefully considered when electing a patient for surgery. Due to the shortage of organs for transplantation and the risks associated with lifelong systemic immunosuppression mean the transplant is normally only performed on patients who fall into high risk groups of diabetics, with unstable (or brittle) T1D with severe hypoglycemic unawareness who have failed conservative medical management. These factors combined have led to a broad range of research to find alternative methods for islet transplantation.

1.5 Extravascular islet transplantation

Significant progress has been accomplished in the outcomes of clinical islet transplantation such as, improvements in immunosuppression and preparation of sufficient quantities of highly viable islets for transplantation [113,127]. Although intravascular transplantation provides nutritional and physical support for islets, the hepatic portal vasculature may be considered a hostile environment that limits successful islet engraftment and function [128]. Two of the biggest challenges facing the intravascular islet transplantation procedure are the need for life-long systemic immunosuppression and the requirements for multiple donor pancreases to reach the 10,000 IEQ/kg body weight for a successful treatment. As a consequence many investigations in this field have pursued alternative extravascular implantation sites, aim to establish an unlimited source of islet tissue for transplantation and/or encapsulation of the islets/cells within an immunoprotective supportive biomaterial in order to optimise islet engraftment and function, reduce necessary implantation mass, and decrease immunogenicity [129,130]. This approach is referred to as a 'bioartificial pancreas' [131].

1.5.1 Sources of cells for transplantation

The number of human islets available for transplantation is a major limitation with an average 70kg male patient requiring upwards of 700,000 IEQ for a successful transplantation. Previous research has demonstrated that a minimum of 250,000 IEQ are required to be isolated to be considered a successful isolation procedure [132,133]. In order to reach this target IEQ, a minimum of three donor pancreases are required for a successful islet transplantation using the Edmonton protocol per recipient. To put these numbers into context, in 2018, there were a total of 81 deceased organ donors with approximately 20,000 people suffering from T1D in Ireland [39,134]. This statistic is common to all countries, demonstrating the scarcity of donor pancreases versus the potential demand. Therefore, the establishment of an unlimited source of islet tissue for transplantation has been a long-sought-after goal.

Xenotransplantation of pancreatic islets has been studied as a potential option for the treatment of diabetes for many years, with the first pancreatic xenotransplantation being performed in 1894; pieces of sheep pancreas were implanted subcutaneously and demonstrated some effect in reducing blood glucose levels [135]. It was not until 1994 that fetal porcine islet like cell clusters were transplanted to 10 human patients, and although the treatment was not efficacious, it was shown that the xenografts could survive for many months [136].

Porcine islets have been extensively studied as a potential source of islets for xenotransplantation. Similarities between porcine and human insulin are well documented, contributing to the use of porcine insulin prior to the development of conventional manufacturing processes for human insulin [137]. Porcine islets share a similar size and morphological arrangement to human islets, consisting of a core of β -cells with some islets containing α -cells at the centre [13,138]. Pig islets are an ethically sound source of mammalian islets, as opposed to islets from non-human primates, and a near unlimited supply of pig islets could be made available through controlled farming [135]. Like all transplantations, rejection of transplanted islets is a risk. However, xenogeneic islets may induce a larger immunological reaction than allogeneic tissue, increasing the risk of rejection, ultimately requiring a more intensive immunosuppression regime [139,140]. Likewise, the use of xenogeneic porcine islets may increase the potential for transmission of zoonotic infections such as porcine endogenous retroviruses. However, recent advances in genetic engineering have enabled the breeding of pigs with significantly lower immunogenicity [141] and retroviral burden [142–144]. that ideally would enable β -cell replacement therapy with less immunosuppression than is presently required for alloislets. The advances in and availability of pig islets for xenotransplantation make them a very useful alternative to human islets in the treatment of T1D. Pig islets will likely act as a useful bridge in the islet transplantation therapy, between allogenic donor islets and iPSCs.

Recent progress in the generation of functional islet β -cells from human stem cell sources has raised hope for the establishment of another unlimited source of islet tissue for transplantation [145]. Induced pluripotent stem cells (iPSCs) are derived directly from adult tissues (*Figure 1.11*). These cells bypass the need for embryos, and can be made in a patient-matched manner, meaning that each individual could have their own pluripotent stem cell line. These unlimited supplies of autologous cells could be used to generate transplants without the risk of immune rejection. Several research groups have successfully differentiated autologous cells into functional β -cells [146,147], the results of the first clinical trial of transplanted human partially differentiated endocrine progenitors of β -cells for the treatment of diabetes will be available in the near future [148]. However, a major limitation is that patient iPSC-derived β -cells have demonstrated modest function, with animal studies revealing that these cells require a long period (12-19 weeks) post transplantation to functionally mature. Without this maturation period patient iPSCs simply cannot establish normoglycemia therefore creating the need to establish a functional autologous source of replacement β -cells.

Millman *et al.* have started to address this problem by developing patient derived iPSCs that have efficaciously differentiated and reversed pre-existing severe diabetes following CRISPR-Cas9 correction of WFS1, a diabetes-inducing gene variant in rodents. These gene edited patient derived iPSCs caused no teratoma or cystic structure formation. Correction of diabetes-inducing gene variant in patient-derived β -cells could potentially be used as an autologous source that could be implanted back to a diabetic patient without the need of immunosuppressants [149].

Companies such as SERAXIS and Semma Therapeutics have developed their own forms of iPSC-derived β -cells, which are encapsulated and delivered in immunoprotective devices [150]. SERAXIS has submitted an Investigation New Drug application for a combination product based off preclinical trials that demonstrated SeraGraft™, their immunoprotective device is retrievable, biocompatible and protects SR-01, their iPSC-derived β -cells in immune-competent diabetic mice models and promoted vascularisation without inducing an FBR [151]. While, Semma Therapeutics have previously demonstrated successful restoration of glycemic control for over 70 days in diabetic rodents and also demonstrated maximal cell survival, minimal FBR, and sustained insulin secretion in response to stimulation in healthy pigs [152]. These proof of concept preclinical studies led to the \$950 million Vertex Pharmaceuticals acquisition [153]. These macroencapsulated iPSC-derived β -cells are expected to enter a clinical trial early 2021 in patients with T1DM [152,154]

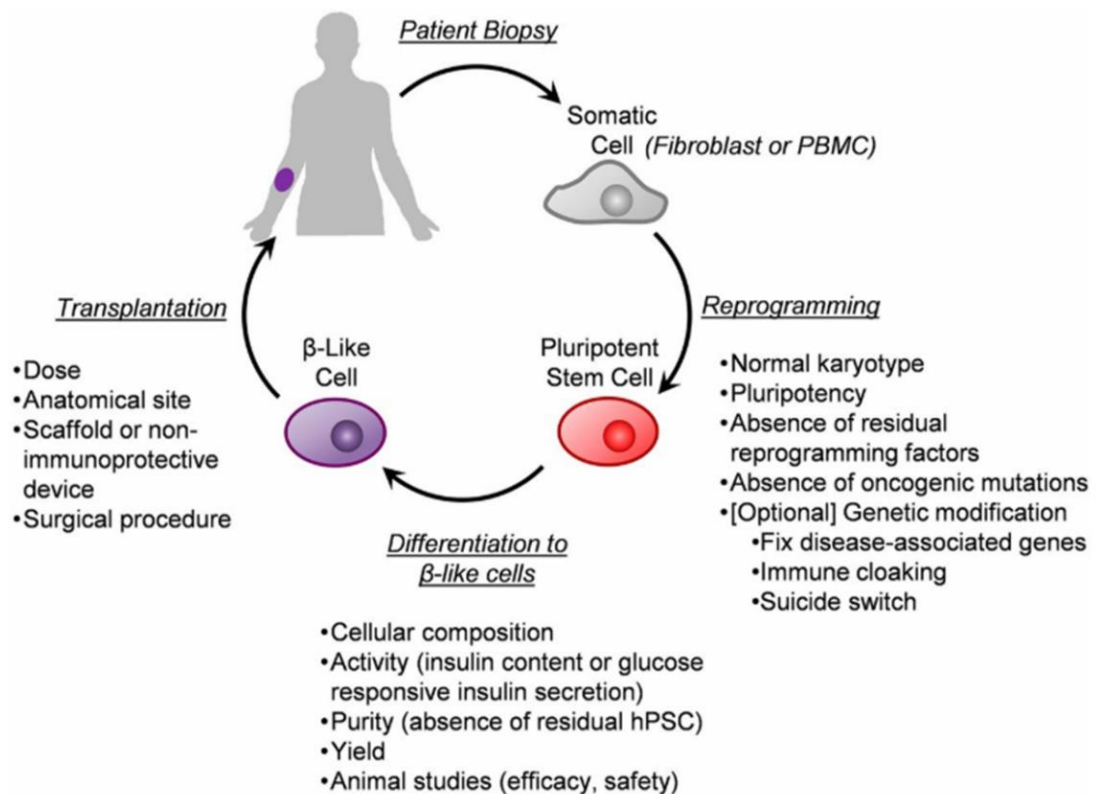


Figure 1.11: Overview of utilising a patient’s own somatic cells for a cell transplantation to treat T1D. The patient’s somatic cells are harvested and reprogrammed into iPSCs; these cells are cultured to a suitable yield and differentiated into an insulin producing β -cells; the β -cells can now be transplanted back into the patient [146].

1.6 Cell encapsulation technology

Cell encapsulation technology permits islet cell survival in the absence of immunosuppressive drugs. The principle of encapsulation is that transplanted cells are contained within an artificial compartment separated from the immune system by a semipermeable membrane. The capsule should protect the cells from potential damage caused by antibodies, complement proteins, and immune cells. Therefore, the capsule is often referred to as an “immunoisolation device” [155]. This was originally demonstrated by Prehn *et al.* from as early as 1954 who utilised a type of immunoisolation instrument called the diffusion chamber device [156]. In that study, the diffusion chamber device was used to prevent the homograft from inducing an immune reaction in the host. Subsequently, this technology was used to protect transplanted cells, known as “artificial cells” [157–161]. Given that isolation and transplantation of islets was well established, encapsulation technology was soon applied in the field of islet transplantation.

Many types of encapsulation technologies have been investigated over the last three decades in different animals such as mice [162], rats [163], dogs [164,165], and monkeys [166,167]. These studies demonstrate the feasibility of restoring normoglycemia by implanting allo- and xenografts without immunosuppression. The major challenges in the development of optimal encapsulation devices are the levels of biocompatibility, immunoprotection, all while maintaining the viability of cells. Biomaterials, including polymers, are the most important aspect for the fabrication of immune-isolating capsules. The biomaterial can provide additional secondary-properties such as flexibility and mechanical resistance to maintain the viability of the encapsulated material.

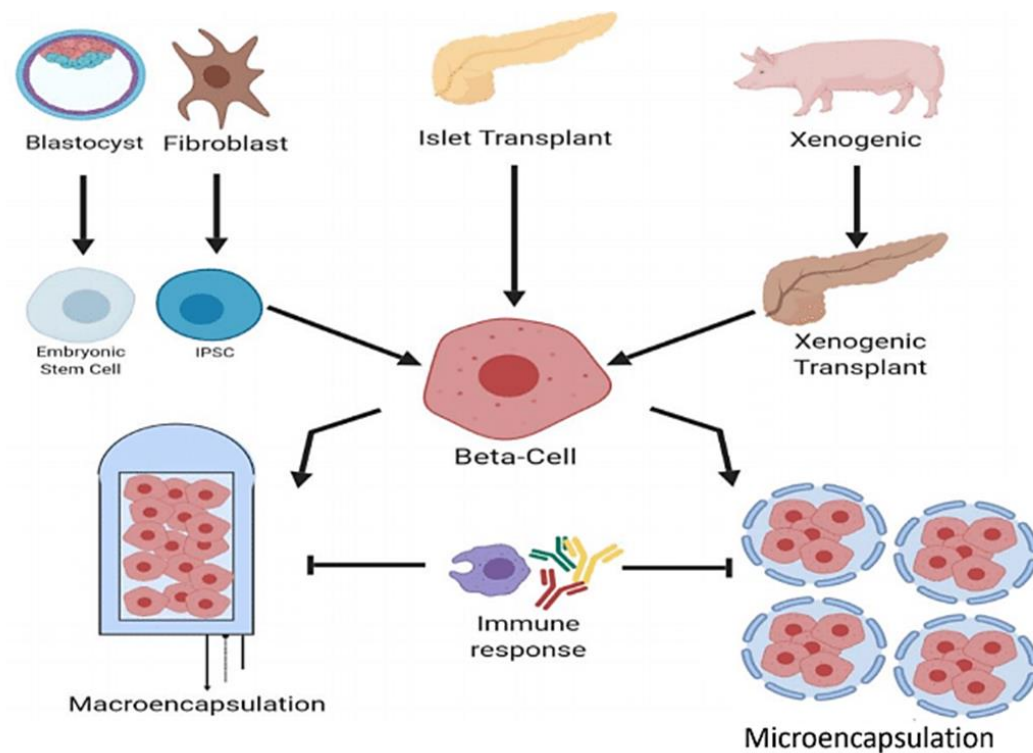


Figure 1.12: Overview of current encapsulation processes for pancreatic islets/ β -cells. Various sources including embryonic stem cells, reprogrammed fibroblast derived Induced Pluripotent Stem Cell (iPSCs), pancreatic islet transplants, and xenogeneic islet sources have been used to derive β -cells for use in diabetic encapsulation devices. The distinction between macro and micro-encapsulation is dependent on the volume being encapsulated. (R. Bagnall M.Sc.)

Encapsulation systems are commonly separated into two categories, intravascular and extravascular devices. The latter can further be divided into macroencapsulation and microencapsulation devices. The macroencapsulation and microencapsulation classifications depend on whether it contains one or more islets in the device. Cells within the capsules can also release insulin to control blood glucose levels, since this membrane enables small molecules to diffuse in (glucose, oxygen, and nutrients) and out (metabolic wastes) [155,168]. Thus, the encapsulation system is also regarded as a “bioartificial pancreas.” Details of micro- and macroencapsulation which have progressed to clinical trials are summarised in Table 1.1.

1.6.1 Microencapsulation systems

Microencapsulation involves surrounding individual β -cells within a semi-permeable material enabling therapeutic cell function without eliciting an immune response (*Figure 1.12*). The semi-permeable material not only facilitates the release of insulin but also allows for nutrient diffusion needed for healthy cell function. The main advantages of the microencapsulation system over macroencapsulation are its stable mechanical structure, large surface area-to-volume ratio, and improved diffusion profile. Due to the flexible and adjustable characteristics, the microcapsules are mostly fabricated from hydrogels. The principle of making microcapsules is based on the envelopment of individual islets in a droplet, which is transformed into a rigid capsule by gelification (in the case of alginate beads) followed by polycation coating (in the case of multiple-layered microcapsules).

Over the past 30 years, hydrogels including alginate [169], poly(hydroxyethyl methacrylate-methyl methacrylate), agarose [170], acrylonitrile copolymers, chitosan [171], and polyethylene glycol (PEG) [172] have been frequently used for microencapsulation. To date, the most preferable material for microencapsulation is alginate. Inexpensive alginate hydrogel microcapsules have dominated islet encapsulation research since their introduction in 1980 [173]. The nearly instantaneous gelation mechanism of these seaweed-derived alginate polymers enables simple fabrication of microcapsules that can be easily injected into a patient. Additionally, these capsules have been established as both durable and non-toxic to host organisms [165,174,175]. Another material of interest for encapsulation is hyaluronic acid (HA). HA-based hydrogels have been steadily gaining recognition as an interesting class of biomaterial for tissue engineering and cell therapy applications due to their unique mechanical and biological properties [176,177]. However, due to the foreign nature of hydrogel material, they are notoriously prone to fibrotic overgrowth, ultimately leading to necrosis of encapsulated cells and premature graft failure [167,175,178].

Some progress has been made with the development of ultra-purification processes, surface treatments, co-encapsulated materials, and more stringent control of capsule microstructure, but despite these advances, the performance of alginate microcapsules still does not meet the clinical needs for islet transplants [165,167,169,179].

1.6.2 Macroencapsulation systems

Macroencapsulation devices provide the dual possibility of immunoprotecting transplanted pancreatic islet cells while also being retrievable, the latter bearing importance for safety in future trials with stem cell-derived cells. Macroencapsulation involves encapsulation of islets within a single immunoprotective device that additionally can include a biomaterial to support islet viability and function (*Figure 1.12*). These devices are typically used to deliver islets extravascularly and essentially act as a bioartificial pancreas [155]. These devices are also typically retrievable or flushable and refillable, which is an important consideration for regulatory purposes. Macroencapsulation devices have been developed since the early 1950s and have emerged in various formats; pouch-like structures [180–182], hollow fibres [183,184], polymeric hydrogel sheets [185,186] and planar membranes [15]. The structure of the device depends on its primary goal, increased flow rate or decreased surface area. There are three main considerations when designing a macroencapsulation device: the need for a device shell, the use of a biomaterial to support islet viability and an extravascular site for transplantation.

The shell of a macroencapsulation device originated first as a transplantation chamber, membranous bags to hold transplanted cells without providing much function other than retaining the encapsulated cells [187]. Research eventually moved towards diffusion chambers that were formulated to be immuno-isolating. By reducing pore sizes in the diffusion chambers researchers found that they could impede the movement of immune cells and immune factors (immunoglobulins) into the device [188]. Immune cells can be readily blocked due to their large approximately 10 μ m diameter however, large antibodies (IgM) and complement proteins (C1q) could only be hindered at pore diameters of 30nm. To block cytokines the membranes must be even more selective, as Stokes diameters show small differences between factors such as TNF- α (3.80nm) and insulin (2.64nm) [189].

There has been a great deal of research into a suitable biomaterial to support islet graft viability following transplantation. A number of hydrogels have taken the fore-front of this research due to their tunable physical properties, biocompatibility and ability to further functionalise the backbone of the hydrogel to further improve functionality [190].

A number of sites have been investigated for extravascular encapsulation with key factors being to ensure there is sufficient space for the device and access to the vascular network to ensure the encapsulated islets are sufficiently oxygenated and sensitive to changes in blood glucose [191]. The intraperitoneal wall has been used in the past for its volume and ease of access in a surgical procedure [192]. The omentum has also been researched more recently as a highly vascularised tissue which could support a macroencapsulation device. To date studies have focused on transplanting naked islets to an omental pouch, but it is possible that a macroencapsulation device could be transplanted here also [193].

1.6.3 Challenges

While macroencapsulation and delivery to an extravascular site is a promising alternative to the current islet isolation protocol, there are a number of challenges that must be addressed when developing a macroencapsulation device. These challenges primarily arise as a result of the diffusional barriers to nutrients and oxygen into the device and the diffusion of products like insulin and waste out of the device. Hypoxia is a state of insufficient oxygen for cellular functions resulting in dysfunction and eventual cell death. In macroencapsulation devices the encapsulated islets have been isolated, destroying their complex microvasculature, and encapsulated within a biomaterial and shell. Immediately following transplantation, graft survival is reliant on diffusion of oxygen and nutrients from the surrounding environment or the transplantation site for survival. With a low oxygen pressure (pO_2) the encapsulated islets are at high risk of developing hypoxia induced cell death, necrotic cores and ultimately failure of the graft. Solutions to hypoxia can be built i) into the device through the inclusion of oxygenation technologies, ii) into site choice by choosing a suitably vascular such that the pO_2 is high enough to provide the encapsulated islets with sufficient oxygen [194] or by iii) various vascularisation strategies or prevascularising the implanted device before filling it with cells [195].

Diffusion of insulin out of a macroencapsulation device is a critical parameter in the design of the device, as failure of insulin to diffuse into the blood in response to raised glucose levels is a failure of the device to adequately treat DM. The diffusion of both glucose into the device and insulin out are time limited factors that must be accounted for in the device permeability [187]. Careful device dimension considerations could optimise diffusion across the membrane and biomaterial to address this challenge [196]. Fibrotic tissue forms when fibroblasts attach to the macroencapsulation device.

The fibrotic scar tissue is very damaging to the success of the device as it can prevent further vascularisation of the device, compounding the challenges that have previously been discussed [197]. Ultimately fibrotic response can be limited by shell design and material selection, where smoother shell surfaces prevent adhesion of fibrotic cells and choice of different materials may not activate fibroblasts and fibrosis can be avoided [192].

1.6.3.1 The foreign body response

Surgical implantation of biomaterials induces a series of events known as the foreign body response [198,199]. The implantation procedure results in a disruption of normal homeostatic mechanisms which trigger the typical host responses of inflammation and wound healing [200,201]. Following implantation, vascularised tissue is injured resulting in blood-material interactions and triggering occur the initial inflammatory responses [198–201] (Figure 1.13). Thrombus formation on the surface of the device caused by protein adsorption by blood serum proteins, and the recruitment of immune components forms the provisional matrix [202,203]. Generally, neutrophils predominate the implant site during the first several days following injury. As chemotactic factors for neutrophil migration are activated early in the inflammatory response, neutrophils are short-lived, disintegrating and/or disappearing after 24 to 48 h. Following migration from the vasculature, monocytes differentiate into macrophages. Monocyte migration may continue for days to weeks, depending on the injury and implanted biomaterial, as chemotactic factors for monocytes are activated over longer periods of time.

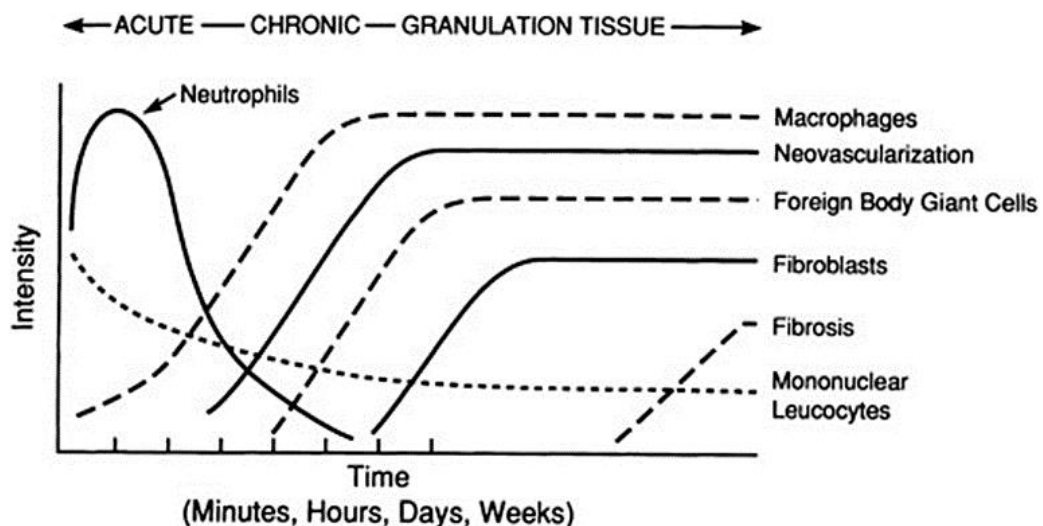


Figure 1.13: Inflammatory and healing processes that occur following the *in vivo* implantation of a biomaterial [469].

These macrophage populations migrate to the site of implantation in an attempt to phagocytose the foreign material however, the large size of the macroencapsulation device inhibits this process, leading to macrophage fusion and the creation of persistent multi-nucleated foreign-body giant cells which secrete several cytokines and chemokines [203,204].

These pro-inflammatory compounds further modulate the foreign body response by stimulating the migration of fibroblasts, which deposit several layers of fibrous collagen and matrix proteins at the device interface, forming a pericapsular overgrowth that can impair diffusion [205]. Myofibroblasts are also present at the site of implantation and they are associated with the over-production of collagen in pro-inflammatory reactions, ultimately regulating tissue contraction and fibrosis [206].

The foreign body response occurs at different magnitudes to all foreign material including natural and synthetic polymeric materials [204]. Several attempts have been made to regulate fibrosis, including the alteration of physicochemical properties of an implanted material, the addition of specific cell-surface ligands to modulate the immune response and the application of specialised coatings to resist cell adsorption [207]. Fibrosis is modulated by a variety of factors including material chemistry and microstructure, and device shape and thickness [208]. Ideally, the device would integrate with the host tissue with a minimal fibrotic reaction over time [168].

1.7 Advances in macroencapsulation systems for the treatment of T1DM

1.7.1 TheraCyte

The concept for the TheraCyte device began in the late 1990s, when Baxter Healthcare Corporation discovered the angiogenic properties of their PTFE membranous gene therapy delivery device [209]. TheraCyte Inc. was founded in 1999 as a spin-out from Baxter Healthcare Corporation. TheraCyte was based on this PTFE proprietary medical device technology developed by Baxter due to its angiogenic potential and suitability for islet macroencapsulation device design [196,210]. The TheraCyte device was designed primarily for minimally invasive subcutaneous implantation, consisting of an outer layer of woven polyester mesh, a middle layer of 5 μm porosity PTFE and an inner layer of 0.4 μm porosity PTFE [180,211,212] (*Figure 1.14*). This design approach was utilised to decrease the radial diffusion distances by encouraging the development of a dense vascular network using the outer most layer as a scaffold. The innermost membrane of 0.4 μm porosity acts as an immunomodulatory barrier between the encapsulated cells and the hosts immune response.

Preclinical studies performed in small animals have demonstrated diabetes reversal for four weeks in immunocompromised mice [213], for greater than six months in allogenic rat recipients [214] and thirty days in a mouse model resembling autoimmune diabetes [215]. Further studies demonstrated the survival of encapsulated xenogeneic islets implanted in mice and non-human primates for up to eight weeks [166,216]. However, the IEQ used in these studies were considerably below curing doses. Research into the encapsulation of differentiated adult human mesenchymal stromal cells within diabetic canine model, showed diabetes reversal for up to eighteen months in four/seven of device recipients [217].

Research into the TheraCyte device has not proceeded beyond preclinical studies to clinical trials. When the patent this device expired, ViaCyte, a competing company used the TheraCyte technology as a platform to develop the Encaptra[®] drug delivery system.

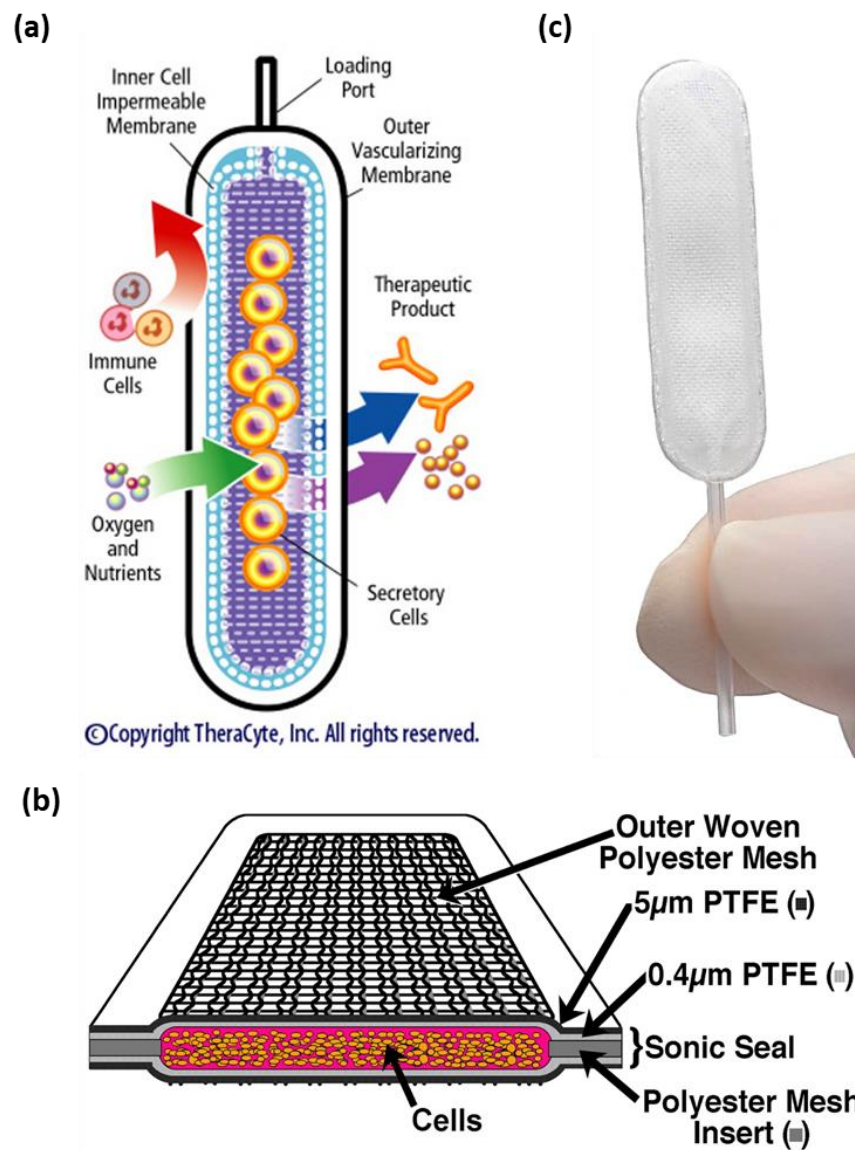


Figure 1.14: TheraCyte encapsulation system. (a) Immunisolation concept of the TheraCyte System [210]. (b) Cross-sectional view features cells encapsulated in a three-layer TheraCyte device [470]. (c) A 40 µl capacity TheraCyte device [471].

1.7.2 ViacYTE

ViaCytE, a regenerative medicine company based in California, has developed three devices for the purpose of encapsulating stem cell-derived pancreatic progenitor cells (PEC-01) for the treatment of T1D and a next-generation treatment for insulin-requiring type 2 diabetes. The PEC-01 cell line, mature into glucose-responsive insulin-secreting beta-like cells, used to overcome the issue of donor pancreatic islet shortages. More recently, ViaCytE demonstrated that when effectively engrafted, PEC-01 cells can mature into glucose-responsive insulin producing cells in patients with T1D [218,219]. To accelerate and expand its efforts, ViaCytE has established collaborative partnerships with leading companies including CRISPR Therapeutics and W.L. Gore & Associates to develop these immune-evasive stem cell lines from its proprietary CyT49 pluripotent stem cell lines. These immune-evasive stem cell lines, which are being used in the PEC-QT program, have the potential to further broaden the availability of cell therapy for all patients with insulin-requiring diabetes, type 1 and type 2, as well as other potential indications.

PEC-Direct and PEC-Encap devices are both in clinical stages whereas the PEC-QT is in the early discovery stages. PEC-Direct was developed for the treatment of high-risk T1D patients who are unable to detect hypoglycemic episodes, extreme glycemic lability or recurrent severe hypoglycemic episodes that could lead to possible coma or death. The PEC-Direct and PEC-QT encapsulation systems are highly porous to allow blood vessel penetration and infiltration of the encapsulated cells (*Figure 1.15*). This strategy requires immunosuppressive therapies in order to protect the implanted cells from immune rejection. The PEC-Encap device also known as VC-01, was primarily developed as a replacement pancreas and a for diabetic patients who require exogenous insulin. The PEC-Encap, utilises the Encaptra® system which is designed to isolate the implanted cells from the host's alloimmunity and autoimmunity. The devices are manufactured from medical-grade plastic called expanded polytetrafluoroethylene (ePTFE) specifically selected for long-term biocompatibility. All devices are designed to be subcutaneously implanted and permit bidirectional diffusion of oxygen, nutrients, insulin, glucagon and other molecules to and from the encapsulated cells and the blood vessels on the surface of the device. In addition, these devices would be suitable for use with other therapeutic agents, providing a platform for enzyme or hormone replacement therapies.

In 2014, ViaCytE commenced a phase I/II clinical study to determine the safety, tolerability, and efficacy of subcutaneously implanted PEC-Encap devices over 2 years [220].

Two cohorts of T1D patients were subcutaneously implanted with either two or four-six devices. Subsequently, a one-year follow-up safety study was performed on these patients implanted with the PEC-Encap devices [221]. A statement released in 2018 said that results indicate that the PEC-Encap product candidate, delivered at a sub-therapeutic dose, has to date been safe and well tolerated. The Encaptra Cell Delivery System appears to protect the implanted cells from allo- and auto-immune rejection and the patients from sensitisation which supported resuming trial enrolment in 2019.

In 2017, a phase I clinical trial began to examine the safety and tolerability of the PEC-Direct device [222]. Up to now three participants have been enrolled and subcutaneously implanted with up to six devices each. Finally, in 2017, a fourth multi-center study commenced to test the safety, tolerability, and efficacy study of the PEC-Direct devices in subjects with T1D and hypoglycemia unawareness [223]. The estimated enrolment for this study is seventy-five, with the first cohort of patients to undergo explant to test for engraftment and maturation of cells. A second cohort of approximately 40 individuals will be used to examine the ability of the PEC-Direct device to achieve sufficient levels of insulin independence. While optimisation of the procedure was continuing, preliminary results of the Pec-Direct clinical studies were presented at Cell & Gene Meeting on the Mesa in 2019. This preliminary data demonstrated that implanted cells, when effectively engrafted, are capable of producing circulating C-peptide, a biomarker for insulin, in patients with T1D [224]. In 2019 the Center for Beta Cell Therapy in Diabetes, coordinator of an international consortium in translational medicine in diabetes, and ViaCyte, Inc., announced that a human stem cell-derived product candidate has been implanted in T1D patients at a sub-therapeutic dose. These are the first patients in Europe to receive the PEC-Direct. This work complemented the clinical evaluation of PEC-Direct underway in North America. During the first phase of the European trial, implants will be evaluated for their ability to form β -cells; the second phase will examine their capacity to produce systemic levels of insulin that establish glucose control [225].

In May 2020, ViaCyte announced \$27 million financing to advance next generation cell therapies for diabetes. They strive to share their achievements and pipeline by presenting their work at large conference proceedings, the most recent of those being, the Jeffries Virtual Healthcare Conference, Biotech Showcase 2020 in San Francisco, and ISSCR International Symposium: Stem Cell Biology to New Therapies [226].

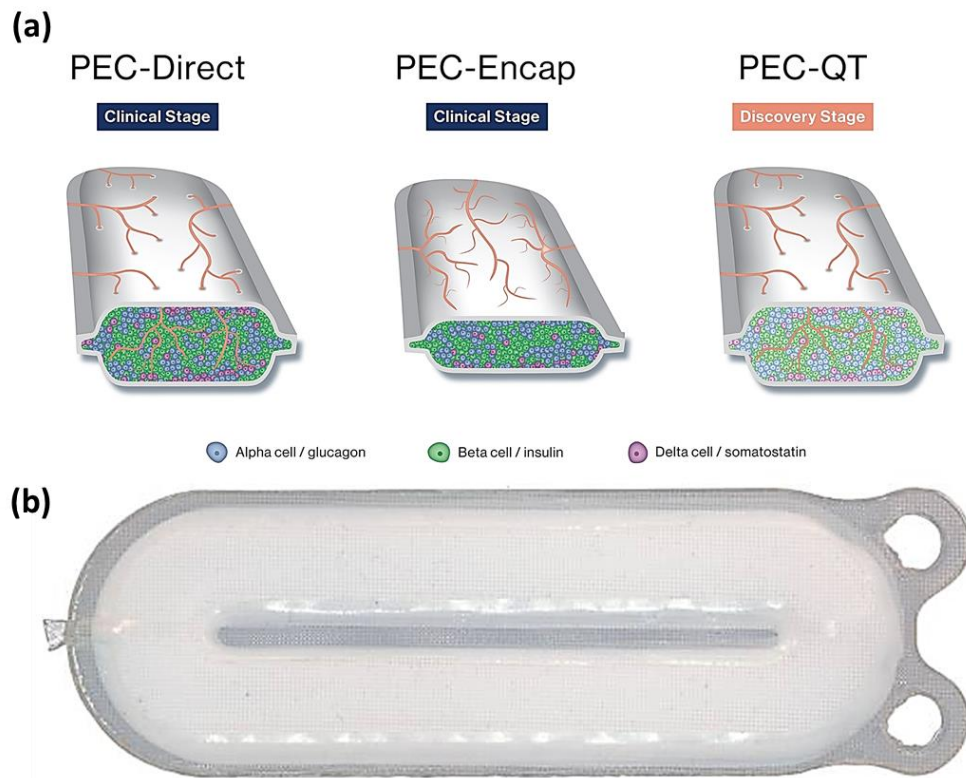


Figure 1.15: Viacyte encapsulation systems. **(a)** Cross-sectional schematics of PEC-Direct, PEC-Encap and PEC-QT devices [472]. **(b)** The PEC-Encap device prototype [473].

1.7.3 β Air

The β Air macroencapsulation device was developed by Beta-O₂ Technologies. β Air employs a novel strategy by providing continuous oxygenation of cells from the moment of encapsulation. This approach could potentially negate prolonged hypoxic stress which typically contributes to the loss of 60% of transplanted islets during the first 48 hours post-transplantation [227,228] and prolong the survival of encapsulated islets. This disc-shaped device consists of two parts; a cell reservoir and a refillable gas chamber. The cell reservoir houses islets encapsulated within an alginate hydrogel disc. This is separated from the gas chamber by silicone membranes which permit the diffusion of exogenous oxygen, delivered through an integrated tubing [229]. This design strategy permits highly metabolic islets to be supplied with oxygen for up to 30 hours before a refill is required. The gas reservoir must be replenished daily via an external port with a gas blend of 95% oxygen and 5% carbon dioxide [230]. The device has a solid polyether ketone exterior with two hydrophilic porous polytetrafluoroethylene (PTFE) membranes impregnated with high viscosity mannuronic acid alginate acting as an immuno-protective barrier.

This device is implanted subcutaneously with polyurethane tubes connecting the gas chamber to access ports located in the central upper dorsum for refilling with oxygen (*Figure 1.16*). Preclinical studies in both small and large animal models demonstrated that daily replenishment with oxygen could maintain islet efficacy for 90 days [230]. In 2012, a 63-year-old T1D patient was the first patient implanted with the β Air device in Dresden, Germany. The subject was monitored closely for a period of 10 months. Results from the phase I study demonstrated that the encapsulated islets were efficacious in the absence of any immunosuppressive therapy [231]. In 2018, a phase I/II clinical trial was performed to evaluate the safety and efficacy of an implanted β Air device containing allogeneic human pancreatic islets in four patients with well-controlled and uncomplicated T1D [232]. One/two devices containing 1800-4600 IEQ / Kg of body weight were implanted subcutaneously in each subject for three to six months. Following explantation of devices, a fibrotic encapsulation was observed. The results from this study demonstrated that the β Air device is safe and can support survival of allogeneic islets for up to several months. However, a hindered or dampened glucose-stimulated insulin response and the accumulation of islet amyloid polypeptide was observed, most likely attributed to insufficient vascularisation thus impacting islet efficacy [233].

Beta-O₂ Technologies have confirmed development of the 2nd generation β Air devices. The 2nd generation device design separates the oxygen tank compartment and cell encapsulation device permitting each component to be developed separately. The design enhancement of the encapsulation device has an increased capacity to house the islet-hydrogel mixture without compromising diffusion properties as the thickness of the device has decreased from 600 to 200 μm (*Figure 1.16*). The new oxygen tank component has been designed to cater for the increased oxygen demands of the cell cargo, enabling maximum insulin secretion from the device. The rat-size device is currently in preclinical trials and the human-size device is next to follow. Further clinical studies will be conducted in order to evaluate the safety and efficacy of a 2nd generation β Air devices containing stem cell derived insulin-producing cells over an extended period of time.

Although the β Air bioartificial pancreas has become a promising implantable therapy for the treatment of T1D, this approach still requires daily injections to function correctly. Each patient is required to take one daily injection of oxygen by placing a needle for a duration of 3 minutes into the port delivering a pre-measured and automatically pressurised amount of oxygen. Therefore, this therapy still requires important patient interaction in order to function accurately. However, Beta-O₂ sees this as only an interim obligation on the patient and that eventually a means of automated oxygen generation will be developed, removing the responsibility from the patient completely.

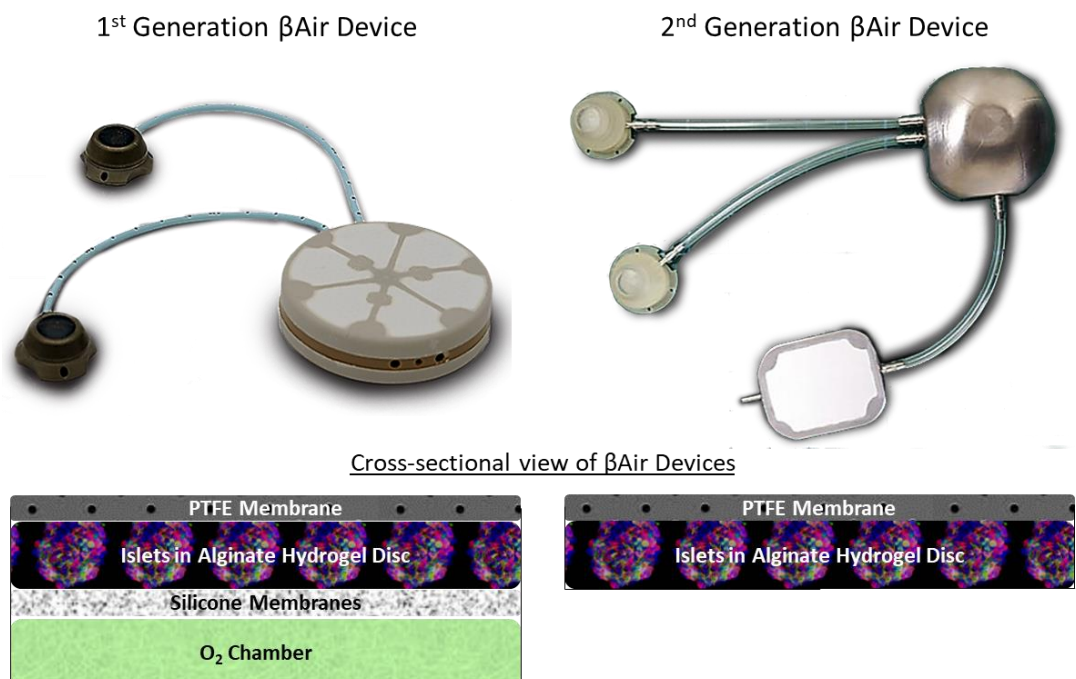


Figure 1.16: Generation 1 and 2 of the β Air device with cross-sectional schematics of device interiors [474].

1.7.4 Sernova Cell Pouch

The Sernova Cell Pouch System™ is a macroencapsulation device developed by Sernova Corp. The cell pouch is specifically designed to be implanted subcutaneously for a period of 30-40 days to promote the development of surrounding microvasculature, essentially creating a vascularised tissue chamber. The device is composed of a non-biodegradable polypropylene based matrix with large diameter pores. Its interior is filled with an array of rods, or a single rod to act as plugs during the prevascularisation process (*Figure 1.17 (a)*). Following the implantation period, these rods are removed to reveal a series of voids which are subsequently infused with islets (*Figure 1.17 (b)*). As this device prioritises vascularisation, it does not have an immunomodulatory barrier, thus immunosuppression is necessary to prevent rejection of implanted islets. In light of this, Sernova Corp has developed the Sertolin technology (*Figure 1.17 (c-d)*). This involves the microencapsulation of cells within a polymer sphere which permits the diffusion of nutrients and insulin through pores, while simultaneously preventing immune cell attack. The combination of these technologies could potentially reduce or eliminate the need for immunosuppressive drugs while maintaining the efficacy of implanted cells over an extended time period.

In a preclinical efficacy study performed in rats, the cell pouch was implanted for a period of four-five weeks before the introduction of islets into the prevascularised space. Results of this study demonstrated successful incorporation into the host vasculature with little to no, fibrous encapsulation. The encapsulated islets were shown to be viable and able to maintain normoglycemia comparable to a control kidney capsule islet transplant for up to 100 days [182,234].

In 2012, a Phase I/II study of the safety and efficacy of Sernova's Cell Pouch for therapeutic islet transplantation and recruited three patients [235,236]. Initial results demonstrated that the Cell Pouch met its primary end-point of safety, attributed to an abundance of neovascularisation following the 6-week prevascularisation period and maintenance of healthy islet morphology. However, the study was later terminated in 2016, as the device failed to meet its functional endpoint of insulin independence most likely attributed to early functional failure of the engraftment in all cases.

A second clinical trial is currently underway to examine the safety, tolerability and efficacy of the Cell Pouch for clinical islet transplantation [237]. This study aims to enrol seven participants who will undergo subcutaneous implantation of the cell pouch for 3 weeks before initiation of immunosuppression for another 3 weeks as the prevascularisation step. Subsequently, 3000 IEQ/kg bodyweight will be transplanted with the principal aim to examine the safety of the pouch for up to 1 year. Sernova Corp have confirmed that further clinical trials will be performed to evaluate the safety of the cell pouch containing insulin-producing cells differentiated from human stem cells.

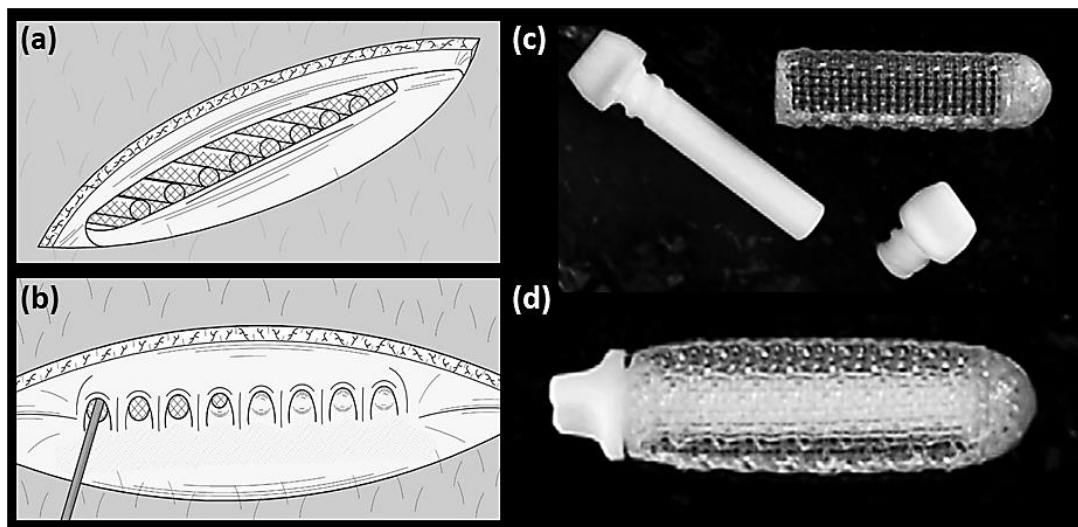


Figure 1.17: Sernova Cell Pouch System. **(a)** Illustration of plugs in situ within the Cell Pouch. **(b)** Illustration of islet infusion within the chambers of the Cell Pouch. **(c)** Unassembled Cell Pouch showing the rod-like plug, cap, and device chamber. **(d)** Assembled Cell Pouch. Device dimensions \approx 60 mm diameter x 60 mm height [235].

1.7.5 MailPan

The MailPan (MAcroencapsulation of PANcreatic Islets) is a macroencapsulation device developed originally by the European Centre for Diabetes Studies, with Defymed in charge since 2011. The MailPan device is specifically designed to allow for a non-surgical replacement of cells due through an integrated input and output connections. This device is circular in shape and approximately 15 cm in diameter (*Figure 1.18*). It is composed of a copolymer of acrylonitrile and sodium methallyl sulfonate (AN69) selectively permeable membrane which is commonly selected for dialysis applications [238]. The selected membrane will encapsulate and immune-protect insulin-secreting cells while permitting the bidirectional transport of oxygen, nutrients, glucose, and insulin [239]. This device is deigned to be implanted in the peritoneal cavity with input and output ports left superficial for the replenishment of cells. The device would require no patient interaction other than two-four visits to a designated diabetes center for the replacement of cells per annum.

A previous preclinical study performed in rats demonstrated the implantation of an AN69 membrane in the peritoneal cavity suffered from 50% decreased permeability of insulin and glucose due to the adherence of macrophages and fibroblasts at the device surface [240,241]. Following rigorous experimentation, a polycarbonate membrane was selected. The membrane underwent surface treatments, plasma and copolymer adsorption to improve permeability and biocompatibility to improve the permeability [242].

In 2016, Defymed began its collaboration with Semma Therapeutics with the goal of utilising the MailPan device to encapsulate Semma's stem cell-derived insulin-secreting cells. In May of 2020, MailPan published an investigation into the safety and efficacy of the MailPan macroencapsulation device performed in rodents. Results demonstrated excellent safety and biocompatibility while demonstrating the devices immunoisolating properties by preventing a heightened immune response against encapsulated allogenic islets. Moreover, the injection of a rat β -cell line into the device normalised fasting glycemia of diabetic rats with retrieval of viable cell clusters after 2months. In addition, this publication showcased its entry/exit system allowing cell replacement by simple subcutaneous injection facilitating cell therapy by patients themselves [243]. Further small and large animal preclinical studies are ongoing [244,245]



Figure 1.18: The MailPan (MAcroencapsulation of PANcreatic Islets) Device [245].

Table 1.1: Summary of Encapsulation systems in clinical trial.

Company	Device and Clinical Trial Outcome	Design	Inclusion Criteria	Endpoints	Ref.
Microencapsulation Devices					
Living Cell Technologies & Diatranz Otsuka Ltd.	DIABECCELL® was safe and reduced the occurrence of hypoglycemic events, and the dose of insulin without increasing HbA1c  Scale Bar 500 µm	NCT00940173 (N=16) <ul style="list-style-type: none"> • 5,000 IEQ/kg • 10,000 IEQ/kg • 15,000 IEQ/kg • 20,000 IEQ/kg 	<ul style="list-style-type: none"> • Informed consent • 35-65 years • Brittle T1DM ≥5 years • HbA1c ≥7% and ≤10% • Plasma C-peptide <0.2 ng/ml 	<ul style="list-style-type: none"> • Phase I – Safety • Phase II –Efficacy (reduction in HbA1c levels) 	[475]
		NCT01739829 (N=8) <ul style="list-style-type: none"> • 2 x 5,000 IEQ/kg • 2 x 10,000 IEQ/kg • 3 months between doses 	<ul style="list-style-type: none"> • Informed consent • 18-65 years • Brittle T1DM ≥5years • HbA1c ≥7% and ≤15% • Plasma C-peptide <0.3 ng/ml 	<ul style="list-style-type: none"> • Phase I – Safety • Phase II – Efficacy (reduction in hypoglycemic events w/o increase in HbA1c values) 	[476]
		NCT01736228 (N=14) <ul style="list-style-type: none"> • 2 x 10,000 IEQ/kg • 12 weeks apart 	<ul style="list-style-type: none"> • Informed consent • 18-65 years • Brittle T1DM ≥5 years • HbA1c ≤12% • Plasma C-peptide <0.3 ng/ml 	<ul style="list-style-type: none"> • Phase I – Safety • Phase II – Efficacy (restoration of euglycemia w/o increase in insulin) 	[477]
Macroencapsulation Devices					
Sernova	Cell Pouch™ was safe, reduced the number of hypoglycemic events, improved glycemic control, and increased production of C-peptide and insulin.	NCT03513939 (N=7) <ul style="list-style-type: none"> • Device implanted for 3 wks. • Immunosuppressants optimised for 3 weeks • Then 3000 IEQ/kg transplanted into device 	<ul style="list-style-type: none"> • Informed consent • 18-65 years • T1DM onset <40 years of age • Brittle T1DM ≥5 year • Plasma C-peptide <0.3 ng/ml 	<ul style="list-style-type: none"> • Phase I – Safety • Phase II – Efficacy (endocrine tissue survival in Cell Pouch™, and reduction in hypoglycemic events and HbA1c) 	[174, 229, 240]

Company	Device and Clinical Trial Outcome	Design	Inclusion Criteria	Endpoints	Ref.
Viacyte	PEC-Direct™ was safe and initial data suggests PEC-01 cells engrafted and functioned as they produced C-peptide. Device dimensions ≈ 45 mm length x 25 mm width, <1 mm height	NCT03162926 (N=3) • ≤6 implants per person over 4 months	<ul style="list-style-type: none"> • Stable T1DM ≥5 years • Willing to use a CGM 	<ul style="list-style-type: none"> • Phase I – Safety 	[214, 242, 243]
		NCT03163511 (N=75) • ≤6 VC-02-20 implants within 2 years (n=15) • 6 VC-20-300 implants and ≤4 additional VC-02-20 (n=60)	<ul style="list-style-type: none"> • Brittle T1DM ≥5 years • Willing to use a CGM 	<ul style="list-style-type: none"> • Phase I – Safety • Phase II – Efficacy (improvement in C-peptide production) 	[215, 242, 243]
	PEC-Encap™ initially showed biocompatibility issues, which are expected to be addressed with new membrane. Device dimensions ≈ 18 mm diameter, <1 mm thick	NCT02239354 (N=69) • VC-01-250 and VC-01-20 implants (n=19) • 4 or 6 VC-01 implants (n=50)	<ul style="list-style-type: none"> • Stable T1DM ≥3 years • Willing to use a CGM 	<ul style="list-style-type: none"> • Phase I – Safety • Phase II – Efficacy (improvement in C-peptide production) 	[212, 242, 243]
		NCT029391181 (N=200)	<ul style="list-style-type: none"> • Previous implantation and explantation of Pec-Encap™ 	<ul style="list-style-type: none"> • Safety follow-up 	[152, 248]
Cliniques universitaires Saint-Luc- Université Catholique de Louvain	Monolayer Cellular Device has no published results from trial concluded in 2015 and has been withdrawn. 10-30 m ²	NCT00790257 (N=15)	<ul style="list-style-type: none"> • Informed consent • 30-80 years - T1DM • C-peptide-negative • Phase IA: on immunosuppressants • Phase IB: no immunosuppressants 	<ul style="list-style-type: none"> • Phase I – Safety • Phase II – (insulin production) 	[480]

1.8 The DRIVE project

The Diabetes Reversing Implants with enhanced Viability and long-term Efficacy (DRIVE) project aimed to develop a macroencapsulation system for the delivery islets to treat T1D. The system was to consist of a functionalised biomaterial (β -gel), a macroencapsulation device (β -shell), and a surgical tool (β -Cath) and procedure (O-fold) to deliver the implant in minimally invasive procedure.

The β -Gel will be a hydrogel formulation, loaded with the key components to ensure optimal cell survival. A biocompatible hydrogel will be functionalised with native pancreatic niche proteins and compositional efficacy cues which will encourage islets growth and survival. The β -Gel will also contain an oxygen delivery system; oxygen carriers will be loaded in the hydrogel to improve islet viability and survival in the hypoxic conditions of the delivery site through the first week following transplantation, prior to angiogenesis (*Figure 1.15*).

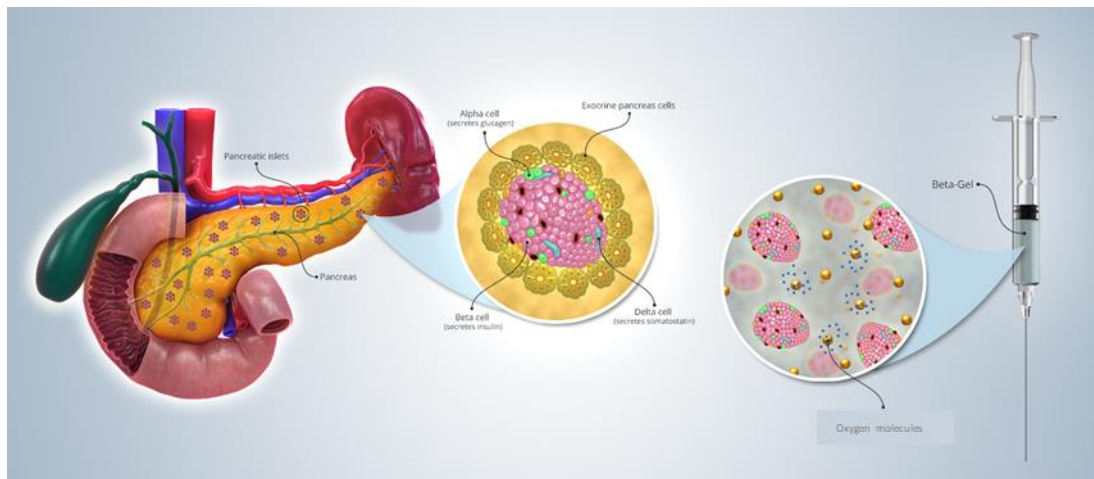


Figure 1.19: The aim of the DRIVE project. Islets extracted from the pancreas will be included in the β -Gel. The hydrogel will contain a combination of materials including the oxygen carriers which will release oxygen to the islets in vivo. This cell compound will then be immunoprotected and encapsulated within the within the β -Shell.

The β -Shell is a macroencapsulation device, which will enable the delivery of the β -Gel to an extra-hepatic site. The β -shell will consist of a semi-permeable, immunoisolating, retentive, and protective membrane. The β -shell will additionally support vascularisation onto the surface of the membrane and vascularisation will be further promoted by the inclusion of pro-angiogenic VEGF microparticles in the device. The immunoprotective membrane will facilitate the free transfer of glucose, oxygen, and other nutrients into the device while facilitating the release of insulin and clearance of waste back into systemic circulation, while inhibiting immune cells.

This will allow for allografted islets to be transplanted without the need for immunosuppression. The β -Cath will be a minimally invasive, custom designed catheter which will allow for the delivery of the β -shell to an extra-hepatic site, and filling of the device *in situ*. The DRIVE project was ongoing alongside this thesis project, and the additive manufactured multi-scale porous macroencapsulation devices, utilised as the lead β -Shell device design for the DRIVE project, were examined throughout this PhD thesis from small to large animal studies. Due to nature of a consortium setting, individual components of the DRIVE macroencapsulation system were continuously modified between studies. *Table 1.2* has been included to highlight and explain the reasoning behind modification of components throughout the chapters of this thesis

Table 1.2: Modifications and adaptations of the DRIVE macroencapsulation system throughout this thesis.

Study	Device Design	Functionalised Biomaterial	Site of Implantation
<p>Chapter 2: Examining the Angiogenic and Foreign Body Response of soft tissue implants with various 3D printed porous topographies</p>	<p>Implants. Dimensions: 12 x 1 mm. Each subsequent implant in the series was progressively more complex than the previous, achieved by increasing the quantity of both rope-coil-derived macro-pores, and salt spray derived micro-pores.</p>	<p>None</p>	<p>Submuscularly in the dorsum.</p>
<p>Chapter 3: Assessing the effects of VEGF releasing microspheres on the angiogenic and foreign body response to a multiscale porosity macroencapsulation device</p>	<p>Pouch. Dimensions: 10 x 20 x 2 mm. Design based upon the s5 implant from Chap 2: Microporous with multi-layered macro structure. <i>Chosen due to its increased affinity for integration and angiogenesis in surrounding tissue.</i></p>	<p>200 µL of native HA hydrogel formulation for encapsulation of a 25 mg/mL VEGF microsphere suspension.</p>	<p>Submuscularly in the dorsum.</p>
<p>Chapter 4: To examine the potential of the multiscale porosity islet encapsulation device for the treatment of diabetes in STZ-induced diabetic rodents</p>	<p>Pouch. Dimensions: 10 x 20 x 2 mm. Microporous with multi-layered macro structure.</p>	<p>200 µL of native HA/Perfluorodecalin oxygenated emulgel formulation with encapsulation of 2,400 IEQ of syngeneic islets and 25 mg/mL VEGF microsphere suspension. <i>Perfluorodecalin incorporated due to its long history of use as an oxygen carrier.</i></p>	<p>Intraperitoneal implantation. Both unsutured and sutured internally to the anterior abdominal wall. <i>Chosen due to its size, translatability and proximity to our chosen clinically relevant site within the transversus abdominus plane.</i></p>
<p>Chapter 5: To examine the scalability and functionality of multiscale porous islet encapsulation devices in an STZ-induced diabetic porcine model</p>	<p>Pouch. Dimensions: ~ 75 x 125 x 1 mm. Microporous with multi-layered macro structure.</p>	<p>10 ml of native HA gel containing an iodixanol emulsion was injected into the device for positioning of the device visualised with fluoroscopy.</p>	<p>Transversus abdominus plane within the anterior abdominal wall. <i>Chosen as a clinically relevant site due to its size, robust blood supply, accessibility, and because it is commonly accessed during common clinical procedures.</i></p>

1.9 Thesis Objectives

While there has been much advancement in conventional diabetes management, returning endogenous insulin production to the diabetic patient will remain the best treatment option for patient health outcomes and quality of life. Current treatment methodologies, such as the Edmonton protocol, although successful in reversion of diabetes in the short-term and improving patient outcomes, still require the use of systemic immunosuppression, meaning the treatment is not suitable for all patients. The scarcity of human pancreata and islets required for a successful transplantation also greatly limit the application of the current procedure to a greater patient population. Islet encapsulation and the bioartificial pancreas are a potential solution to all of these problems, by improving transplanted islets viability and function without the need for systemic immunosuppression.

The overall aim of the research in this PhD thesis is to determine the most suitable surface topography to promote an abundant vascularised network and tissue integration surrounding a novel macroencapsulation device. In order to complete this aim, the following objectives were pursued:

1. Examining the angiogenic and foreign body response of silicone implants with various 3D printed porous topographies to determine a suitable surface architecture for the promotion of optimal vascularisation and tissue integration. (*Chapter 2*)
2. Assessing the effects of VEGF releasing microspheres on the angiogenic and foreign body response surrounding multiscale porosity macroencapsulation devices. (*Chapter 3*)
3. Examining the efficacy of the multiscale porosity macroencapsulation device loaded with syngeneic islets in STZ-induced diabetic rodents. (*Chapter 4*)
4. Examining the scalability and potential functionality of multiscale porosity macroencapsulation devices in a STZ-induced diabetic porcine model. (*Chapter 5*)

Chapter 2

Examining the Angiogenic and Foreign Body Response of
soft tissue implants with various 3D printed porous
topographies.

2.1 Introduction

Implants placed in soft tissue tend to evoke a foreign body response (FBR), particularly when a polymeric implant features a smooth surface [246,247]. Modulating the FBR is particularly crucial when an implanted device requires tissue integration and vascularisation to support its function – for example, in cosmetic reconstruction [248], drug delivery [249], biosensors [250] and immunoprotective cellular-encapsulation devices [180]. Surgical implantation disrupts native tissue initiating an inflammatory response and causing protein adsorption to the implant surface. Vascular injury can lead to deposition of fibrin/thrombus on the device surface. Macrophages migrate and adhere to the implant surface eventually forming giant cells and generating a caustic local environment (focal glucose depletion zones, elevated reactive oxygen species, and acidic pH). The latter stages of the FBR involve deposition of an avascular, collagen-rich capsule around the implant by myofibroblasts that can result in significant impairment in device functionality. This dense fibrosis can lead to the implant being walled off thus preventing the device from functioning or integrating as intended [251]. Fibrous tissue does not generally adhere to the polymer, and instead allows sliding and friction between the tissue and implant. This lack of tissue integration and resulting friction can promote the accumulation of serous fluid and inflammatory cells at the interface [252,253].

The foreign body response to synthetic materials is an enormous impediment to the development and efficacy of immunoprotective cellular-encapsulation devices [180]. A successful islet encapsulation device must facilitate; normal insulin and glucose kinetics for the maintenance of normoglycemia, optimal nutrient and waste exchange, all while maintaining the viability of encapsulated cells. Subsequent fibrotic encapsulation by dense impermeable avascular layers of collagen, impaired tissue integration and lack of vascularisation severely affects the pharmacokinetics of mass transport in the peri-device tissue [254,255] and can limit nutrient and oxygen diffusion and cell response. Promoting tissue integration and blood vessel formation surrounding encapsulation devices is imperative to ensure positional fixation within the host tissue and thus prevent inflammation [256,257]. Extensive efforts have been focused on investigating the most superior biocompatible approach, including device material and surface modification techniques, implant site, configuration of device, and methods to improve vascularisation and immune modulation [251,258,259].

2.1.1 Aims

The overall aim of this research chapter is to determine an optimal surface topography with the ability to harness the desired degree of tissue integration and vascularisation to enhance viability and long-term efficacy of an islet macroencapsulation device.

The specific aims of Chapter 2 were to:

- Assess the morphology of the fibrous capsule surrounding each 3D printed porous topography using histological assessment, MicroCT and SEM imaging
- To characterise the composition of the resultant fibrous capsules using immunofluorescent and histological staining
- To establish whether the varying 3D printed porous topographies affected the activation, abundance and polarisation of macrophages at the tissue interface capsule using immunofluorescent staining
- To investigate whether 3D printed porous topographies influenced angiogenesis and vessel maturity using immunohistochemical and immunofluorescent staining.

To achieve these aims, novel additive manufacturing techniques were utilised to create soft-tissue implant topographies featuring multiscale porosity in both micro (<20 μm) and macro (>1 mm) scale. Five implants exhibiting progressively more complex surface topography were implanted sub-muscularly in the dorsum of rodents for a period of 14 days.

2.2 Materials and Methods

2.2.1 Implant fabrication

Implant design and manufacturing was carried out by the O’Cearbhaill Lab, UCD, Dublin. I worked very closely with UCD to develop these rodent size implants, providing inputs on the experimental design, implant site, number of implants, rotation plan and sample size.

A series of five 12 mm disk shaped implants were fabricated from medical grade silicone (*Figure 2.3*). Each subsequent implant in the series was progressively more complex than the previous, which was achieved by increasing the quantity of both rope-coil-derived macro-pores, and salt spray derived micro-pores. The composition of each implant is described in Table 2.1.

2.2.1.1 Creation of macro-porous layers

Macrotexture was formed using the liquid rope-coil effect. The liquid rope-coil effect occurs when viscous material is extruded from a nozzle positioned above a moving substrate (*Figure 2.1*). Implant grade silicone of various hardness and modulus was obtained and mixed in standard recommended form 50:50 part A:B. The materials used were Soft (Shore A20: NuSil MED4820), Medium (Shore A40: Nusil MED 4840), Hard (Shore A80: Nusil MED 4880). To aid visualisation, a silicone pigment (Smooth-On SilPig) was added at 0.5 wt% in various colours. The two-part silicone was mixed in a planetary mixer (Thinky ARE-310) for 10 minutes at 1850 rpm, placed in a fridge for 30 minutes, and centrifuged at 4000 rpm for 5 minutes to remove air bubbles. When the material is loaded into an ECOpen extruder mounted in a custom 3D printing station, and the system purged of air-bubbles, a 27 Gauge (200 μm I.D.) conical tip was added. ‘Steady coil’ regime was used as it was most repeatable and with useful geometry when creating open porous scaffolds and coatings with a curved pore structure.

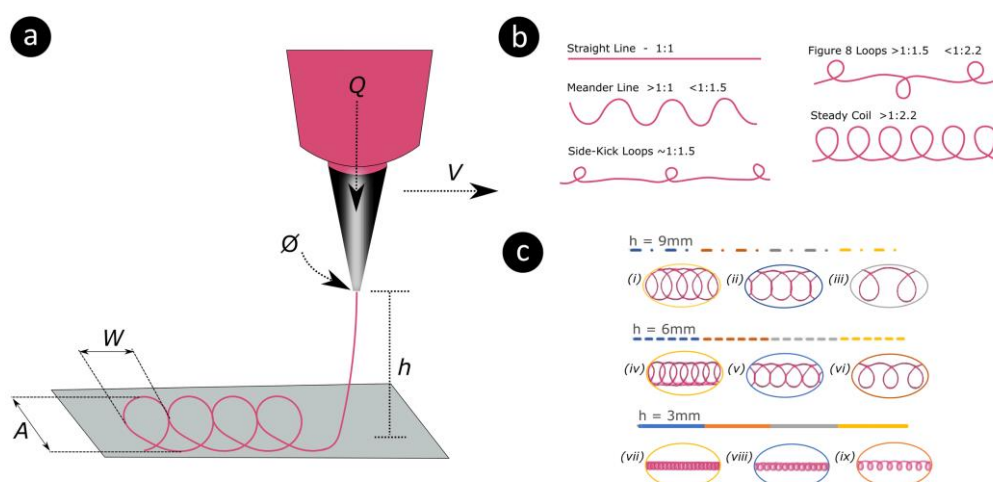


Figure 2.1: Control of the liquid rope-coil effect. **(a)** Parameters that affect the Loop Amplitude (A) and Width (W) of an extruded rope coil: Q – Material Flow, \varnothing – Nozzle Diameter (the product of which can be used to calculate the extruded bead length per unit time), V – Printhead (nozzle) velocity – The ratio of V to bead length per time defines loop shape and period length, h – Nozzle height above substrate – This defines the amplitude of the rope coil loops (at certain fixed values of Q , V and \varnothing , the loop A will be linearly proportional to h). **(b)** Illustrations of the different loop regimes at various ratios of extrusion rate to substrate speed. **(c)** Scanned images of loops at various heights and feed rates, illustrating the difference in loop amplitudes and overlap frequencies.

2.2.1.2 Creation of microporous texture

Surface textures in the 1–10 μm range can encourage cellular adhesion [246,249]. In order to fabricate a microporous texture upon the substrate surface in this range, a novel ink formulation was utilised and sprayed through atomization. The salt water solution was formulated by heating DI water to 80°C, followed by the addition of 40 wt% Sodium Chloride salt (Sigma Aldrich) and stirring with a magnetic stirrer until fully saturated. The liquid was then filtered through a 10 μm filter to remove any undissolved particles. A separate mixture of DI water with 20 wt% PEG 6000 was created through stirring at room temperature, and similarly filtered. This was incorporated into the solution to increase the hydrophilicity. The two mixtures were combined at a ratio of 3:1 in favour of the salt solution and this mixture was then filtered through a 0.22 μm syringe filter to remove contaminants. A high consistency medical grade silicone (NuSil MED4840) was combined as Part A and B and mixed at a standard 1:1 ratio. This was then diluted using 99.1% n-Heptane (Sigma Aldridge chemicals), at a ratio of 1:3 wt%. mixed in a planetary mixer for 10 minutes at 1850 rpm.

A surfactant blend with a hydrophilic/lipophilic balance (HLB) number of 11.5 was created by combining Span 85 (Sorbitan Trioleate) with Tween 40 (PEG-20 Sorbitan Monopalmitate) at a ratio of 3:7. On combining the pore-generating water solution with the silicone solution at a 1:3 ratio, the surfactant blend was added at a quantity of 3 wt% of overall liquid. The combination was mixed at 1750 rpm for 8 minutes in a planetary mixer. The salt crystals still embedded in the silicone matrix after over spraying can be seen in *Figure 2.2 (a) and (b)*. The sodium chloride crystals are non-ortho-rhombic, likely due to the presence of PEG 6000 during crystal nucleation. The sodium chloride crystals are removed over a 24-hour period using an ultrasonic bath with deionised water, after which the surface is heavily textured. An average pore size of 8.4 μm over 12 different samples was found when using the material composition and spray parameters described. *Figure 2.2 (c) and (d)* show a microtextured surface. The inner structure of two sample pores are shown in *Figure 2.2 (e) and (f)*. *Figure 2.2 (g)* shows a macro image of a two-sided 3D printed porous topography implant, corresponding with implant s4 described in the next section.

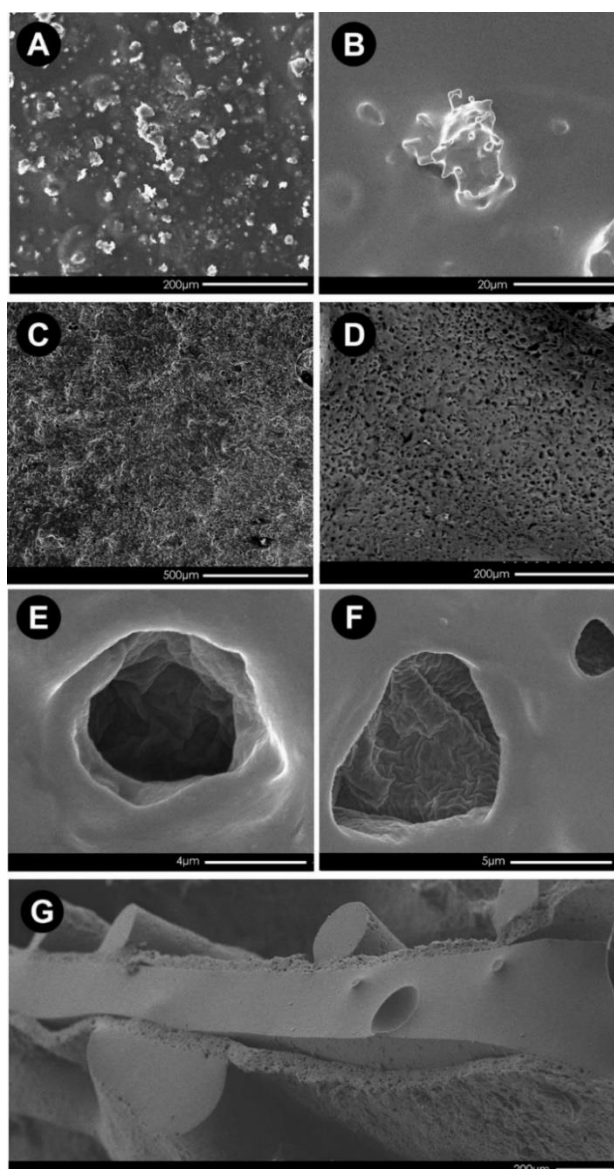


Figure 2.2: Microporous coating with salt nucleation. **(a)** A silicone and salt solution was sprayed on a hotplate at 80°C, allowing salt crystals to nucleate. **(b)** A close-up of the non-cubic salt crystal shape, caused by the influence of PEG during nucleation. **(c)** Surface texture of silicone after salt crystal removal. **(d)** Closer view of porous surface. **(e)** Close-up of a single salt-generated pore. **(f)** Alternative view of pores showing unusual surface topology inside the pore. **(g)** Cross-section of a 500 µm thick silicone body that has been sprayed on both sides with a 100 µm porous layer, with rope coil-generated pores extruded over the top, on either side.

Table 2.1: Description of features of each implant.	
s1	'Standard' smooth silicone implant: Two non-porous silicone (NuSil MED4840) membranes – 60 μm thick, produced by spraying, then bonded together into a pouch using an extruded ring of NuSil4840.
s2	Smooth implant with outer macro-structure: Non-porous silicone membranes, formed into a pouch as per s1, but with a single layer of 3mm diameter rope-coiled MED4840 silicone macrostructure, adhered to the outside of the membranes.
s3	Micro structure and macro structure on a non-porous implant: Non-porous silicone membranes with a single layer of MED4840 rope-coil as per s2, followed by an over-spray using $2 \times 5 \mu\text{m}$ layers of salt/silicone solution (described in Materials and Methods). The salt is washed out post-cure leaving a thin microporous coating over the surface.
s4	Porous inner membrane with micro and macro structure: The two membranes are fabricated entirely of salt/silicone solution ($12 \times 5 \mu\text{m}$ layers). The MED4840 rope-coil layer is extruded onto the surface, followed by over-spraying using another two salt/silicone solution layers. The salt is washed out of the membranes over a 24 hour period.
s5	Microporous and multi-layer macro structure with softness gradient: Membrane as per s4, but with two extra layers of rope-coil (on each side) composed of a softer MED 4820 silicone. The entire implant is over-sprayed with two layers of salt/silicone solution, cured and then washed.

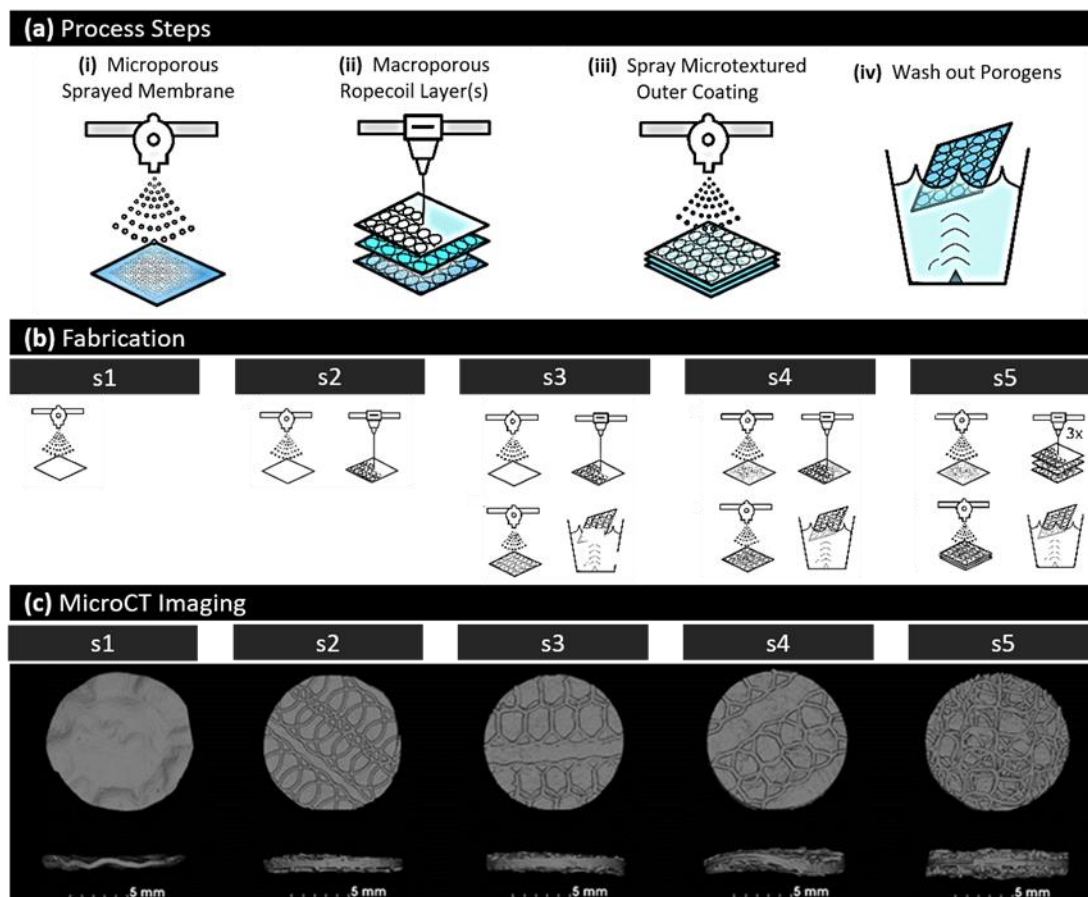


Figure 2.3: Manufacturing of increasingly complex 3D printed porous topographies. **(a)** Process steps of multiscale porosity implants. **(b)** Fabrication steps of s1 to s5. **(c)** MicroCT imaging of implants s1-s5.

2.2.2 Subdermal implantation in rats

These procedures were carried out by Abiel srl., Palermo, Sicily. I contributed to the design and planning of this study, provided direction, travelled to Palermo to receive training and witnessed the implantation process, provided support for explantation of implants and tissue en bloc, and trained individuals on our tissue fixation and shipping protocols.

Rodent studies were approved by the Italian Ministry of Health (Authorization No. 66/2017-PR). 10 Rats RccHan Wistar (ENVIGO) 150/200 g females, age 12 weeks were used during this study. Rats were anesthetized by isofluorane and hair was removed in the area of implantation. Six incisions were made lateral to the midline of the dorsum, five for the implants s1-s5 and the sixth as a negative control. Implant sites were rotated on each animal to account for any site-specific effects (Figure 2.4). Each incision cut through the dermis to the muscles of the dorsum. Each implant was placed in the cavity following enlargement with a pair of scissors.

Each implant site was closed with 2/3 stitches and the animals were treated with anti-biotic ceftriaxone (25 mg/Kg) and painkiller tramadol (4 mg/Kg), for 5 days. After 2 weeks, before being sacrificed, the animals were perfused with Iopamiro 370 (15 mL / hr) by cannulation (cannula 26G) at the level of a tail vein and analysed by computerized axial tomography (Capiler CT-Scannet, PerkinElmer). This imaging enabled visualisation of the implants to accurately pinpoint its location and monitor its movement. Rats were euthanized at 2 or 4 (s4 only) weeks, each implant and the immediate surrounding tissue were extracted.

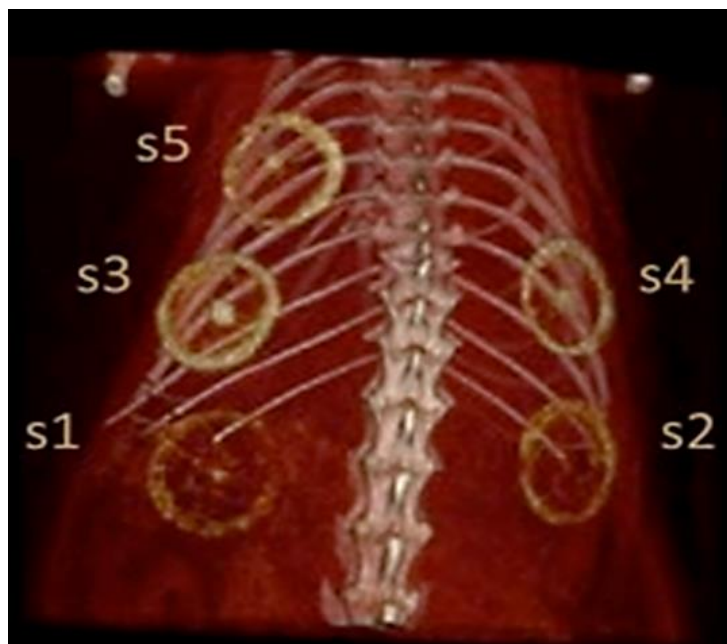


Figure 2.4: Micro-CT imaging of implant implantation sites within the dorsum of rat

2.2.3 Fixation, embedding and staining

Tissues were fixed overnight using 4% paraformaldehyde (pH 7.4). The tissue allocated for histological analysis was then washed in 0.2 M phosphate-buffered saline with a final wash in 70% ethanol. Samples transected in half, orientated and embedded in paraffin wax blocks. Sections of 5 μm were cut and stained with Masson's trichrome, picosirus red and αSMA for fibrous capsule analysis. Additional sections were stained with a CD31, αSMA , CD68, CCR7 and CD163 for analysis of angiogenesis and immune response.

2.2.4 X-ray microtomography (Micro-CT)

Unstained explanted implants from rats were stored in 70% ethanol and imaged in a Micro-CT 100 micro-CT scanner (Scanco Medical, Switzerland). Samples were scanned at 45 kVp and 200 μ A with a 0.1mm Aluminium filter. The manufactured implants were clearly visualized while surrounding tissue could not be detected. Images and videos of each implant iteration were generated with CTVox software (Bruker, USA). For soft tissue visualizations, samples were stained in a solution of 2.5% phosphomolybdic acid in 70% ethanol for 5-7 days h. Micro-CT images were captured using a μ CT 100 scanner at 70 kVp and 85 μ A with a 0.5mm Aluminium filter. Images and videos were generated using ImageJ software.

2.2.5 Scanning Electron Microscopy (SEM)

Each tissue sample was bisected longitudinally to create a cross-section of the implant and surrounding tissue. Samples were post-fixed overnight in 2.5% glutaraldehyde in 0.2 M PBS (pH 7.4). Samples were washed twice in 0.2 M PBS for 10 minutes before dehydration through a series of graded alcohols (30%, 50%, 70%, 90% and 100%). Following dehydration, samples were transferred to the EMITECH K850 critical point dryer. This removed all the liquid in a precise and controlled way, so fragile tissue is not damaged or distorted in the process. Samples were then mounted onto aluminium stubs using carbon adhesive tabs. An Emscope SC500 was used to lightly sputter coat the samples. Specimens were imaged using a Hitachi S2600N Scanning Electron Microscope using a secondary electron detector (Vacuum 15 kV, electron Beam 50). SEM images were pseudo-coloured using MountainsMap[®] SEM Color 7.3.7984.

2.2.6 Fibrous capsule analysis

2.2.6.1 Masson's Trichrome with Gomori's Aldehyde Fuchsin

For assessment of fibrotic capsule size, sections were deparaffinised in xylene, rehydrated through graded ethanol washes (100–70% v/v) to water. Slides were oxidised in 0.5% KMnO_4 / 0.5% H_2SO_4 (equal parts) for 2 minutes before rinsing in water and bleaching in 2% sodium metabisulphite ($\text{Na}_2\text{S}_2\text{O}_5$) for 2 minutes. Slides were washed in water for 30 seconds, immersed in 70% alcohol for 1 minute, washed again for 30 seconds and then stained with Gomori's aldehyde fuchsin for 1 minute. Slides were rinsed in water (very quickly), 95% alcohol for 10 seconds, and water again before staining with celestine blue for 4 minutes. Slides were rinsed in water before staining with Mayer's haemalum for a further 4 minutes. These were then rinsed, differentiated in acid alcohol for 20 seconds before being placed in running tap water for 4 minutes to blue the nuclei.

Slides were then stained in Masson's cytoplasmic stain for 1 minutes before rinsing very quickly in water and differentiating in 1% dodeca-Molybdophosphoric Acid ($H_3PO_4 \cdot 12MoO_3 \cdot 24H_2O$) for 2 minutes. Slides were washed in water and counterstained in fastgreen or light green, for 1 minute before differentiating in 1% acetic acid for a further 1 minute. Following this, the sections were rapidly dehydrated through graded ethanol washes (70–100% v/v). The slides were then mounted using DPX mountant (Sigma Aldrich) and left to dry horizontally for five hours. All histologically stained slides were imaged using an Olympus VS120 Virtual Slide Scanner at 20X magnification.

2.2.6.2 Fibrous capsule thickness

Morphometric and stereological methods were used to analyse the thickness of the fibrotic capsule surrounding the implants stained with Masson's Trichrome with Gomori's Aldehyde Fuchsin. Slide scanned images were opened with Olympus OlyVIA version 2.9. From each tissue section, 10 non-overlapping random images were taken of both the fibrotic capsule superficial and deep to the implanted implants at 4X magnification. The exclusion criteria included regions where capsule was not visible due to artefact, folding of tissue, or damage to the capsule. Images captured using this software were compiled into stacks using Image J Fiji version 2.0.0 in preparation for quantification. All measurements were taken using Image J Software and data was collected using Microsoft excel. The thickness of the capsule was measured by calculating the arithmetic mean thickness.

Using Image J Fiji version 2.0.0, a random offset stereological square grid (cyan lines) was superimposed onto the image stacks to provide test lines. Where the tissue-implant interface of the capsule intersected a test line, an orthogonal line is drawn from this point to the edge of the capsule (yellow line) as seen in *Figure 2.5*. These measurements were compiled and averaged to calculate the mean fibrous capsule thickness per implant.

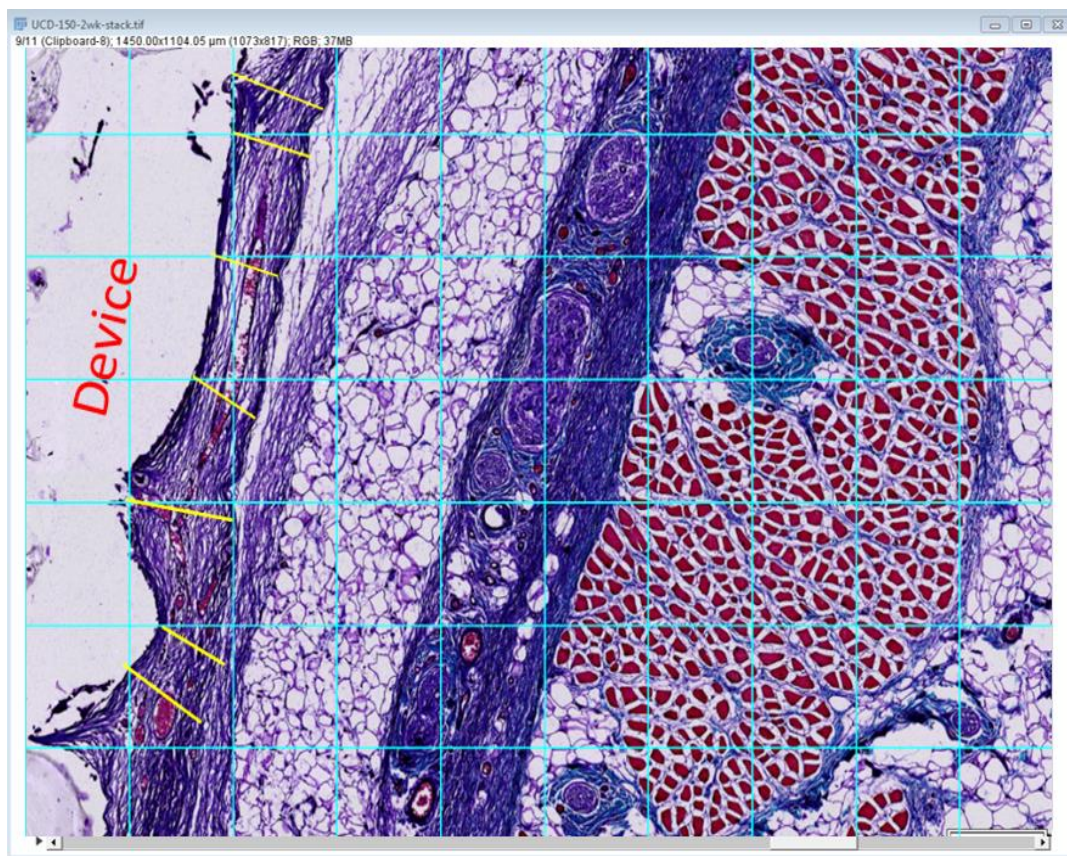


Figure 2.5: Morphometric and stereological method used to analyse fibrous capsule thickness surrounding the implanted implants stained with Masson's Trichrome with Gomori's Aldehyde Fuchsin.

2.2.6.3 Myofibroblast abundance

Any stromal spindle cells which stained positive for α SMA, and were not associated closely with any CD31+ staining were regarded as myofibroblasts. 20 random fields at of view were acquired at the tissue/implant interface to assess whether the abundance of myofibroblasts was influenced by varying surface topographies. Primary antibodies of CD31 (ab28364, Abcam) (1:200), α SMA (ab5694, Abcam) (1:100) were incubated for 1 hour at 37 °C. Secondary antibodies of Alexa Fluor® 594 goat anti-rabbit IgG (ThermoFisher Scientific) (1:100) and AlexaFluor® 488 goat anti-mouse IgG (ThermoFisher Scientific) (1:100) were incubated for 60 minutes at room temperature. Sections were stained with Hoechst and coverslipped using fluoromount. Immunofluorescence-stained slides were observed using a spinning disc inverted confocal microscope (Yokagawa CSU22) combined with Andor iQ 2.3 software. Area Fraction was estimated using the systematic point counting method using Image J (Fiji version 2.0.0) software.

A random offset stereological square grid was superimposed onto the images to provide test points. To calculate area fraction of myofibroblasts, intersections falling on α SMA+ and CD31- cells were counted and expressed as a ratio of total intersections within the region of interest.

2.2.6.4 Collagen organisation and maturity

For assessment of fibrotic capsule collagen maturity and arrangement, sections were deparaffinised in xylene, rehydrated through graded ethanol washes (100–70% v/v) to water before staining as previously described. Briefly, fibrotic capsule was assessed using picosirius red and stained in 0.1% fast green (pH 7, Fast Green FCF; Sigma Aldrich) and 0.1% Sirius red in saturated picric acid (picrosirius red stain), both in the same solution at a 1:1 ratio for 1 hour according to previously established protocols [260]. Following this, the sections were rapidly dehydrated through graded ethanol washes (70–100% v/v). Staining was performed using a Leica ST5010 Autostainer XL (Leica Biosystems; Wetzlar, Germany). The slides were then mounted using DPX mountant (Sigma Aldrich) and left to dry horizontally for five hours. Polarised light micrographs were captured using an Olympus BX4 polarised light microscope (Mason Technology Ltd. Dublin, Ireland) at 20x magnification. The polarising lenses were positioned on the light path before the sample and the second polariser (analyser) after the sample. Images were taken whereby maximum polarisation was achieved by adjustment of the polarising filters, and again orthogonal to this maximum polarisation. The two captured images were merged using the MAX function in ImageJ software (freely available from <https://imagej.nih.gov/>) which enables a complete visualisation of the collagen fibres present.

2.2.7 Macrophage response

The CD68 glycoprotein is commonly used as a pan-macrophage marker secreted by monocytes and tissue macrophages. The CD68 (MCA341r, BIORAD) (1:300) primary antibody, was incubated for 1 hour at 37 °C. Secondary antibody of Alexa Fluor® 594 goat anti-mouse IgG (ThermoFisher Scientific) (1:100) was incubated for 60 minutes at room temperature. Sections were stained with Hoechst and coverslipped using fluoromount. Immunofluorescence-stained slides were observed using a spinning disc inverted confocal microscope (Yokagawa CSU22) combined with Andor iQ 2.3 software. 20 random fields of view were acquired from each tissue section.

Volume fraction (Vv): Vv measures the proportion of a particular feature (in this case macrophages) within the reference tissue, describing the volume of that tissue taken up by the feature [261,262]. The Vv of stained macrophages was estimated using 20x confocal images and ImageJ. This was done by thresholding to eliminate auto fluorescence and calculating the % area of tissue occupied.

$$\frac{A}{A} = \frac{V}{V}$$

Numerical density (Nv): Nv refers to the number of particles within a unit volume of tissue. This was attained using ImageJ, via the creation of an unbiased sampling frame (30,000µm) and using the physical disector method. The number of sampled particles divided by the disector provides an unbiased estimation of numerical density [262,263] (*Figure 2.6*). Image pairs, 4µm apart (t=4), were taken from 60x mag Z-stacks and the number of macrophages present in the first image but not the second were counted. The area (a) of the frame occupied by tissue was noted. The numerical density was calculated from these counts as follows;

$$Nv = \frac{N}{t \times a}$$

Volume weighted mean volume (\overline{Vv}): Volume weighted mean volume provides an unbiased estimate of particle volume[261,264]. It gives a larger weighting to larger particles. This was calculated using the point sampled intercept (PSI) method and a staggered point grid to sample particles based on volume. This was done by randomly placing the point grid on the area of interest. The length of any macrophage intercepting the points was measured along the transect line and the following formula was applied;

$$\bar{V}_v = \frac{\pi}{3} (\bar{l}_o)^3$$

taking \bar{l}_o to be the mean cube of intercept lengths

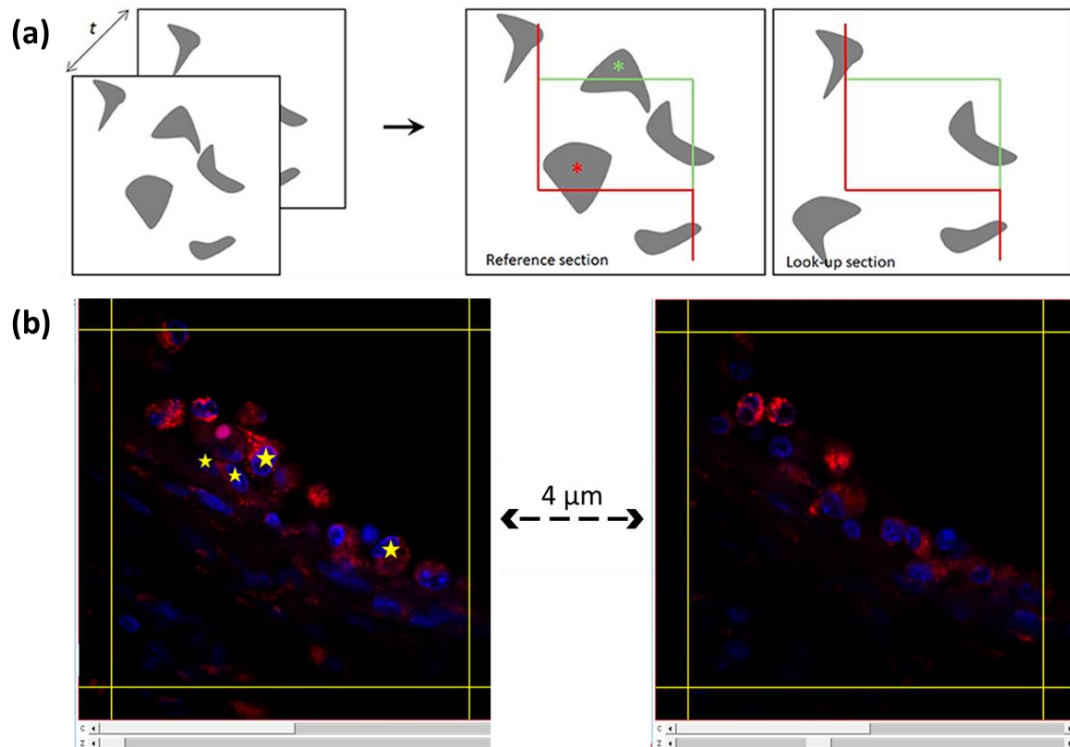


Figure 2.6: The physical dissector method. **(a)** Schematic of method – The number of macrophages present in the reference section (starred) which are not present in the look-up section are counted. **(b)** Example of reference section and look-up section encountered in this study.

2.2.8 Angiogenesis

2.2.8.1 Blood vessel abundance

The visualisation of blood vessels was facilitated by immunohistological staining for CD31, an endothelial cell marker. A HRP/DAB detection IHC Kit, for use with mouse and rabbit primary antibody (ab64264) was used. This kit provides a peroxidase block, a peroxidase labelled polymer and a substrate chromogen. The primary antibody used CD31 (ab28364, Abcam) (1:200) was incubated for 1 hour at 37 °C. Slides were counterstained with haematoxylin and coverslipped using D.P.X.

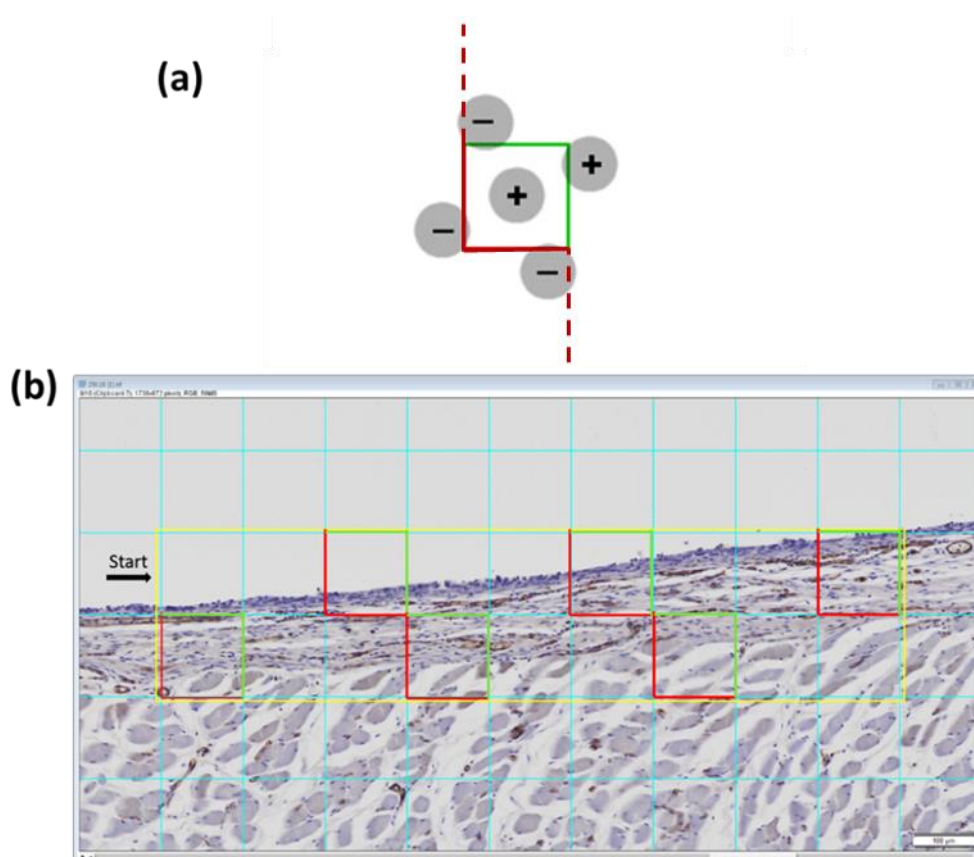


Figure 2.7: Unbiased counting frame, the principal. **(a)** Schematic of unbiased counting rule. Any blood vessel that is cut by a forbidden line is not counted (-). Blood vessels that appear inside the counting frame or are cut by the acceptance lines without also cutting the forbidden line are counted (+). **(b)** Example of this principal being executed on the fibrous capsule.

A systemic random sampling strategy was used. From each tissue section, ten non-overlapping images were taken of the Fibrous capsule surrounding each implanted implant. *Volume Fraction*: Using Image J Fiji version 2.0.0, a simple point counting method [265,266], was used to assess the volume fractions (V_v) of the blood vessel. The numbers of points which coincided with blood vessels were counted. The volume fractions of blood vessels were then calculated by expressing the proportion of points hitting blood vessels as a fraction of the total number of points observed in the tissue, from which the final V_v was calculated.

Number of Blood Vessels per Unit Area (N_a): This was calculated using an unbiased counting frame using the forbidden line rule which consists of red forbidden lines and green acceptance lines (*Figure 2.7*). Any blood vessel that is cut by a forbidden line is not counted. Blood vessels that appear outside the counting frame or are cut by the acceptance lines without also cutting the forbidden line are counted. The application of this counting rule generates an unbiased estimate of the number of blood vessels per unit area [261,267,268];

$$N_a = \frac{cN}{cPts \times A}$$

taking cN as cumulative no. of blood vessels counted and $cPts$ as cumulative no. of points in the area of interest

Length Density (L_v): method of estimating the length of the blood vessels within the tissue [266,268]

$$L_v = N_a \times 2$$

Radial Diffusion (R_d): refers to the cylindrical perfusion space surrounding a blood vessel and is used as a measure of Krogh's distance. This was calculated using the formula below [263,266];

$$R_d = \frac{1}{\sqrt{\pi(L_v)}}$$

Diameter of Blood Vessels: The minimum blood vessel diameter was measured, using ImageJ, for each blood vessel counted in an unbiased sampling frame. Measurements obtained were divided into size brackets (0-5 μ m, 6-10 μ m, 11-15 μ m, up to 40 μ m+) and expressed as percentages [268].

2.2.8.2 Blood vessel maturity

In order to further analyse the angiogenic response, the abundance of α SMA, a cell marker indicative of vessel maturity was quantified. Typically, as blood vessels mature, they become abundant in α SMA expressing cells such as smooth muscle cells, myofibroblasts or pericytes [269,270]. Primary antibodies of CD31 (ab28364, Abcam) (1:200), α SMA (ab5694, Abcam) (1:100) were incubated for 1 hour at 37 °C. Secondary antibodies of Alexa Fluor® 594 goat anti-rabbit IgG (ThermoFisher Scientific) (1:100) and AlexaFluor® 488 goat anti-mouse IgG (ThermoFisher Scientific) (1:100) were incubated for 60 minutes at room temperature. Sections were stained with Hoechst and coverslipped using fluoromount. Immunofluorescence-stained slides were observed using a spinning disc inverted confocal microscope (Yokagawa CSU22) combined with Andor iQ 2.3 software. 20 random fields at of view were acquired at the tissue/implant interface to assess whether the abundance of myofibroblasts was influenced by varying surface topographies. Blood vessels positive for α Smooth Muscle Actin in the capsule were counted using the ImageJ Cell Counter and expressed as a ratio of total.

2.2.9 Statistical analysis

GraphPad Prism (8.1.0) was used for statistical analysis. Normality of distribution was assessed by the Shapiro-Wilk test. Subsequent parametric and/or non-parametric tests were performed. For parametric data, a one-way or two-way analysis of variance (ANOVA) with post-hoc Tukey's multiple comparison was performed to compare between groups. For non-parametric data, a Kruskal-Wallis test was performed for comparing more than two groups. Statistical significance was accepted when $p < 0.05$. A minimum of two blinded counters were used for all analysis.

2.3 Results

2.3.1 Post-explantation imaging of implants

Differences in encapsulation tissue were noted upon gross examination, with *Figure 2.8 (a)* showing an example of these unmagnified samples viewed via transillumination. The s1 and s2 implants appeared reasonably transparent. With increasing microtexture in samples s3 to s5, there was a greater degree of opaqueness and thus incorporation of the implants into surrounding tissue. The increase in pericapsular outgrowth was further verified by micro-CT imaging shown in *Figure 2.8 (b)*. In the control and non-textured samples of s1 and s2, there are significant gaps between the implant surface and surrounding tissue. The microtextured surface of s3 displayed better contour matching than that of s1 or s2, and this became more apparent, with distinct tissue on-growth, as the micro-porosity of the surface increased in s4. The inclusion of multiple layers of rope-coiled pores resulted in excellent tissue ingrowth in s5. These phenomena were also observed in the SEM images shown in *Figure 2.8 (c)*. While there is minor delamination of tissue from the implants because of the sample processing, an imprint of the rough surface of the implants was seen in the tissue of s3 and s4. Like the micro-CT imaging, large gaps between the implant and surrounding tissue was seen in s1 and s2. The tissue in-growth encouraged by s5 prevented this delamination. The increase in tissue on-growth is starkly obvious when comparing SEM of s1 and s5 explants in *Figure 2.8 (d, e)* which was also verified by microCT imaging.

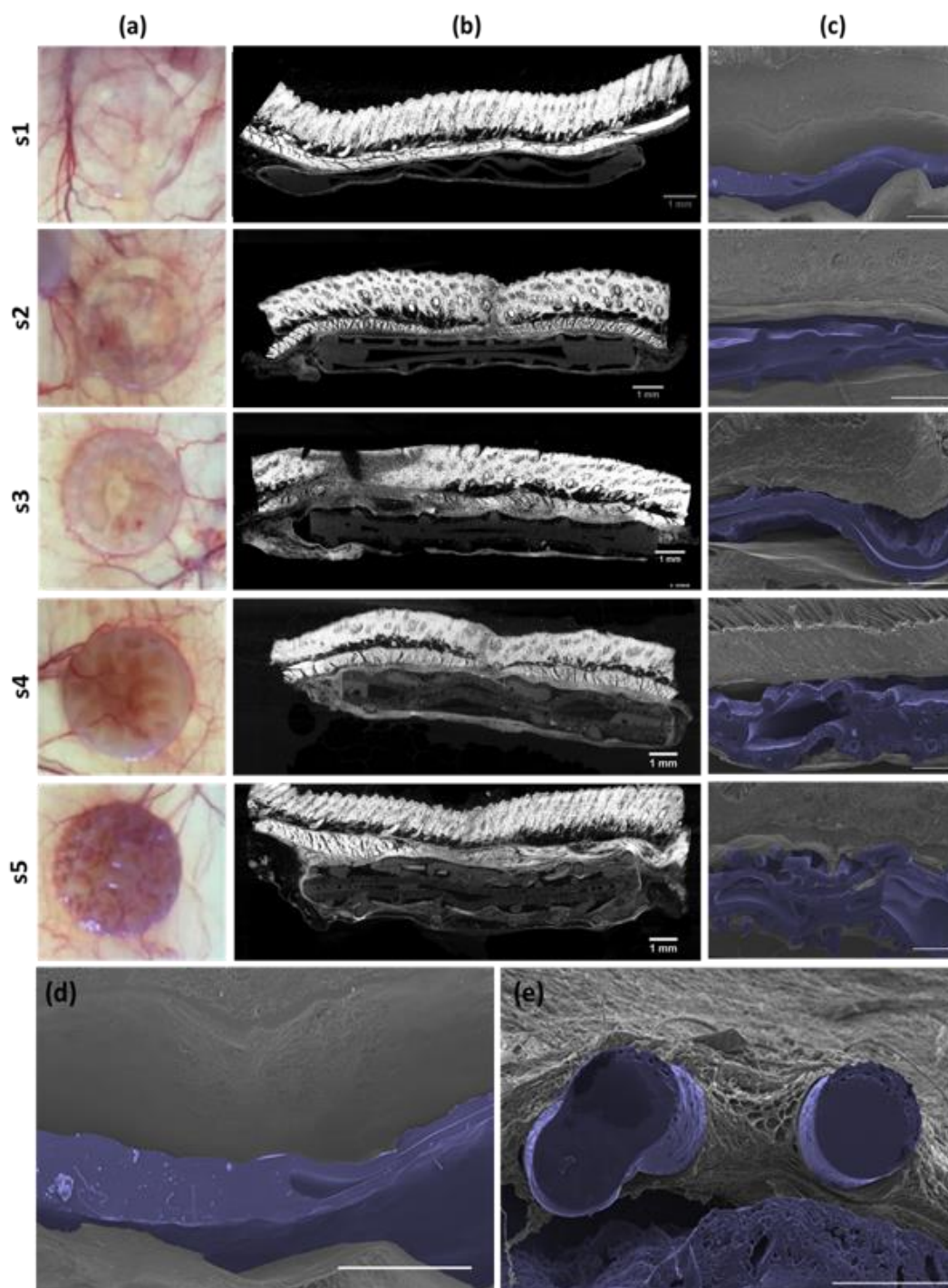


Figure 2.8: Post-explantation representative images of implants in-situ. **(a)** Transillumination of implant s1–s5 post-explantation on a light box allowing visualisation of blood vessels and the fibrous capsule surrounding the implants. **(b)** MicroCT cross sections of implants s1–s5. **(c)** SEM cross-sections of implants s1–s5. Scale bar: 1 mm. **(d)** SEM image of smooth implant s1 demonstrating no tissue integration. Scale bar: 1 mm. **(e)** SEM image of multiscale porosity implant s5, demonstrating tissue integration surrounding rope coil. Scale bar: 250 μm

2.3.2 Fibrous capsule analysis

2.3.2.1 Fibrous capsule thickness

In order to quantify the degree of implant incorporation into the surrounding soft tissue, a thickness assessment was performed on the fibrous capsule surrounding the s1 through s5 implants. Histology was performed on 2 week explants and capsular outgrowth was calculated by measuring thickness of the hyper-dense collagen made visible by Masson's trichrome stain, shown in *Figure 2.9 (a)*. Normal distribution was observed in all groups and a one-way ANOVA was carried out with post hoc Tukey's analysis. A significant increase in pericapsular outgrowth was seen as implant surface topography complexity increased (**** $P < 0.0001$) illustrated in *Figure 2.9 (b)*. To account for the imprints of the external macrotexture, the total area of tissue between the implant and the panniculus carnosus was also measured. Although there was an increased fibrous capsule thickness around implant s5, the area between the implant interface and the superficial muscle layer remains unchanged across all implant configurations, as shown in *Figure 2.9 (c)*. This finding suggests that although capsule thickness is larger in rope coil groups, the overall amount of capsule is not increased, it merely appears thicker due to its more tortuous development and increased affinity for tissue integration around the rope coil.

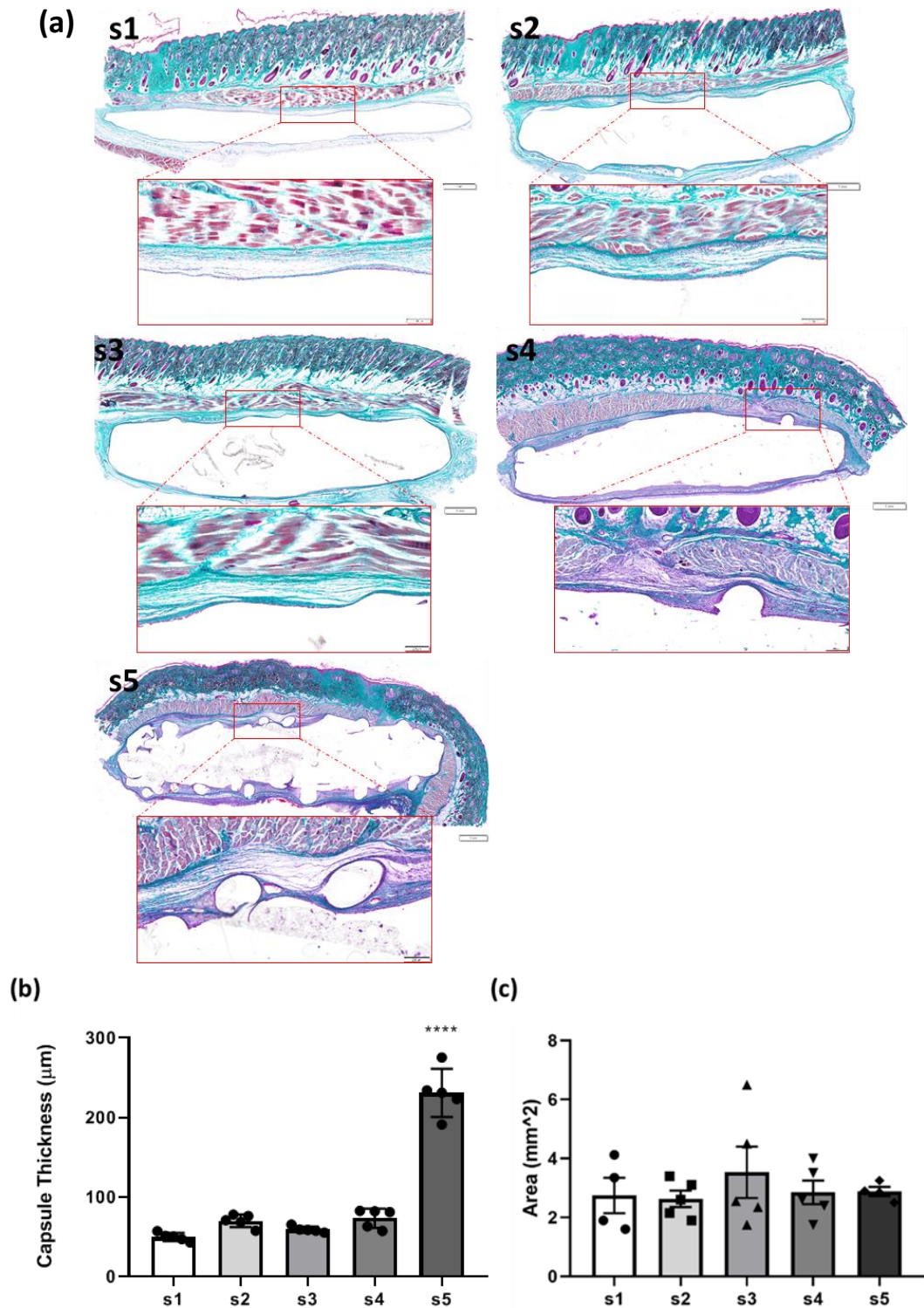


Figure 2.9: Analysis of the fibrous capsule. **(a)** Representative Masson's trichrome-stained histological sections (Scale bar=1 mm) and associated high magnification images of the fibrous capsule (Scale bars = 200 μ m). **(b)** Mean fibrous capsule thickness, data +/- SD. **(c)** Areas of tissue extending from the tissue/implant interface to the panniculus carnosus, data +/- SD of s1-s5. ****= $P < 0.0001$.

2.3.2.2 Myofibroblast abundance

The volume fraction of α SMA⁺ cells within 100 μ m of the implant interface was estimated using an unbiased stereological counting technique. Normal distribution was observed in all groups and a one-way ANOVA was carried out with post hoc Tukey's analysis. A significantly increased differentiation and proliferation of myofibroblasts (*P<0.05), seen in *Figure 2.10* was evident surrounding the s5 implant group suggesting an increase in ECM production which would correlate with an increased fibrous capsule thickness seen in *Figure 2.9*.

2.3.2.3 Collagen organisation and maturity

Polarised Light Microscopy (PLM) of picosirius red stained tissue sections was performed to better characterise the collagen network surrounding the implants. Picosirius red stain has been increasingly used for decades for collagen studies in medical research [271]. Collagen is birefringent or double refractive and this property is mainly due to ground substance acid mucopolysaccharides which are also anisotropic. Collagen which is abundant in basic amino groups reacts with acidic dyes exclusively such as Picosirius red stain which when bound to collagen in an ordered method, enhances collagen birefringence [271]. Stained fibers exhibit a spectrum of colours when viewed under polarized light depending on the fibre size, packing density and thus shows clear orientation of collagen fibre [272]. A greater anisotropic orientation of collagen deposition was more evident in s1 and s2 when compared to s3-s5, which exhibited an increasingly organised collagen structure in *Figure 2.11*. The collagen structure generated in these groups was arranged into bundles orientated parallel to the implant surface, forming a fibrous capsule of concentric layers intertwined around the external features of the implants. Picosirius red stains collagen type I, II, III [273–275] increasing their normal birefringency enabling very fine type I collagen fibres with weak birefringence to appear green in colour and mature type III collagen fibres appearing orange or red indicative of a further maturative stage [276]. The majority of the capsule in s1 and s2 appeared red/orange implying the presence of mature collagen type I. However, in s1-s3 there is an increased proportion of green and yellow fibres (thin, collagen type III-like) indicative of an earlier remodelling phase [276–278]. Taken together these data suggest that increasing the surface topography macrotecture promotes increased integration of the soft implant in vivo and positively modifies the ECM composition present at the tissue/implant interface to promote integration of the implant surface with surrounding soft tissues.

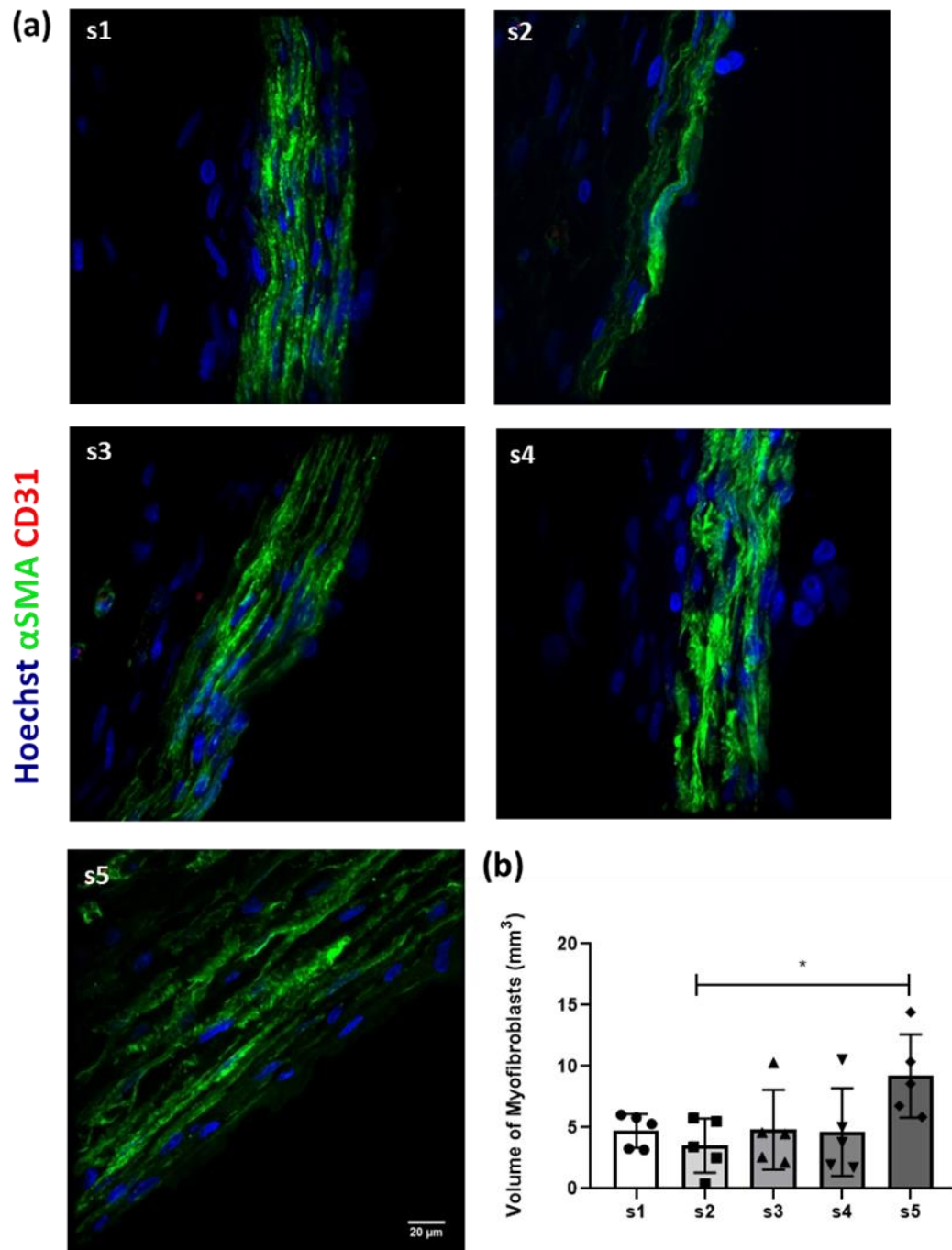


Figure 2.10: Analysis of the volume fraction of myofibroblasts within the surrounding fibrous capsule. **(a)** Representative immunofluorescent images of α SMA stained tissue (Blue = Hoechst, Green = α SMA, Red = CD31). **(b)** Volume fraction of α SMA+ cells $n=5$ /group, Data are mean \pm SD. * = $P < 0.04$.

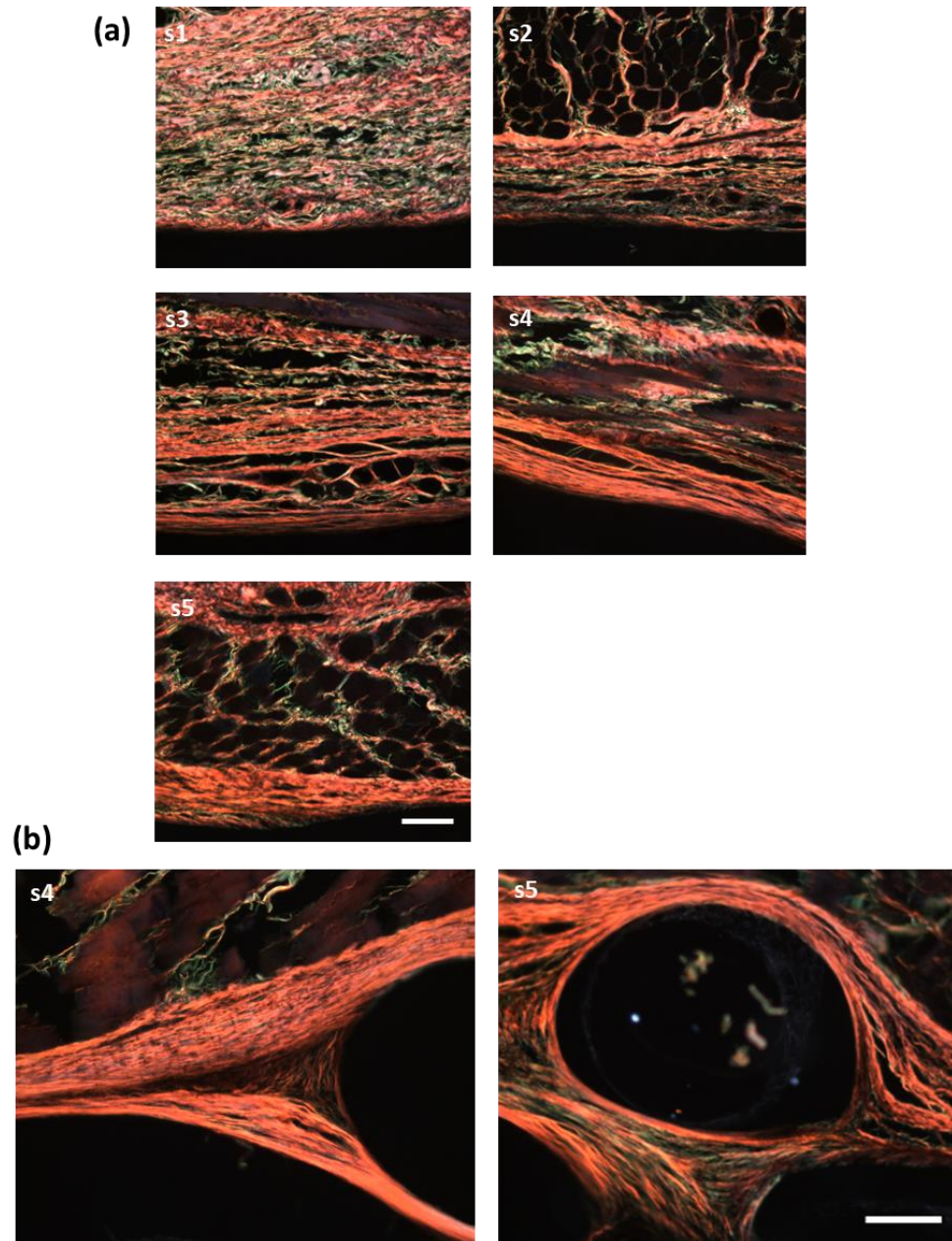


Figure 2.11: Analysis of collagen maturity and organisation at the tissue/implant interface. **(a)** Representative polarised light microscopy images of s1-s5. Scale bar = 100 μm . **(b)** Representative images of collagen surrounding rope-coil feature on s4 and s5. Scale bars = 50 μm . Orange/red= mature collagen, Green= immature collagen.

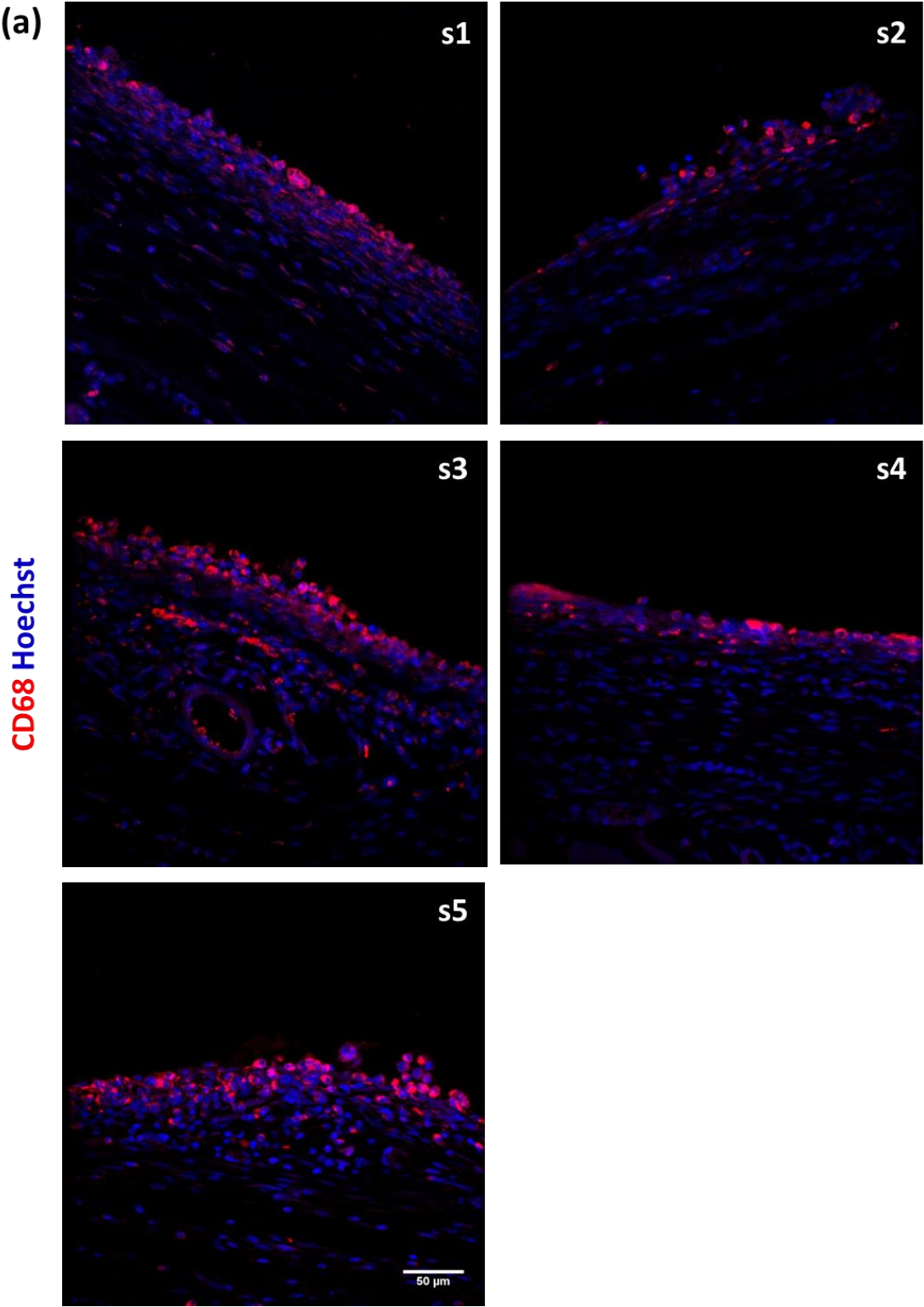
2.3.3 Macrophage response

2.3.3.1 Macrophage abundance

To establish whether the varying surface characteristics affected the activation and abundance of macrophages within the fibrous capsule, tissue sections were stained with a pan-macrophage marker (CD68) (*Figure 2.12 (a)*). Volume Fraction and numerical density analysis of CD68+ cells surrounding each implant was calculated. Normal distribution was not observed and a one-way ANOVA was carried out with a Kruskal-Wallis test which revealed no significant difference between groups (*Figure 2.12 (b, c)*). Volume weighted mean volume was used to estimate the volume of macrophages within the tissue. This method of analysis gives larger weighting to larger macrophages and thereby accounting for macrophage fusion to form foreign body giant cells. Using non-parametric statistical analysis, no significant difference was found however, the spread of the data suggests that implants s2 and s4 have larger amounts of giant cells than other implant groups.

2.3.3.2 Macrophage polarisation

To assess the impact of the varying surface characteristics on macrophage polarization, tissue sections were co-stained with both CD68/CCR7 and CD68/CD163. The ratio of CCR7+ cells out of total CD68+ cells was compared to the ratio of CD163 positive cells out of total CD68+ cells using confocal microscopy images (*Figure 2.13 (a)*). A 2-way ANOVA was performed with a Bonferroni's multiple comparisons test which found a significantly higher ratio of CCR7+ macrophages (M1) compared to CD163+ macrophages (M2) across all implant designs (**** $P < 0.0001$), suggesting the majority of macrophages present display an M1, or pro-inflammatory phenotype (*Figure 2.13 (b)*). Normal distribution was not observed and a one-way ANOVA was carried out with a Kruskal-Wallis test which revealed no significant in the ratio of M1 or M2 across groups. A second cohort of s4 implants was left implanted for 4 weeks ($n=4$), and macrophage staining revealed no difference in ratio of CCR7+ or CD163+ macrophages at a later time point. These data indicate that increasingly complex topographies do not evoke an enhanced macrophage response and that macrophage populations are consistent across all groups, with a consistent phenotype up to 4 weeks.



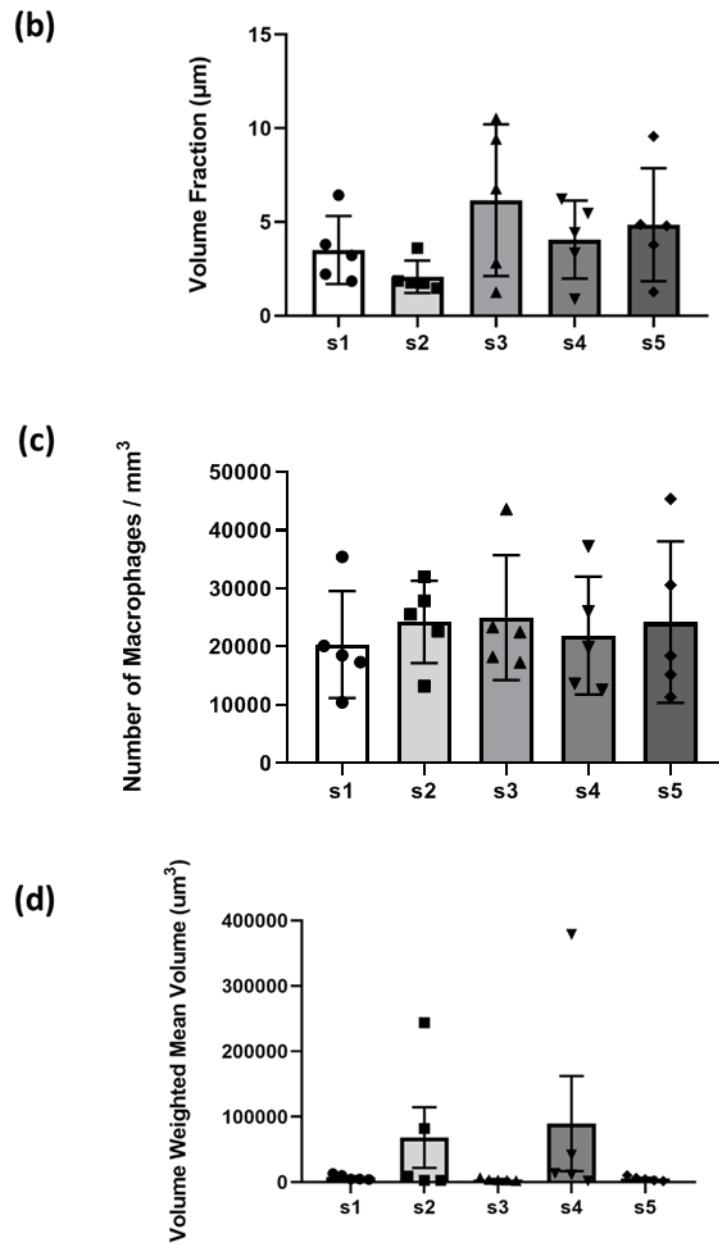


Figure 2.12: Analysis of the macrophage response at the tissue/implant interface. **(a)** Representative fluorescent images of CD68 (red) staining of s1-s5. Scale bar = 50 µm. **(b)** Volume fraction of CD68+ cells, data +/- SD. **(c)** Number of CD68+ cells per mm³, data +/- SD. **(d)** Volume weighted mean volume µm³ +/- SD (n=5).

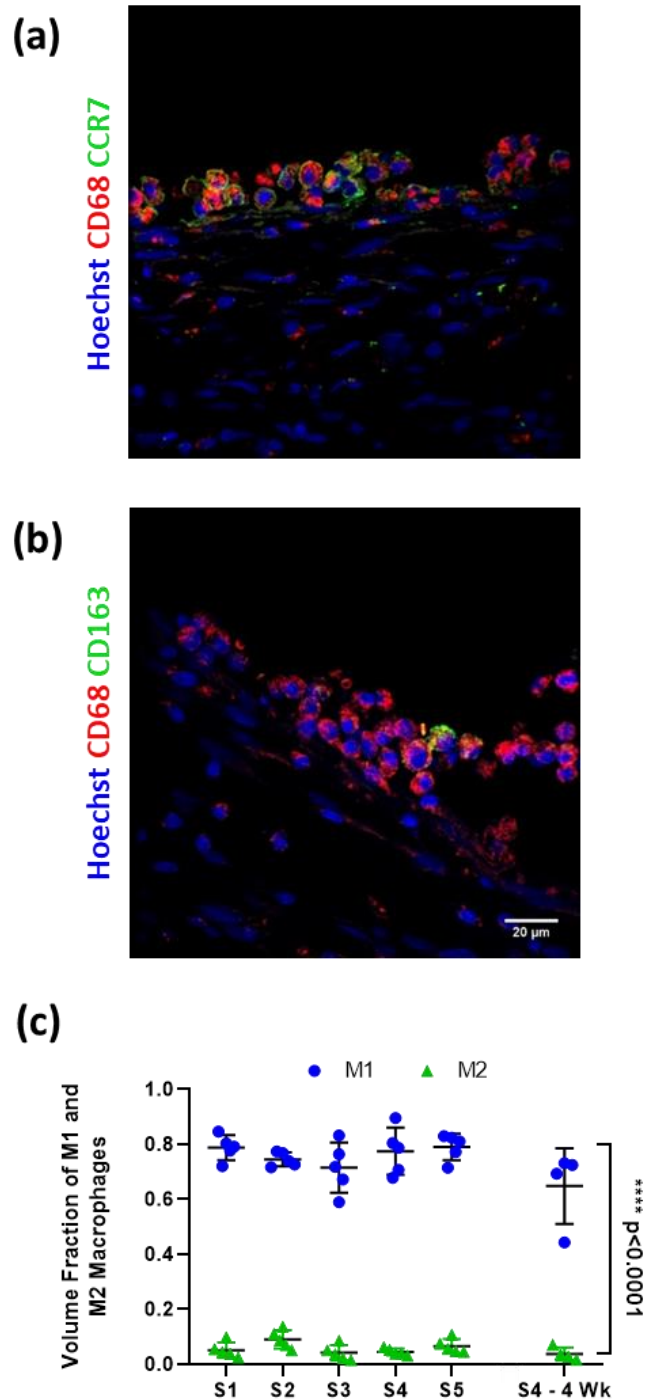


Figure 2.13: Analysis of the macrophage phenotype surrounding the 3D printed porous topography implants. **(a)** Representative immunofluorescent image of CD68 and CCR7 (M1 phenotype marker). **(b)** Representative immunofluorescent image of CD68 and CD163 (M2 phenotype marker). Scale bar = 20 μm . **(c)** Volume fraction of CCR7 and CD163 macrophages, data +/- SD of s1-s5 at 2 weeks and S4 implant at 4 weeks. M1 vs M2 s1-s5. ****P<0.0001

2.3.4 Angiogenesis

2.3.4.1 Blood vessel abundance

To investigate if surface texturing impacted neovascularisation at the implant surface. Tissue samples were stained for CD31, an endothelial cell marker, and a stereological analysis was performed to quantify blood vessel density surrounding each implant. Normal distribution was observed in all groups and a one-way ANOVA was carried out with post hoc Tukey's analysis. Assessment of the tissue/implant interface revealed that increasing complexity of the surface architecture led to a significant increase in the volume fraction, number per unit area, length density, and radial diffusion distances of blood vessels between s1 and s5 (* $P < 0.05$, ** $P < 0.01$, *** $P < 0.001$, **** $P < 0.0001$) (Figure 2.14). Analysis of blood vessels within 100 μm of the implant surface was also performed. Analysis of this revealed the increased surface complexity correlated with increased vessel density and that radial diffusion distances were significantly reduced in the s5 group when compared to s1. Across all five implant configurations, approximately 60% of blood vessels were found to be between 10 and 15 μm in diameter, suggesting young/new vessel formation.

2.3.4.2 Blood vessel maturity

In order to further analyse the angiogenic response, the abundance of $\alpha\text{SMA}+$ blood vessels, a marker indicative of vessel maturity was quantified. As blood vessels mature, they become abundant in αSMA expressing cells such as smooth muscle cells, myofibroblasts or pericytes [269,270]. A ratio of $\alpha\text{SMA}+$ vessels to total CD31+ vessels was obtained using confocal microscopy (Figure 2.15). Normal distribution was not observed and a one-way ANOVA was carried out with a Kruskal-Wallis test. This analysis revealed a significant increase in $\alpha\text{SMA}+$ vessels surrounding s5 when compared to s1 (* $P = 0.0303$). Taken together, this data indicated that the complex surface of s5 led to a recruitment of blood vessels and promoted increased vessel maturation at the interface with the tissue

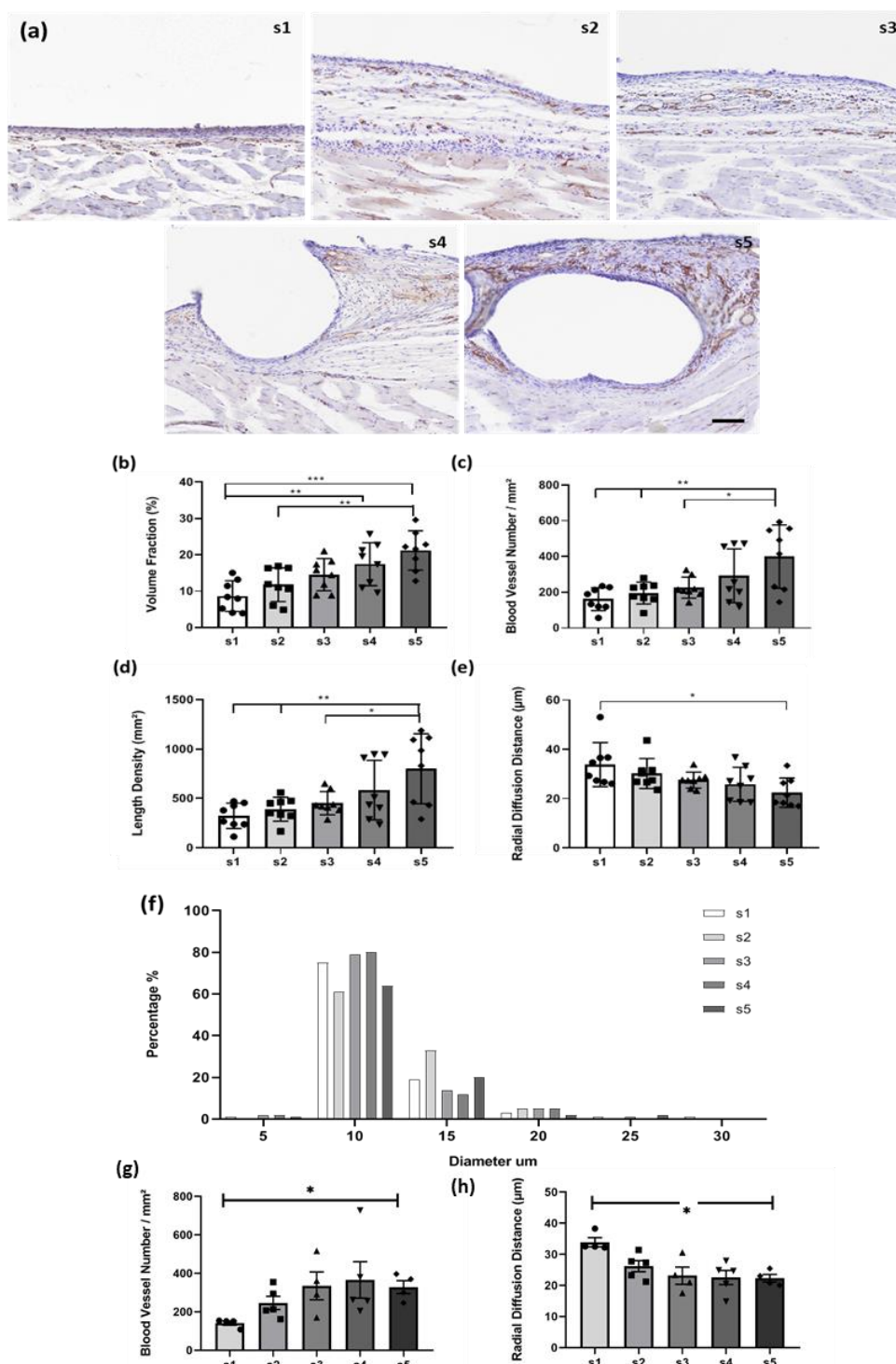


Figure 2.14: Analysis of angiogenesis between the tissue/implant interface and the panniculus carnosus. **(a)** Representative Images of CD31 staining s1-s5. Scale bar = 100 μm . **(b)** Volume Fraction of Blood Vessels. **(c)** Numerical Density of Blood Vessels **(d)** Length Density of Blood Vessels. **(e)** Radial Diffusion Distance. **(f)** Average blood vessel diameter for s1-s5. **(g)** Numerical Density of Blood Vessels within 100 μm of implant. **(h)** Radial Diffusion Distance within 100 μm of implant. Data represented as means \pm SD. * $P < 0.05$, ** $P < 0.01$ & *** $P < 0.001$.

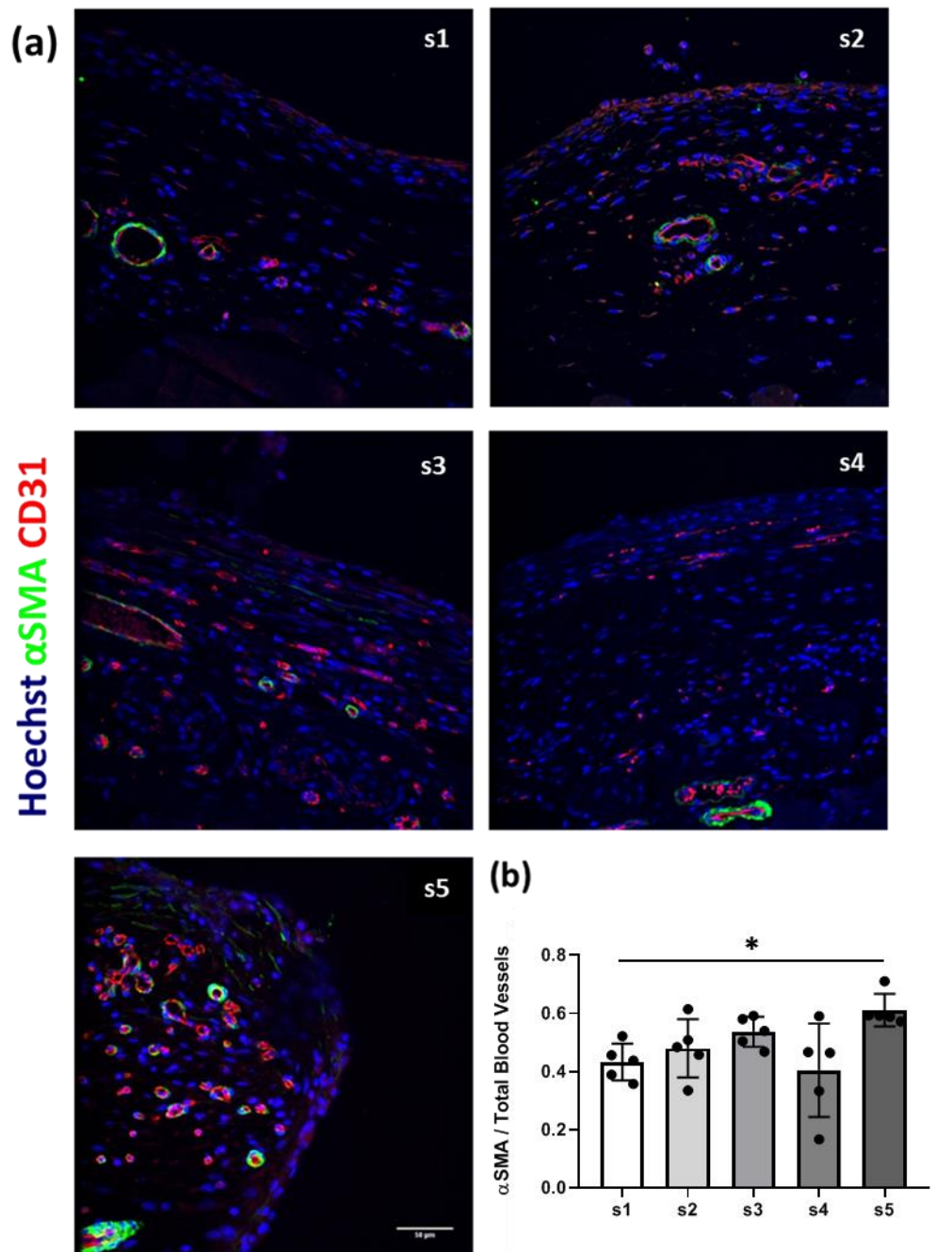


Figure 2.15: Analysis of vessel stability and maturity at the tissue/implant interface. **(a)** Representative fluorescent images of α SMA (green) and CD31 (red) staining of s1-s5 at the tissue/implant interface. Scale bar = 50 μ m. **(b)** Ratio of α SMA to CD31+ vessels, data \pm SD of s1-s5. $^* = P < 0.03$.

2.4 Discussion

The primary aim of this study was to determine an optimal surface topography (degree of micro- and macrotecture) for an islet macroencapsulation devices which harness the desired degree of tissue integration and vascularisation needed for encapsulated islet cell survival and function. Biocompatibility of device polymers, integration into the host tissue without a heightened immune response, and vascularisation are of crucial importance to the potential long-term efficacy of islet macroencapsulation. Previous studies have demonstrated that micro-range surface texture can modify cellular responses in the surrounding tissue, dampen chronic inflammation and promote angiogenesis, resulting in improved implant integration [279,280].

In the 14-day rodent study described in this chapter, it was demonstrated that implants possessing micro- and macropore structures (implants s4 and s5) showed an excellent propensity to encourage tissue attachment when compared to smooth implants. Increased tissue integration correlated with a significantly thicker fibrous peri-capsular outgrowth, increased myofibroblast abundance and collagen maturity (*Figures 2.9, 2.10 and 2.11*). Additional area/volume measurements of the hyper-dense collagenous capsules surrounding the implants demonstrated that peri-capsular outgrowth area was consistent across all implant groups (*Figure 2.9 (b), (c)*). This finding suggests that the overall amount of newly formed hyper-dense collagen did not increase, but merely appeared thicker due to its more tortuous development and increased affinity for tissue integration around the rope coil groups.

Macrophage activity surrounding the implants was assessed as a measure of the FBR [280]. Volume fraction and numerical density of macrophages were examined at the tissue/implant interface and although no significant differences between implants was observed, all implants elicited a FBR (*Figure 2.12*). All afore mentioned parameters are useful in the diagnosis of an inflammatory response but none take into account the degree of inflammation [280]. This can be accounted for by assessing the number of giant cells (FBGCs) within the fibrous capsule by measuring the macrophage volume as opposed to number/numerical density. Volume fraction accounts for total macrophage presence but not the presence/absence of FBGCs which are an integral part of an active FBR and important in assessing successful implant integration [204,281]. This was done by quantifying the volume weighted mean volume of the macrophages, which will inevitably be larger if FBGCs are present. No significance differences were found between each implant design however, due to the increased sizes of s2 and s4, it would suggest that they possess a higher abundance of

FBGCs. Previous studies have suggested that chronic immune responses may promote vascular development and induce angiogenesis [282]. The implant with the lowest angiogenic response (s1) also displayed indication of lower FBR associated macrophage counts. As well as this, s1 displayed little to no evidence of FBGCs. Macrophages are crucial in regulating the process of fibrous encapsulation [207], and typically the M2 polarization is seen with improved implant integration and long-term functionality [283–285]. However, in this study we see persistently higher levels of the M1 (proinflammatory) macrophage compared to M2 (anti-inflammatory) macrophages across all implant topographies (*Figure 2.13*). While the M1 polarisation seen across all implants would seem to indicate a reduced potential of integration and remodelling, it is likely that at the 2-week time point observed here the FBR is in the latter phases and is thus driven by myofibroblasts. This data correlates with the previous macrophage data (*Figure 2.12*), proving that increasingly complex topographies do not evoke a significantly enhanced macrophage response and that macrophage populations are consistent across all groups, with a consistent phenotype up to 4 weeks [283,286,287].

The formation of new vessels is imperative for the mass-diffusion of nutrients, waste, and oxygen to encapsulated cells. Without sufficient vascularisation, cellular function and device efficacy cannot be maintained. The results of this study indicate that vascular beds surround all implants which could potentially facilitate encapsulated islet survival and subsequent insulin diffusion. However, this analysis proved that significant increases in vascular density correlate with increased complexity of implant surface topography as seen in *Figure 2.14*. Crucially, the most complex implants, s4 and s5 were also associated with a reduction in radial diffusion distance (Rd), suggesting the presence of optimally vascularised tissue to facilitate the survival of encapsulated cells [168].

The use of modified surface topography to regulate fibrous capsule deposition surrounding implanted polymers is well documented [288,289] however, its combined use for to promote tissue integration and vascularisation to enhance diffusion potential is novel. Encapsulation devices such as the β Air aim to reduce the FBR but have attempted to do so with the expense of natural neovascularisation. This method of immunological communication has been demonstrated as effective in reducing overall FBR in large animals [290,291]. But this approach does not aim to directly use the fibrous capsule formation to enhance integration. It is therefore possible that reduced fibrous capsule formation may not trigger the same sequential wound healing response leading to vascularisation of the implant site. Due to this reduced vascularisation, oxygen supplementation to encapsulated cells is

required. Although the β Air device has been designed to compensate this and its effectiveness of this approach has been demonstrated in the long-term, the possibility of a loss in oxygen supplementation function is possible unless regularly monitored [292].

The patterning techniques described are completely versatile and are of huge potential to the medical device industry by offering tenability of fibrous capsule formation and angiogenesis through surface modification enabling increase or decrease of tissue integration, increase or decrease of fibrous capsule formation and increase or decrease of angiogenesis. The manufacturing technique could also provide a novel platform for drug delivery applications. The improved tissue integration and peri-implant vascularity could enhance the systemic uptake of small molecules or macromolecules infused into the implant, and the interconnected porous structures allow for diffusion of active therapies across the implant.

The manufacturing technique presents an alternative approach to prevascularisation with growth factors [293,294], that may help resolve the diffusion limitations of current devices and simulate the native microarchitecture of the cellular cargo [235,295,296]. However, the response seen in this study could be even further augmented with the addition of growth factors. Scheiner *et al* investigated an *in-vitro* strategy by incorporating VEGF loaded microspheres in 3D-printed poly(dimethylsiloxane) (PDMS)-based devices prior to their prospective loading with transplanted cells. *In-vitro* release studies demonstrated that incorporation of VEGF-releasing microspheres ensures adequate release of VEGF for a time window of four weeks [297]. By combining surface texturing and VEGF microspheres you can potentially stimulate the development of a stable vascular network while simultaneously encouraging successful tissue integration. This will be further investigated in *Chapter 3* of this thesis.

In conclusion, it was determined that a complex micro- and macrotecture were optimal surface topographies to enhance tissue integration and vascularisation needed for encapsulated islet cell survival and function. Implant s5 was therefore identified as the favourable designs for further experimentation. Their design enhancements provide a scaffold for tissue and blood vessel development, tissue attachment and integration in the absence of a heightened macrophage response. This finding has the potential to resolve the diffusion limitations of current devices and simulate the native microarchitecture of the cellular cargo for the maintenance of normoglycemia.

Chapter 3

Assessing the effects of VEGF releasing microspheres on the angiogenic and foreign body response to a multiscale porosity macroencapsulation device

3.1 Introduction

The islets of Langerhans are a highly metabolic group of cells which require ample amounts of oxygen and glucose to function correctly. Typically they receive between 5-15 % of the pancreatic blood supply even though they account for as little as 1-2% of the healthy pancreatic mass [15–17]. These native islet cells are encompassed by a dense capillary network, with radial diffusion distances equating to ~10–15 μm [18,19]. This high islet blood-flow rate guarantee that these specialised cells receive adequate oxygen and nutrient supply for survival and function [20]. Islet isolation procedures can often destroy the native islet vascular networks causing prolonged hypoxic stress contributing to a loss of 60% of transplanted islets during the first 48 hours post-transplantation [227,228]. In order to supply sufficient oxygen to islet cell mitochondria, the maximum radial diffusion distance between an islet cell and a capillary must not exceed 200 μm [298,299]. For these reasons, the development and distribution of neovascularisation adjacent to encapsulation device surface as well as the spatial arrangement of the encapsulated cells are essential to promote survival of encapsulated islets and is a primary limiting factor in long-term device success.

Islet survival and functional capacity are usually determined in the first three days post-transplantation, at which time the surrounding graft is largely avascular [130]. Previous studies by Padera and Colton examining the ideal time course of microarchitecture-driven vascularisation demonstrated a time frame comparable to the typical wound healing cascade of 7-21 days and diminishing by day 329. They found the number of stable vascular structures plateaued at day 21 and remained consistent until day 329. This differed from the typical wound healing cascade as the abundance of stable vessels is expected to decline due to regression [300]. Devices which utilise novel polymers or surface topographies to promote vessel formation can significantly enhance neovascularisation surrounding the implant [191,301,302]. Another approach to enhance oxygen supply and graft survival is prevascularisation, whereby a non-vascularised encapsulation device is implanted days/weeks prior to islet delivery [192,303]. Sernova's Cell Pouch™, consisted of a multi-channel sheet interleaved with an array of rods [182]. This pouch implanted subcutaneously for a month creates a prevascularised environment. Once microvasculature surrounds the device, the rods are removed to expose channels that allow the infusion of transplanted islets into the device. Unlike this, Beta O₂ Technologies has developed an alternative strategy to combat the delay in vascularisation by producing the β Air device. This device has an incorporated refillable oxygen tank, aiming to provide exogenous oxygen to implanted islets[230].

This technique would by-pass the necessity of the integral prevascularisation period preventing any limitation to the diffusion of oxygen and nutrient supply. In the previous chapter we examined novel additive manufacturing techniques to tailor multiscale porosity on the surface of soft tissue implants. We found that the degree of tissue integration and vascularity in proximity to the implant is shown to increase 2.5 fold with precisely controlled surface structural complexity.

Rapid vascularisation in the vicinity of devices has been promoted by the protein-based delivery of growth factors such as vascular endothelial growth factor (VEGF) to extra-hepatic sites by facilitating the controlled release of angiogenic stimuli [192,259,304,305]. VEGF is eventually released by transplanted islets to promote blood vessel formation and its early delivery within encapsulation strategies has been associated with enhanced engraftment and islet function [293,294,306]. In vitro release studies by Scheiner *et al*, demonstrated that incorporation of VEGF-releasing microspheres ensures adequate release of VEGF for a time window of four weeks. Inclusion of these VEGF-releasing microspheres within our silicone multiscale porosity devices could enhance angiogenesis and act as an innovative vascularisation strategy for artificial pancreas implants[307].

3.1.1 Aims

The overall aim of this research chapter is to assess whether encapsulating VEGF microspheres within the s5 designed device - referred to as the 'multiscale porosity macroencapsulation device' - can promote the formation of a substantial vascular network at the device surface.

The specific aims of Chapter 3 were:

- To investigate whether the addition of VEGF microspheres increased blood vessel formation around the multiscale porosity macroencapsulation device using in-vivo imaging and ex-vivo immunohistochemical and immunofluorescent staining
- Assess the morphology of the fibrous capsules surrounding each multiscale porosity macroencapsulation device using histological assessment, MicroCT and SEM imaging
- To characterise the compositions of the resultant fibrous capsules using immunofluorescent and histological staining
- To establish whether the addition of VEGF affected the activation, abundance and polarisation of macrophages at the tissue interface capsule using immunofluorescent staining

To achieve these aims, multiscale porosity macroencapsulation devices +/- VEGF microspheres were implanted sub-muscularly in the dorsum of a rodent model for a period of 28 days.

3.2 Materials and Methods

3.2.1 Macroencapsulation device and contents

3.2.1.1 Device fabrication

Device design and manufacturing was carried out by the O’Cearbhaill Lab, UCD, Dublin. I worked very closely with UCD to develop these rodent sized macroencapsulation devices, providing design inputs including shape, size and volume parameters.

16 devices of dimensions 10 x 20 x 2 mm were fabricated from medical grade silicone (*Figure 3.1*). Devices possessed a porous inner membrane with a micro and macro structure: Two membranes are fabricated entirely of salt/silicone solution ($12 \times 5 \mu\text{m}$ layers). The MED4840 rope-coil layer is extruded onto the surface, followed by over-spraying using another two salt/silicone solution layers. The salt was washed out of the membranes over a 24-hour period. A detailed description of the device manufacture process can be found in section 2.2.1 *Device Fabrication*. Each device was to be filled with 200 μL total of HA gel with the addition or absence of VEGF microspheres.

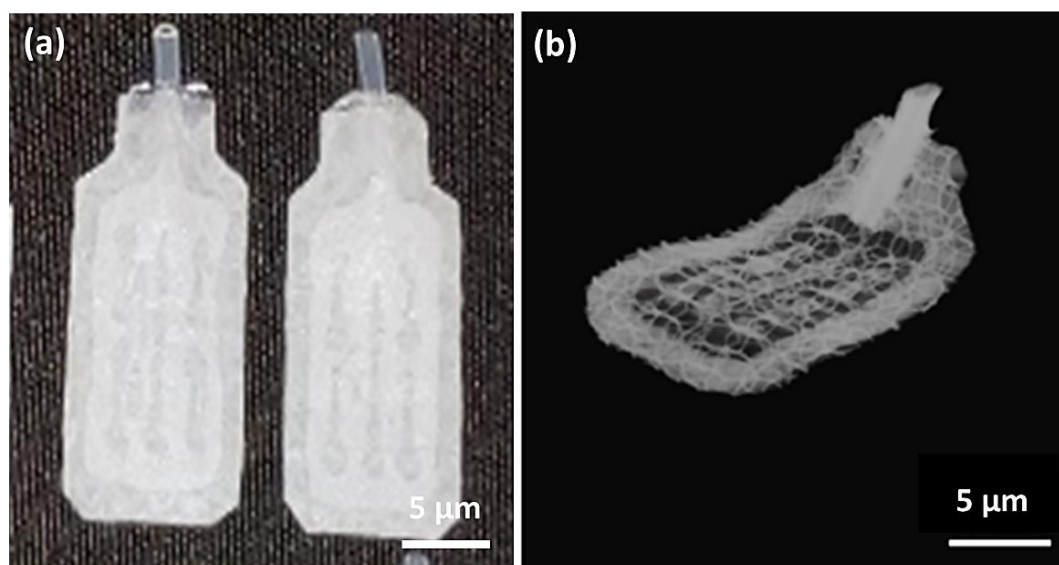


Figure 3.1: Rat sized (10 x 20 x 2 mm) macroencapsulation devices. **(a)** Photograph of devices. **(b)** MicroCT overview depicting complex surface architecture.

3.2.1.2 Hyaluronic acid gel formulation

These formulations and procedures were carried out by a DRIVE PhD candidate, Liam McDonough, RCSI, Dublin. I visited RCSI to receive training in procedure and production of gels for this study.

200 μ L of a 1% native HA hydrogel (Contipro a.s. Czech Republic) formulation was injected into each device. For –VEGF devices, a 1 % w/v native HA hydrogel was used to accommodate and deliver VEGF microspheres used in this study. For +VEGF devices, a 1 % w/v native HA hydrogel with the VEGF microspheres was formulated. This was formulated by making a native HA hydrogel with a concentration greater than 1% which was then diluted back to 1% with a 25 mg/mL VEGF microsphere suspension.

3.2.1.3 Vascular Endothelial Growth Factor (VEGF) microsphere formulation

These procedures were carried out by Dr Karina Scheiner in the Kok Lab, Utrecht Institute of Pharmaceutical Sciences, Utrecht University, The Netherlands and InnoCore Pharmaceuticals B.V., Groningen, The Netherlands.

In order to acquire a sustained local delivery of VEGF for a period of 4 weeks, monodisperse VEGF-loaded microspheres [Recombinant human VEGF₁₆₅ (PeproTech Inc. Rocky Hill, NJ, USA)] were used (*Figure 3.2*)[307]. VEGF₁₆₅ is a heparin-binding homodimeric glycoprotein involved in embryonic vasculogenesis and angiogenesis. These VEGF-loaded microspheres were prepared with blends of [PCL–PEG–PCL]-*b*-[PLLA] multiblock copolymers with various PEG molecular weight and content, using a solvent extraction-based membrane emulsification process. The microspheres had a VEGF loading of 0.79 wt % and loading efficiency of 78%. VEGF release is governed by diffusion through the water-swollen polymer matrix. *Scheiner et al* [297,307], the creators, provide a detailed documentation on the fabrication of these microspheres.

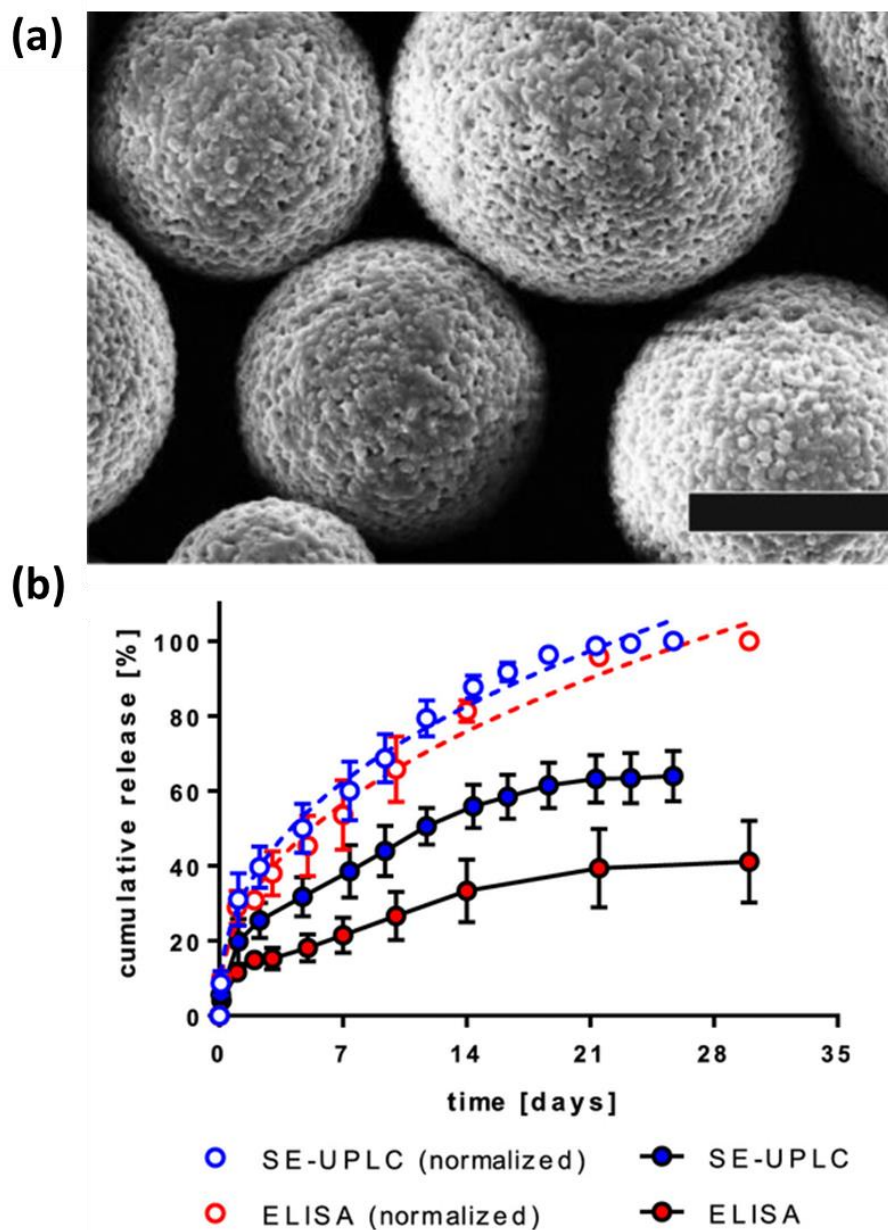


Figure 3.2: Vascular Endothelial Growth Factor (VEGF) microspheres. **(a)** Morphology of VEGF-loaded microspheres [307]. Scale bar=20 μm . **(b)** Cumulative release of VEGF from microspheres based on a 50:50 blend and a target VEGF loading of 1.0 wt %. The release study was performed at 37 $^{\circ}\text{C}$ in PBS pH 7.4 supplemented with 0.025% Tween 20 and 0.02% NaN_3 . Released VEGF was measured by ELISA (red) and SE-UPLC (blue), and plotted as cumulative release (filled blue and red circles, connected by a black line) and as a normalized cumulative release (blue and red circles). Normalized cumulative release data were fitted using the Korsmeyer–Peppas model (blue and red dotted lines) [307].

3.2.2 Subdermal implantation in rats

These procedures were carried out by Abiel srl., Palermo, Sicily. I contributed to the design and planning of this study, provided direction, travelled to Palermo to receive training and witnessed the implantation process, provided support for explantation of implants and tissue en bloc, and trained individuals on our tissue fixation and shipping protocols.

Rodent studies were approved by the Italian Ministry of Health (Authorisation No. 66/2017-PR). 8 rats RccHan Wistar (ENVIGO) 150/200 g females, age 12 weeks were used during this study. Rats were anesthetized by isofluorane and hair was removed in the area of implantation on the dorsum. Three incisions were made in each rat. Two of which were located to the left and right of the midline in the thoracic portion of the dorsum. Each incision cut through the dermis to the muscles of the dorsum. Each rat was implanted with 2 devices of the same treatment group (-VEGF or +VEGF) to provide a technical replicate (*Figure 3.3*). Devices were placed in the cavity following enlargement with a pair of scissors and filled. Each implant site was closed with 2/3 stitches and the animals were treated with anti-biotic ceftriaxone (25 mg/Kg) and painkiller tramadol (4 mg/Kg), for 5 days. Devices were also analysed by computerized axial tomography (Capiler CT-Scanner, PerkinElmer). This imaging enabled visualisation of the implants to accurately pinpoint its location and monitor its position. Before sacrifice at 4 weeks, angiogenesis at the implant site was evaluated using Iopamiro 370 staining. This was performed by cannulation of rat tail vein (cannula 22G) and continuous perfusion of warmed Iopamiro 370 at 10 mL/hour.

Images were acquired with FOV73 and FOV40 cameras. Using the OsiriX Lite program, low and high resolution images were constructed and used in combination with this software to isolate the complex vessel network surrounding each device and provide an estimation of vascular volume. Rats were euthanized at 4 weeks, each device and the immediate surrounding tissue were extracted.

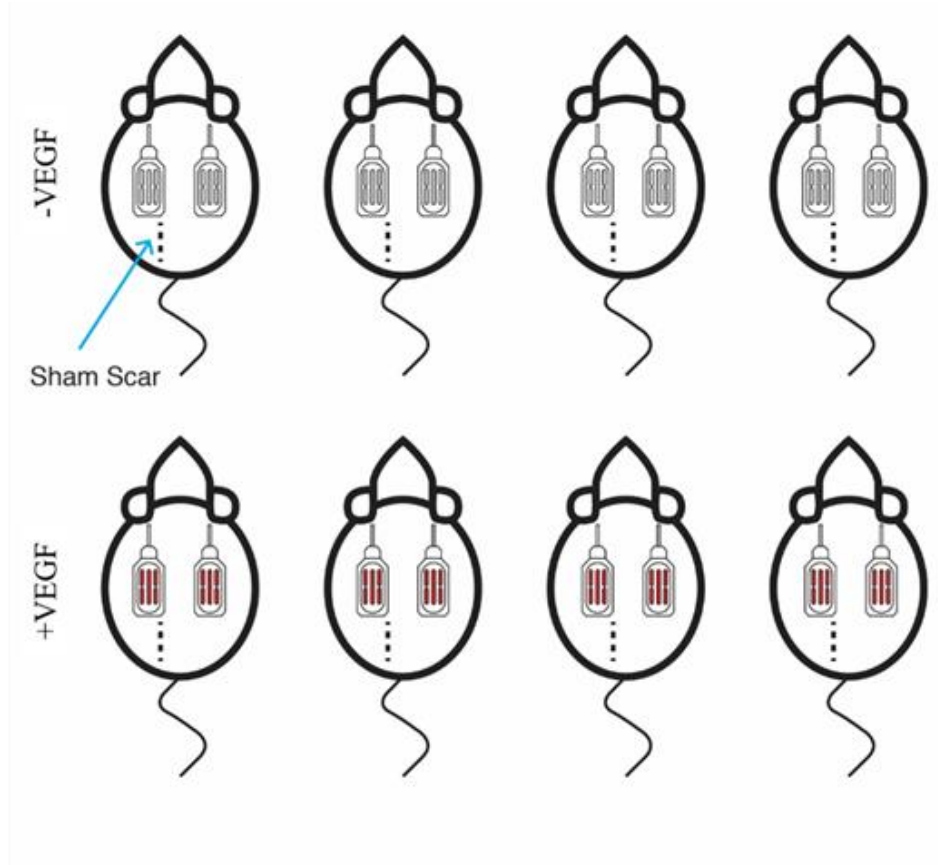


Figure 3.3: Study Design **(a)** 4 rats were each implanted with 2 multiscale porosity devices containing a standard HA gel composition. **(b)** 4 rats implanted multiscale porosity devices containing a standard HA gel with addition of VEGF microspheres (Robert Wylie BDes, MSc)

3.2.3 Fixation, embedding and staining

Tissues were fixed overnight using 4% paraformaldehyde (pH 7.4). The tissue allocated for histological analysis was then washed in 0.2 M phosphate-buffered saline with a final wash in 70% ethanol. Samples were transected in half, orientated and embedded in paraffin wax blocks. Sections of 5 μm were cut and stained with Masson's trichrome, picrosirius red and αSMA for fibrous capsule analysis. Additional sections were stained with a CD31, αSMA , CD68, CCR7 and CD163 antibodies for analysis of angiogenesis and immune response. The staining protocols are provided in detail in *Chapter 2*.

3.2.4 Angiogenesis

3.2.4.1 Blood vessel abundance

The visualisation of blood vessels was facilitated by immunohistological staining for CD31, an endothelial cell marker. A HRP/DAB detection IHC Kit, for use with mouse and rabbit primary antibody (ab64264) was used. This kit provides a peroxidase block, a peroxidase labelled polymer and a substrate chromogen. The primary antibody used CD31 (ab28364, Abcam) (1:200) was incubated for 1 hour at 37 °C. Slides were counterstained with haematoxylin and coverslipped using D.P.X. A systemic random sampling strategy was used to estimate *volume fraction (Vv)*, *Number of Blood Vessels per Unit Area (Na)*, *Length Density (Lv)* and *Radial Diffusion Distance (Rd)*. These methods of analysis are described in detail in section 2.2.8 *Angiogenesis* in the previous chapter.

3.2.4.2 Blood vessel maturity

In order to further analyse the angiogenic response, the abundance of αSMA , a cell marker indicative of vessel maturity was quantified. This was to assess whether the vessel maturity was influenced by the presence of VEGF microspheres. Immunofluorescent staining using CD31 and αSMA primary antibodies is described in detail in section 2.2.8.2 *Blood vessel maturity* in the previous chapter. Immunofluorescence-stained slides were observed using a spinning disc inverted confocal microscope (Yokagawa CSU22) combined with Andor iQ 2.3 software. 20 random fields at of view were acquired at the tissue-device interface. Blood vessels positive for αSMA in the fibrous capsule were counted using the ImageJ Cell Counter and expressed as a ratio of total.

3.2.5 Scanning Electron Microscopy (SEM)

Each tissue sample was bisected longitudinally to create a cross-section of the device and surrounding tissue. Samples were post-fixed overnight in 2.5% glutaraldehyde in 0.2 M PBS (pH 7.4). Samples were washed twice in 0.2 M PBS for 10 minutes before dehydration through a series of graded alcohols (30%, 50%, 70%, 90% and 100%). Following dehydration, samples were transferred to the EMITECH K850 critical point dryer. This removed all the liquid in a precise and controlled way, so fragile tissue was not damaged or distorted in the process. Samples were then mounted onto aluminium stubs using carbon adhesive tabs. An Emscope SC500 was used to lightly sputter coat the samples. Specimens were imaged using a Hitachi S2600N Scanning Electron Microscope using a secondary electron detector (Vacuum 15 kV, electron Beam 50). SEM images were pseudo-coloured using MountainsMap® SEM Color 7.3.7984.

3.2.6 Fibrous capsule analysis

3.2.6.1 *Fibrous capsule thickness*

Using Masson's Trichrome with Gomori's Aldehyde Fuchsin stained tissue sections, morphometric and stereological methods were used to analyse the thickness of the fibrotic capsule surrounding the encapsulation devices. This method is described in detail in 2.2.6.1 *Fibrous capsule thickness* and *Figure 2.1* in the previous chapter.

3.2.6.2 *Myofibroblast abundance*

Any stromal spindle cells which stained positive for α SMA, and were not associated closely with any CD31+ staining were regarded as myofibroblasts. 20 random fields at of view were acquired at the tissue-device interface to assess whether the abundance of myofibroblasts was influenced by the presence of VEGF within the devices. The immunofluorescent staining procedure is described in 2.2.6.2 *Myofibroblast abundance*. Area Fraction was estimated using the systematic point counting method using Image J (Fiji version 2.0.0) software. A random offset stereological square grid was superimposed onto the images to provide test points. To calculate area fraction of myofibroblasts, intersections falling on α SMA+ and CD31- cells were counted and expressed as a ratio of total intersections within the region of interest.

3.2.6.3 Collagen organisation and maturity

For assessment of fibrotic capsule collagen maturity and arrangement, sections were stained with picrosirius red and counterstained with fast green as previously described by Monaghan *et al.* [308] and in section 2.2.6.3 *Collagen organisation and maturity* of this thesis.

3.2.7 Macrophage response

The CD68 glycoprotein is commonly used as a pan-macrophage marker secreted by monocytes and tissue macrophages. The CD68 immunofluorescence staining is described in detail in 2.2.7 *Macrophage response*. Immunofluorescence-stained slides were observed using a spinning disc inverted confocal microscope (Yokagawa CSU22) combined with Andor iQ 2.3 software. 20 random fields of view were acquired from each tissue section to analyse the volume fraction of macrophages within the fibrous capsule (*described in 2.2.7 Macrophage response*).

3.2.8 Statistical analysis

GraphPad Prism (8.1.0) was used for statistical analysis. Normality of distribution was assessed by the Shapiro-Wilk test. Subsequent parametric and/or non-parametric tests were performed. For parametric data, an unpaired t-test was performed for comparing between two groups and a one-way or two-way analysis of variance (ANOVA) with post-hoc Tukey's multiple comparison for comparing between groups. For non-parametric data, a Mann-Whitney U was performed for comparing between two groups and a Kruskal-Wallis test for comparing more than two groups. Statistical significance was accepted when $P < 0.05$. A minimum of two blinded counters were used for analysis.

3.3 Results

3.3.1 X-ray microtomography (Micro-CT)

Micro-CT imaging was performed on a weekly basis to enable visualisation of the macroencapsulation devices to accurately pinpoint their location and monitor position over the 4 weeks. Extreme changes to the device position could disrupt the newly forming tissue and vasculature surrounding each device. Over the 4-week implantation period, devices maintained their position and therefore were approved for further analysis as seen in *Figure 3.4*.

3.3.2 *In-vivo* analysis of angiogenesis

Before sacrifice at 4 weeks, Iopamiro 370 staining was performed to permit visualisation of the complex vessel network surrounding each device and allow an estimation of vascular volume to be calculated. Qualitative analysis using high resolution imaging showed a greater aggregation / density of vessels surrounding the +VEGF devices when compared to the vessels surrounding -VEGF devices. Quantitative analysis using the OsiriX Lite provided estimation of vascular volume. Normal distribution was observed in both groups and an un-paired t-test was performed. A significant increase in vascular network volume (*P=0.0132) was observed in the +VEGF group (*Figure 3.5*). This finding suggested that the addition of VEGF microspheres promoted increased formation of vessels surrounding the devices.

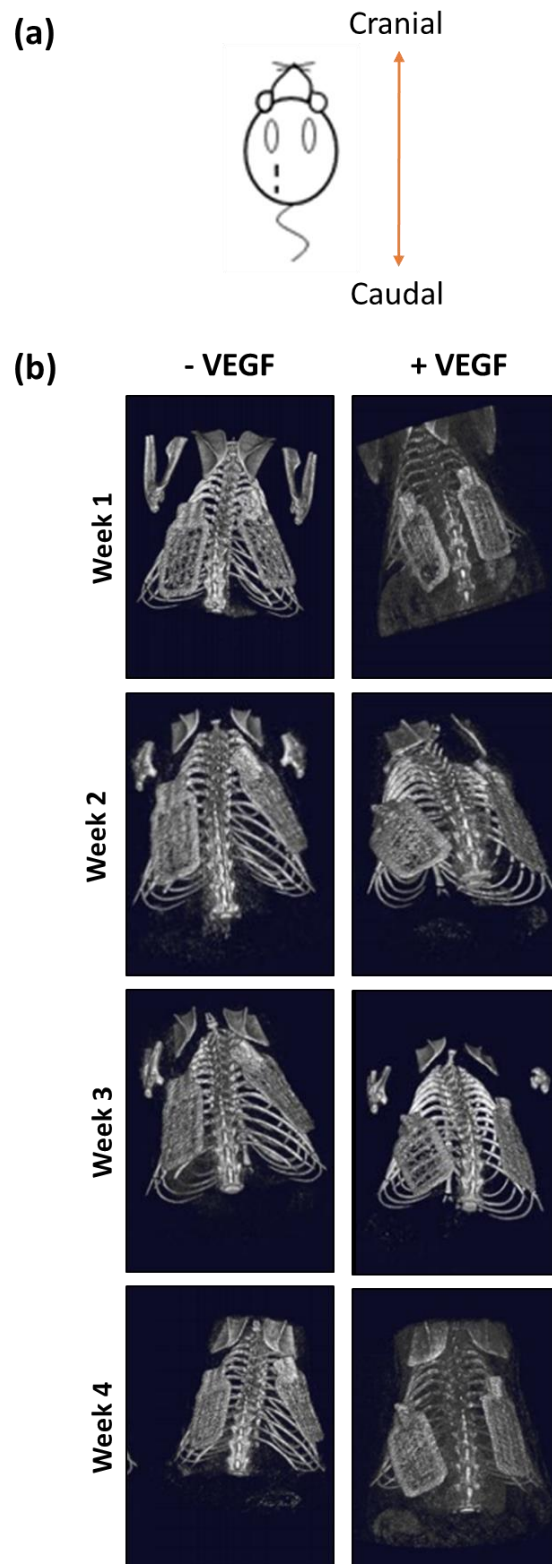


Figure 3.4: Micro-CT images of devices implanted subcutaneously in the dorsal thoracic region of rats. **(a)** Schematic describing orientation of micro-CT images. **(b)** Representative micro-CT images of implanted –VEGF and +VEGF devices at time 0 – 4 weeks.

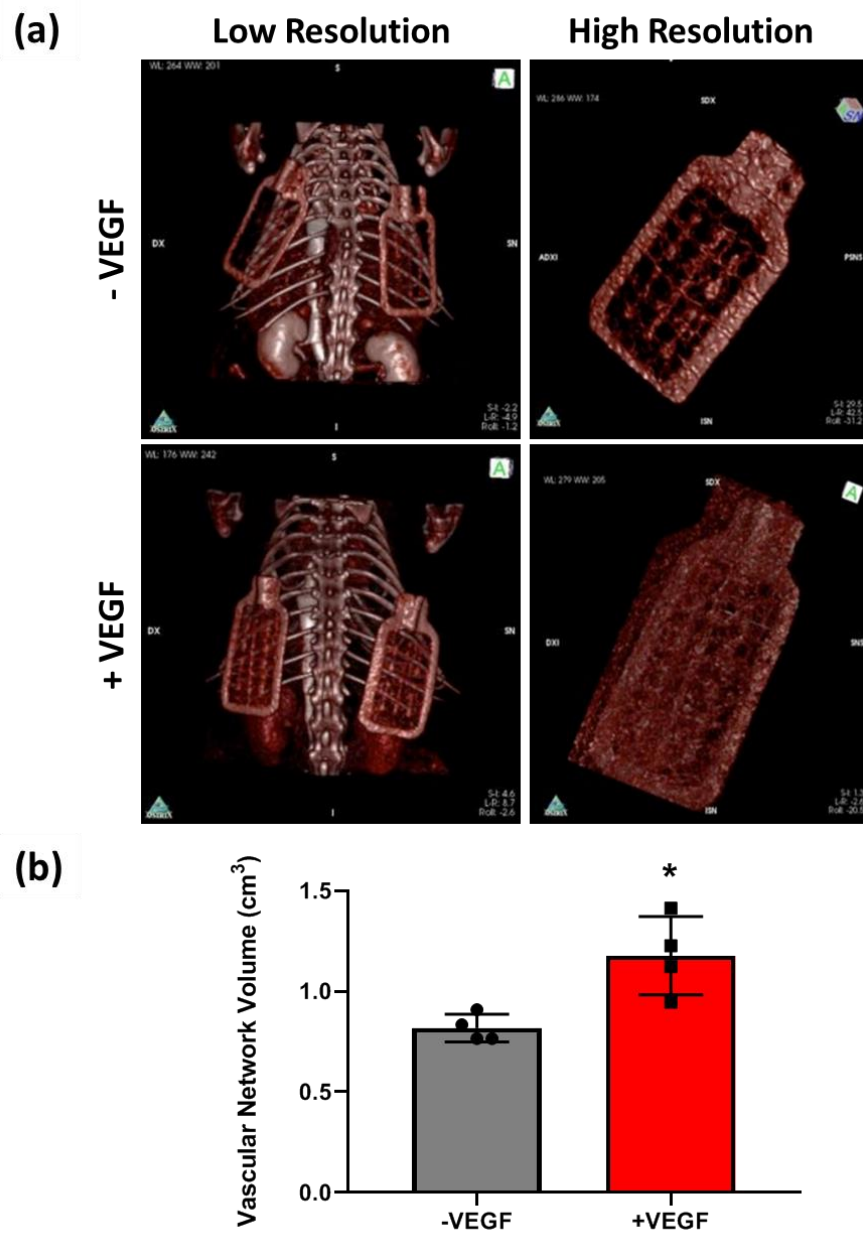


Figure 3.5: In-vivo evaluation of angiogenesis at 4 weeks. **(a)** Representative images of lopamiro 370 stained -VEGF and +VEGF devices were captured at both low (FOV73 camera) and high resolutions (FOV40 camera). **(b)** Mean volumes of surrounding vascular network estimated using the OsiriX lite program. $n = 4$ per group, data are means \pm SD, $*=P<0.05$.

3.3.3 Angiogenesis

3.3.3.1 Blood vessel abundance

To investigate if the addition of VEGF microspheres promoted neovascularisation at the implant surface sections were stained for CD31 (an endothelial cell marker) and stereological analysis was performed to quantify blood vessel density surrounding each device (*Figure 3.6*). Normal distribution was observed in all groups and an unpaired t-test was performed. Assessment at the tissue-device interface revealed no significant difference in number per unit area ($P=0.3288$), length density ($P=0.3413$), and radial diffusion distance ($P=0.7811$) of blood vessels between -VEGF and +VEGF groups.

3.3.3.2 Blood vessel maturity

In order to further analyse the angiogenic response, the abundance of α SMA+ blood vessels, a marker indicative of vessel maturity was quantified. As blood vessels mature, they become abundant in α SMA expressing cells such as smooth muscle cells, myofibroblasts or pericytes [269,270]. A ratio of α SMA+ vessels to total CD31+ vessels was obtained using confocal microscopy (*Figure 3.7*). Normal distribution was observed and an unpaired t-test was performed. A significantly higher ratio of α SMA+ vessels was observed in the +VEGF group compared to the -VEGF (** $P=0.0040$).

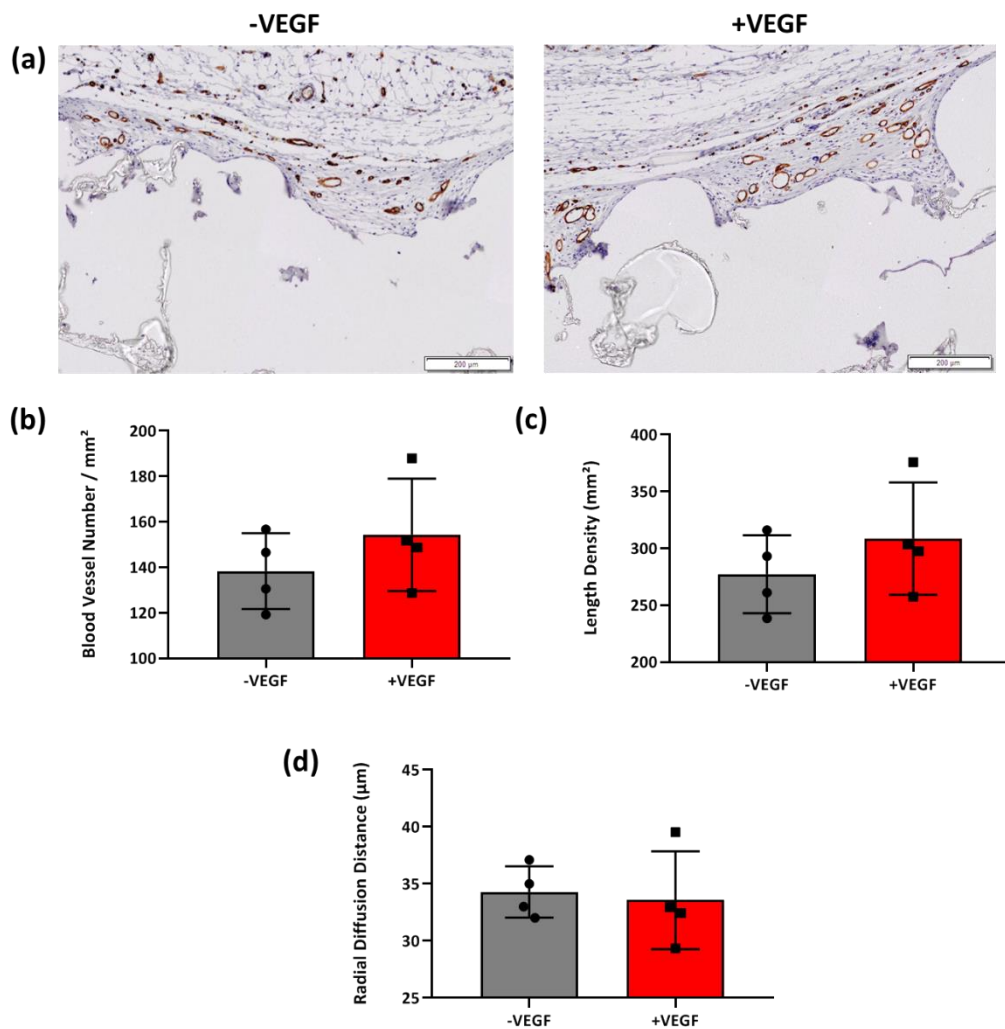


Figure 3.6: Analysis of angiogenesis between the tissue-device interface and the panniculus carnosus. **(a)** Representative Images of CD31 staining of tissue/device interface in –VEGF and +VEGF samples. Scale bar = 200 µm. **(b)** Numerical Density of Blood Vessels. **(c)** Length Density. of Blood Vessels. **(d)** Radial Diffusion Distance. $n = 4$ per group, data are means \pm SD.

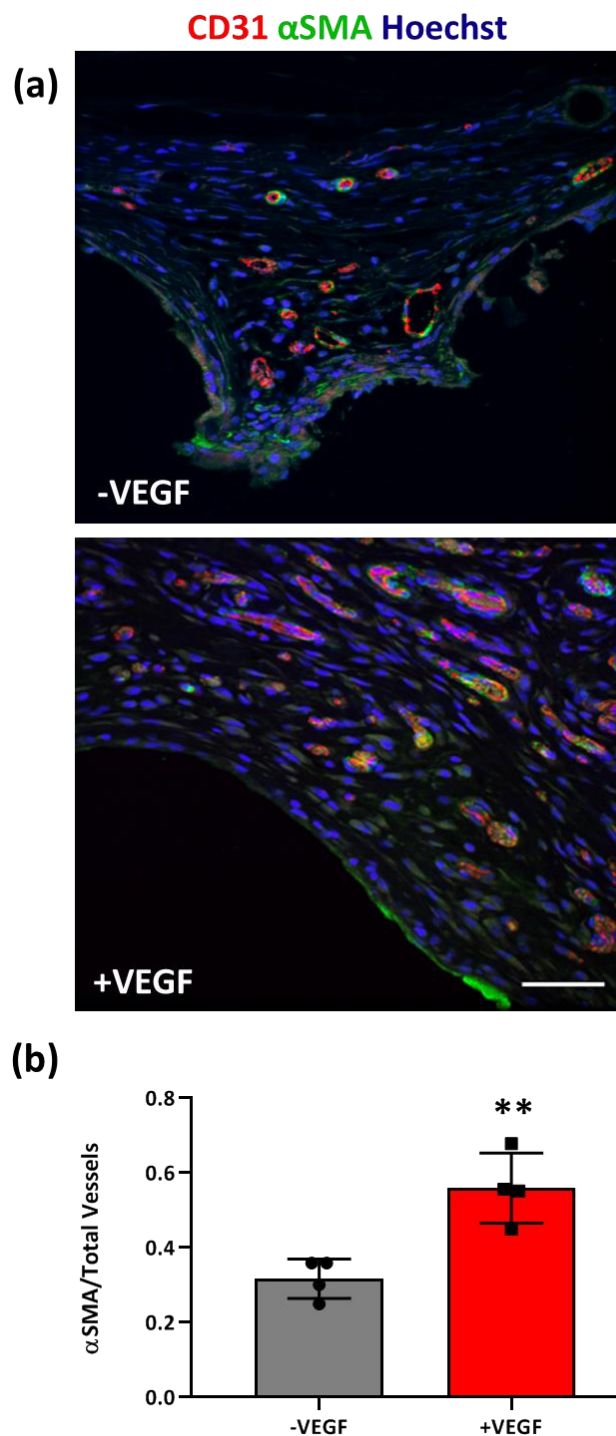


Figure 3.7: Analysis of vessel stability and maturity at the tissue-device interface. **(a)** Representative fluorescent images of α SMA (green) and CD31 (red) staining of $-$ VEGF and $+$ VEGF at the tissue/device interface. Scale bar = 50 μ m. **(b)** Ratio of α SMA+ to total CD31+ vessels, for analysis of vessel stability and maturity. $n = 4$ per group, data are means \pm SD, **= $P < 0.01$.

3.3.3.3 Blood vessel diameter

Subsequently, due to contrasting results an investigation into blood vessel diameter was carried out. The lumen diameters of 250-700 CD31+ stained blood vessels were measured per animal and were sampled based on unbiased stereological sampling techniques. Diameters were represented as mean \pm SD (*Figure 3.8 (a)*). A large variation in data was observed contributing to a non-normally distributed population. A non-parametric t-test was performed with subsequent Mann Whitney U analysis. Blood vessels surrounding devices containing VEGF microspheres demonstrated a significant increase in diameter when compared to -VEGF devices (**P=0.0002). A percentage frequency distribution of vessel diameters was also constructed in order to display the spread of the data based on diameter size (coefficient of variation = 49 vs 60%) (*Figure 3.8 (b)*). The majority of vessels were between 5-10 μ m in diameter. When comparing the size distribution of +VEGF and -VEGF devices, fewer +VEGF blood vessel diameters were found in the 5-10 categories with a higher proportion of +VEGF vessels found in the 20-35 μ m categories when compared to -VEGF diameters (median = 7.7 vs 8.2 μ m and 90th percentile = 14 vs 16 μ m).

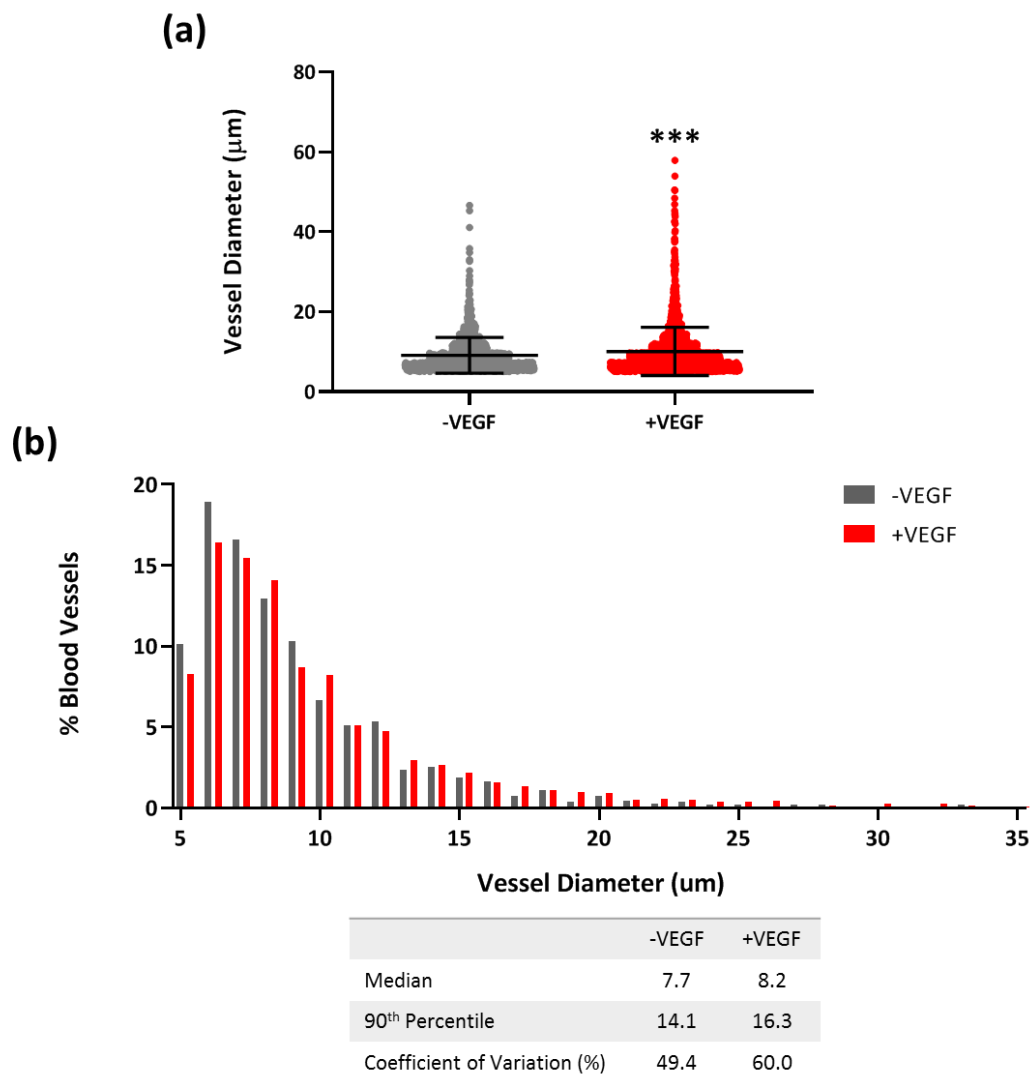


Figure 3.8: Analysis of blood vessel diameters (a) Blood vessel diameters (b) Percentage frequency distribution of blood vessel diameters surrounding -VEGF and +VEGF devices. $n = 4$ per group, data are means \pm SD, ***= $P < 0.001$.

3.3.4 Scanning Electron Microscopy (SEM)

SEM was performed in order to examine the relationship between the macroencapsulation devices and the surrounding tissue. As demonstrated in the previous chapter of this thesis, the inclusion of multiple layers of rope-coil and micro-porosity results in excellent tissue integration. This finding was also confirmed in the present study with both –VEGF and +VEGF devices exhibiting an excellent propensity for tissue on-growth and integration into the surrounding tissue as seen in *Figure 3.9*.

3.3.5 Fibrous capsule analysis

3.3.5.1 Fibrous capsule thickness

In order to assess whether the addition of VEGF microspheres impacted the degree to which devices became incorporated into surrounding soft tissue, a thickness assessment was performed on the fibrous capsule surrounding both –VEGF and +VEGF groups. Histology was performed on the 4 week explants and fibrous capsule thickness was calculated by measuring thickness of the hyper-dense collagen made visible by Masson's trichrome stain, shown in *Figure 3.10*. Normal distribution was observed in both groups and an unpaired t-test was performed. No significant difference was found ($P=0.3478$) between the treatment groups indicating that VEGF microspheres do not promote increased fibrous capsule formation.

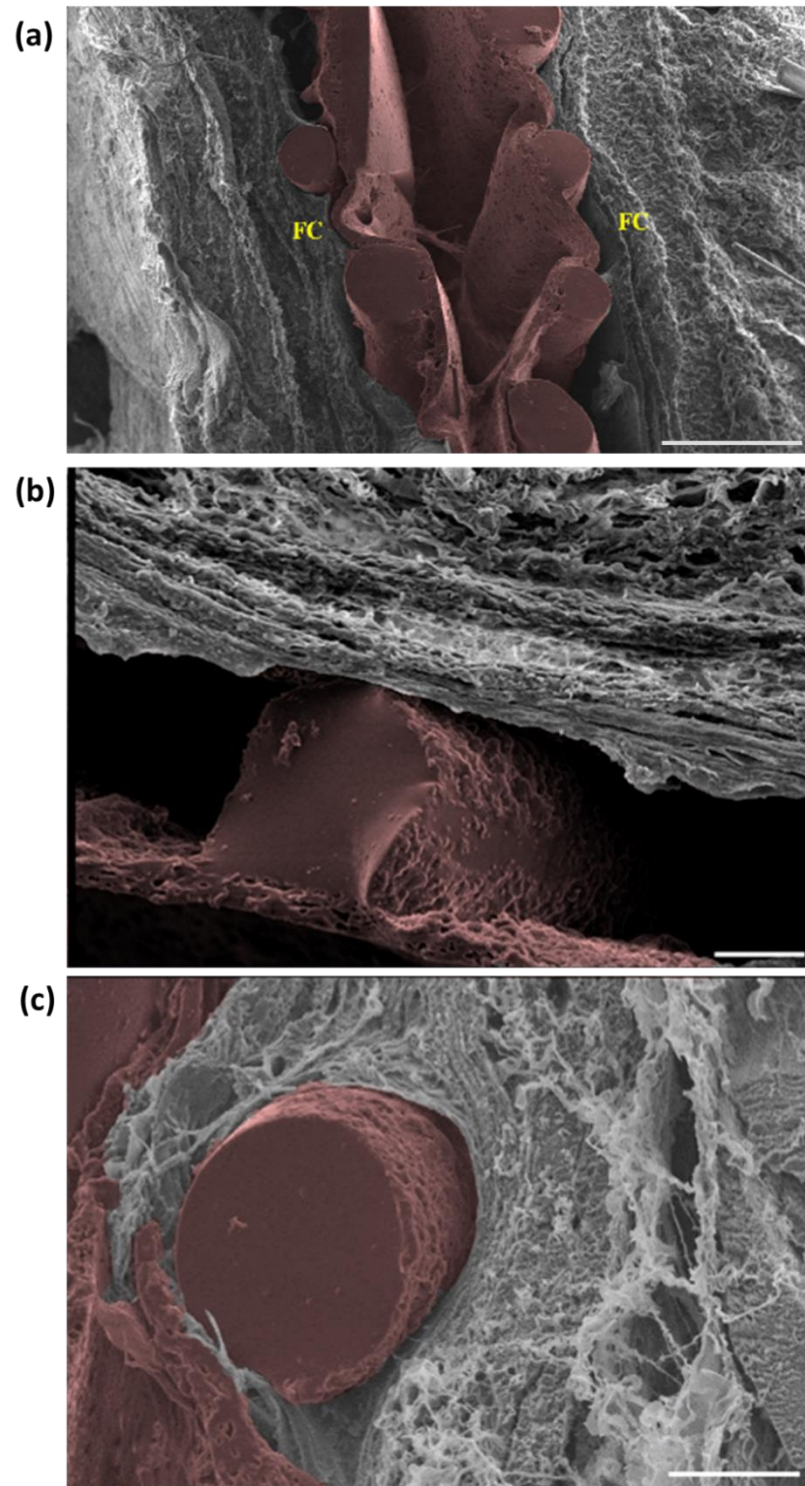


Figure 3.9: Representative Scanning Electron Microscopy (SEM) images of -VEGF and +VEGF devices. **(a)** Overview of encapsulation device (pseudo-coloured in brown) in-situ with surrounding fibrous capsule (FC). Scale bar = 500 μm . **(b)** Topological modification rope coil (RC) in intimate contact with fibrous capsule (FC). Scale bar = 100 μm . **(c)** Fibrous capsule surrounding rope coil on external surface of +VEGF device. Scale bar = 100 μm .

3.3.5.2 Myofibroblast abundance

The volume fraction of α SMA+ cells within 100 μ m of the device interface, excluding those associated with CD31+ blood vessels, was estimated using an unbiased stereological point counting technique. Normal distribution was observed in both groups and an unpaired t-test was performed seen in *Figure 3.11*. No significant difference was found ($P=0.8685$) between the treatment groups indicating that VEGF microspheres do not promote increased abundance of myofibroblasts within the fibrous capsule. This finding generally correlates with the fibrous capsule thickness results seen in *Figure 3.10 (b)*.

3.3.5.3 Collagen organisation and maturity

Polarised Light Microscopy (PLM) of picosirius red stained tissue sections was performed to better characterise the collagen network surrounding the implanted devices. Isotropic orientation of collagen deposition with highly organised collagen structure was evident in both treatment groups (*Figure 3.12*). Similar to the s4 and s5 groups in the previous chapter, the collagen structure generated in these groups was arranged into bundles orientated parallel to the device surface, forming a fibrous capsule of concentric layers intertwined around the external features of the devices. The majority of the fibres appeared red/orange implying the presence of mature collagen type I [276–278]. Taken together these data suggest that the addition of VEGF microspheres does not influence the devices affinity for integration into the surrounding tissue.

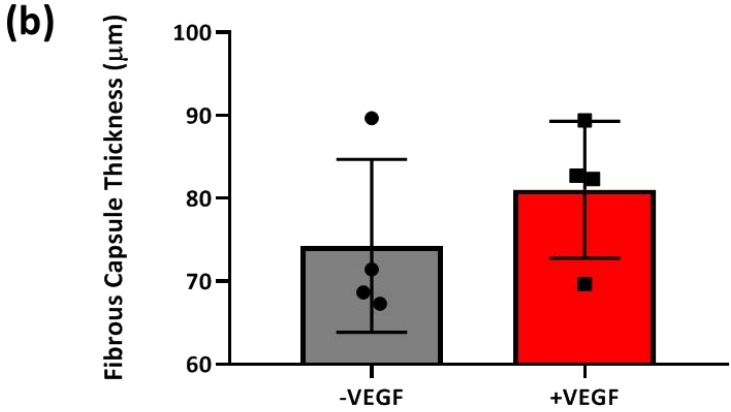
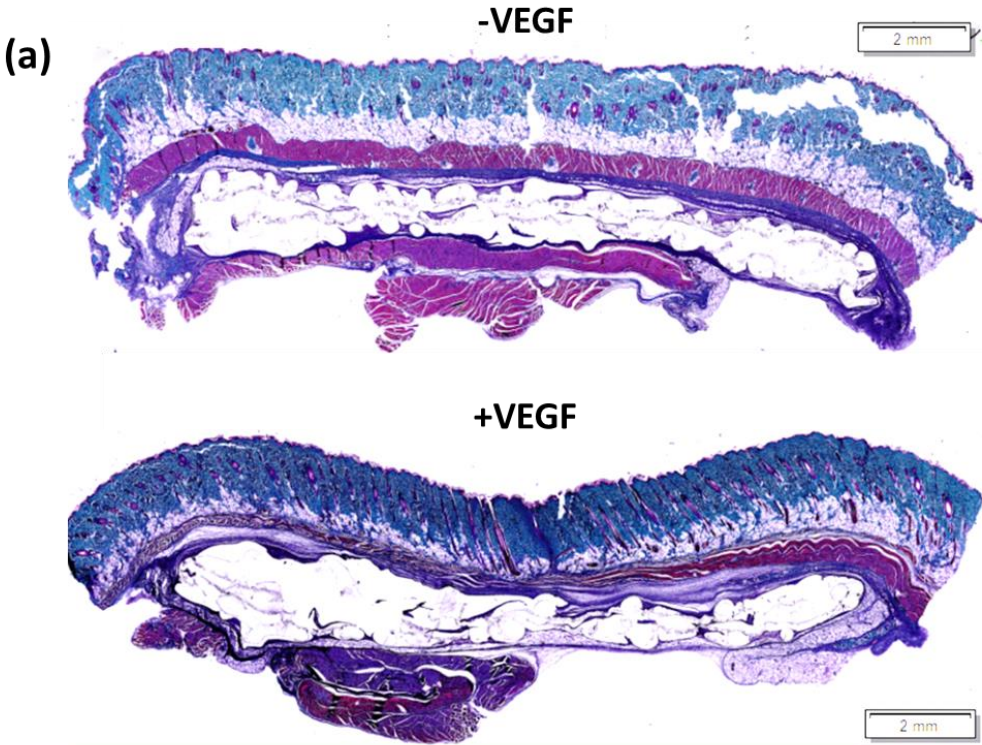


Figure 3.10: Analysis of the fibrous capsule thickness. **(a)** Representative Masson’s trichrome-stained histological sections of –VEGF and +VEGF groups. Scale bar = 2 mm **(b)** Mean fibrous capsule thickness. $n = 4$ per group, data are means \pm SD.

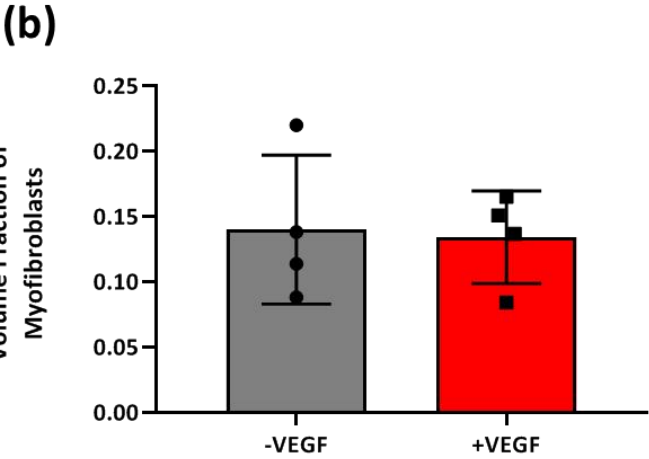
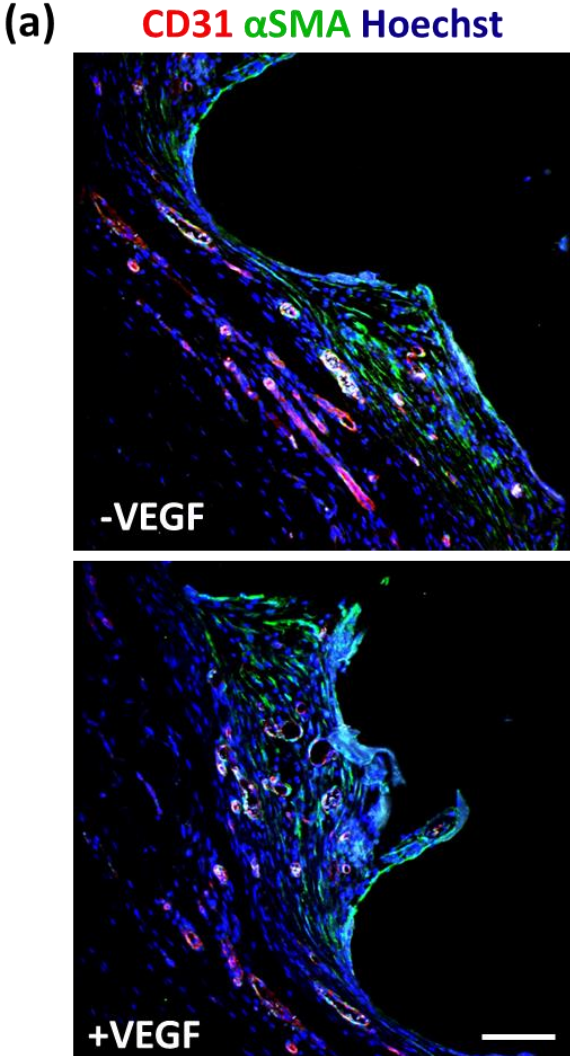


Figure 3.11: Analysis of the volume fraction of myofibroblasts within the surrounding fibrous capsule. **(a)** Representative immunofluorescent images of α SMA stained tissue (Blue = Hoechst, Green = α SMA, Red = CD31). **(b)** Volume fraction of α SMA+ cells. $n = 4$ per group, data are means \pm SD.

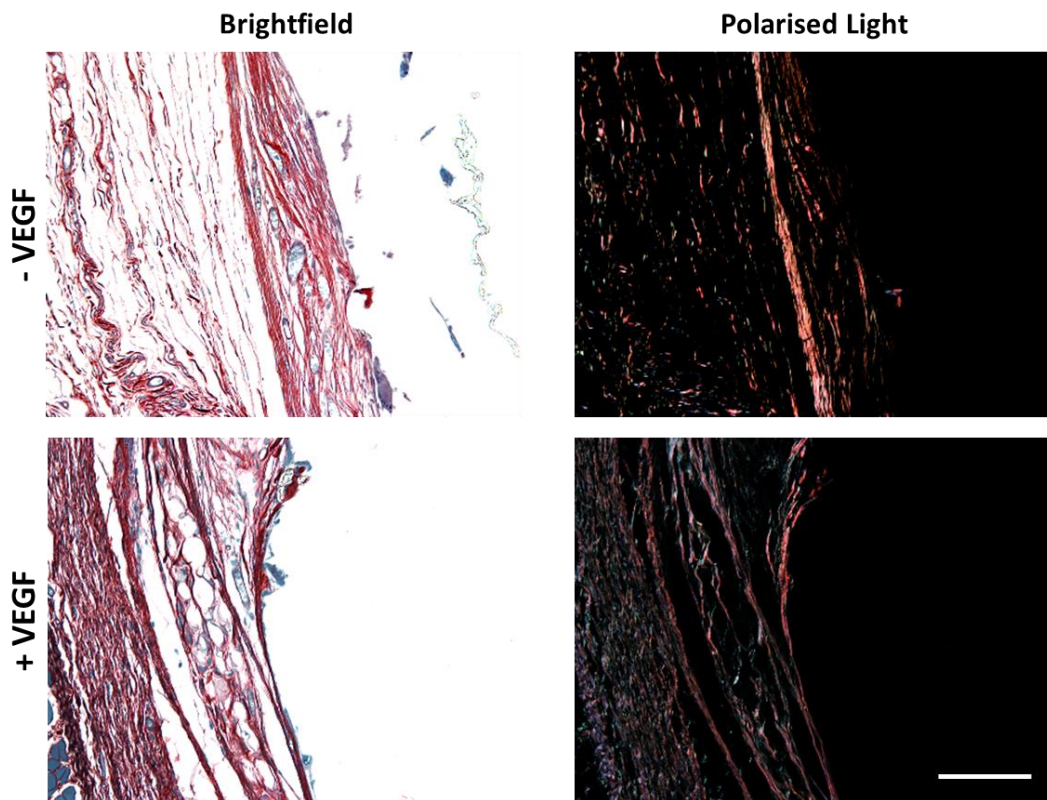


Figure 3.12: Analysis of the fibrous capsule and collagen maturity at the tissue device interface. Representative polarised light microscopy images –VEGF and +VEGF samples. Scale bar = 100 μm . Orange/red= mature collagen, Green= immature collagen.

3.3.6 Macrophage response

3.3.6.1 Macrophage abundance

To establish whether the addition of VEGF release affected the activation and abundance of macrophages within the fibrous capsule, tissue sections were stained with a pan-macrophage marker (CD68) (*Figure 3.13 (a)*). Multinucleated giant cells were apparent at device interface in both groups (*Figure 3.13 (b)*) SEM imaging enabled visualisation of immune cell aggregation on the device surface (*Figure 3.13 (c)*). Volume Fraction of CD68+ cells surrounding each device was calculated. Normal distribution was observed and a parametric unpaired t-test was carried out which revealed no significant difference between groups ($P=0.7014$) (*Figure 3.13 (d)*).

3.3.6.2 Macrophage polarisation

To assess the impact of the varying surface characteristics on macrophage polarization, tissue sections were co-stained with both CD68/CCR7 and CD68/CD163. The ratio of CCR7+ cells to total CD68+ cells was compared to the ratio of CD163 positive cells to total CD68+ cells using confocal microscopy images (*Figure 3.14 (a)*). Multiple t-tests were performed which found no significant differences between M1 or M2 phenotypes between -VEGF and +VEGF treatment groups ($P=0.13$). A significantly higher ratio of CCR7+ macrophages (M1) compared to CD163+ macrophages (M2) was seen in both treatment group ($****P<0.0001$), suggesting the majority of macrophages present display an M1, or pro-inflammatory phenotype (*Figure 3.14 (b)*). This data indicates that the presence of VEGF microspheres do not evoke an enhanced macrophage response and that macrophage populations are consistent across all groups, with a consistent phenotype up to 4 weeks.

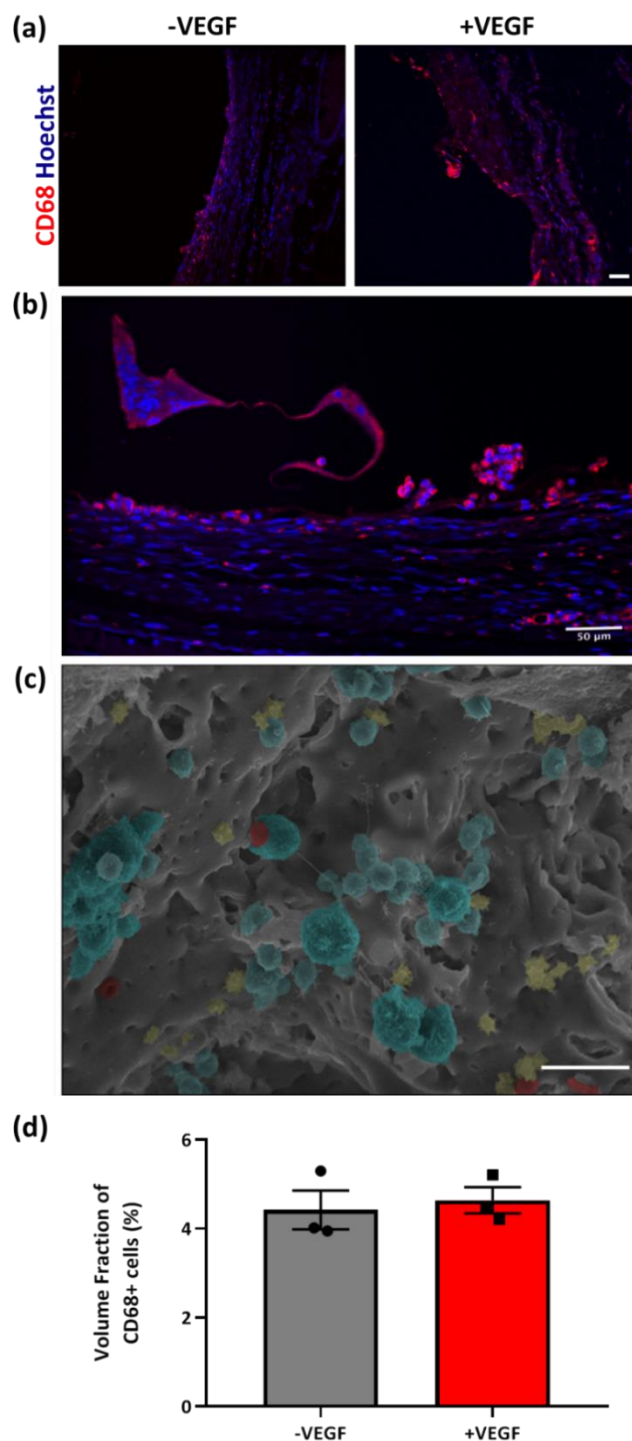


Figure 3.13: Analysis of the macrophage response at the tissue/device interface. **(a)** Representative fluorescent images of CD68 (red) staining at the tissue/device interface of 4 weeks -VEGF and +VEGF devices. Scale bar = 50 μm . **(b)** Multinucleated foreign body giant cells accumulation at the tissue/device interface of a +VEGF sample. Scale bar = 50 μm . **(c)** SEM image demonstrating an aggregation of cells on the diffusion membrane of the device. Macrophages = blue, Erythrocytes = red, lymphocytes = yellow. Scale bar = 50 μm . **(d)** Volume fraction of CD68+ cells. $n = 4$ per group, data are means \pm SD.

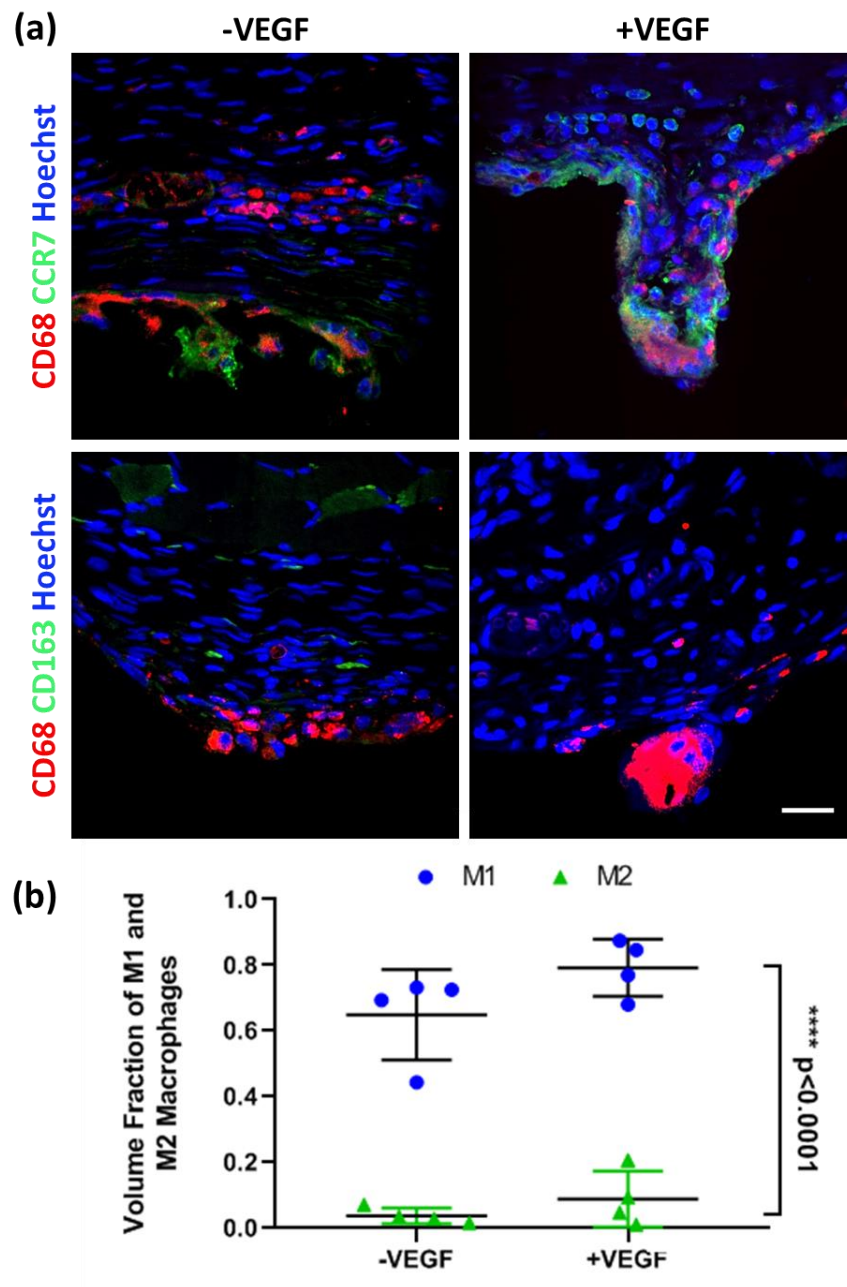


Figure 3.14: Analysis of the macrophage phenotype surrounding the implanted devices. **(a)** Representative immunofluorescent image of CD68 and CCR7 (M1 phenotype marker) and CD68 and CD163 (M2 phenotype marker) for -VEGF and +VEGF treatment groups. Scale bar = 20 μ m. **(b)** Volume fraction of CCR7 and CD163 macrophages. $n = 4$ per group, data are means \pm SD. M1 vs M2 **** $P < 0.0001$.

3.4 Discussion

In this study we describe a 4-week rapid vascularisation strategy which consisted of VEGF microspheres encapsulated within a multiscale porosity encapsulation device, implanted sub-muscularly in a rodent model. It has been established that successful development of a highly interconnected vascularised network has the potential to resolve the diffusion limitations of newly seeded/transplanted islet cells and ultimately reduce the time of cellular reconnection to host vasculature and improve islet survival within the macroencapsulation device [309–311]. Without sufficient vascularisation, cellular function and device efficacy cannot be maintained.

In vivo analysis of angiogenesis demonstrated a significantly increased (* $P=0.0132$) density of vessels surrounding the +VEGF devices when compared to the vessels surrounding -VEGF devices. However, no significant difference was observed in the CD31 histological analysis of number of vessels per area, length density and radial diffusion distance. These findings were unexpected, contradicting the *in vivo* angiogenesis analysis and therefore warranted further examination of vascularisation. Subsequently, an analysis of vessel stability and maturity was carried out which demonstrated a significantly higher (** $P=0.004$) ratio of mature vessels surrounding the VEGF loaded devices. This finding suggested that the addition of VEGF, may promote the development of more stable and mature blood vessels. Consequently, an investigation into the diameters of the newly formed vasculature was performed, as the histological analysis performed did not account for the sizes of the vasculature which may account for the larger vessel density seen with *in vivo* imaging. Blood vessels surrounding the +VEGF devices possessed significantly increased diameter measurements when compared to -VEGF devices (** $P=0.0002$). When comparing the size distribution of +VEGF and -VEGF devices, fewer +VEGF blood vessel diameters were found in the 5-10 μm categories with a higher proportion of +VEGF vessels found in the 20-35 μm categories when compared to -VEGF diameters. This increase in vessel diameter and maturity correlates with previous *in vitro* and *in vivo* studies suggesting that VEGF₁₆₅ not only promotes angiogenic sprouting but may also play a key role in determining lumen diameter [312–315]. Interestingly in quail embryos, VEGF₁₆₅ was shown to induce vessels with large lumens by stimulating the fusion of blood vessels [314]. However, Nakatsu *et al* found the process to be dose dependant. Low concentrations (0 ng/mL to 35 ng/mL) of VEGF₁₆₅ promoted growth of long, thin vessels, whereas higher concentrations of VEGF, which correlate with the dosage chosen for the present study [297,307], remarkably enhance vessel diameter [316]. While VEGF₁₆₅ was used in this study, it must be acknowledged that

several VEGF isoforms exist, each uniquely stimulating the growth of pre-existing (angiogenesis) or *de novo* vessels (vasculogenesis) [317,318]. It's likely that the ideal angiogenic stimulating microsphere must contain more than one of these isotypes in order to achieve a more substantial and rounded angiogenic response.

Our findings also correspond with Trivedi *et al.* [15], who infused VEGF into TheraCyte devices implanted subcutaneously in a rodent model. This study reported a three-fold increase in blood vessels per field of view in proximity to devices subject to the highest dose, compared to an un-infused control. Researchers implanted the Theracyte device for a prevascularisation phase of 3 months prior to the introduction of islets. Results of this study showed that the required dose of encapsulated islets was reduced 10-fold in the prevascularised devices when compared to a device and islets which were simultaneously implanted [319].

In the previous chapter we showed that the 3D printed porous topography of the s5 implant can increase vascularity in proximity over 2-fold. As this optimal topographical design was used in this study, it is expected that it further promoted blood vessel formation which is most likely attributed to improved cell attachment, alignment patterns and ability to support a vascularised network. Previous studies have suggested that novel surface topographies can influence the behaviour of cells however, this response is dependent on the dimensions and the specific morphology of the surface topographies utilised [320,321]. Brauker *et al* produced a hugely influential paper in this field which described how membrane pore size has a positive correlation to the cell infiltration and an altered foreign body reaction that allowed vascular structures to form in close proximity to the device wall [301]. In more recent study, greater abundances of blood vessels were formed around a large pore mesh in very close proximity to the immunomodulatory membrane which should improve mass transfer [322]. Rosengren *et al* examined the effects of surface roughness by implanting smooth and textured low-density polyethylene disks and found observed that the smooth topography developed a thicker fibrous capsule [323]. Following this hypothesis, Khosravi *et al* also demonstrated that a nanotopographical surface significantly increased peri-implant blood vessel density on days 7, 11, and 28 [324].

We further investigated the effect of VEGF microspheres on the fibrous capsule composition and FBR. Both groups showed an excellent propensity to encourage tissue attachment. Thickness measurements of the newly formed hyper-dense collagen deposited around the devices was consistent in both treatment groups. These similarities in tissue

integration and fibrous capsule thickness correlated with myofibroblast abundance and collagen maturity results. Macrophage activity surrounding the devices was assessed as a measure of the FBR [280]. The volume fraction and macrophage phenotype was examined at the tissue–device interface and although no significant differences between devices was observed, all devices elicited a FBR.

Like the previous studies, persistently higher levels of the M1 phenotype are seen in both -/+ VEGF devices [283,286,287]. This data correlates with the volume fraction data, suggesting that the addition of VEGF microspheres does not evoke a significantly enhanced macrophage response and that macrophage populations are consistent across all groups, with a consistent phenotype up to 4 weeks [283,286,287].

In conclusion, this data indicated that the addition of VEGF microspheres combined with a multiscale porosity device had a statistically increased angiogenic response by promoting increased vessel stability, maturity and vessel size within a 4-week period. The successful development of a highly interconnected vascularised network demonstrated in this study, has the potential to resolve the diffusion limitations of newly seeded/transplanted islet cells and ultimately reduce the time of cellular reconnection to host vasculature, improving potential islet survival within our macroencapsulation device. The results obtained are comparable to published angiogenic analysis performed on devices developed by TheraCyte, Beta-O₂ Technologies, Defymed and the Sefton Lab, University of Toronto (*Table 3.1*). The VEGF microspheres in this study have many potential uses, and could be incorporated in the silicone device structure if more complex geometries were desired as demonstrated in a previous *in vitro* strategy [297]

Table 3.1: Summary of published angiogenic analysis surrounding macroencapsulation devices.

Company / Research institute	Device	Vascularisation Strategy	Implant site	Duration of Implantation	Blood Vessels /mm ²	Volume fraction of blood vessels	Ref.
DRIVE Project	12 mm disk shaped implants fabricated from medical grade silicone with 3D printed porous topography	3D printed porous topography	Subcutaneous	2 weeks	375 ± 344	26 ± 10	(See Chap. 2)
	Multiscale porosity macroencapsulation device composed of medical grade silicone with 3D printed porous topography	VEGF-releasing microspheres within 3D printed porous topography devices	Subcutaneous	4 weeks	155 ± 43	8 ± 0.84	(See Chap. 3)
TheraCyte	TheraCyte Device: Rectangular device with outer layer of woven polyester mesh (vascularisation membrane), a middle layer of 5 µm porosity PTFE and an inner layer of 0.4 µm porosity PTFE (immunoisolating membrane)	VEGF infused at 100 ng/day (low dose) and 500 ng/day (high dose)	Subcutaneous	10 days	Low dose : 133 ± 17	Data not available	[15]
					High dose: 75 ± 16		
Beta-O ₂ Technologies	βAir: Circular device composed of two hydrophilic porous PTFE membranes impregnated with high viscosity mannuronic acid alginate acting as an immuno-protective barrier	Platelet micro-particles (PMP) - releasing device	Subcutaneous	3 weeks	150 ± 50	Data not available	[298]
Defymed	Mailpan - Circular device 15 cm in diameter composed of a copolymer of acrylonitrile and sodium methallyl sulfonate	Pre-vascularisation period of 6 weeks	Peritoneal	6 months	Data not available	15 ± 7.7	[243]
Sefton Lab, University of Toronto.	Silicone tubes (1.57 mm inner diameter (ID) x 3.18 mm outer 109 diameter (OD))	Methacrylic Acid copolymer (MAA) - based coating as a pre-vascularisation strategy for a period of 2 and 3 weeks	Subcutaneous	2 weeks	200 ± 20	Data not available	[481]

Chapter 4

To examine the potential of the multiscale porosity islet encapsulation device for the treatment of diabetes in STZ-induced diabetic rodents

4.1 Introduction

The current gold standard treatment for type 1 diabetics is administration of daily exogenous insulin. This treatment requires life-long patient compliance for accurate blood glucose monitoring and daily insulin injections. However, this treatment strategy fails in mimicking natural patterns of insulin secretion, as subcutaneous insulin injections suffer from suboptimal onset, peak and duration which can ultimately hinder the regulation of glucose metabolism [325,326].

Pancreatic islet transplantation has been validated as a valuable therapy for T1D patients as islets have the ability to provide tight regulation of circulating blood glucose. However, the availability of this treatment is limited by the shortage of pancreas donors, the low islet yield from each pancreas, the loss of islets proceeding intra-portal islet infusion (>60%), and the requirement of lifelong immunosuppression [327,328].

Encapsulating islets within a semipermeable immunoisolating device represents a promising approach to enable replication of the native islet micro- and macro-environment, the protection of islet grafts, reduce or eliminate immunosuppression, while simultaneously providing a safer platform for the use of alternative cell sources [298,329]. Numerous pre-clinical studies of encapsulated cells have demonstrated that immunoprotection is achievable [231,330–332] however, the same cannot be said for efficacy which can be attributed to the hypoxic conditions created by the surrounding biomaterial barrier [191,333–335]. The FBR can further impair device functionality due to the development of an avascular, collagen-rich capsule around the implant. This dense fibrosis can lead to the implant being walled off thus preventing the device from functioning or integrating as intended [251].

As discussed previously in *Chapter 3*, the development and distribution of neovascularisation adjacent to encapsulation device surface as well as the spatial arrangement of the encapsulated cells is essential. Standard radial diffusion distances can be disrupted by macroencapsulation devices, often resulting in extensive hypoxic-induced cell death and dysfunction [335–337]. However, in the previous chapters, it was found that the degree of tissue integration and vascularity in proximity to the device was shown to increase 2.5 fold with precisely controlled surface structural complexity. This approach, in combination with encapsulated VEGF microspheres presents an improved approach to vascularisation that may help resolve the diffusion limitations of current pre-clinical encapsulation devices.

Likewise, the site of implantation can affect integration, biocompatibility and efficacy of the implanted device. The most suitable site for transplantation of macroencapsulation devices is widely debated. In clinical islet transplantation, islets are infused into the portal vein, as the portal circulation matches the true physiological route of insulin release [338]. Typically, insulin is secreted by pancreatic β -cells and reaches the liver via the portal vein [339]. This is a crucial metabolic pathway known as the hepatic first-pass effect (HFPE), and is required for the maintenance of normoglycemia by increasing the concentration of blood glucagon thus preventing hypoglycemia [340,341]. Currently insulin is administered subcutaneously, which does not provide an adequate HFPE [342].

Historically the peritoneal cavity was a frequently used implantation site favoured due to the space available for large implant volume and ease of access [331,343–347]. Varying degrees of success have been reported from this site, from exogenous insulin independence for 9 months in diabetic patient [345], to gravity-dependent movement, lack of vascularisation leading to limited oxygen and nutrient diffusion [292]. However, more recent pre-clinical and clinical studies have confirmed that physiological delivery of insulin directly to the intra-peritoneal space results in faster pharmacokinetics/pharmacodynamics and thus superior glycemic regulation compared to subcutaneous insulin delivery [348–351].

4.1.1 Aims

The overall aims of this chapter are to optimise intra-peritoneal cavity delivery of islets encapsulated within multiscale porosity macroencapsulation devices and to determine whether this device can support syngeneic islet survival and function in an STZ-induced Type 1 model.

The specific aims of Chapter 4 were:

- To develop a rodent sized multiscale porosity macroencapsulation device
- To determine the most efficacious intra-peritoneal surgical and encapsulation strategy for the treatment of diabetic rats
- Assess the morphology of the fibrous capsules surrounding each multiscale porosity macroencapsulation device using histological assessment, MicroCT and SEM imaging
- To characterise the compositions of the resultant fibrous capsules using immunofluorescent and histological staining
- To examine the angiogenic response using immunohistochemical and immunofluorescent staining
- To examine the activation, abundance and polarisation of macrophages at the tissue interface capsule using immunofluorescent staining

To achieve these aims, a hydrogel suspension of VEGF microspheres and syngeneic rat islets were encapsulated within multiscale porosity macroencapsulation devices, implanted free intra-peritoneally or subsequently sutured to the AAW of STZ-induced diabetic rodents for a period of 4-8 weeks.

4.2 Materials and Methods

4.2.1 Isolation and purification of syngeneic islets

These procedures were carried out by Abiel srl., Palermo, Sicily in accordance with device fill volume and gel seeding density as specified in the study design and planning which I contributed to.

Rodent studies were approved by the Italian Ministry of Health (Authorization No. 1236bbbb). The rodent islet isolation protocol was adapted from Carter *et al*, for use with collagenase enzymes [352]. Rats were euthanised by CO₂ asphyxiation and cervical dislocation and hair was removed from the abdomen. A door shape incision was made in the midline of the abdomen. Once the ribs were removed, the duodenum was identified and gently spread to expose the pancreatic tissue and the common bile duct. The bile duct was clamped at both ends to prevent flow into the liver and duodenum. Immediately before perfusion, 100 µL of thermolysin was added to the 10mL collagenase solution made from 40U of ColG and 170U ColH, to form the digestion solution. Following cannulation of the bile duct, 5mL of digestion solution was perfused into the pancreas which became visible distended after 1-3 mL. Once the full volume was perfused the needle was removed followed by the removal of the clamps. The pancreas was extracted and transferred to a petri dish where excess tissue was removed before being immersed in the remaining 5 mL of digestion solution and placed on ice for up to 1 hr.

The pancreas in digestion solution was agitated at 100RPM at 37°C for 10 minutes to digest the tissue further before adding 20 mL of media containing serum to neutralise and further dissociate by vigorous shaking. The tubes were then centrifuged and the media was replaced by 10mL of fresh media. The cell suspension was then passed through a 0.419mm wire sieve to filter out non-digested tissue, fat and lymph. The sieved material was collected and washed with fresh media to bring the final volume to 25mL. This was then centrifuged to isolate a cell pellet before resuspending in 15mL ice-cold heavy Histopaque-1119 (1.119g/mL). 20 mL ice-cold light Histopaque-1077 (1.077g/mL) was carefully layered to make a sharp interface. Finally, 15 mL of media was layered on top of the Histopaque-1077 with another sharp interface. The tube containing the gradient was centrifuged at 800G for 5 min, using the slowest acceleration and deceleration. The islets formed a visible ring at the interface and were collected using a pasteur pipette. Finally, the islets were washed thrice. Prior to encapsulation the rat islets were pooled into a 5mL volume and 4 x100 µL samples were taken for counting.

Islets were imaged using a Leica System microscope and measured using the ImageJ (Fiji version 2.0.0) software. The islet diameters were compared to table for calculating IEQ for human islets from the Integrated Islet Distribution Program (IIDP)[353].

4.2.2 Induction of diabetes in rats

Adult RccHan Wistar rats (ENVIGO) 150/200 g females, age 12 weeks were used during this study. Rodent studies were approved by AREC (Authorization No. 66/2017-PR), and performed by Abiel Srl (Italy). Subsequent to an 8 hour fasting period, rats were fed 2 g/kg of glucose via a gastric tube. Circulating blood glucose (BG) levels were monitored between 0-180 minutes of this feeding every 3/4 days. Initially the circulating BG levels of healthy (non-diabetic) rats were monitored for a period of 4 weeks to establish normal BG levels. Following this, an intra-venous injection of 60mg/kg dose of Streptozotocin (STZ) was used to induce diabetes. STZ is a broad-spectrum antibiotic that is toxic to the insulin producing β -cells of pancreatic islets which is used experimentally to induce diabetes in small and large animals studies within 2-4 days [354–359]. Rats exhibiting a repeating basal circulating BG level of greater than 300 mg/dL were considered diabetic. Before proceeding with transplantation experiments, the BG of 4 rats was analysed for a period of 4-weeks to confirm permanency of induced diabetic state.

4.2.3 Macroencapsulation device and contents

4.2.3.1 Device fabrication

These procedures were carried out by Fergal Coulter and the O’Cearbhaill Lab, UCD, Dublin. I worked very closely with UCD to develop and enhance these rodent sized macroencapsulation devices, providing design inputs including volume, position delivery in the peritoneum, suture points, islet dose and oxygenated hydrogels.

Devices of dimensions 10 x 20 x 2 mm were fabricated from medical grade silicone (*Chapter 3 Figure 3.1*). Devices possessed a porous inner membrane with a micro and macro structure: Two membranes are fabricated entirely of salt/silicone solution (12 × 5 μ m layers). The MED4840 rope-coil layer is extruded onto the surface, followed by over-spraying using another two salt/silicone solution layers. The salt was washed out of the membranes over a 24-hour period. A detailed description of the device manufacture process can be found in section 2.2.1 *Device Fabrication*.

4.2.3.2 Native Hyaluronic acid/Perfluorodecalin emulgel formulation with incorporation of islets and VEGF microspheres

These formulations and procedures were carried out by a DRIVE PhD candidate, Liam McDonough, RCSI, Dublin. I visited RCSI to receive training in procedure and production of gels for this study.

Lyophilised native hyaluronic acid (natHA; Contipro a.s. Czech Republic) was rehydrated in PBS (pH 7.4) up to concentrations of 1.8 % w/v over 1-2 days. Perfluorodecalin (PFD) emulsions were prepared by diluting lipoid with PBS and sonicating while immersed within an ice bath at 50% amplitude for 7 minutes. The hydrogel was produced by homogenization of the 66.78% (w/v) PDF emulsion within the 1.8 % (w/v) Nat/HA hydrogel by mixing between 2 syringes. The resulting emulgel is oxygenated by flowing oxygen through the emulgel via a Y static mixer. The oxygenated emulgel was mixed and diluted with a suspension of 25mg/mL VEGF microspheres and 2400 IEQ in complete media to produce the final emulgel formulation to be encapsulated within the devices.

4.2.4 Intra-peritoneal implantation in rats

These procedures were carried out by Abiel srl., Palermo, Sicily. I contributed to the design and planning of this study, provided direction, performed extensive data interpretation and analysis of glucose readings, provided support for explantation of implants and tissue en bloc, and trained individuals on our tissue fixation and shipping protocols.

Rodent studies were approved by the Italian Ministry of Health (Authorisation No. 1236bbbb). Rats were anesthetized by isoflurane and hair was removed in the area of implantation on the abdomen. One incision was made in each rat located in the midline of the abdomen. Each incision cut through the dermis to the muscles of the anterior abdominal wall. Each implant site was closed with 2/3 stitches and the animals were treated with antibiotic ceftriaxone (25 mg/Kg) and painkiller tramadol (4 mg/Kg), for 5 days. Animals were partially immunosuppressed by administering mycophenolate mofetil 40 mg/kg and ciclosporin 5 mg/kg every day for 2 weeks and then every 3 days for the remainder of the experiment. Subsequent to an 8 hour fasting period, rats were fed 2 g/kg of glucose via a gastric tube. Circulating blood glucose (BG) levels were monitored between 0-180 minutes of this feeding every 3/4 days.

4.2.4.1 Implantation of syngeneic islets within a collagen gel

Corning Collagen Type-I, rat tail, was used at a concentration of 3 mg/ml. This gel formulation was prepared by diluting a stock solution of Collagen Type-I, rat tail, with PBS (pH 7.4) and neutralising using 1N sodium bicarbonate while sonicating immersed within an ice bath at 50% amplitude for 7 minutes. 2,000 IEQ encapsulated within 500 mL of Type-I collagen gel was implanted intra-peritoneally in 4 rats. This was performed by making a small incision through the abdominal wall and extracting a loop of the large intestine and associated mesentery. The gel and cell mixture was placed upon the mesentery's fan-like arrangement, which was sandwiched together before being reinserted into the abdominal cavity. After 4 weeks, animals were euthanised and gels with immediate surrounding tissue were extracted.

4.2.4.2 Implantation of syngeneic islets encapsulated within a multiscale porosity macroencapsulation device

Each multiscale porosity device containing HA + PFD + MSPs-VEGF + 2,000 IEQ was implanted intra-peritoneally in 4 rats. This was performed by making a small incision through the abdominal wall and extracting a loop of the large intestine and associated mesentery (*Figure 4.1 (a)*). The device was placed upon the loop of mesentery (*Figure 4.1 (b)*) as was carefully sandwiched between the mesentery while being carefully reinserted into the abdominal cavity (*Figure 4.1 (c-e)*). After 4 weeks, animals were euthanised and devices with immediate surrounding tissue were extracted.

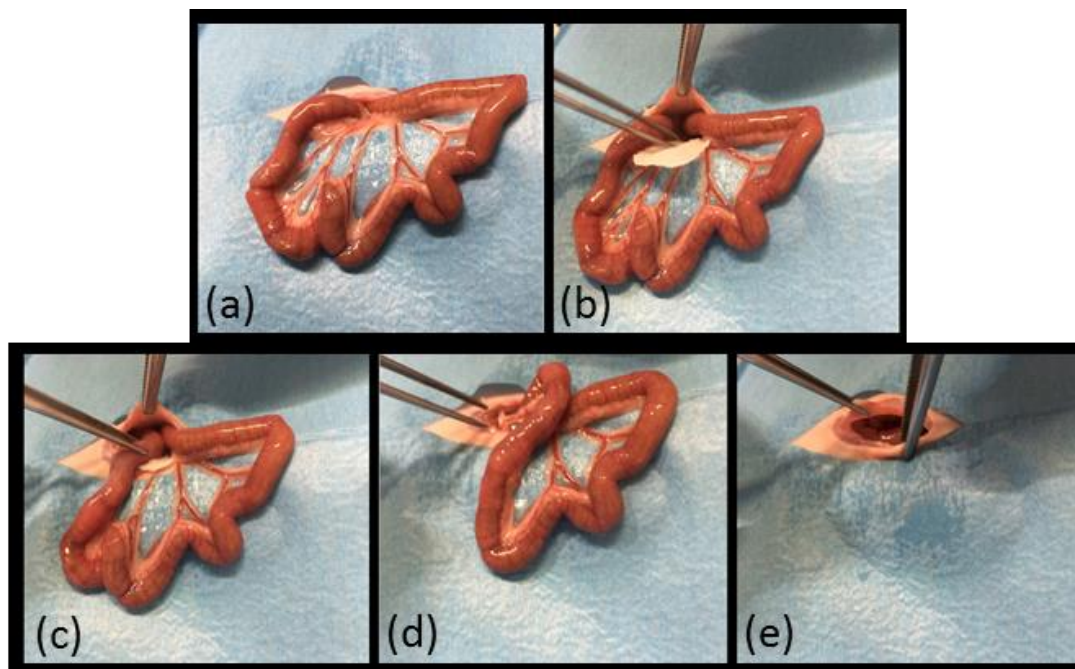


Figure 4.1: Implantation process of multiscale porosity device. **(a)** Extraction of Large intestine and associated mesentery. **(b)** Device placement upon the mesentery. **(c-e)** Sandwiched device implantation.

4.2.4.3 Implantation of syngeneic islets encapsulated within a multiscale porosity macroencapsulation device sutured to the anterior abdominal wall

Each device containing HA + PFD + MSPs-VEGF + 2.000 IEQ was implanted intraperitoneally in 8 rats. Findings from the previous study led to a modification in the design of the macroencapsulation device. Two diametrically opposed suture holes were incorporated into the device and enabled devices to be sutured to the internal anterior abdominal wall (peritoneum) with the configuration peritoneum/omentum/device. Computerised axial tomography (Capiler CT-Scanner, PerkinElmer) was performed. This imaging enabled visualisation of the implants to accurately pinpoint its location and ensure no movement of folding of the device had occurred. Another variation was to support the animals with exogenous insulin (1 U/rat) in the first week after transplant in order to prevent immediate stress to the transplanted islets as seen in the previous studies. At 8.5 weeks, 4 animals were euthanised and each device with immediate surrounding tissue were extracted. The remaining 4 rats were anaesthetised by isofluorane and had their respective devices removed. Their BG levels would be monitored for a further 2.5 weeks to monitor progression back into a diabetic state. Explanted devices and surrounding tissue were processed.

4.2.5 X-ray microtomography (MicroCT)

Unstained explanted devices from rats were stored in 70% ethanol and imaged in a microCT 100 scanner (Scanco Medical, Switzerland). Samples were scanned at 45 kVp and 200 μ A with a 0.1mm Aluminium filter. Images and videos of each device iteration were generated with CTvox software (Bruker, USA). For soft tissue visualisations, samples were stained in a solution of 2.5% phosphomolybdic acid in 70% ethanol for 5-7days. μ -CT images were captured using the μ CT 100 scanner at 70 kVp and 85 μ A with a 0.5mm Aluminium filter. Images and videos were generated using ImageJ software.

4.2.6 Scanning Electron Microscopy (SEM)

Each tissue sample was bisected longitudinally to create a cross-section of the device and surrounding tissue. Samples were post-fixed overnight in 2.5% glutaraldehyde in 0.2 M PBS (pH 7.4). Samples were washed twice in 0.2 M PBS for 10 minutes before dehydration through a series of graded alcohols (30%, 50%, 70%, 90% and 100%). Following dehydration, samples were transferred to the EMITECH K850 critical point dryer. This removed all the liquid in a precise and controlled way, so fragile tissue is not damaged or distorted in the process. Samples were then mounted onto aluminium stubs using carbon adhesive tabs. An Emscope SC500 was used to lightly sputter coat the samples. Specimens were imaged using a Hitachi S2600N Scanning Electron Microscope using a secondary electron detector (Vacuum 15 kV, electron Beam 50). SEM images were pseudo-coloured using MountainsMap[®] SEM Color 7.3.7984.

4.2.7 Fixation, embedding and staining

Tissues were fixed overnight using 4% paraformaldehyde (pH 7.4). The tissue allocated for histological analysis was then washed in 0.2 M phosphate-buffered saline with a final wash in 70% ethanol. Samples transected in half, orientated and embedded in paraffin wax blocks. Sections of 5 μ m were cut and stained with Hematoxylin and Eoin, Masson's trichrome and α SMA for fibrous capsule analysis. Additional sections were stained with a CD31, α SMA, CD68, CCR7 and CD163 antibodies for analysis of angiogenesis and immune response. The staining protocols are provided in detail in *Chapter 2*.

4.2.8 Polarised Light Microscopy (PLM)

4.2.8.1 *Picrosirius red staining*

Slides underwent 2 x 10 minute changes of xylene to remove the paraffin present. Xylene is then removed by two changes of absolute alcohol before bringing to water through 95%, 70% and 50% alcohols. Alcohol is removed in running tap water for 2 minutes. Slides are stained in 0.1% Fast Green for 45 minutes before washing in tap water for 2 minutes. Slides are then stained in 0.1% sirus red in saturated picric acid for 1 hour. Slides were then dehydrated through graded alcohols and cleared in two changes of xylene. The slides are cover slipped using DPX mounting medium and left to dry.

4.2.8.2 *Polarised light imaging*

Two polarised images of the fibrous capsule were captured using Capture 2.0 software using the Olympus BX43 polarised light microscope (Mason Technology Ltd. Dublin, Ireland). The images were captured at 20x magnification in 10 regions of interest of the fibrous capsule. The exposure time was set to 600 ms and light intensity was kept constant. First, the polariser positioned on the light path before the sample and the second polariser (analyser) were set to 90 and 0 degrees, respectively. For the second image these were set to 135 and 45 degrees, respectively. The two captured images were added together using the MAX function in ImageJ software enabling a complete view of the collagen fibres present.

4.2.8.3 *Image analysis*

4.2.8.3.1 **Collagen fibre colour under polarised light**

The total area covered by collagen was first calculated in number of pixels, using ImageJ. This was achieved through adjusting the brightness from approximately between 50 and 65 up until 255 and selecting the highlighted area. This excluded the dark background of the images. Then, using colour thresholding and selecting consistent hue ranges, the areas of collagen that was red, orange, yellow or green was recorded separately for each colour in pixels. The colour thresholds used were; Red (0-9 and 185-255), Orange (10-38), Yellow (39-51), and Green (52-184). Calculations were carried out as follows;

$$\% \text{ of collagen fibres area that is red or orange} = \frac{\text{Area of Red Pixels} + \text{Orange Pixels}}{\text{Total Area of Collagen Pixels}} \times \frac{100}{1}$$

$$\% \text{ of collagen fibres area that is yellow or green} = \frac{\text{Area of Yellow Pixels} + \text{Green Pixels}}{\text{Total Area of Collagen Pixels}} \times \frac{100}{1}$$

4.2.8.3.2 Collagen fibre coherency under polarised light

The coherency of the collagen fibres was evaluated for the polarised images using the OrientationJ plugin on ImageJ, based on Fourier Transform analysis. The images were each converted to 32-bit for this image analysis process. For each image, the Dominant Direction function was used. The Dominant Direction function determines the most common direction/ orientation of the fibres. This function also determines how random or uniform the image is as a whole on a scale from 0 (random) to 1 (uniform). For example, if every line in the image was travelling in the same direction then the coherency value would be 1.

4.2.9 Statistical analysis

Statistical analysis was performed using GraphPad Prism (8.1.0) was used. Normality of distribution was assessed by the Shapiro-Wilk test. Subsequent parametric and/or non-parametric tests were performed. For parametric data, an unpaired t-test was performed for comparing between two groups and a one-way or two-way analysis of variance (ANOVA) with post-hoc Tukey's multiple comparison for comparing between groups. For non-parametric data, a Mann-Whitney U was performed for comparing between two groups and a Kruskal-Wallis test for comparing more than two groups. Statistical significance was accepted when $p < 0.05$. A minimum of two blinded counters were used for analysis.

4.3 Results

4.3.1 Induction of diabetes in rats

Prior to establishing a robust diabetic rat model, the circulating BG levels of healthy (non-diabetic) rats were monitored for a period of 4 weeks to establish normal fasting BG levels (*Figure 4.2 (a)*). These results demonstrate that the average value for fasting BG concentration was 100 mg/dL, which remained consistent over the 4-week period. Pancreatic islets exhibited a normal morphology as seen in *Figure 4.2 (b)*. Following, an intravenous injection of STZ, circulating BG levels were measured for a period of 4 weeks. All rats exhibited erratic fasting BG concentrations and considered diabetic once fasting BG was greater than 200 mg/dL (*Figure 4.2 (c)*). In contrast to islet morphology seen in healthy rats, the induction of diabetes caused disruption to islet morphology with a marked visible reduction of insulin producing β -cells (*Figure 4.2 (d)*). Before proceeding with transplantation experiments, the concentrations were analysed for a period of 4-weeks to confirm permanency of induced diabetic state.

4.3.2 Implantation of syngeneic islets within a collagen gel

Circulating BG levels of transplanted rats were monitored for a period of 4 weeks to establish the efficacy of collagen gel encapsulated islets. Fasting BG concentrations indicated a partial reversion of diabetes within 2.5 weeks, demonstrating an average value below 200 mg/dL, a value within the condition of "normal". However, BG concentrations become more erratic between 2.5 and 4 weeks with values at 3 and 4 weeks >300 mg/dL (*Figure 4.3 (a)*). After 4 weeks, animals were euthanised and gels with immediate surrounding tissue were extracted. Masson trichrome staining of the gels demonstrated a highly irregular arrangement of islet cells with few islets exhibiting normal morphology (*Figure 4.3 (b)*). Immunofluorescent staining of insulin and glucagon positive cells confirm this highly irregular arrangement with no obvious islet morphology (*Figure 4.3 (c)*). Cells positive for insulin or glucagon were present however, did not appear throughout the collagen gel construct. To assess the impact of gel-encapsulated islets on macrophage abundance and polarization, tissue sections were co-stained with both CD68/CCR7 and CD68/CD163 (*Figure 4.3 (d)*). This image data demonstrated that macrophages had infiltrated the gel Volume fraction and number per mm^3 of CD68+ cells was largely consistent across all three animals (*Figure 4.3 (e-f)*). The ratio of CCR7+ cells to total CD68+ cells was then compared to the ratio of CD163 positive cells to total CD68+ cells which demonstrated a higher ratio of CCR7+ macrophages (M1) compared to CD163+ macrophages (M2), suggesting that the majority of macrophages present display an M1, or pro-inflammatory phenotype (*Figure 4.3 (g)*).

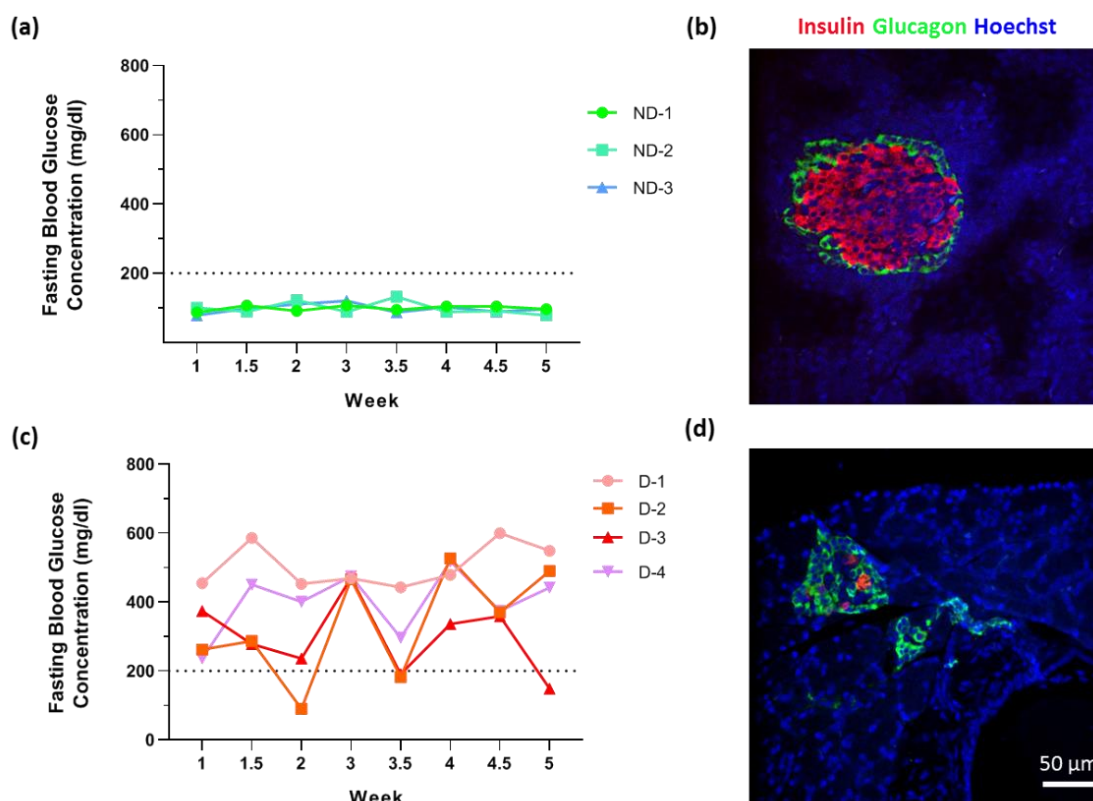


Figure 4.2: Establishing STZ-induced diabetic rats **(a)** Representative fasting blood glucose concentrations (mg/dL) for healthy, non-diabetic (ND) rats. **(b)** Representative immunofluorescent image of healthy rat pancreas with functional islets (Hoechst, blue; Glucagon, green; Insulin, red) Scale bar = 200 μ m. **(c)** Representative fasting blood glucose concentrations (mg/dL) for STZ-induced diabetic (D) rats. **(d)** Representative immunofluorescent image of STZ-induced diabetic rat pancreas with malformed islets (Hoechst, blue; Glucagon, green; Insulin, red) Scale bar = 200 μ m. $n = 3-4$ per group.

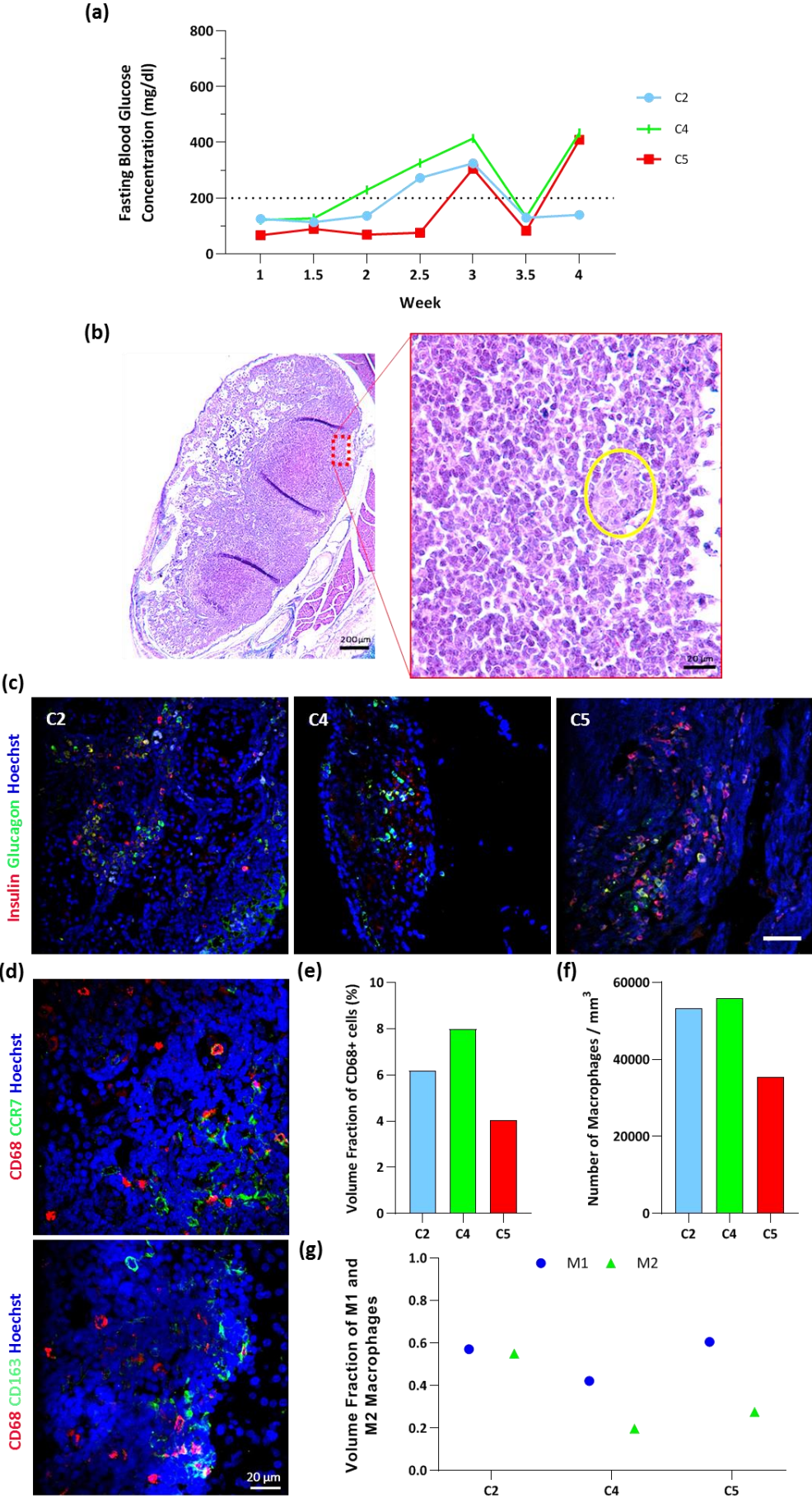


Figure 4.3: Islet cell encapsulation within a collagen gel implanted intra-peritoneally. **(a)** Fasting blood glucose concentrations (mg/dL) for diabetic rats treated with islets encapsulated within a collagen gel for 4 weeks. $n = 3$ per group. **(b)** Masson's trichrome image of collagen encapsulated islets in rat C2, with high magnification demonstrating one islet structure (circled in yellow). Scale bars = 200 μm & 20 μm . **(c)** Representative immunofluorescent images of islets encapsulated within collagen gel (Hoechst, blue; Glucagon, green; Insulin, red). **(d)** Representative immunofluorescent image of CD68 and CCR7:M1 phenotype marker (Hoechst, blue; CCR7, green; CD68, red) and CD68 and CD163:M2 phenotype marker (Hoechst, blue; CD163, green; CD68, red). Scale bar = 20 μm . **(e)** Volume fraction (%) of CD68+ cells. **(f)** Number of CD68+ (pan-macrophage marker) cells per volume. **(g)** Volume fraction of CCR7+ and CD163+ to total CD68+ macrophages. $n = 1$ per group, data are represented as means \pm SD, $n = 3$ per group.

4.3.3 Implantation of syngeneic islets encapsulated within a multiscale porosity non-sutured macroencapsulation device

Circulating BG levels of transplanted rats were monitored for a period of 4 weeks to establish the efficacy of a hydrogel-based macroencapsulation of islets within a non-sutured multiscale porosity device. All rats exhibited erratic fasting BG concentrations of >200 mg/dL (*Figure 4.4 (a)*). These results were consistent with BG concentrations of diabetic rats and thus did not successfully revert the diabetic status of the animal. As seen in previous chapters, Micro-CT imaging was performed to enable visualisation of the macroencapsulation devices to accurately pinpoint their location and monitor movement over the 4 weeks. Significant changes to the device position could ultimately disrupt the newly forming tissue and vasculature surrounding each device affecting islet viability and efficacy. As seen in *Figure 4.4 (b)* devices did not maintain their correct configuration and position, slipping and folding into the infero-lateral portion of the abdomen, which may account for the impaired functionality of implanted islets.

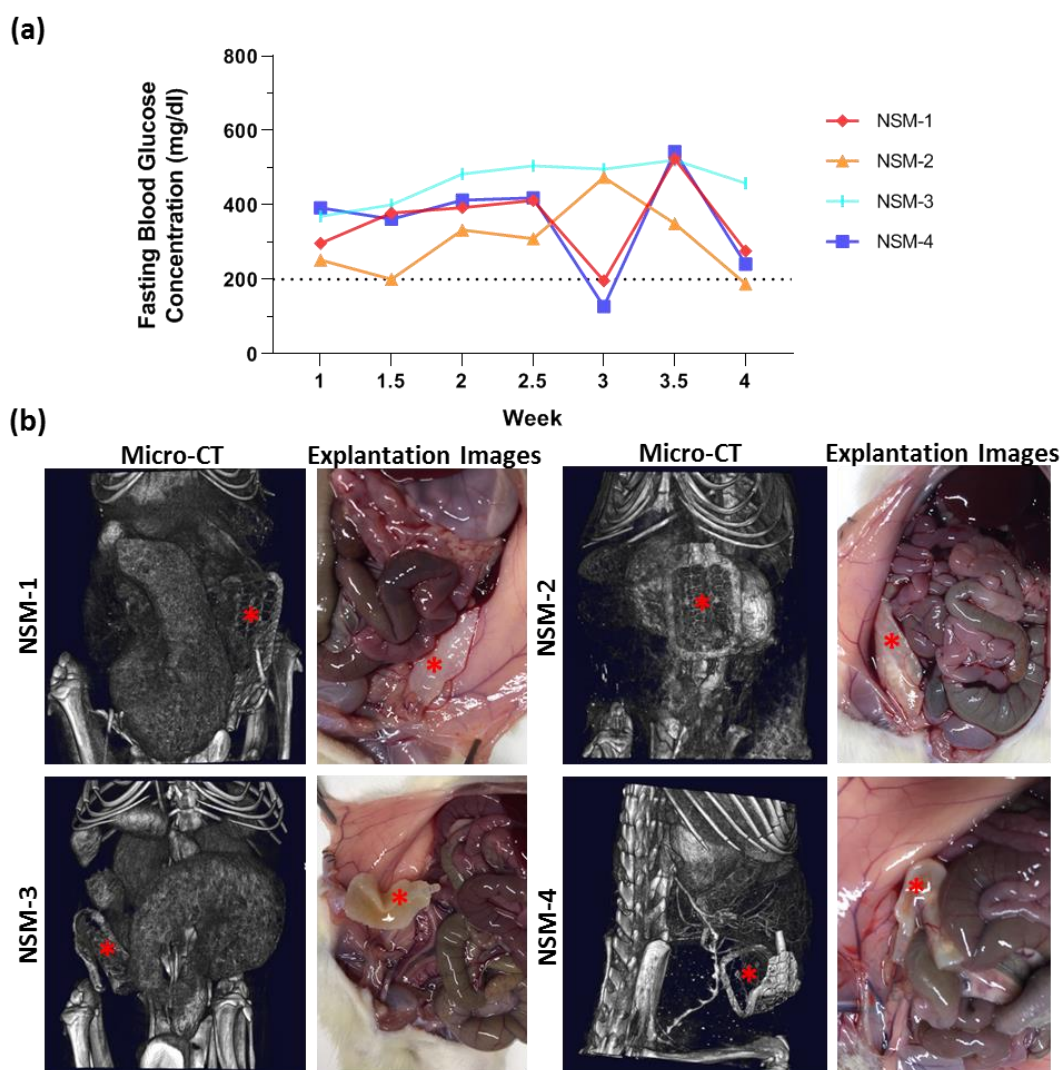


Figure 4.4: Non-sutured macroencapsulation devices containing islets implanted intra-peritoneally. **(a)** Fasting blood glucose concentrations (mg/dL) of non-sutured macroencapsulation devices (NSM) containing islets. **(b)** Micro-CT images of non-sutured devices in-situ to accurately monitor movement and associated explantation images of NSM-1 to 4 in-situ within the abdominal cavity. Devices are labelled with red asterisks. $n = 4$.

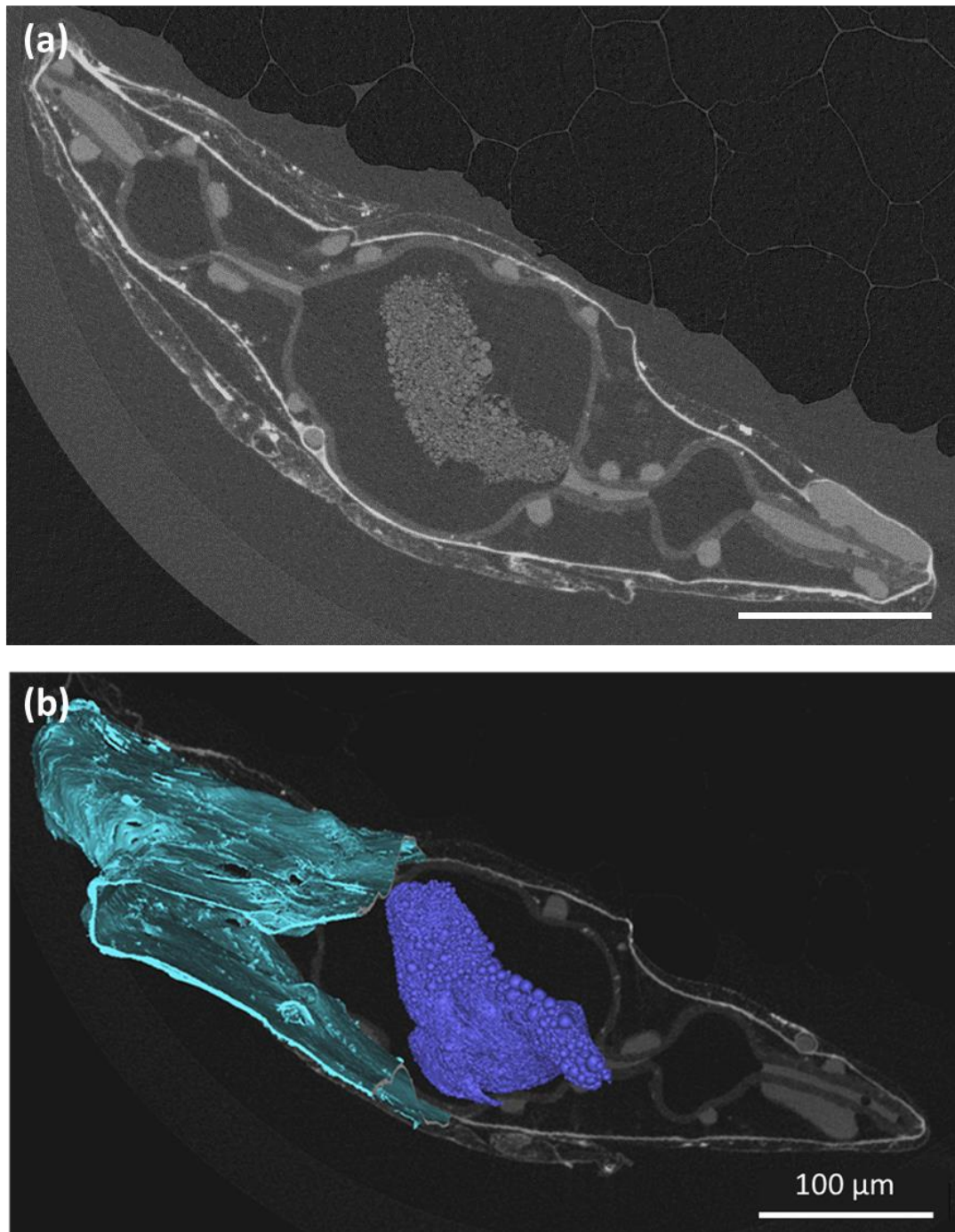


Figure 4.5: Micro-CT imaging of non-sutured macroencapsulation devices containing islets implanted intra-peritoneally. **(a)** Micro-CT cross section of islet encapsulation device. **(b)** A volumetric rendering of implant after microCT demonstrating the fibrous capsule (turquoise) and device contents; islets and VEGF microspheres (purple). Scale bar = 100 μm .

4.3.4 MicroCT Analysis of the multiscale porosity non-sutured macroencapsulation device

The development of a surrounding fibrous capsule was verified by microCT imaging shown (*Figure 4.5 (a)*). While there is some delamination of tissue from the device most likely due to sample processing, an imprint of the contours of the surface of the devices can be seen in various regions of the cross-sectional image. Evidence of encapsulated islets and VEGF microsphere structures can be seen within the device. A 3D volumetric rendering of the device and contents was generated using the microCT data which successfully demonstrates the surrounding fibrous capsule (turquoise) and device contents; islets and VEGF microspheres (purple) (*Figure 4.5 (b)*).

4.3.5 Implantation of syngeneic islets encapsulated within a multiscale porosity macroencapsulation device sutured to the anterior abdominal wall

Findings from the previous study, *section 4.3.3*, led to a modification in the design of the macroencapsulation device. Two diametrically opposed suture holes were incorporated into the device and enabled devices to be sutured to the internal anterior abdominal wall. Circulating BG levels of transplanted rats were monitored for a period of 4 weeks to establish the efficacy of a hydrogel-based macroencapsulation of islets within a sutured multiscale porosity device.

Four out of $n=8$ rats (S-1, S-3, S-5 and S-6) demonstrate an average fasting BG concentration of 100 mg/dL, indicative of successful reversion of diabetes (*Figure 4.6 (a)*). Fasting BG concentrations of S-2 and S-4, indicate a partial reversion of the diabetes, while S-7 and S-8 (non-responders) exhibited inconsistent fasting BG concentrations of ≥ 200 mg/dL. These results were more consistent with BG concentrations of diabetic rats and thus did not successfully revert the diabetic status of each animal. Micro-CT imaging confirmed maintenance of device configuration and position, which could account for more positive outcome of this study (*Figure 4.6 (b)*).

Taken together the fasting BG concentrations of rats implanted with non-sutured ($n=4$) and sutured devices ($n=8$) were compared to the standard non-diabetic ($n=3$) and diabetic ($n=4$) mean readings \pm SD (*Figure 4.7*). This graph demonstrates the stark difference between non-sutured and sutured devices. By simply suturing the device to the anterior abdominal wall BG concentrations can be maintained to within the non-diabetic fasting range

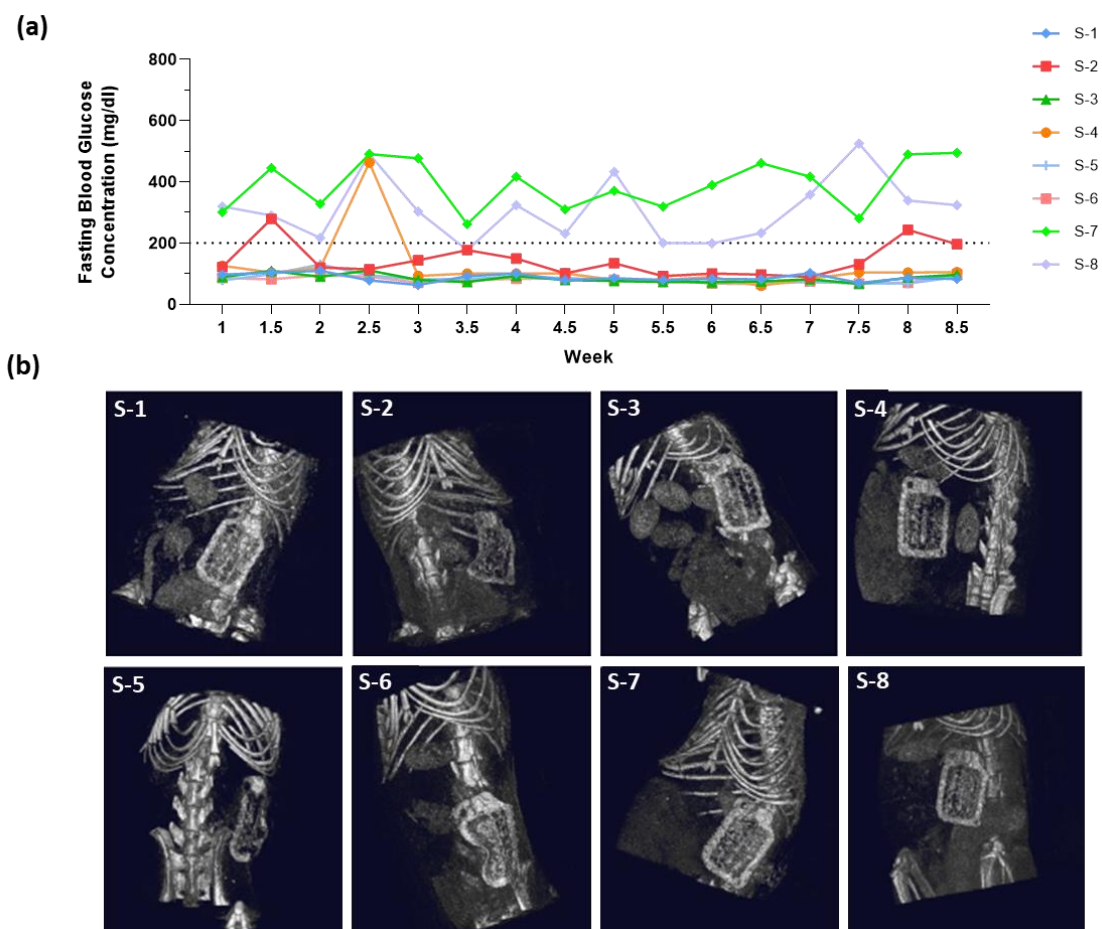


Figure 4.6: Sutured macroencapsulation devices containing islets intra-peritoneally. **(a)** Fasting blood glucose concentrations (mg/dL) of sutured devices (S) containing islets for 8.5 weeks. **(b)** Micro-CT images of sutured devices in-situ to accurately monitor movement at 3 weeks post implantation. $n = 8$.

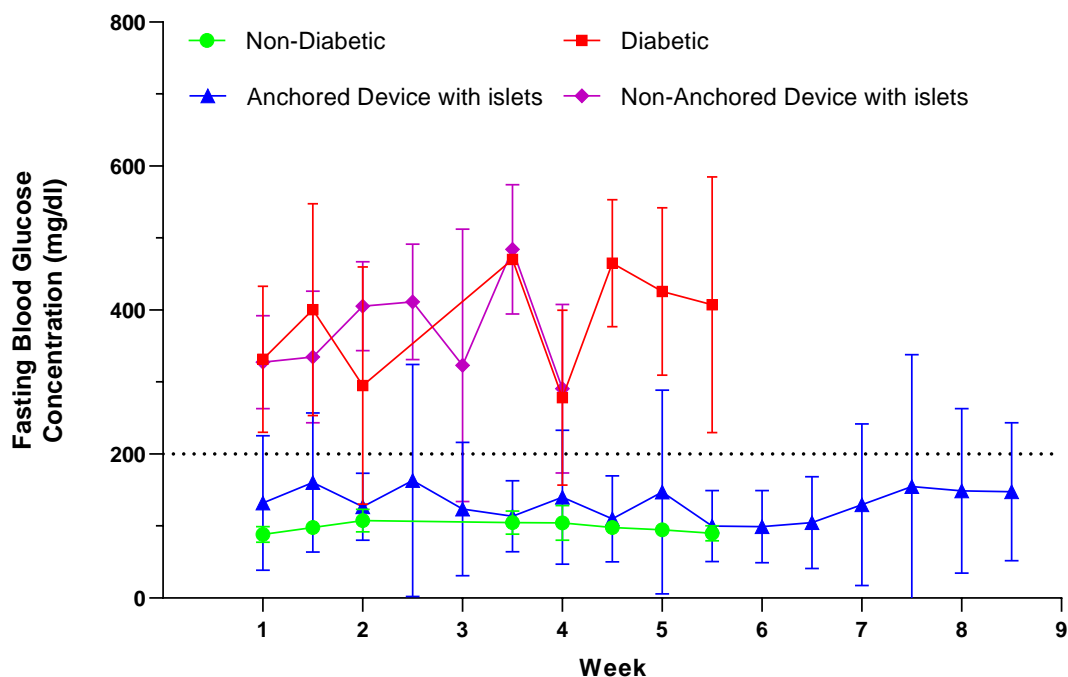


Figure 4.7: Summary fasting blood glucose concentrations (mg/dL) for 0-8 weeks. $n = 3-8$ per group, data are means \pm SD.

4.3.6 Analysis of blood glucose levels 2.5 weeks following explant of devices

Responder rats S-1, S-3, S-5 and S-6, which demonstrated successful reversion of diabetes for 8 weeks in *section 4.3.4* were chosen for further analysis. At 8.5 weeks, these four rats were anaesthetised by isoflurane and had their respective devices removed. Their BG levels were tested at 2.5 weeks to monitor progression back into a diabetic state. Following feeding, the percentage reduction in BG concentration between feed-induced hyperglycemia and return to basal BG levels was calculated (*Figure 4.8 (a)*). This measurement would demonstrate the ability of each rat to maintain glycemic control without intervention. At 8.5 weeks, prior to explant, three of the $n=4$ (S3, S-5 and S-6) demonstrated a 30-85% reduction compared to 0-15% reduction in circulated blood glucose at 2.5 weeks post explant. In contrast, the percentage reduction in rat S-1 increases from 8 to 20% at 2.5 weeks post explant. Animals were euthanised and each pancreas was processed for histological analysis. Immunofluorescent staining of insulin and glucagon positive cells within each pancreas demonstrate highly disrupted islet morphology (*fig*) which corresponds with typical diabetic islet morphology as shown in *Figure 4.8 (b)*.

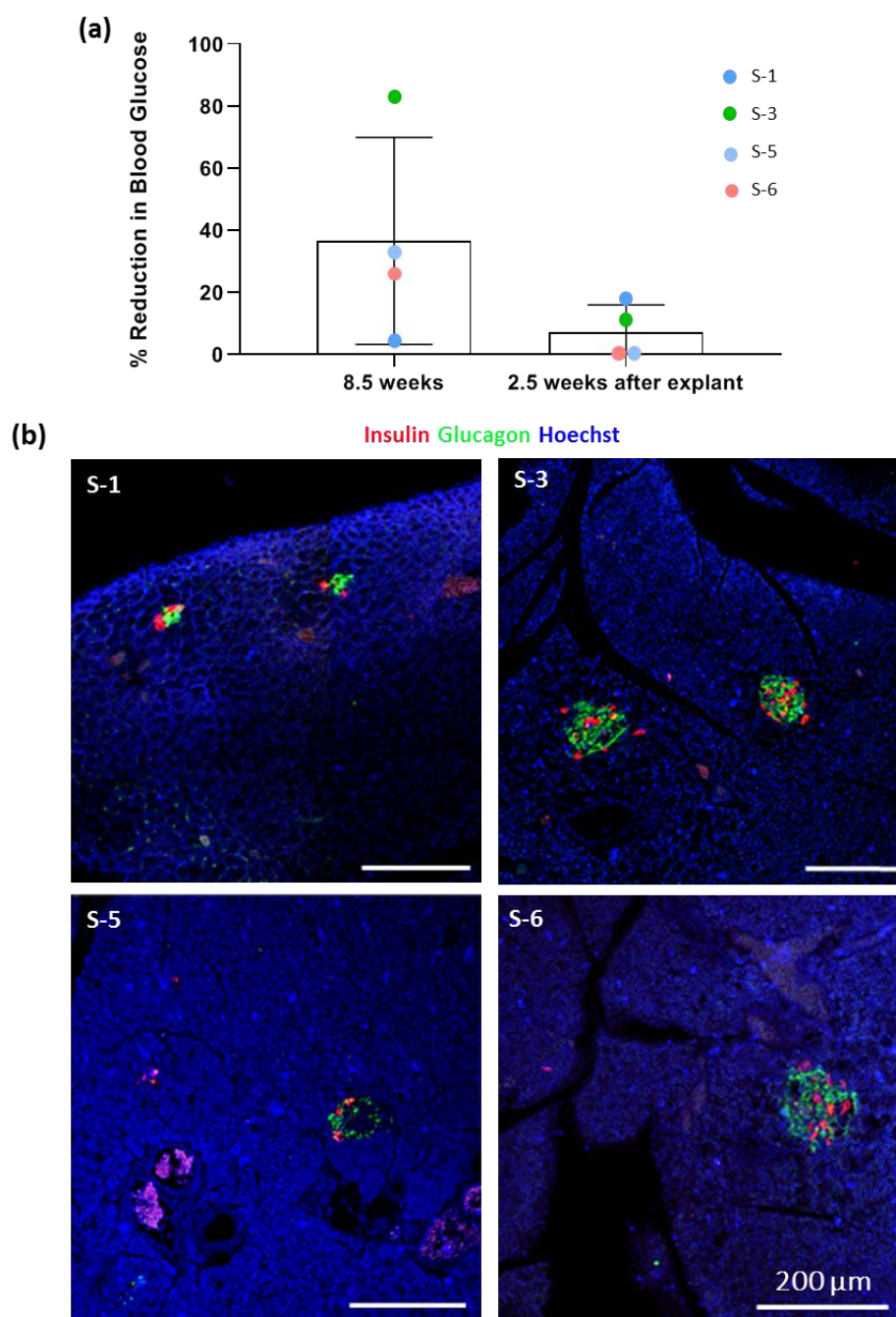


Figure 4.8: Analysis of blood glucose levels 2.5 weeks following explant of devices & histological analysis of associated pancreatic tissue. **(a)** Percentage reduction in blood glucose at 8.5 weeks of implantation and 2.5 weeks after explant. **(b)** Representative immunofluorescent images of pancreases several weeks following explant of devices (Hoechst, blue; Glucagon, green; Insulin, red). Scale bar = 200 μ m. $n = 4$ per group, data are represented as means \pm SD.

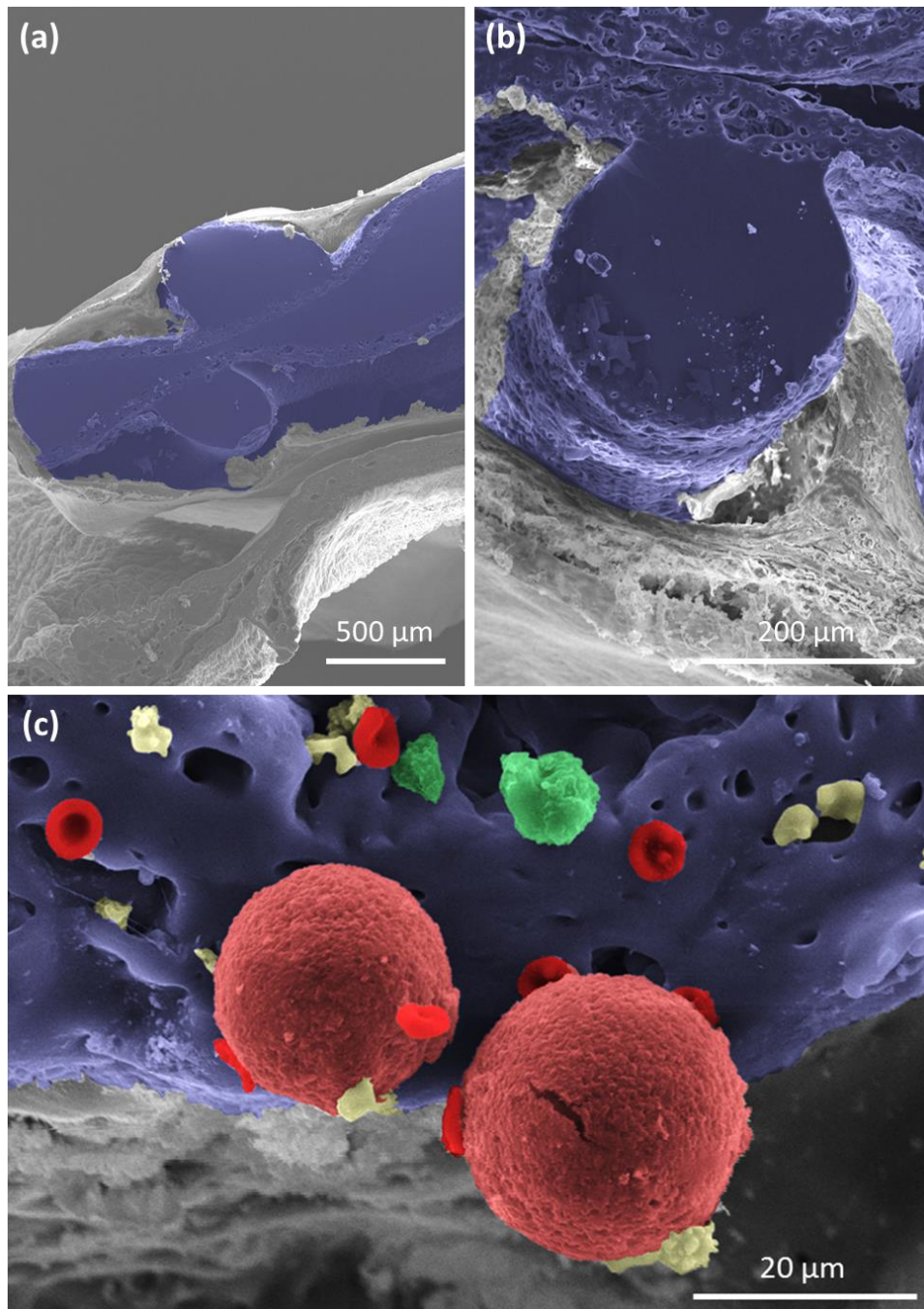


Figure 4.9: SEM imaging of sutured macroencapsulation devices with associated surrounding tissue. **(a)** Overview image of sutured device demonstrating integration into the surrounding tissue. Scale bar = 500 μm . **(b)** Image of rope-coil surface feature integrated into the surrounding tissue. Scale bar = 200 μm . **(c)** High mag image of VEGF microspheres (light red), red blood cells (red), leucocytes (yellow) and macrophage (green). Scale bar = 20 μm .

4.3.7 Analysis of the fibrous capsule surrounding sutured macroencapsulation device

4.3.7.1 Scanning Electron Microscopy (SEM)

SEM was performed in order to examine the development and integration between the macroencapsulation devices and the surrounding tissue. As demonstrated in the previous chapter of this thesis, the inclusion of multiple layers of rope-coil and micro-porosity results in excellent tissue integration (*Figure 4.9 (a)*).

4.3.7.2 Fibrous capsule thickness

To assess the degree of fibrous capsule development surrounding the sutured macroencapsulation devices, a thickness assessment was performed of the newly formed hyper-dense collagen made visible by Masson's trichrome stain (*Figure 4.10 (a)*). Representative images of fibrous capsule surrounding non-responders (S-7 and S-8) and strong responders (S-1, S-3, S-5 and S-6) are shown in *Figure 4.10 (b)*. Fibrous capsule thickness ranged from 25-50 μm across the eight devices.

4.3.7.3 Myofibroblast abundance

The volume fraction of immunofluorescent labelled αSMA^+ cells within 100 μm of the device interface was estimated using an unbiased stereological (*Figure 4.10 (c)*) point counting technique. The volume fractions ranged from <0.1 - 0.25 (*Figure 4.10 (d)*). These findings correlated with the fibrous capsule thickness results seen in *Figure 4.10 (b)* the exception of devices S-2 and S-7 which demonstrated lowest volume fraction of myofibroblasts while simultaneously exhibiting the thickest capsules.

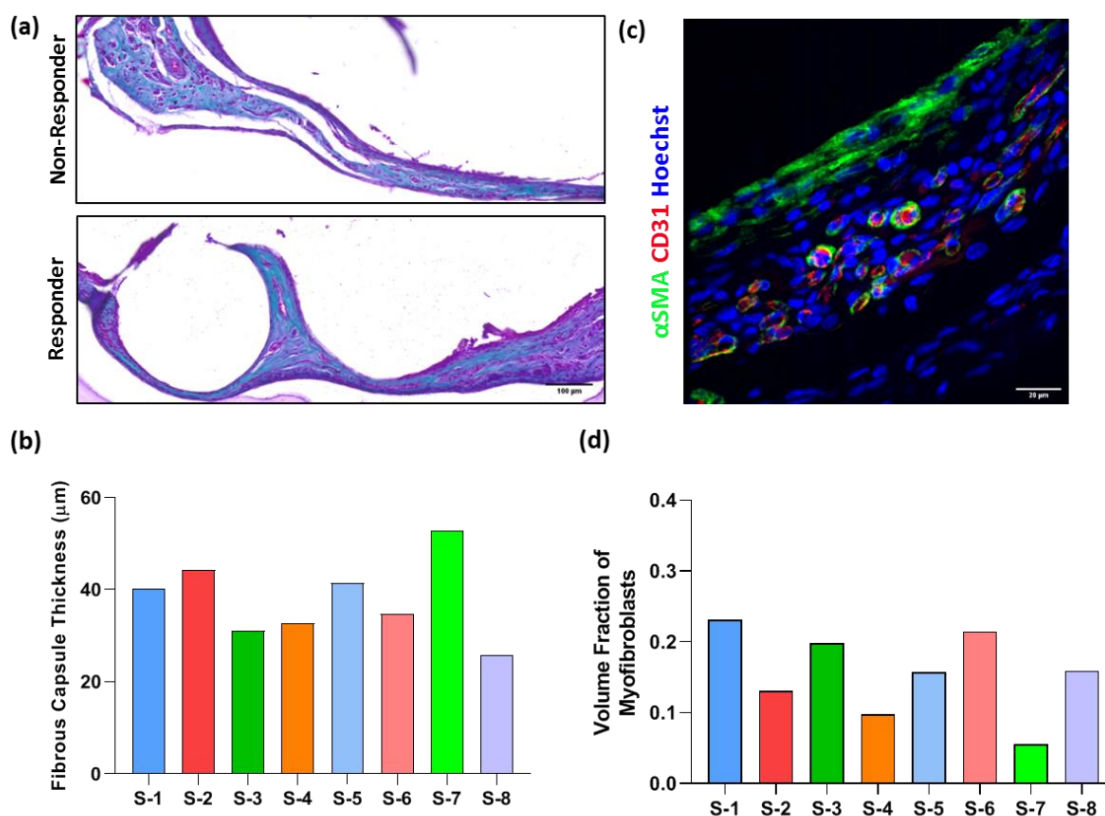


Figure 4.10: Analysis of fibrous capsule formation around sutured macroencapsulation devices. **(a)** Representative Masson's trichrome images of the fibrous capsule surrounding a glucose non-responder and responder Scale bar = 100 μm . **(b)** Fibrous Capsule thicknesses (μm). **(c)** Representative immunofluorescent image for analysis of myofibroblast abundance (Hoechst, blue; αSMA , green; CD31, red). Scale bar = 20 μm . **(f)** Volume fraction of $\alpha\text{SMA}+$ cells (myofibroblasts) within the fibrous capsule. $n = 1$ per group, data are represented as means.

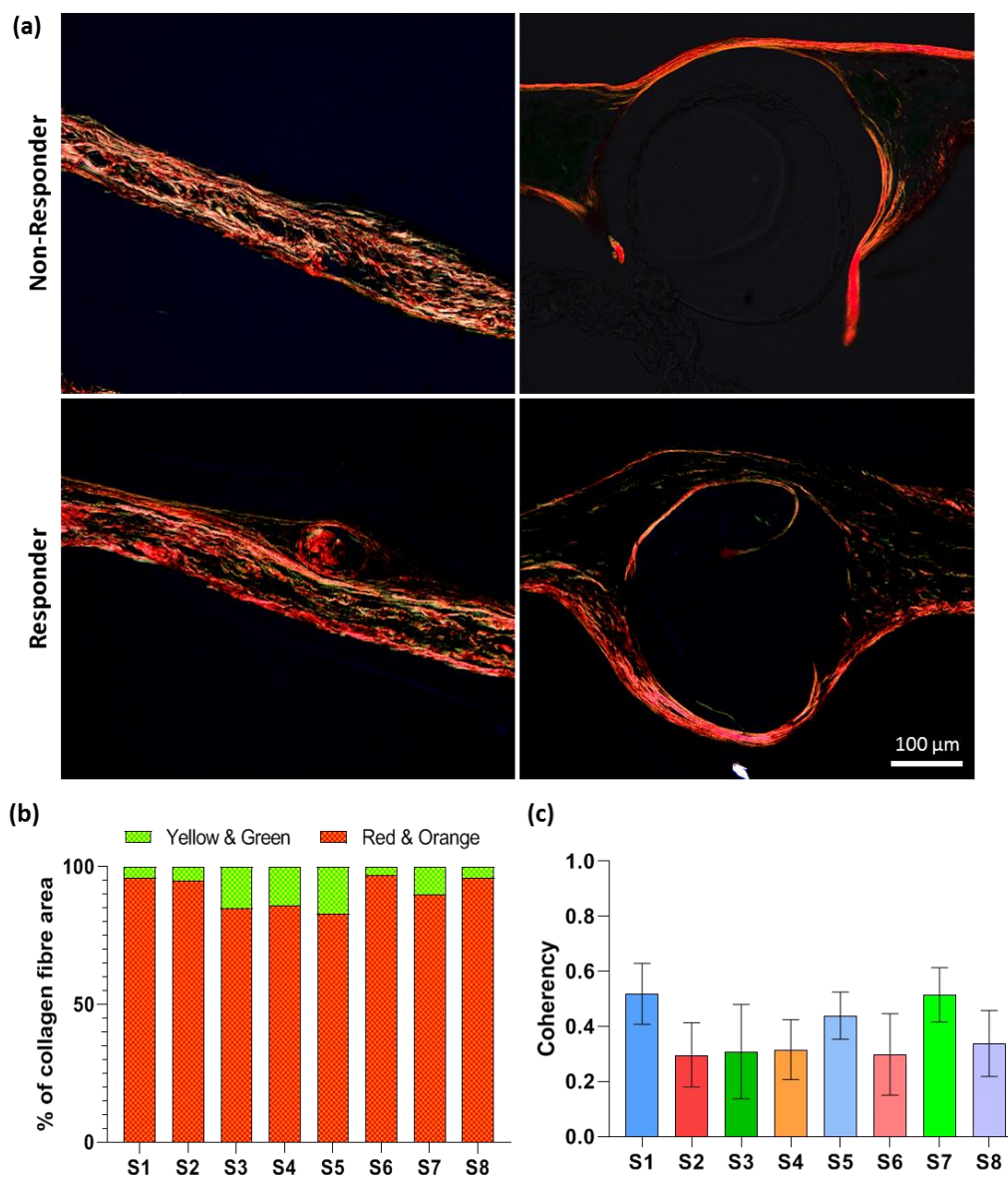


Figure 4.11: Analysis of fibrous capsule composition around sutured macroencapsulation devices using polarised light microscopy. **(a)** Representative PLM images of the fibrous capsule surrounding a glucose non-responder and responder Scale bar = 100 µm. **(b)** Percentage of the collagenous fibrous capsule composed of yellow and green or red and orange. **(c)** Quantification of the directional uniformity (coherency) of collagen fibres. $n = 1$ per group, data are represented as means \pm SD.

4.3.8 Analysis of fibrous capsule composition around sutured macroencapsulation devices using polarised light microscopy

To characterise the collagen network surrounding the sutured macroencapsulation devices, a picrosirius red stain and PLM was performed (*Figure 4.11*). Representative images of the collagenous fibrous capsule surrounding non-responders (S-7 and S-8) and strong responders (S-1, S-3) are shown in *Figure 4.11 (a)*. Analysis of collagen fibre colour demonstrated that > 80% of collagen fibres were red or orange in appearance, implying the presence of mature collagen type I. The remaining 20% was composed of green and yellow fibres (thin, collagen type III-like) indicative of an earlier remodelling phase[276–278]. This increased proportion red/orange fibres is indicative of a more mature and established fibrous capsule however, this proportion did not differ between responders and non-responders (*Figure 4.11 (b)*). Quantification of the directional uniformity (coherency) which determined how random or uniform the fibres are as a whole on a scale from 0 (random) to 1 (uniform) demonstrated values <0.5 in all groups (*Figure 4.11 (c)*). This suggested that collagen organisation was more anisotropic.

4.3.9 Analysis of the angiogenesis surrounding sutured macroencapsulation devices

4.3.9.1 Blood vessel abundance

To investigate the degree of neovascularisation development surrounding the sutured macroencapsulation devices, tissue sections were stained for CD31, an endothelial cell marker, and stereological analysis was performed to quantify blood vessel density surrounding each device. Representative images of the CD31 stained fibrous capsule surrounding non-responders (S-7 and S-8) and strong responders (S-1, S-3, S-5 and S-6) are shown in *Figure 4.12 (a)*. The number of blood vessels per unit area ranges between 250-650, length density ranging from 500-1200, and quite similar radial diffusion distances of 15-24 μm across all devices (*Figure 4.12 (b-d)*).

4.3.9.2 Blood vessel maturity

In order to further analyse the angiogenic response, the abundance of αSMA^+ blood vessels, a marker indicative of vessel maturity was quantified. A ratio of αSMA^+ vessels to total CD31+ vessels was obtained using confocal microscopy (*Figure 4.12 (e, f)*). From this analysis, it was demonstrated that 50-80% of blood vessels were classified as mature.

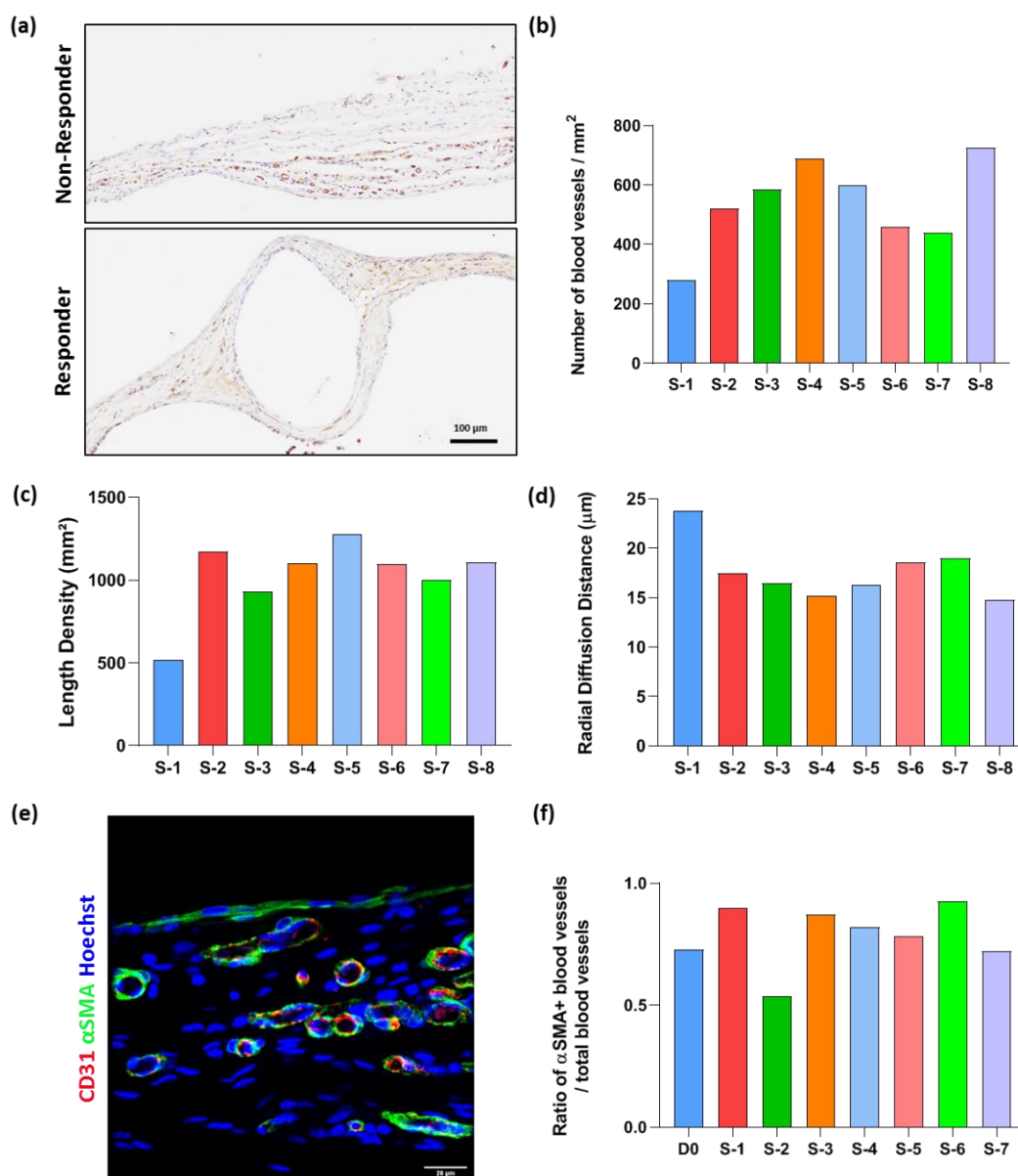


Figure 4.12: Analysis of angiogenesis surrounding sutured devices. **(a)** Representative CD31 stained histological image. Scale bars = 200 μm . **(b)** Number of blood vessels per mm^2 . **(c)** Length density. **(d)** Radial diffusion distance. **(e)** Representative immunofluorescent image for analysis of vessel maturity and stability (Hoechst, blue; αSMA , green; CD31, red). Scale bar = 20 μm . **(f)** Ratio of $\alpha\text{SMA}+$ blood vessels to total blood vessels. $n = 1$ per group, data are represented as means.

4.3.10 Analysis of the macrophage response surrounding sutured macroencapsulation devices

To assess the impact of a sutured multiscale porosity device on macrophage abundance and polarization, tissue sections were co-stained with both CD68/CCR7 and CD68/CD163 (*Figure 4.13 (a)*). Representative immunofluorescent images show macrophage aggregation directly at the tissue-device interface. Volume fraction of CD68+ cells demonstrated that 10-21% of the volume of the capsule is composed of macrophages (*Figure 4.13 (b)*). The number of CD68+ cells per mm³ varied as strong responders S-1 and S-3 demonstrated a reduced response compared to other device (*Figure 4.13 (c)*). The ratio of CCR7+ cells to total CD68+ cells was then compared to the ratio of CD163 positive cells to total CD68+ cells which demonstrated a higher ratio of CCR7+ macrophages (M1) compared to CD163+ macrophages (M2), suggesting that the majority of macrophages present display an M1, or pro-inflammatory phenotype (*Figure 4.13 (d)*).

4.3.11 Comparison of histological analysis of devices sutured to the anterior abdominal wall vs submuscular implantation

To assess whether the implantation duration and site of the multiscale porous devices affected fibrous capsule composition, angiogenic and macrophage responses, the histological results were directly compared. Fibrous capsule thickness assessments performed demonstrated a 2-fold increase in capsule thickness in the submuscular vs sutured AAW devices (****P<0.0001) with little variation in the volume fraction of myofibroblasts (*Figure 4.14 (a, b)*). Interestingly the reduced fibrous capsule thickness exhibited a 3-fold increase in the number of blood vessels per area (****P=0.0001), and thus demonstrated a significant reduction in the radial diffusion distance between vessels (**P=0.004) and increased vessel maturity (*P=0.0136) when compared to the submuscular devices (*Figure 4.14 (c-e)*). However, this increase in the angiogenic response was associated with a 3-fold increase in the volume fraction of macrophages (***P=0.0004) (*Figure 4.14 (f)*). This data indicates that a pre-peritoneal space may be an ideal site for implantation due to its reduced fibrous capsule thickness and increased angiogenic response when compared to the submuscular implantation in the dorsum. The increase in macrophage response is possible associated with the formation of this rich vascular network.

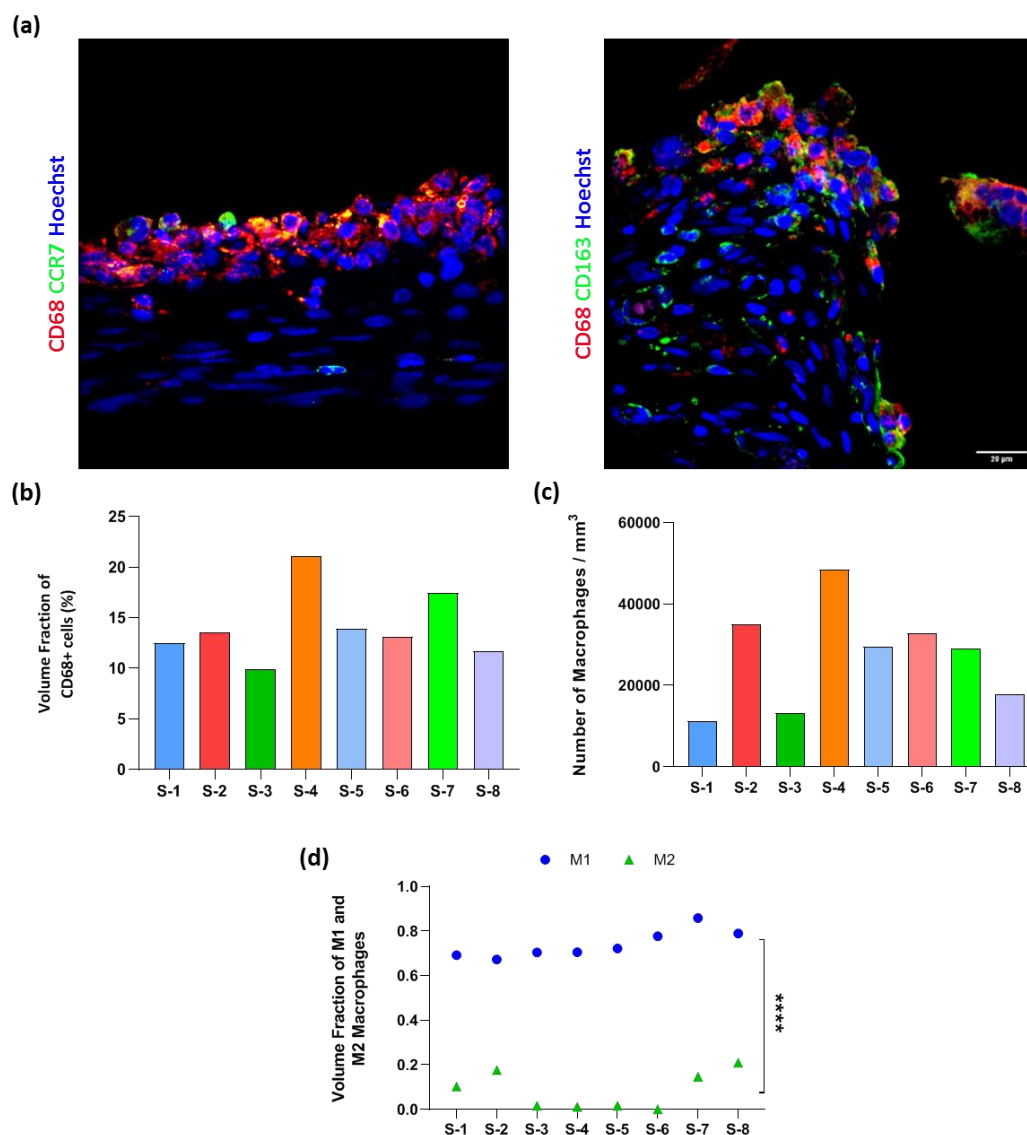


Figure 4.13: Analysis of the macrophage response surrounding sutured devices. **(a)** Representative immunofluorescent image of CD68 and CCR7:M1 phenotype marker (Hoechst, blue; CCR7, green; CD68, red) and CD68 and CD163:M2 phenotype marker (Hoechst, blue; CD163, green; CD68, red). Scale bar = 20 μm . **(b)** Volume fraction (%) of CD68+ cells. **(c)** Number of CD68+ (pan-macrophage marker) cells per volume. **(d)** Volume fraction of CCR7+ and CD163+ to total CD68+ macrophages. $n = 1$ per group, data are represented as means, M1 vs M2 **** $P < 0.0001$.

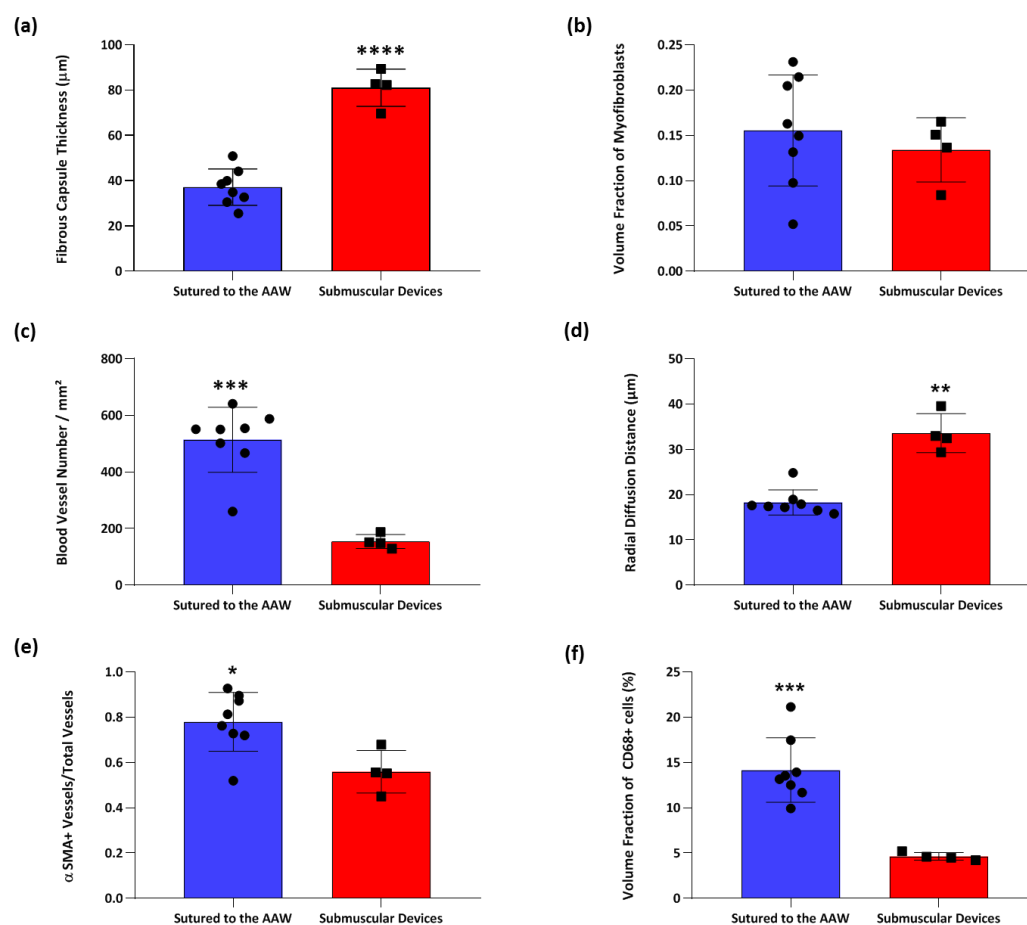


Figure 4.14: Comparing histological analysis of devices sutured to the Anterior Abdominal Wall (AAW) vs submuscular implantation (*Chapter 2*) **(a)** Fibrous Capsule thicknesses (µm). **(b)** Volume fraction of αSMA+ cells (myofibroblasts) within the fibrous capsule. **(c)** Number of blood vessels per mm². **(d)** Radial diffusion distance (µm). **(e)** Ratio of αSMA+ blood vessels to total blood vessels. **(f)** Volume fraction (%) of CD68+ cells. *n* = 4-8 per group, data are represented as means ±SD *P<0.05, **P<0.01, ***P<0.001, ****P<0.0001.

4.4 Discussion

To develop an efficacious islet encapsulation system, one must recognise the complex relationship between, device design, islet quality, implantation site, and integration into the host site. In this study, we describe the optimisation of intra-peritoneal transplant methodology to achieve adequate angiogenic and tissue integration for increased viability and long-term efficacy of encapsulated syngeneic islets.

Identification of alternative, extrahepatic sites for islet transplantation has been extensively examined in preclinical studies such as the spleen [360], renal capsule [361], muscle [362], gastric submucosa [363], intestinal submucosa [364], venous sac [365], omentum [193], bone marrow [366] and peritoneum [367]. Traditionally intra-peritoneal implantation of encapsulated islets is associated with some sub-optimal performance due to lack of integration, development of an avascular fibrous capsule, gravity-mediated aggregation and impaired graft viability and functionality [347,368–370]. However, this site maintains its attractiveness due to its ability to absorb insulin directly into the portal system to facilitate HFPE [350,371,372] and also its ability to host a macroencapsulation device in rodent models. Most successes are limited to rodent models or in vitro experimentation but despite this, intra-peritoneal implantation of micro- and macro-encapsulation is frequently chosen for clinical trials [373–376].

These suboptimal findings were reflected by both gel encapsulation and non-sutured macroencapsulation of islets within the peritoneal cavity. Both implantation approaches demonstrated largely erratic fasting blood glucose concentrations above 200 mg/dL, consistent with diabetic levels (*Figure 4.7*). Histological analysis of gel-encapsulated islets revealed disrupted islet morphology and the infiltration of macrophages throughout the cell graft (*Figure 4.3 (d-g)*) which most likely reduced the therapeutic potential of these cells. MicroCT visualisation of the non-sutured macroencapsulation devices demonstrate extreme changes to the device configuration and position over the 4-week implantation period (*Figure 4.4 (b)*). This movement disrupted tissue integration and the development of a highly interconnected vascularised network which potentially compromised islet survival.

Optimisation of the implantation procedure by suturing the macroencapsulation device internally to the pre-peritoneal site resulted in a positive functional read out for the encapsulated islets possibly indicative for improved efficacy of encapsulated cells (*Figure 4.6 (a)*). As devices maintained their configuration and position throughout the implantation period, the potential for tissue integration and vascularisation increased.

Typically, peritoneum has an imperative role in effective solute transport, which constitutes the rationale for peritoneum dialysis and attributes do its rich vascularisation [377]. Over a period of 8 weeks, over half (6/8) of implanted rodents achieved graft-derived insulin levels, sufficient to prevent STZ-induced hyperglycemia (*Figure 4.6 (a)*).

Unlike intra-peritoneal implantation, subcutaneous transplantation is hugely popular among the most current encapsulation systems, such as β Air [230,298], Viacyte [220–223], Mailpan [378] and Sernova's Cell Pouch [182,234] from preclinical through to clinical trials. Although popular, an unaltered subcutaneous site has produced no evidence that cells transplanted can ameliorate diabetes in humans or in animal models, hypothesized in part to be a result of poor neovascularisation [20,379–381]. These findings directed investigations into alternative transplant sites. However, subcutaneous sites have many beneficial attributes compared to other sites due to its large transplantable surface area, accessibility, availability for biopsy, imaging, retrieval without compromise to collateral organs and translatability from small to large animal models. While these attributes are attractive for encapsulation systems they are balanced with reduced vascularity and tissue oxygen tension compared to other more richly vascularised sites which are also suited for transplant [382]. In order to reap the benefits of subcutaneous sites, encapsulation systems must utilise novel polymers or surface topographies to promote vessel formation that can significantly enhance neovascularisation [191,301,302]. Alternatively rapid vascularisation in the vicinity of devices could be promoted by previously reported potent angiogenic molecules such as VEGF, fibroblast growth factor, hepatocyte growth factor, insulin-like growth factor, angiopoietin-1, and angiopoietin-2 [383,384]. Protein-based delivery of growth factors such VEGF, can facilitate the controlled release of angiogenic stimuli [192,259,304,305] and has been associated with enhanced engraftment and islet function within encapsulation strategies [293,306]. These strategies are discussed in *Chapter 3*.

In conclusion, the combination of an optimised intra-peritoneal implantation procedure and a multiscale porosity encapsulation device can facilitate efficacious islets and the maintenance of normoglycemia in diabetic rodents for up to 8 weeks. By choosing a site with abundant endogenous vasculature with the possibility for proangiogenic manipulation, it can enable the development of a highly interconnected vascularised network surrounding the encapsulation device. This network largely mirrors the natural physiological vascularisation of the native pancreas, and can provide adequate oxygenation and nutrient supply for active and sustained engraftment.

Chapter 5

To examine the scalability and functionality of multiscale porous islet encapsulation devices in an STZ-induced diabetic porcine model

5.1 Introduction

Promising approaches for islet cell encapsulation are translated through large animal models that ultimately pave the way to proceed to Phase I and II of clinical trials in human subjects. In this chapter we aim to detail the first steps in translating a rodent sized multi-scale porous device to a large scale, functional macroencapsulation device implanted in a diabetic porcine model.

As discussed in *Chapter 4*, the site of implantation can affect integration, biocompatibility and efficacy of the implanted device. The most suitable site for transplantation of macroencapsulation devices is widely debated. However, investigating novel implant sites is limited by the wide spread use of rodent models in the evaluation of devices. These animal models are insufficient for the identification of novel sites due to the scale of rodent anatomy, preventing examination of potential spaces which are easily accessible in humans. The requirement for more appropriate implant sites is highlighted by advances in encapsulated β -cell replacement therapy. Encapsulating islets within an immunisolating device represents a promising approach to enable protection of islet grafts, reduce or eliminate immunosuppression, while simultaneously providing a safer platform for the use of alternative cell sources [168,208,385]. The restoration of glycemic control in animal studies has resulted in several encapsulation technologies advancing to late preclinical/early clinical testing [203,208,332,386]. However, efficacious implant sites in rodents, for examples the kidney capsule, will lack the ability to host a human-sized implant due to inaccurate anatomical correlation, thus precluding the delivery of cells [387,388].

To fully appreciate the benefits of islet cell encapsulation, a more appropriate implant site must be identified. Such a site must be clinically accessible through a low risk procedure, enable long term monitoring of islet function, enable retrievability in the event of a complication, and provide a suitable environment for the safeguarding of efficacious islet cell function. For this study, three potential sites within the Anterior Abdominal Wall (AAW) were identified due to their ability to accommodate a macroencapsulation device. The transversus abdominus plane (TAP) is a potential space between the transversus abdominus and the internal oblique muscles of the abdomen, and is routinely accessed by anaesthesiologists with ultrasound guidance to provide analgesia for abdominal surgery via a TAP block [389]. The plane of the posterior rectus sheath lies between the muscle belly of the rectus abdominus and the fascia of the posterior rectus sheath, and can be accessed in similar fashion using ultrasound to provide analgesia for abdominal surgery [390].

The supra-inguinal trapezoid plane, referred to as Pre-Peritoneal Space in this thesis, lies superior to the inguinal ligament, in a plane deep to the rectus muscle belly and transversus abdominus fascia but superficial to the peritoneum. This space is developed during laparoscopic inguinal hernia repairs with the total extraperitoneal technique[391].

5.1.1 Aims

The aims of this chapter are to determine the most clinically favourable AAW site for implantation of multiscale porosity macroencapsulation devices and also to determine the scalability and functionality of these devices.

The specific aims of Chapter 5 were to:

- To define the dimensions of potential implant sites in the AAW using a clinical image database
- Determine the scalability of the multiscale porosity macroencapsulation device, from rodent size to porcine sized with translatability for human implantation
- Determine whether the bioavailability of insulin diffusion through the multiscale porosity macroencapsulation device is equivalent to conventional subcutaneous insulin delivery
- Assess the morphology of the fibrous capsules surrounding each multiscale porosity macroencapsulation device using histological assessment, MicroCT and SEM imaging
- Establish whether the multiscale porosity macroencapsulation device affected the activation/abundance of macrophages at the tissue interface capsule using immunofluorescent staining
- Compare the aforementioned fibrous capsule analyses to a smooth surfaced macroencapsulation device under development within our lab.

To achieve these aims, up-scaled multiscale porosity macroencapsulation devices were fabricated and implanted in the most favourable abdominal wall site in STZ-induced diabetic pigs for a period of 21 days.

5.2 Materials and Methods

5.2.1 Determining the most favourable AAW site for implantation of an islet encapsulation device

The majority of the surgical procedures were carried out by Dr Scott Robinson, a vascular surgeon working within the Duffy Lab, NUIG. Drawing on my anatomical knowledge and cadaveric dissection experience from my undergraduate degree and teaching I assisted in both cadaveric assessments of the AAW and optimisation of surgical procedures for this study.

5.2.1.1 Determining the suitability of potential implant sites in the AAW

To identify an optimal recipient site (*Figure 5.1 (a)*) for the implantation of islet encapsulation device, several design constraints were considered that, if adequately addressed, would provide significant improvement over currently used transplant sites (*Table 5.1*). While the tissue planes in the AAW only represent potential spaces, these spaces must be able to accommodate 1mm thick multiscale porosity encapsulation device (to allow for adequate diffusion of glucose, oxygen and insulin) so that predicted volumes for each space can be approximated from 2D anatomic measurements.

5.2.1.2 Determining the dimensions of potential implant sites in the AAW

To define and compare the geometry of the potential AAW sites for translation from pigs to humans, analytic morphomics was used. This involved the use of high quality computational techniques to link image-based biomarkers with different disease states to improve patient outcomes. This approach was developed by the Wang Lab and colleagues at the University of Michigan Morphomics Analytics Group (MAG). It involves the use of a series of semi-automated algorithms to compare body composition measures (e.g. psoas muscle density, visceral and subcutaneous fat distribution, bone mineral density) from a cohort of patient computed tomography (CT) scans. This technique has been used extensively to predict surgical outcomes after liver [392–394], lung [395], kidney [396,397], and bone marrow transplant [398]. The MAG possesses a repository of over 40,000 unique CT scans from patients at the University of Michigan from which a core set of morphomic parameters has been calculated. Additionally, MAG has generated a Reference Analytics Morphomics Population (RAMP) derived from the CT scans of 6,000 healthy patients age 1-91 providing a control group for comparison to a diseased cohort. However, this imaging database is also a useful technique for medical device design. Through modification of the existing MAG algorithms written in MATLAB 2013a (MATLAB 2013a, MathWorks Inc., Natick, MA), the area and volume ($n=2$) of the potential spaces of the AAW could be calculated.

To measure the TAP space, “seams” are identified at bone and muscle borders. The term seams refer to the approximate anatomical boundaries of each potential implant site. As demonstrated in *Figure 5.1 (b)*, the TAP seams are identified at the medial (semilunar line) and lateral (lumbosacral fascia) are connected and extended superior to the costal margin, and inferiorly to the inguinal ligament. The posterior rectus sheath was defined as an area bounded by the linea alba seam, lateral rectus seam, pubic bone, and costal margin. The pre-peritoneal space was defined as an area bounded by the linea alba seam, the dorsal muscle group seam, a line extending from the pubic symphysis to anterior superior iliac spine, and the L3-L4 vertebral level. From this user delineation, a point cloud is created of the area of interest, which enables to software to accurately map the area of interest. Surface area measurements were computed by measuring the Hounsfield units of each individual pixel and averaging these values across all pixels in bilateral site cross-sectional slices [397] (*Figure 5.1 (d)*). Similar forms of this algorithm can be applied to approximate the pre-peritoneal and posterior rectus sheet sites, such that from a large cohort of imaging studies we can generate a population based “map” of the geometry of these potential spaces. These area and volume measurements were performed both on pig and human CT images to allow easy translatability of large animal study finds, to future clinical studies.

To determine if delivery of an macroencapsulation device to an implant site within the AAW is clinically feasible, we used commercially available supplies to access the TAP space in a pig. The layers of the AAW were clearly visualised with ultrasound, allowing for ultrasound guided hydro dissection along the appropriate transversus abdominus plane (*Figure 5.1 (c)*).

Table 5.1: Design criteria for implant site
1. Must have adequate arterial blood supply
2. Adequate venous drainage
3. Site should be extraperitoneal to avoid intra-abdominal procedure
4. Site should be easily accessible to allow for device refill/removal
5. Site should allow for longitudinal monitoring of implant function
6. Presence of device should not cause pain
7. Minimal potential complications, or easily managed complications
8. Location of device should prevent device migration
9. Device placement should not impact or be impacted by movement
10. Accommodate a volume of 0.5 mL/kg, thickness of 1 mm
11. Accessible through a minimally invasive procedure

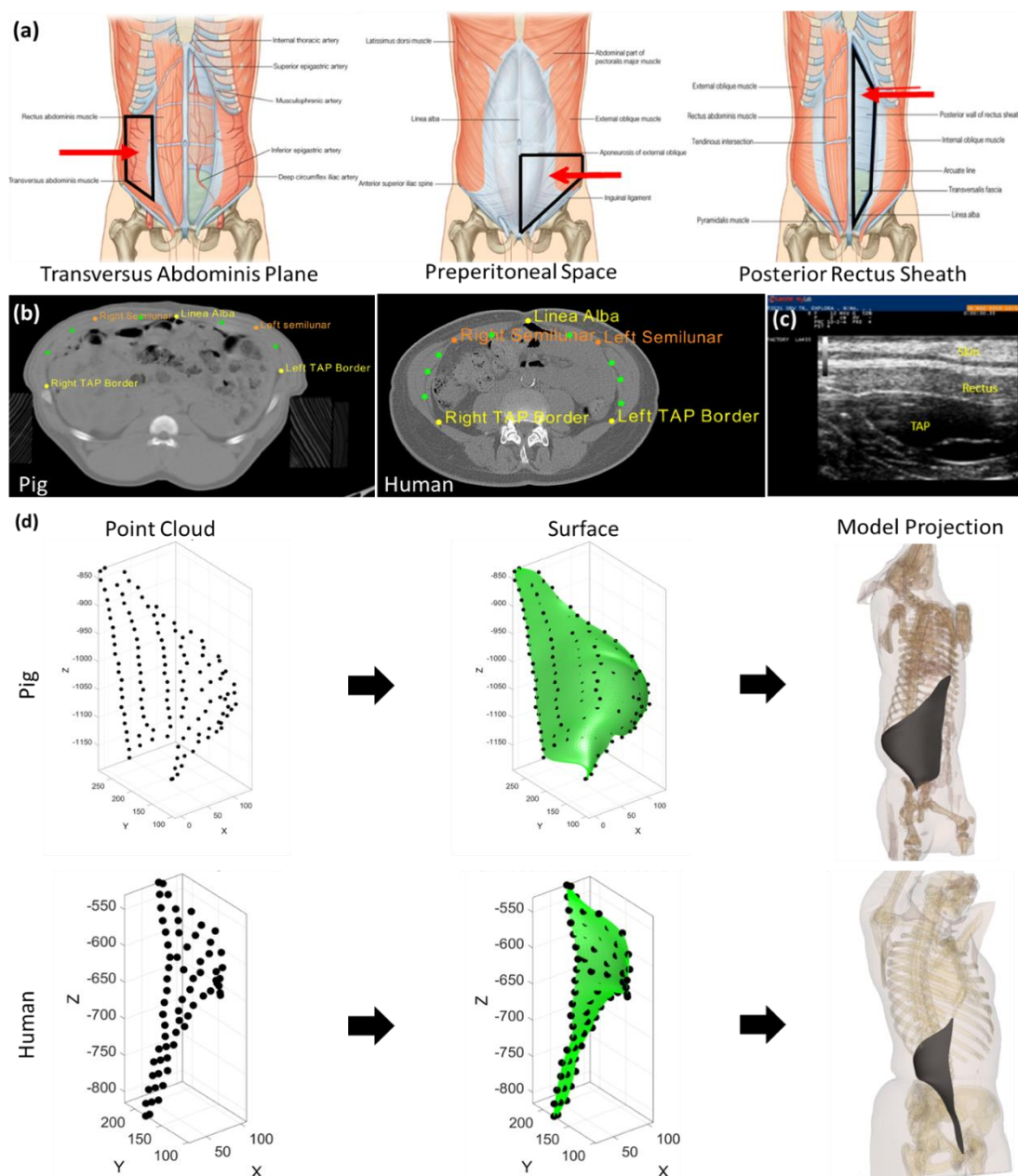


Figure 5.1: Determining the dimensions of potential implant sites in the AAW. **(a)** Schematic of potential spaces in the AAW. **(b)** Morphomic seams to identify the borders of the AAW on CT scan. The curved green lines represent the boundary of the TAP space. **(c)** Ultrasound visualization and hydro dissection of TAP space. **(d)** Creation of point cloud enabling software to accurately map the area of interest, permitting surface area

5.2.2 Device fabrication

These procedures were carried out by Fergal Coulter and the O’Cearbhaill Lab, UCD, Dublin. I worked very closely with UCD to develop and enhance these human sized macroencapsulation devices, providing design inputs including volume, position delivery in the peritoneum, and suture points.

In order to validate the clinical relevance of the macro- and micro- texturing processes further, additive manufacturing processes described in detail in *Chapter 2* were used in the fabrication of a porcine sized device with functional attributes for submuscular implantation (*Figure 5.2 (a)*). The 10 mL device was constructed of two porous (5-8 μm micropores) membranes with a rope-coil layer extruded onto the surface, followed by overspraying two salt/silicone solution layers. A layer containing an internal support structure was incorporated by extrusion of MED4840 in a pattern that strengthened the device, prevented ballooning, and directed distal filling (*Figure 5.2 (d)*) of the device cavity with an internal catheter. The device also included a catheter attachment with one-way valve for unidirectional filling and fixation rings reinforced with surgical stainless steel to allow ease of handling and suture fixation of the device without risking damage to the body of the implant. Absolute maximum device thickness 1mm to limit hypoxia and/or necrosis of islets and the ‘Figure of 8’ shape gives maximum flexibility to twist and distort the device without causing kinks, and potentially minimise fibrotic response from hard kink corners (*Figure 5.2 (b)*).

During the time of this study the Duffy lab were simultaneously establishing the ip-Regeneroiv, an implantable therapeutic reservoir system for diverse clinical applications in large animal models [399]. The ip-Regeneroiv device consists of an inner loading chamber that can be infused with therapeutic cells, and an outer bio adhesive channel which can be filled with a bio adhesive to secure the loading chamber to surrounding tissues. This device consisted of a soft, flexible thermoplastic polymer (thermoplastic polyurethane, or TPU) used for the production of the entire reservoir frame. A combination of 0.3 and 0.075 mm thick TPU sheets were used in the construction (HTM-8001-M and HTM-1001 polyether TPU film, American Polyfilm, Inc). The active surface of Regeneroiv consists of a porous layer of TPU that facilitates the therapeutic effect of the cellular cargo. Each component was bonded to this assembly using a heat transfer machine. In order to establish the biocompatibility of these devices within the transversus abdominis plane, n=2 were included within this study.

Polyurethanes have excellent safety records with over 30 years of use in medical applications such as balloon catheters, artificial heart valves and elastic hernia mesh implants [400–405]. These studies utilised TPU due to its customisable properties and biocompatibility. For the purpose of this chapter, this device was used as a comparative group due to its identical surgical implantation site, duration of implantation and its smooth surface exterior.

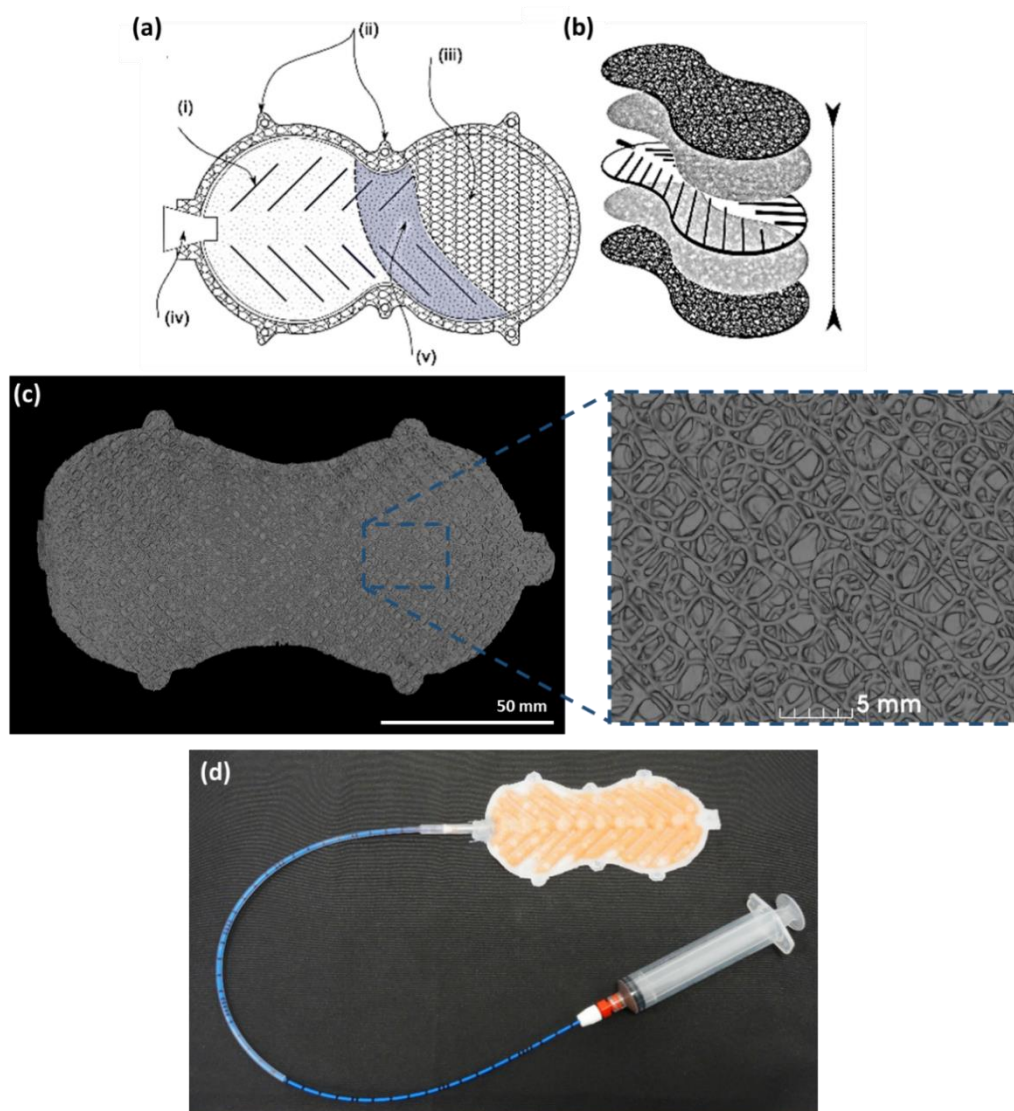


Figure 5.2: Upscaling of multiscale porous device. **(a)** Schematic of multiscale porous device scaled for use in pig studies (i) Inner support structure (ii) surgical tie points (iii) outer rope-coil layers (iv) input valve (v) permeable silicone membrane **(b)** Exploded view. **(c)** A volumetric rendering of implant after microCT imaging with high magnification image demonstrating rope-coil texturing on surface. **(d)** Filling procedure: Catheter inserted through the tube until the distal end of the pouch. Step-by-step filling: Alternated injection of 2ml of coloured gel and retraction of the catheter of 2cm (5 Steps).

5.2.3 Porcine Studies

These procedures were carried out by Explora Biotech Srl Rome, Italy. I contributed to the design and planning of these studies, provided direction, travelled to Rome to receive training and witnessed the implantation process, provided support for explantation of implants and tissue en bloc, and trained individuals on our tissue fixation and shipping protocols, and insulin dose calculations.

Porcine studies were approved by the Italian Ministry of Health (Authorisation No. 976/2017-PR). Prior to the experiments, the animals were housed in single cages and were subjected to a one-week acclimatisation period following Directive 2010/63/EU. Prior to surgery, animals received 10 mg/kg ketamine (KetaVet 100, MSD, Rome, Italy), 0.5 mg/kg diazepam (Hospira, Naples, Italy), 0.02 mg/kg atropine (ATI, Bologna, Italy). Anesthesia was induced by 1–5 mg/kg ketamine and 0.5 mg/kg diazepam. After intubation, 2–3% isoflurane (IsoFlo, Esteve, Rome, Italy) was administered by mask to maintain anesthesia.

5.2.3.1 Establishing an STZ-induced diabetic pig model

Three female Landrace pigs, weighting 25-30 kg were utilised for the study. To induce diabetes animals received a single dose of STZ 150 mg/kg in citrate buffer at pH 4.5 and administered intravenously while under general anaesthesia. An IV bolus of 5% glucose was administered 1 hour after STZ treatment to avoid hypoglycemia, and the animals were carefully monitored for 12 hours after recovery of anaesthesia. Blood glucose was recorded daily over the 21-day time course using a MultiCare® glucometer (Biochemical Systems International, Italia). The study plan is demonstrated in (Figure 5.3 (a)). The primary outcome measures: survival rate at 28 days. The secondary outcome measures: Weight and general physical examination, daily glucose monitoring and assessment of diabetic state. Results of this study demonstrated: 1) 100% Survival rate at 28 days of follow-up. 2) No loss of body weight (growth curve) (Figure 5.3 (b)). 3) Successful daily glucose monitoring (Figure 5.3 (c)). 4) Measurement of glucose metabolism at day 0 (before diabetes) and at day 28 (Intravenous glucose tolerance test, IVGTT) (Figure 5.3 (d)). 5) Confirmation of diabetic state and destruction of insulin producing cell via IHC staining (Figure 5.3 (e)). These *in vivo* trials have confirmed that STZ is a safe and effective to mimic the pathological conditions of T1D and permitted progression onto preclinical feasibility study and subsequent preclinical efficacy study of surgical implantation which I will discuss in detail throughout this chapter.

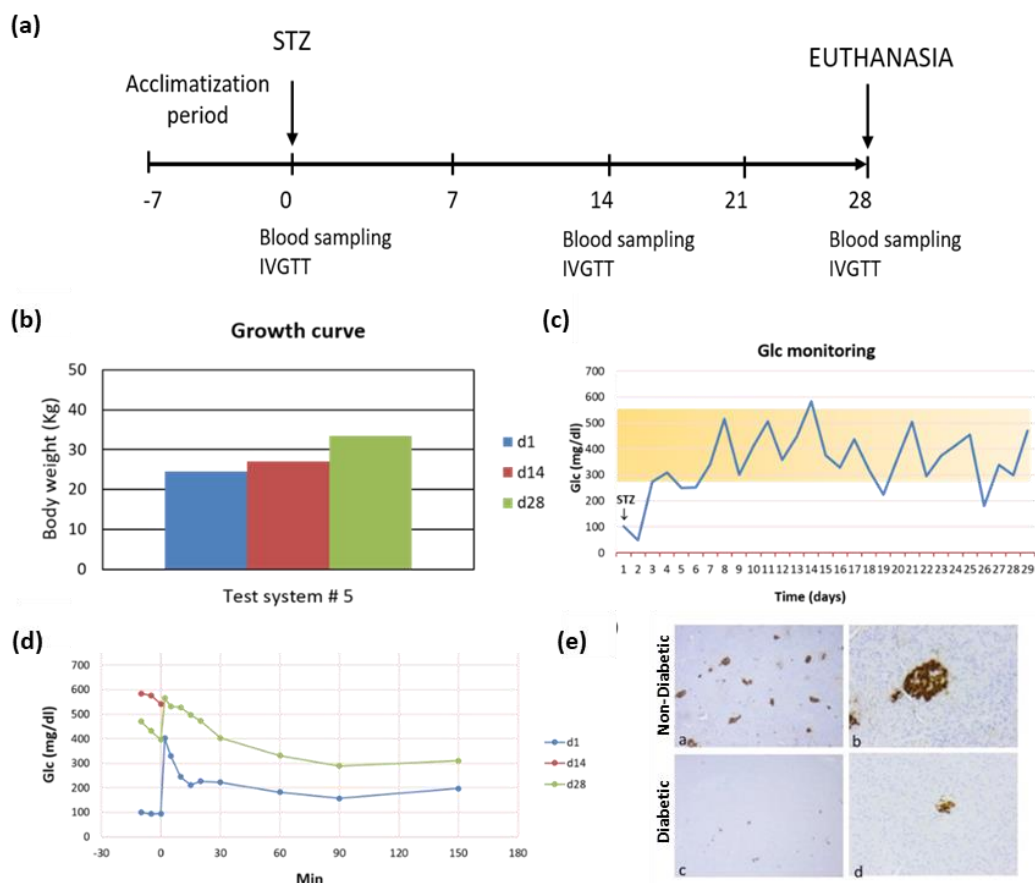


Figure 5.3: Establishing an STZ-induced diabetic pig model - Analysis of the first pig enrolled. **(a)** Study plan. **(b)** The body weight of the diabetic animal increased from day 1-28. **(c)** Blood glucose levels results for a period of 28 days post-STZ induction. These values confirmed diabetic state. **(d)** Intravenous tolerance test performed at day 1 (before STZ-induced diabetes) and at day 28. **(e)** Immunohistochemistry with *anti*-insulin antibody on sections of the pancreas from non-diabetic (ND) control and STZ-treated diabetic pigs.

5.2.3.2 Preclinical feasibility study of surgical implantation

Two female Landrace pigs, weighting 25-30 kg were utilised for the study. The TAP submuscular implant site (*Figure 5.4 (b-c)*) was used for preclinical efficacy testing of the multiscale porous devices. The purpose of this study was to establish an aseptic and surgical technique of implantation while paying particular attention to animal well-being, and physiological status during all phases of protocol to enhance the outcome of future surgeries. To implant the devices, a vertical incision was made just off midline and the dissection was carried down to the transversus abdominis fascia. A second vertical incision was made 15 cm lateral to the initial decision, and the dissection carried down to the transversus abdominis muscle. The space between the two incisions was bluntly dissected, and a rolled device was brought onto the surgical field with preloaded filling catheter placed. A PDMS loop was tied through the distal suture ring, and the device was passed through from the lateral to the medial incision, and then unfolded and positioned. Sutures were used to secure the device to underlying tissue through 4 suture rings. The fill line was then tunnelled through a 3rd, smaller lateral incision. A 1% Hyaluronic Acid gel containing an iodixanol emulsion was injected into the device and positioning of the device was visualised with fluoroscopy (*Figure 5.4 (d-g)*). Animals were euthanised (IV injection of Tanax, 0.3 mL/kg; MSD Animal Health Srl-Italy), and a post-mortem dissection was carried out to confirm positioning of the device.

5.2.3.3 Preclinical efficacy study

Four female Landrace pigs, weighting 25-30 kg were enrolled in the study (*Figure 5.4 (a)*). To induce diabetes animals received a single dose of Streptozotocin (STZ) 150 mg/kg in citrate buffer at pH 4.5 and administered intravenously while under general anaesthesia. An intravenous bolus of 5% glucose was administered 1 hour after STZ treatment to avoid hypoglycemia, and the animals were carefully monitored for 12 hours after recovery of anaesthesia. Blood glucose was recorded daily over the 21-day time course using a MultiCare[®] glucometer (Biochemical Systems International, Italia). On day 7 after induction of diabetes, animals underwent general anaesthesia and received surgical implantation of bilateral multiscale porous devices in the submuscular space of the anterior wall. On day 21, the animals were again placed under general anaesthesia and selected to either receive an injection of insulin in the subcutaneous space or infusion through the device. For animals receiving an infusion of insulin through the device, the inlet tubing was exposed and 10 mL of 1 U/kg regular insulin (Humilin, Eli Lilly and Co.) was injected. Blood glucose was monitored at 2 hours following insulin delivery.

Methods used to compare subcutaneous administration versus device delivery of insulin was adapted from Abramson *et al* [406]. Animals were the euthanised by IV administration of Tanax (0.3 mL/kg; MSD Animal Health Srl-Italy).

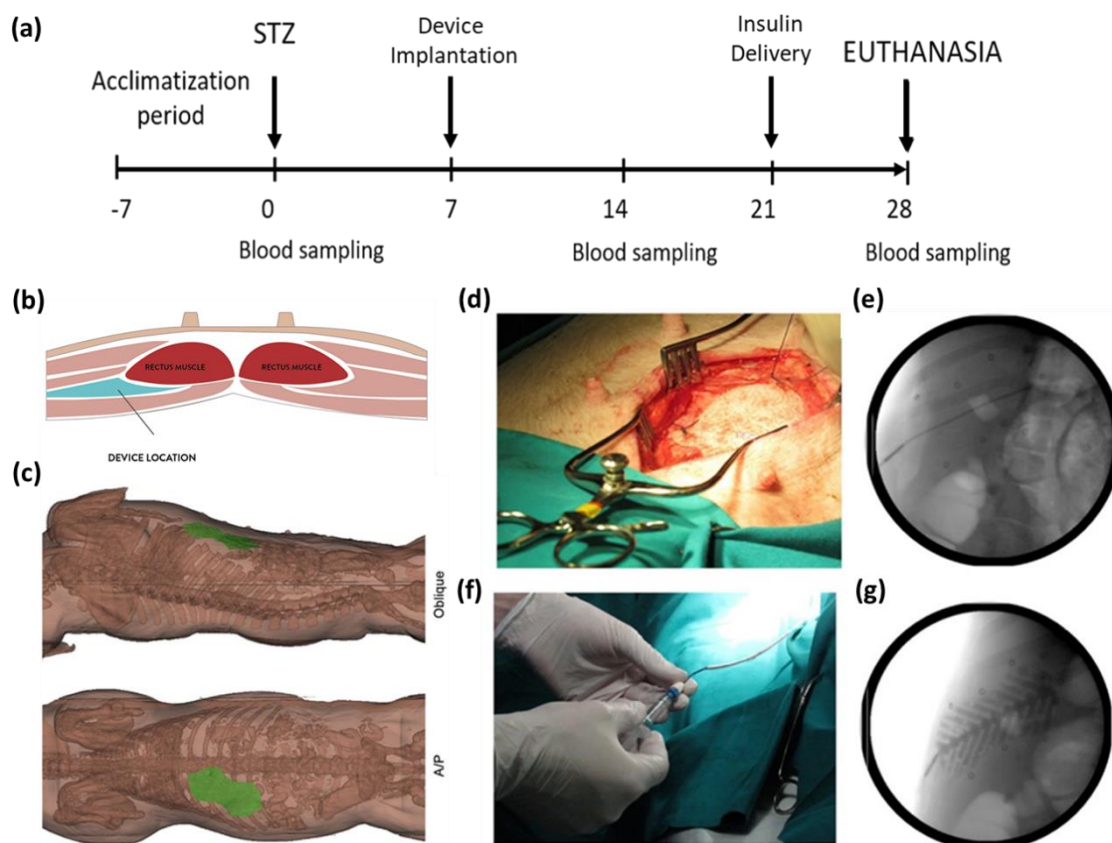


Figure 5.4: Surgical placement of unscaled multiscale porous devices. **(a)** 28-day study plan for Preclinical efficacy study of surgical implantation. **(b)** Schematic of submuscular implant site in the anterior abdominal wall of pig. **(c)** Schematic showing positioning of implant after surgery. **(d)** Surgical placement of implant in submuscular plane. **(e)** X-ray fluoroscopy of device after implantation showing radiopaque markers to confirm positioning. **(f)** Infusion of inner channel of implant with filling catheter. **(g)** X-ray fluoroscopy of implant uniformly filling with 12ml of radiopaque hyaluronic acid (HA) emulsion into the cargo channels created by the internal support structure of the device.

5.2.4 Tissue processing and histology

Following euthanasia, the devices were removed en bloc with surrounding muscle tissue and fixed in 4% PFA for 48 hrs. Core biopsy samples were taken systematically at 5 locations across the device (*Figure 5.5 (a)*) using an 8 mm punch biopsy and placed in a 2% agarose mold to maintain structure (*Figure 5.5 (b)*). 4 of these cores were for histological analysis while the 5th was processed for SEM imaging. Cores for histological analysis were processed and embedded in paraffin wax blocks. Sections of 5-10 μm were cut and stained with Masson's trichrome for fibrous capsule assessment (*Figure 5.5 (c)*).

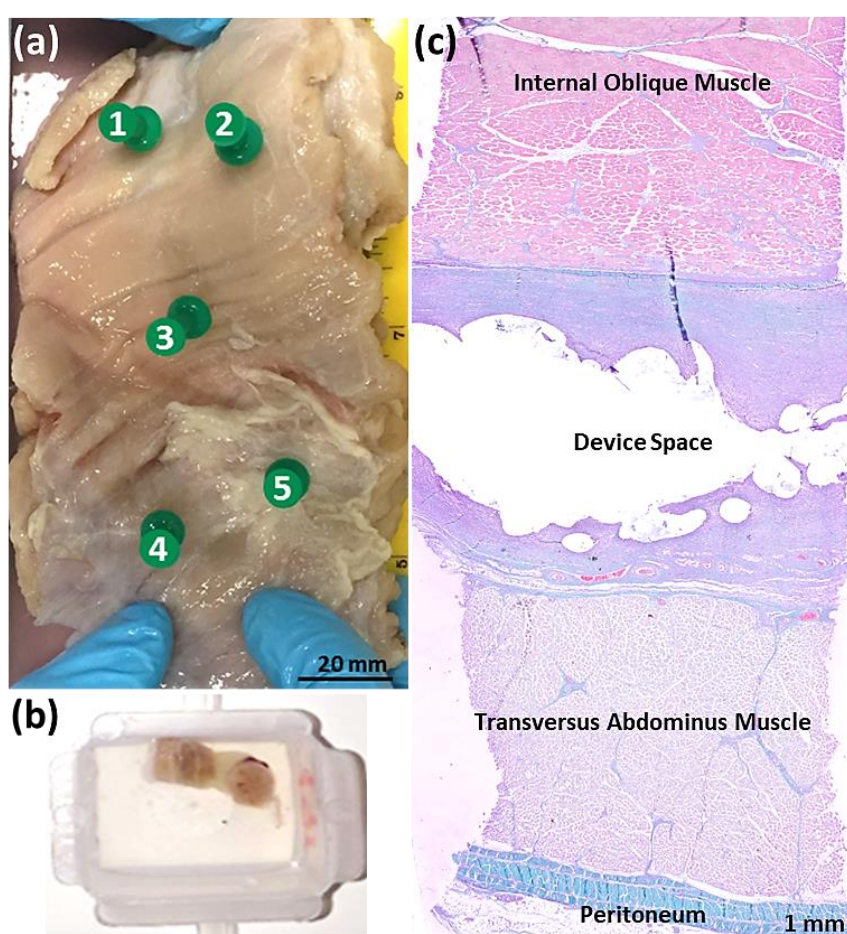


Figure 5.5: Processing of tissue samples en bloc. **(a)** Device and surrounding tissue marked with random core biopsy locations marked 1-5. **(b)** Core biopsy placed in 2% agar to maintain stability of tissue structure. **(c)** Masson's trichrome stain of core biopsy taken through implant and surrounding tissue.

5.2.5 Diffusion tensor imaging and analysis

These procedures were carried out by Brooke Tornifoglio, Alan Stone and the Lally Lab, TCD, Dublin. I contributed to the design and planning, specimen preparation, shipping, data interpretation and analysis.

Diffusion tensor imaging (DTI), a magnetic resonance imaging technique, involves deriving and displaying quantitative parameters that can be correlated to histological or physiological stains as it characterises intrinsic features of tissue microstructure and microdynamics [407,408]. This imaging technique characterises water molecule's diffusion, which can in turn be modelled to visualise macrostructures and fibre tract organisation. In the absence of any obstructing boundaries, the diffusion of water molecules is random and unspecific to any direction. This property is based on the theory of Brownian translational motion and is referred to as diffusion isotropy [409,410]. However, *in vivo* water diffusion can become anisotropic due to interference of complex microstructural barriers in tissue, such as cell membranes or fibres. Anisotropy refers to differing values in different directions [411]. In other words, the water molecules can have a preferential direction of diffusion based on the underlying microstructure of a tissue. The use of DTI can provide quantitative data about the scale and directionality of water diffusion along a vector in a 3D space [408,412–416], which ultimately gives non-invasive insight into tissue architecture.

The diffusion tensor itself is composed of eigenvalues and eigenvectors, which characterise the diffusion within a voxel. From this tensor, multiple indices can be calculated. Specifically, the eigenvalues can be used to calculate the fractional anisotropy (FA). This is one of the most frequently used indices as it quantifies of diffusion anisotropy within a voxel. FA is a scalar value between zero and one and highlights the degree of anisotropic diffusion, which gives insight into the alignment and structural integrity of cellular structures and fibre tracts (e.g. collagen) – as their boundaries and interactions with the water molecules are driving hindered and restricted diffusion [410,412,415–418]. While FA highlights the degree of anisotropy, the mean diffusivity (MD) is the average amount of diffusion occurring in all directions. This index is useful as it takes the diffusion occurring in all directions into account and yields insight into how much diffusion is occurring in a volume. For example, pathological conditions which cause increased spacing between boundaries often cause a decrease in anisotropy, as a result of either increased perpendicular diffusivity and/or reduced parallel diffusivity [419]. Thus, DTI yields insight into the microstructure in the fibrous capsule by measuring the interaction of diffusing water molecules and the structural boundaries like cells and fibres.

5.2.5.1 Image acquisition

The fixed pancreatic device samples were stored at 4 °C in 70% ethanol until MR imaging. All samples were placed in a 3D printed holder custom made to fit the MRI coil. For imaging, the holder containing the sample was filled with fresh PBS at room temperature. A 7T Bruker BioSpec 70/30 Ultra Shield Refrigerated system equipped with Paravision 6 and a volume coil were used for all imaging sequences. T1- and T2-weighted scans, were used to visualise the device and surrounding tissue. T1-weighted parameters were as follows: TE/TR: 7/1452 ms, 20 averages, slice thickness: 0.5 mm, number of slices: 100, image size: 256 x 256, field of view: 70 x 70 mm and acquisition time: 1 hour and 23 minutes. T2-weighted parameters were as follows: TE/TR: 19.55/9137.6 ms, 20 averages, slice thickness: 0.5 mm, number of slices: 30, echo spacing: 6.518 ms, RARE factor: 8, image size: 256 x 256, field of view: 70 x 70 mm and acquisition time: 1 hour and 13 minutes. A 2D diffusion tensor imaging (DTI) sequence was used for all four samples. The first rope coil device was imaged with the following parameters: TE/TR: 18.182/1011 ms, 5 averages, slice thickness: 0.5 mm, slice gap: 0.5 mm, number of slices: 47, image size: 128 x 128, field of view: 64 x 64 mm, b-value: 800 s/mm², 32 diffusion directions, gradient duration: 3.8 ms and gradient separation: 8.802 ms. Acquisition time was 5 hours and 55 minutes. The second rope coil device and two smooth devices were imaged with a refined 2D DTI sequence with the following parameters: TE/TR: 18.182/4000 ms, 4 averages, slice thickness: 0.5 mm, slice gap: 0.5 mm, number of slices: 20, image size: 140 x 140, field of view: 70 x 70 mm and the same diffusion parameters. Acquisition time was 20 hours and 32 minutes.

5.2.5.2 Image analysis

Prior to calculation of the diffusion tensor all diffusion images were de-noised and correction for Gibbs ringing applied [420,421]. Using the corrected diffusion imaging data, the diffusion tensor was estimated using ExploreDTI [422]. Fractional anisotropy (FA) and mean diffusivity (MD) [mm²/s] were calculated from the eigenvalues of the diffusion tensor. Regions of interest (the fibrous cap and native tissue) were defined based on the T1- and T2-weighted scans. The FA and MD values of the fibrous caps in each sample were normalised by the native tissue within each respective sample. Tractography was performed in order to visualise the microstructural arrangement of the tissue. The following parameters were used for both devices: seed point resolution: 0.5 x 0.5 x 0.5 mm, seed point FA threshold: 0.15, FA tracking threshold: 0.15, fiber length: 1–50 mm, angular threshold: 15° and a step size of 0.5.

5.2.6 MicroCT

Before implantation, devices were imaged in a microCT 100 microCT scanner (Scanco Medical, Switzerland) at 45 kVp and 200 μ A with a 0.1mm Aluminium filter and a voxel size of 102.6 μ m. DICOM images of the resulting scan were segmented in 3D slicer and 3D model of the device was generated (*Figure 5.2 (c)*). The targeted submuscular implant site was identified on axial views of a previously obtained non contrast abdominal CT scan of a euthanised Landrace swine (Explora Biotech Srl) CT scan using 3D Slicer and a full-size 3D model of the device was superimposed over the CT images in the submuscular plane (*Figure 5.4 (c)*). This imaging enabled us to provide an input into size requirements of the porcine device, described in *5.2.1 Device fabrication*.

For imaging of the explanted device and surrounding tissue, a gradient ethanol concentration fixation was modified [423]. After fixation, the core biopsy samples were taken and the metal markers in the device were dissected and removed from the sample. The tissue was dehydrated and stained in 2% w/v iodine solution in absolute ethanol for 5 days, washed in 100% ethanol to remove excess iodine, then imaged in absolute ethanol. MicroCT images were captured at 90 kVp and 116 μ A with a 0.1mm Copper filter and voxel size of 88 and 34.13 μ m. Images and videos were generated using ImageJ software.

5.2.7 Pull-off testing of integrated multiscale porosity devices and smooth surfaced control

A Zwick mechanical testing machine (Z050, Zwick/Roell) with a 100N load cell was used for pull-off testing. Explanted tissue with integrated ropecoil devices were cut into 1.5 x 1 x 0.5 cm samples. 0.5 cm of the ropecoil device was carefully decoupled from the underlying tissue on both ends of the length of the sample. The 0.32 cm diameter silicone fill line was used as a control whereby the tissue area in contact with the tubing is equal to the ropecoil (1 x 0.5 cm). The samples were mounted in the tensile tester using pneumatic clamps at 6 PSI run at a shear rate of 20 mm/min [424] and maximum tangential adhesion force was recorded (n=3/group).

5.2.8 Scanning Electron Microscopy (SEM)

Each core was bisected longitudinally to create a cross-section of the device and surrounding tissue. Samples were post-fixed overnight in 2.5% glutaraldehyde in 0.2 M PBS (pH 7.4). Samples were washed twice in 0.2 M PBS for 10 minutes before dehydration through a series of graded alcohols (30%, 50%, 70%, 90% and 100%). Following dehydration, samples were transferred to the EMITECH K850 critical point dryer.

This removed all the liquid in a precise and controlled way, so fragile tissue is not damaged or distorted in the process. Samples were then mounted onto aluminium stubs using carbon adhesive tabs. An Emscope SC500 was used to lightly sputter coat the samples. Specimens were imaged using a Hitachi S2600N Scanning Electron Microscope using a secondary electron detector (Vacuum 15 kV, electron Beam 50). SEM images were pseudo-coloured using MountainsMap® SEM Color 7.3.7984.

5.2.9 Fixation, embedding and staining

The 4 core biopsies were orientated and embedded in paraffin wax blocks. Sections of 5 µm were cut and stained with, Masson's trichrome and αSMA for fibrous capsule analysis. Additional sections were stained with CD31 (ab233364, Abcam) (1:50), αSMA (ab7817, Abcam) (1:100) and CD68 (BA4D5, Biorad) (1:250) antibodies for analysis of myofibroblasts, angiogenesis and macrophage response. The staining protocols are provided in detail in *Chapter 2*.

5.2.10 Statistical analysis

Statistical analysis was performed using GraphPad Prism (8.1.0) was used. Normality of distribution was assessed by the Shapiro-Wilk test. Subsequent parametric and/or non-parametric tests were performed. For parametric data, an unpaired t-test was performed for comparing between two groups and a one-way or two-way analysis of variance (ANOVA) with post-hoc Tukey's multiple comparison for comparing between groups. For non-parametric data, a Mann-Whitney U was performed for comparing between two groups and a Kruskal-Wallis test for comparing more than two groups. Statistical significance was accepted when *P<0.05. A minimum of two blinded counters were used for analysis.

5.3 Results

5.3.1 Determining the most favourable AAW site for implantation of a multiscale porosity macroencapsulation device

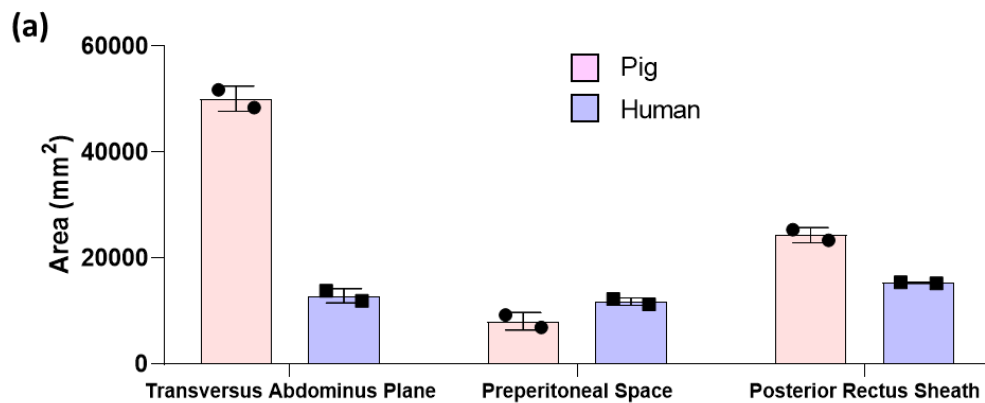
5.3.1.1 *Determining the suitability of potential implant sites in the AAW*

The AAW potentially meets or exceeds each of the design criteria highlighted in Table 5.1. They can provide a nutritive environment with adequate structural boundaries, and contain multiple compartments that are routinely accessed during common clinical procedures (*Figure 5.1 (a)*). The superficial location of the AAW allows for longitudinal monitoring with non-invasive imaging, and access for biopsy if needed. Implantation and retrieval can be performed without violating the peritoneal space, thereby avoiding the numerous complications associated with intrabdominal procedures. The AAW has a robust blood supply, with contributions from the internal mammary artery (superior epigastric and musculophrenic branches), the external iliac artery (inferior epigastric and deep circumflex branches) and common femoral artery (superficial epigastric and superficial circumflex iliac branches). Venous drainage is typically systemic, but in pathologic states (e.g. portal hypertension) venous collaterals develop connecting the portal and systemic systems. The presence of a living implant in the abdominal wall could feasibly develop portal drainage like the native pancreas, thereby providing more physiologic glucose control compared to subcutaneous implants.

5.3.1.2 *Determining the dimensions of potential implant sites in the AAW*

To determine the area of the candidate AAW implantation sites, modification of the existing Morphomics Analytics Group algorithms written in MATLAB were utilised to delineate “seams”, create a point cloud of the space, thus enabling the software to accurately map the area of interest and measure. Results indicate that the area of the three potential implant sites were very similar in humans with comparable areas between pig and human in the pre-peritoneal and posterior rectus sheath sites (*Figure 5.6 (a)*). The TAP, defined as the region between the medial (semilunar line) and lateral (lumbosacral fascia) connecting and extending superiorly to the costal margin, and inferiorly to the inguinal ligament, showed the most considerable difference between pig and human. While the TAP space may be novel as an implantation site, TAP blocks are regional techniques for analgesia of the anterolateral abdominal wall guided by ultrasound. This technique has been used for over two decades for a variety of abdominal surgeries [425–432]. As the most frequently accessed site, the requirement for additional surgical training for implantation procedures would be reduced.

Therefore, the TAP site was chosen as the most suitable site due to its simplified translatability in terms of point of care for implantation by interventional radiology. Area and projected volume measurement data (*Figure 5.6 (b)*) would be crucial in the development of the upscaled device to allow easy size translatability from large animal, to future clinical studies. As the area of the TAP space was substantially larger in pig models, device fixation was important and thus suture hole incorporation into the device design would be necessary.



(b)

Site	Volume (mm ³)
Transversus Abdominus Plane	360,000
Preperitoneal Space	240,000
Posterior Rectus Sheath	427,000

Figure 5.6: Determining the dimensions of potential implant sites in the AAW. **(a)** Area measurements of potential implantation sites in pig and human subjects. **(b)** Volumes of potential implantation sites in humans.

5.3.2 Analysing the diffusion capabilities of the multiscale porosity device

In order to determine whether the bioavailability of insulin through the multiscale porous devices is equivalent to conventional insulin delivery, animals received 1U/kg of insulin suspended in 10 mL of PBS solution through either subcutaneous injection or infused into the device. The percent blood glucose changes after 2 hours in animals that received insulin infusion through the multiscale porosity device was comparable to that seen with subcutaneous delivery (*Figure 5.7 (a)*) indicating that the porosity of the surface texturing could be used to facilitate physiological diffusion necessary for efficacious islet macroencapsulation. Comparing these results to Abramson *et al* [406], who similarly tested the diffusional capacity of their oral biologic delivery system, using insulin as a model drug, the multiscale porous device demonstrated comparable if not equivalent results, when demonstrating the devices ability to deliver insulin compared to gold standard subcutaneous administration (*Figure 5.7 (b)*).

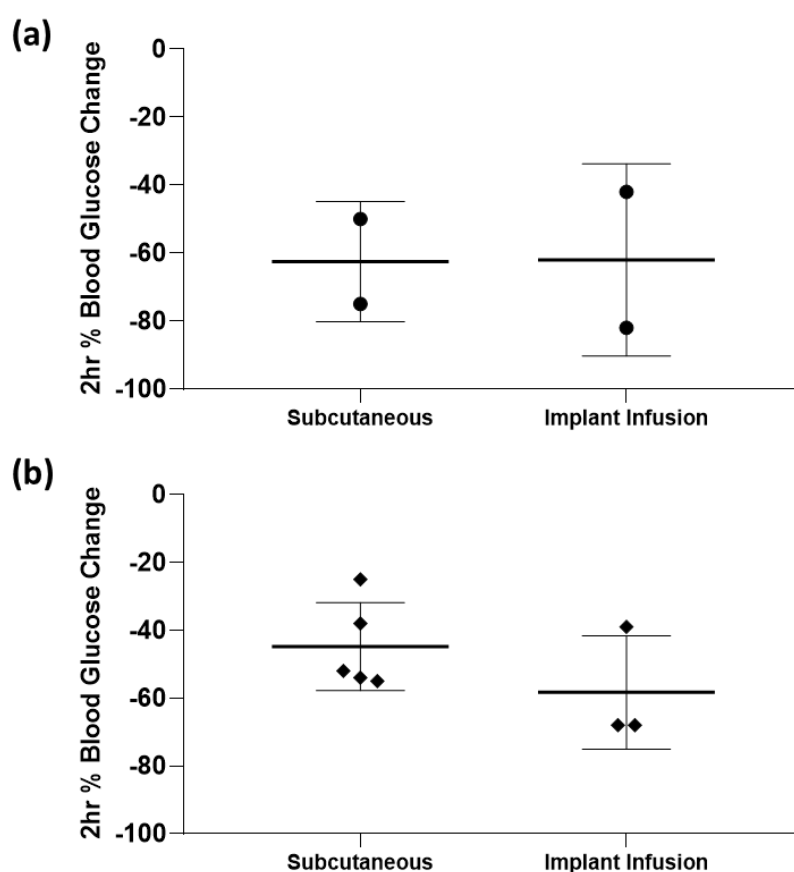


Figure 5.7: Comparing the diffusion capabilities of multiscale porosity devices to an oral biologic delivery system. Response of diabetic animals to insulin delivered through subcutaneous injection vs **(a)** multiscale porosity devices **(b)** oral biologic delivery system.

5.3.3 Diffusion tensor imaging of the fibrous capsule surrounding the multiscale porosity and smooth devices

DTI was used in this study to analyse the structural properties of the collagenous fibrous capsule surrounding devices. DTI permits a 3D measurement of water diffusion within tissue and is used to gain information quantify both the integrity (quantification of diffusivity and anisotropy) and orientation fibres (tractography) [408,433].

The analysis of tractography pathways, depicted via a standard red-green-blue mapping (Anterior-Posterior, green; Right-Left, red; Inferior-Superior, blue) demonstrated a highly unorganised, multidirectional composition fibrous capsule surrounding multiscale porosity devices. In contrast, the tractography of the fibrous capsule surrounding smooth devices revealed a more uniform tractography (*Figure 5.8 (a)*).

DTI was used to measure the FA, a scalar value between zero and one and highlights the degree of alignment of cellular structures within fibre tracts (e.g. collagen), as well as their structural integrity [410,412,415,416,418]. FA was mapped from approximately 100 slices per device. This analysis was performed not only on the surrounding fibrous capsule, but also on an area of native connective tissue uninhibited by the implantation of a device to act as a control measurement in each animal. Comparative analysis between control tissue and the fibrous capsules demonstrated significant differences between the tissue controls and the corresponding surrounding fibrous capsules. The largest of these differences was observed between the fibrous capsule surrounding smooth devices compared to its corresponding control and also compared the fibrous capsule surrounding the multiscale porosity devices (**** $P < 0.0001$) (*Figure 5.8 (b)*). These control tissues were then used to normalise the FA results of the surrounding fibrous capsules, and demonstrated a significantly increased FA of fibrous tissue surrounding the smooth surfaced devices compared to multiscale porosity devices (**** $P < 0.0001$) (*Figure 5.8 (d)*). These results suggested the fibrous capsules surrounding smooth devices, differed structurally due to increased homogeneity, to both its corresponding native tissue control but also the fibrous capsule surrounding multiscale porosity devices.

DTI was used to measure MD which can aid in the understanding of structural integrity. MD analysis describes the capability of multidirectional water diffusion within tissue. Similar to FA, MD of the fibrous capsules and corresponding areas of native connective tissue (acting as a control), was measured from approximately 100 slices per device.

Comparative analysis between control tissue and the fibrous capsules demonstrated significant differences in MD between all the tissue controls and the corresponding surrounding fibrous capsules (**** $P < 0.0001$) (*Figure 5.8 (c)*). Once fibrous capsules were normalized with corresponding controls, a significantly increased MD was observed in the fibrous capsules surrounding multiscale porosity devices (**** $P < 0.0001$) (*Figure 5.8 (e)*). With increased diffusivity comes increased aptitude for the multidirectional diffusion of water molecules [419]. These results demonstrate that multiscale porous macroencapsulation devices can promote a more heterogenous fibrous capsule development, superior tissue diffusion properties when compared to smooth devices.

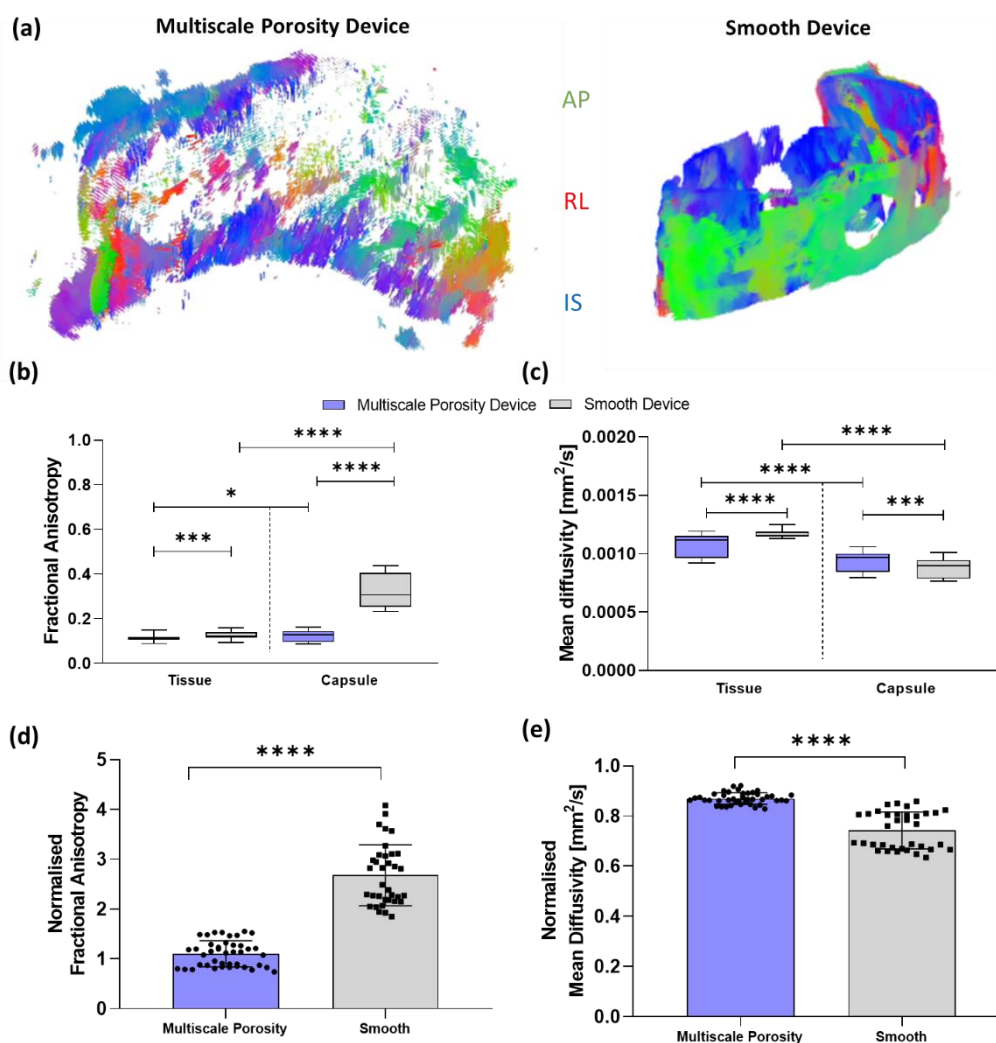


Figure 5.8: DTI analysis of the fibrous capsule surrounding multiscale porosity and smooth macroencapsulation devices. **(a)** Diffusion tensor imaging (DTI) tractography. The color-coding of tractography pathways was based on a standard red-green-blue (Anterior-Posterior, green; Right-Left, red; Inferior-Superior, blue). **(b)** Comparing the fractional anisotropy of a random segment of native tissue with the fractional anisotropy of the fibrous capsules surrounding both multiscale porous and smooth devices. **(c)** Comparing the mean diffusivity of a random segment of native connective tissue with the mean diffusivity of the fibrous capsules surrounding both multiscale porous and smooth devices. **(d)** Fractional anisotropy of the fibrous capsule for each device design normalised accordingly to the fractional anisotropy of their respective native tissues. **(e)** Mean diffusivity of the fibrous capsule for each device design normalised to the mean diffusivity of their respective native tissues. $n=1$ per group, data are represented as means \pm SD. $*$ = $P<0.05$, $***$ = $P<0.001$, $****$ = $P<0.0001$.

5.3.4 Pull-off testing of integrated multiscale porosity devices and smooth surfaced control

In order to quantify the maximum tangential adhesion force or integration of the device into the surrounding tissue, pull-off testing was performed. As shown in *Figure 5.9*, there was a substantially higher maximum force in the multiscale porous device compared to smooth silicone controls. These data indicate that the external texture provides excellent tissue integration when implanted in the submuscular plane of a pig.

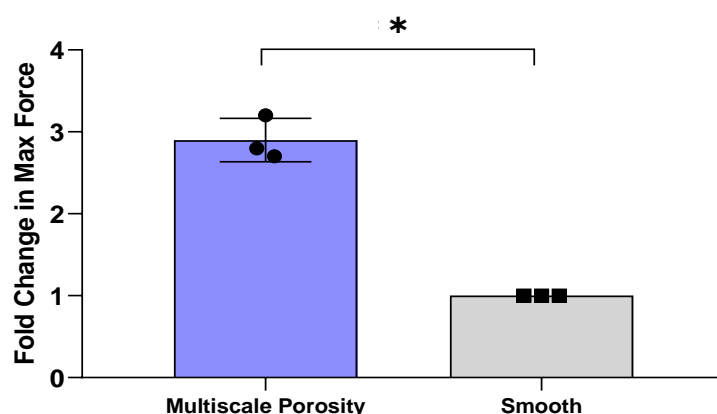


Figure 5.9: Pull-off testing of tissue surrounding multiscale porous devices and smooth control after 2 weeks of submuscular implantation in pig. Data are represented as means \pm SD. *P=0.0103.

5.3.5 MicroCT and SEM imaging of multiscale porosity and smooth devices with associated surrounding tissue

5.3.5.1 MicroCT

MicroCT imaging was performed in order to examine the relationship between the devices and the surrounding tissue. The imprint of the multiscale porous devices surface features in the immediate surrounding tissue were strikingly apparent in the cross-sectional image, indicating an impressive level of tissue integration. MicroCT cross-sectional images of the smooth device showed little tissue attachment or integration with the surrounding tissue. The device appears to be free of the surrounding tissue with a folded configuration (*Figure 5.10*).

5.3.5.2 Scanning Electron Microscopy (SEM)

SEM was performed in order to further examine the development and integration between the devices and the surrounding tissue. As demonstrated in the previous chapters of this thesis, the inclusion of multiple layers of rope-coil and micro-porosity results in excellent tissue integration (*Figure 5.10*). This was further confirmed within this porcine study, as the surface texturing induced a consistently disorganised fibrous capsule to envelope around the rope-coil structures at the device surface resulting in improved integration. In contrast, the fibrous capsule surrounding the smooth device appeared distinctively layered. Due to the absence of any distinct surface features, the formation of the fibrous capsule was unimpeded, which possibly contributed to its concentric layered organisation.

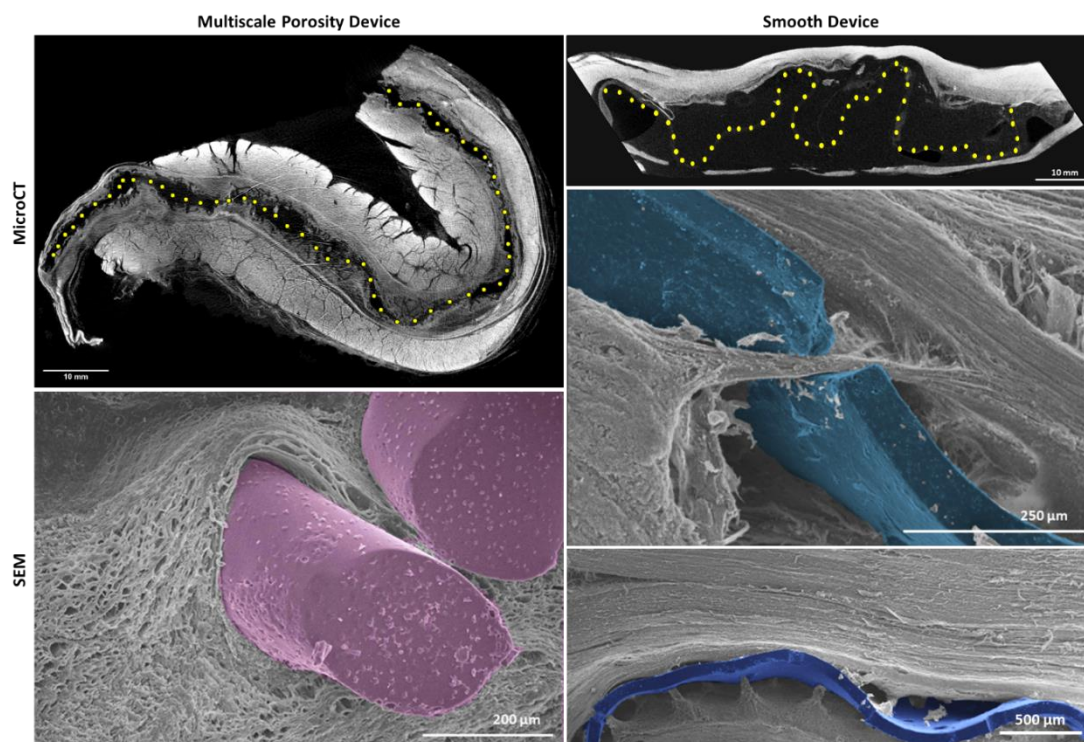


Figure 5.10: MicroCT and SEM imaging of multiscale porous and smooth devices with associated surrounding tissue. MicroCT cross sections of multiscale porous and smooth devices, demonstrating their relationship with the surrounding tissue. Scale bars = 10 μm . High magnification SEM images of rope-coil surface feature integrated into the surrounding tissue and lack of integration surrounding the smooth device. Scale bars = 200 and 250 μm

5.3.6 Analysis of the fibrous capsule surrounding the multiscale porosity and smooth devices

5.3.6.1 Fibrous capsule thickness

To assess the degree of fibrous capsule development surrounding the multiscale porous and smooth macroencapsulation devices, a thickness assessment was performed of the newly formed hyper-dense collagen made visible by Masson's trichrome stain. Representative images of core biopsies taken through the multiscale porous and smooth devices and surrounding of the fibrous capsules with associated magnified images are shown in *Figure 5.11 (a-b)*. The fibrous capsule surrounding the multiscale porous device possessed distinct circular imprints caused by the textured rope-coil structures of the device. Fibrous capsule thicknesses were first determined per animal (*Figure 5.11 (c)*) before being plotted as the average capsule thickness per device design (*Figure 5.11 (d)*). The fibrous capsule thicknesses surrounding the multiscale porous devices averaged $336 \pm 74 \mu\text{m}$ with an average thickness of $388 \pm 152 \mu\text{m}$ surrounding smooth devices. This finding suggests that fibrous capsule thickness is not increased by the addition of an external macrotecture.

5.3.6.2 Fibrous capsule area

To account for the imprints left in the fibrous capsule caused by the external rope-coil macrotecture on the multiscale porous devices, the total area of tissue between the device-interface and the internal oblique muscle (*Figure 5.5 (c)*) within an 8 mm core biopsy was calculated. The area of the fibrous capsules were first determined per animal (*Figure 5.11 (e)*) before being plotted as the average capsule area per device design (*Figure 5.11 (f)*). The fibrous capsule area surrounding the multiscale porous devices averaged $6\text{-}8.7 \pm 1 \text{ mm}^2$ with a similar average area of $6.4\text{-}7.2 \pm 0.6 \text{ mm}^2$ surrounding smooth devices. The area between the device interfaces and the internal oblique muscle within an 8 mm core biopsy remains unchanged across all device configurations. This finding suggests that the overall amount of capsule is not increased with the addition of an external macrotecture. The capsule merely appears more tortuous in its development due to its increased affinity for tissue integration around the rope-coils.

5.3.6.3 Myofibroblast abundance

To assess the degree of myofibroblast abundance surrounding the multiscale porous and smooth macroencapsulation devices, the volume fraction of immunofluorescent labelled αSMA^+ cells within $100 \mu\text{m}$ of the device interfaces (*Figure 5.12 (a)*) was estimated using an unbiased point counting technique.

The volume fractions of α SMA+ cells were first determined per animal (*Figure 5.12 (b)*) before being plotted as the average capsule area per device design (*Figure 5.12 (c)*). The volume fraction surrounding the multiscale porous devices averaged $0.3-0.42 \pm 0.05$ with a similar average area of $0.3-0.34 \pm 0.03$ surrounding smooth devices. These findings correlated with comparable capsule production around each device which were calculated by thickness and area analysis seen in *Figure 5.11 (e-f)*.

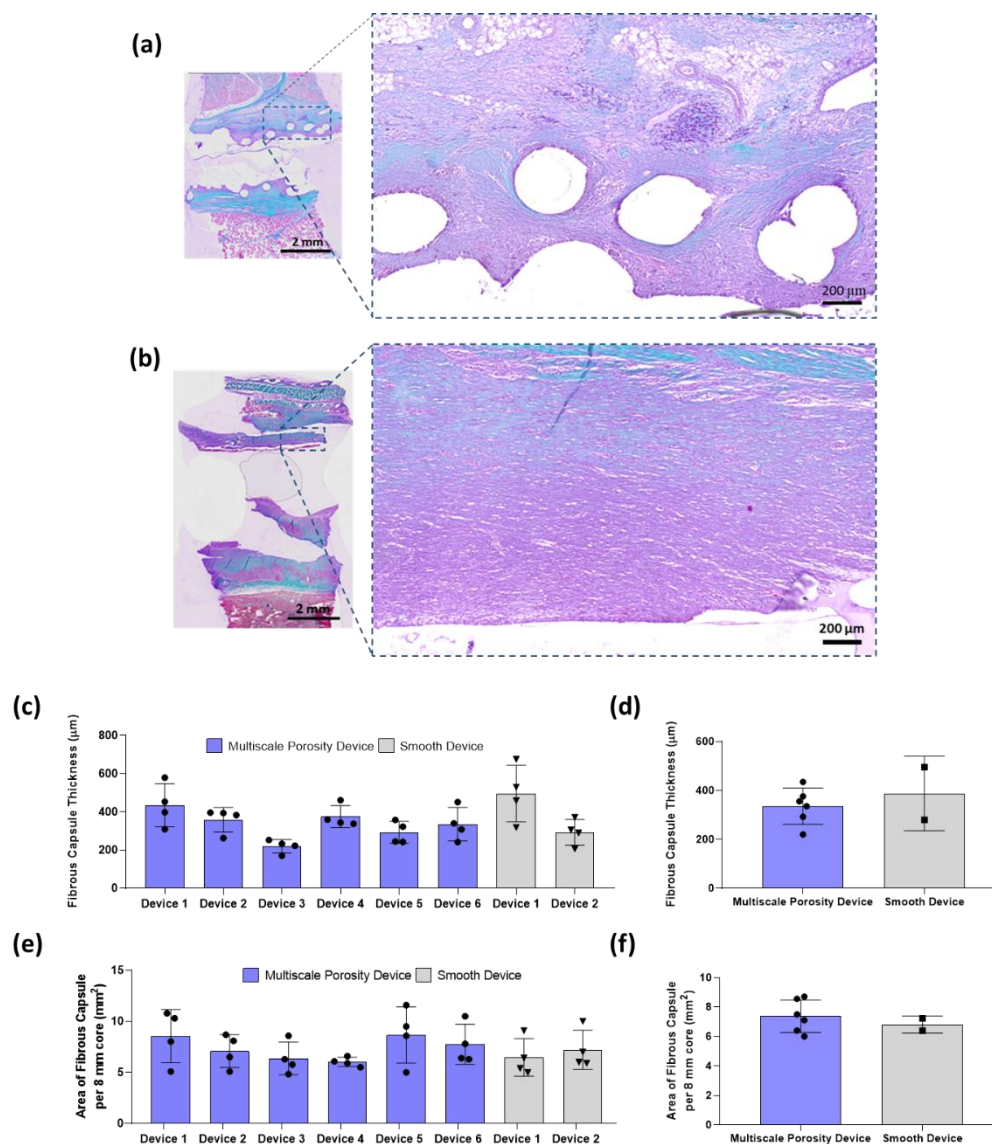


Figure 5.11: Analysis of fibrous capsule formation around multiscale porous and smooth macroencapsulation devices. Masson's trichrome images of core biopsy taken through implant and surrounding of the fibrous capsule (Scale bar = 2 mm) with magnified image of the immediate tissue-device interface (Scale bar = 200 μm) surrounding (a) multiscale porous device and (b) smooth device. (c) Fibrous capsule thickness for each implanted device. Each data point represents the average fibrous capsule thickness for each core biopsy. (d) Average fibrous capsule thicknesses for each device design. Each data point represents the average fibrous capsule thickness surrounding each device. (e) Area of fibrous capsule extending from the tissue-device interface to the overlying internal oblique muscle for each implanted device within the 8 mm biopsy cores. Each data point represents the average fibrous capsule area for each core biopsy. (f) Average area of the fibrous capsule extending from the tissue-device interface to the overlying internal oblique muscle for each device design. Each data point represents the average fibrous capsule area per device design. $n = 2-6$ per group, data are represented as means \pm SD.

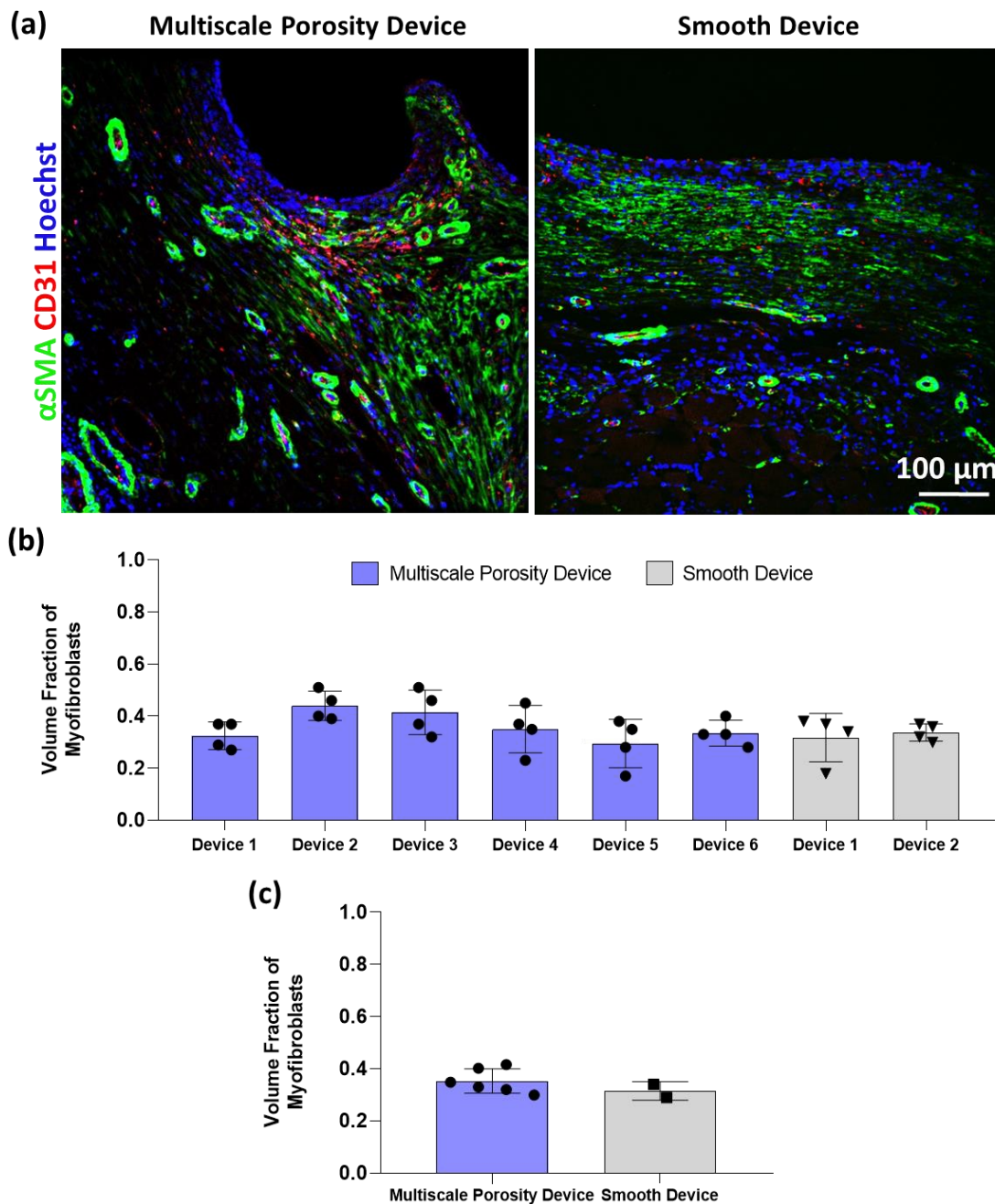


Figure 5.12: Analysis of myofibroblast abundance around multiscale porous and smooth macroencapsulation devices. **(a)** Representative immunofluorescent images for analysis of myofibroblast abundance (Hoechst, blue; α SMA, green; CD31, red). Scale bar = 100 μ m. **(b)** Volume fraction of α SMA+ cells (myofibroblasts) within the fibrous capsule for each implanted device. Each data point represents the average volume fraction for each core biopsy. **(c)** Volume fraction of α SMA+ cells for each device design. Each data point represents the average volume fraction surrounding each device. $n = 2-6$ per group, data are represented as means \pm SD.

5.3.7 Analysis of the angiogenesis surrounding multiscale porosity and smooth devices

5.3.7.1 Blood vessel abundance

To investigate the degree of neovascularisation development surrounding the macroencapsulation devices, tissue sections were stained for CD31, an endothelial cell marker, and stereological analysis was performed to quantify blood vessel density surrounding each device. Representative images of the CD31 stained fibrous capsule surrounding multiscale porous and smooth devices are shown in *Figure 5.13 (a)*. The number of blood vessels per unit area and radial diffusion distances were first determined per animal (*Figure 5.13 (b, d)*) before being plotted as the average per device design. The number of blood vessels per unit area surrounding the multiscale porous devices averaged $140\text{-}282 \pm 50$ vessels/mm² with a similar average of $221\text{-}233 \pm 8$ vessels/mm² surrounding smooth devices (*Figure 5.13 (c)*). The radial diffusion distance surrounding the multiscale porous devices averaged $26\text{-}35 \pm 3$ μm , slightly larger than an average of $28\text{-}29 \pm 6$ μm surrounding smooth devices (*Figure 5.13 (e)*).

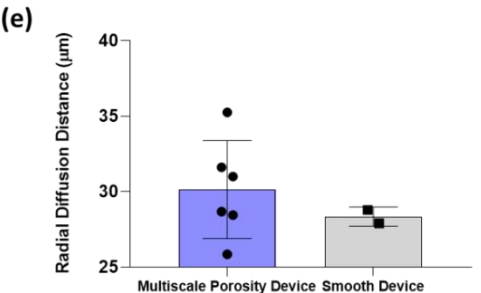
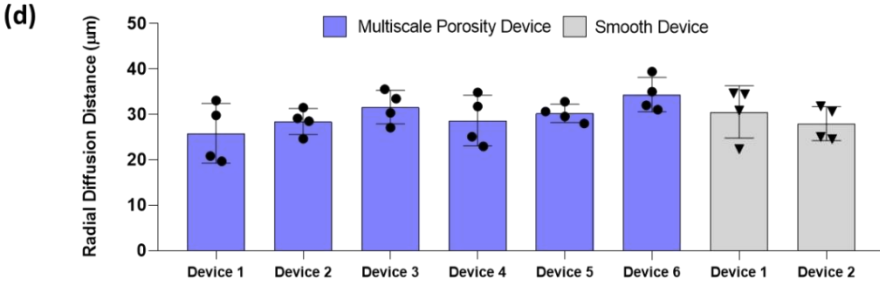
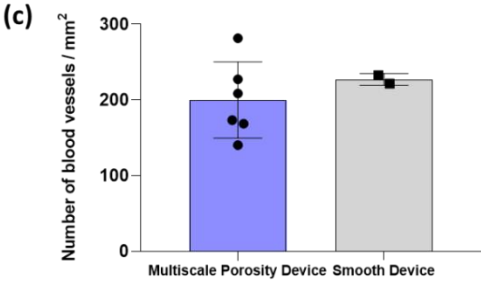
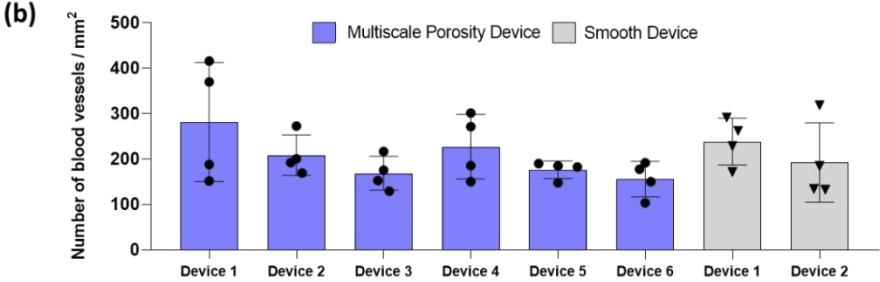
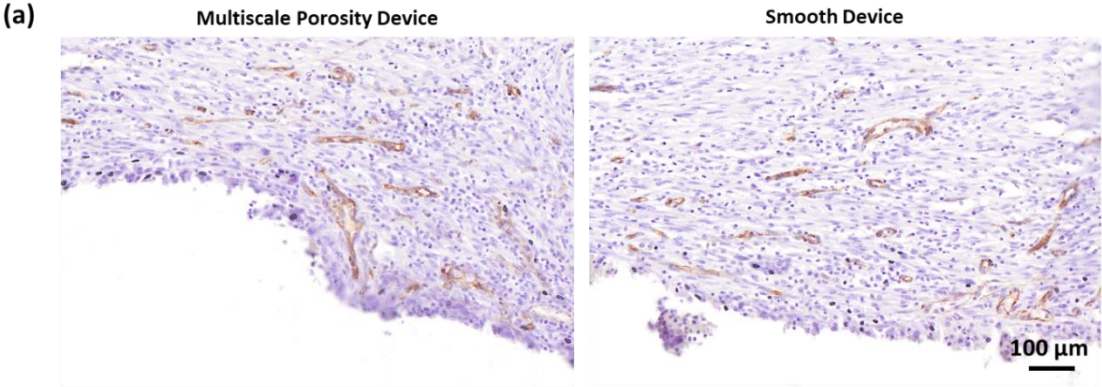
5.3.7.2 Blood vessel diameter

The lumen diameters of >500 CD31+ stained blood vessels were measured per animal and were sampled based on unbiased stereological sampling techniques. Diameters were represented as mean \pm SD (*Figure 5.13 (f)*). A percentage frequency distribution of vessel diameters was constructed in order to display the spread of the data based on diameter size for both the multiscale porous devices (coefficient of variation = 52.3 %) and smooth devices (coefficient of variation = 47.8 %) (*Figure 5.13 (g)*). The majority of vessels surrounding both device designs were between 5-10 μm in diameter. When comparing the size distribution of vessels, multiscale porous devices were surrounded by a greater percentage of blood vessels measuring ≤ 5 μm in diameter. However, the smooth devices had a higher proportion of vessels in the majority of vessel diameter categories ranging from 6-20 μm .

5.3.7.3 Blood vessel maturity

In order to further analyse the angiogenic response, the abundance of $\alpha\text{SMA+}$ blood vessels, a marker indicative of vessel maturity was quantified. A ratio of $\alpha\text{-SMA+}$ vessels to total CD31+ vessels was obtained using confocal microscopy (*Figure 5.14 (a)*). The ratio of $\alpha\text{SMA+}$ blood vessels to total blood vessels within the fibrous capsule was first determined per animal (*Figure 5.14 (b)*) before being plotted as the average ratio per device design (*Figure 5.14 (c)*).

This analysis demonstrated that 70-80% of blood vessels surrounding both multiscale porous and smooth devices expressed α SMA+. This analysis demonstrated that the majority of vessels that developed around each device design were classified as stable and mature.



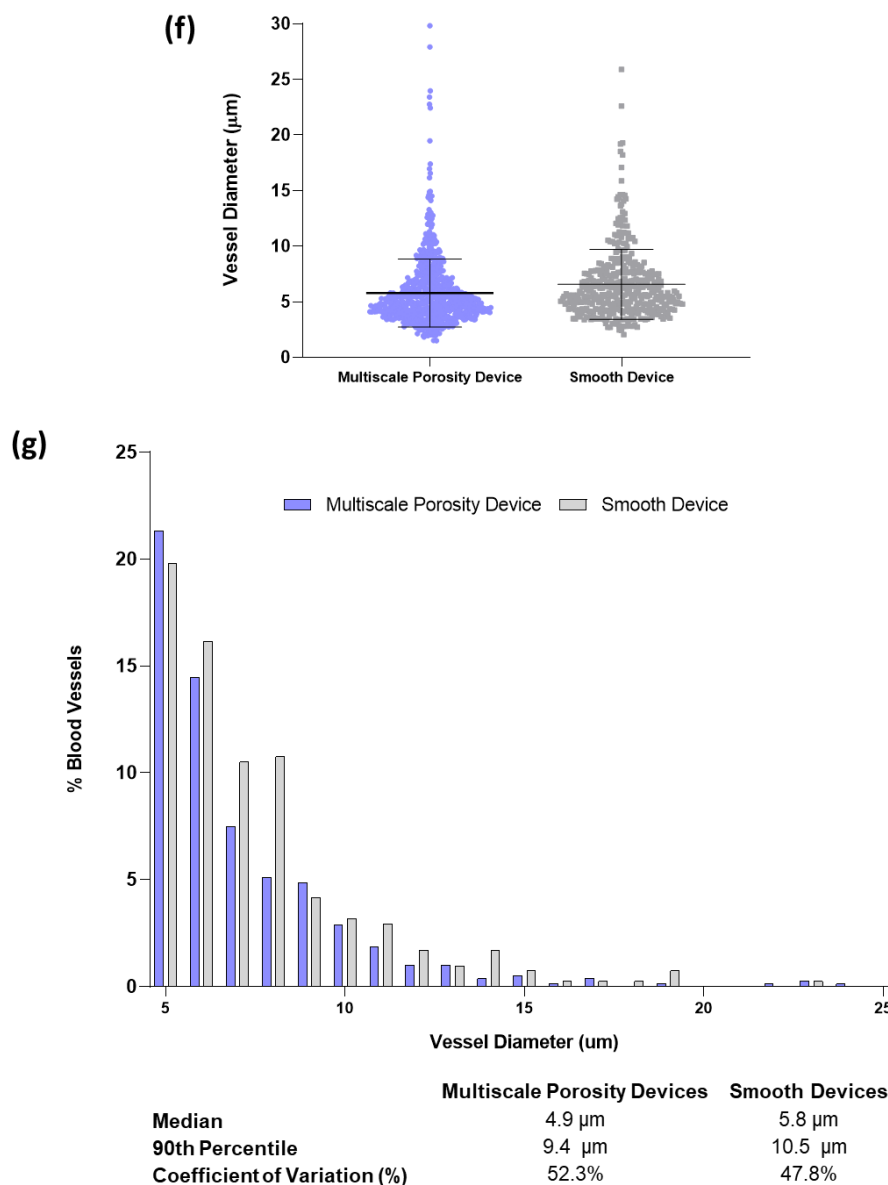


Figure 5.13: Analysis of angiogenesis around multiscale porous and smooth macroencapsulation devices. **(a)** Representative CD31 stained histological image. Scale bars = 100 μm . **(b)** Numerical density and **(d)** radial diffusion distances of blood vessels within the fibrous capsule surrounding each implanted device. Each data point represents the average numerical density/radial diffusion distances for each core biopsy. **(c)** Numerical density and **(e)** radial diffusion distances of blood vessels surrounding each device design. Each data point represents the mean numerical density/radial diffusion distances surrounding each device. **(f)** Blood vessel diameters **(g)** Percentage frequency distribution of blood vessel diameters surrounding multiscale porous and smooth macroencapsulation devices. $n = 2-6$ per group, data are represented as means \pm SD.

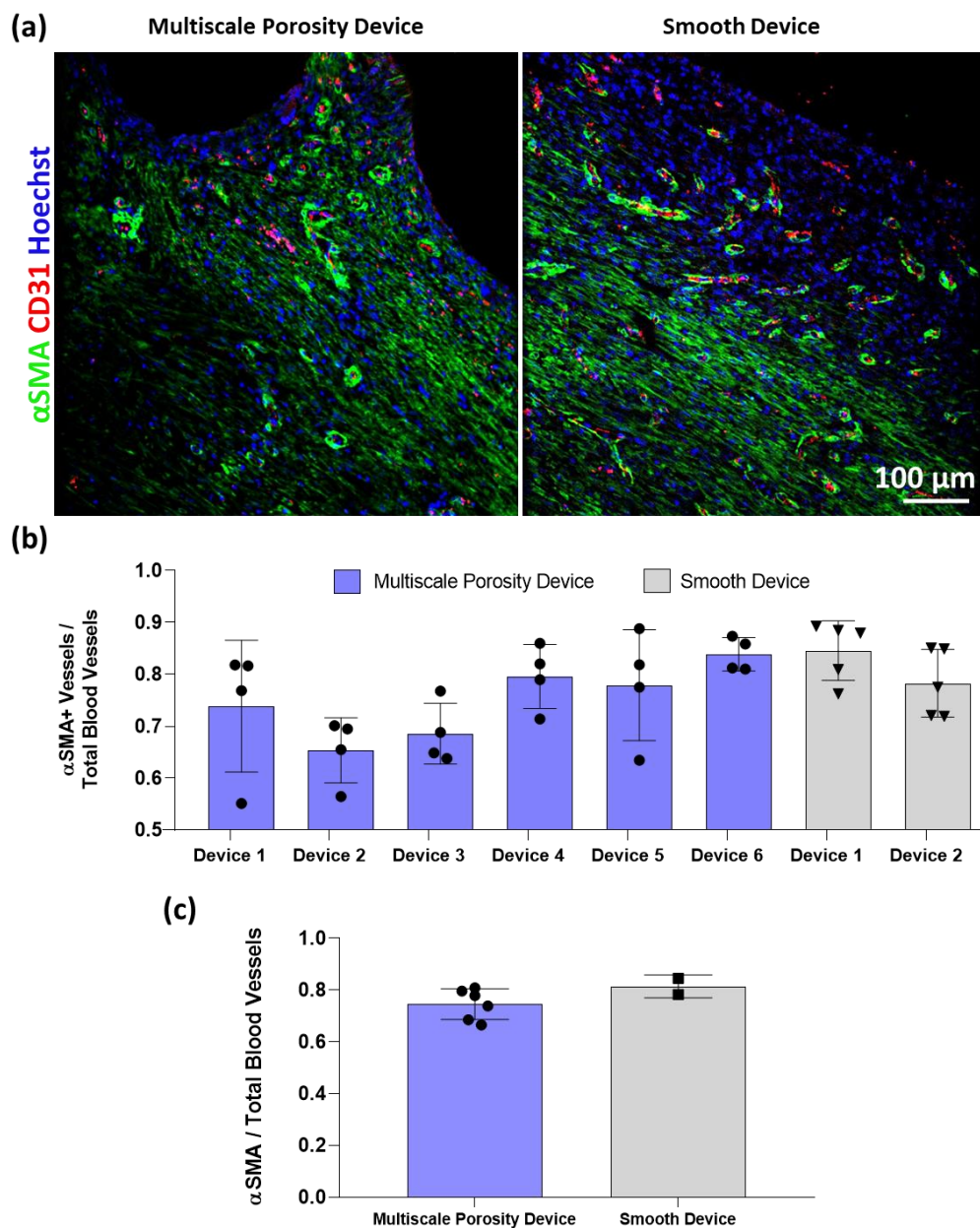


Figure 5.14: Analysis of vessel stability and maturity surrounding multiscale porous and smooth macroencapsulation devices. **(a)** Representative immunofluorescent image for analysis of vessel maturity and stability (Hoechst, blue; α SMA, green; CD31, red). Scale bar = 100 μ m. **(b)** Ratio of α SMA+ blood vessels to total blood vessels within the fibrous capsule for each implanted device. Each data point represents the ratio for each core biopsy. **(c)** Ratio of α SMA+ blood vessels to total blood vessels for each device design. Each data point represents the mean ratio surrounding each device. $n = 2-6$ per group, data are represented as means \pm SD.

5.3.8 Analysis of the macrophage response surrounding multiscale porosity and smooth devices

To assess the impact of surrounding the multiscale porous and smooth macroencapsulation devices on macrophage abundance, tissue sections were stained with a CD68 pan-macrophage marker (*Figure 5.15 (a)*). Representative immunofluorescent images show macrophage aggregation directly at the tissue-device interfaces surrounding both device designs. The volume fraction and number of macrophages per unit volume were first determined per animal (*Figure 5.15 (b, d)*) before being plotted as the average per device design (*Figure 5.15 (c, e)*). Volume fraction demonstrated that 10-20% of the fibrous capsules surrounding both multiscale porous and smooth devices were composed of CD68+ cells (*Figure 5.15 (c)*). The number of CD68+ cells per mm³ surrounding both the multiscale porous and smooth devices ranged between 65,000-80,000 cells (*Figure 5.15 (e)*). These results suggest that increased surface topography did not induce a substantial macrophage response.

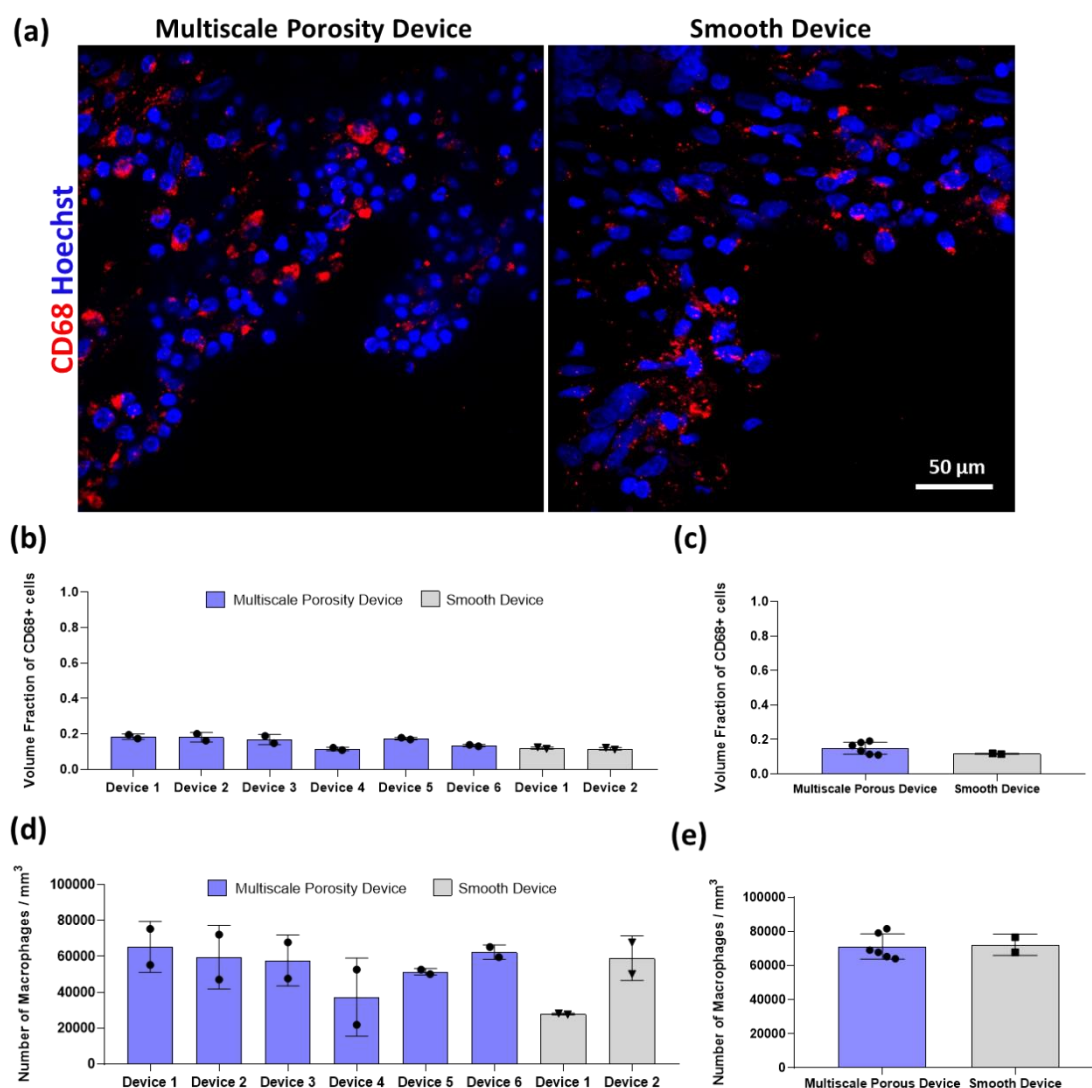


Figure 5.15: Analysis of macrophage response surrounding multiscale porous and smooth macroencapsulation devices. **(a)** Representative immunofluorescent image for analysis of macrophages (Hoechst, blue; CD68, red). Scale bar = 50 μm . **(b)** Volume fraction of macrophages within the fibrous capsule for each implanted device. Each data point represents the volume fraction for each core biopsy. **(c)** Volume fraction of macrophages within the fibrous capsule for each device design. Each data point represents the volume fraction surrounding each device design. **(d)** Number of CD68+ cells per mm^3 of fibrous capsule for each implanted device. Each data point represents the number for each core biopsy. **(e)** Number of CD68+ cells per mm^3 of fibrous capsule for each device design. Each data point represents the number per volume surrounding each device design. $n = 2-6$ per group, data are represented as means \pm SD.

5.4 Discussion

Due to the promising results of the multiscale porous devices in the previous rodent studies, clinically relevant large animal models are necessary to effectively examine the clinical effectiveness of this macroencapsulation system. Efficacious results obtained from this study and future experiments, will potentially satisfy regulatory agencies in order to proceed to clinical trials.

For this study, the Transversus Abdominus Plane (TAP), located in the anterior abdominal wall was identified as a novel and translatable implant site for islet macroencapsulation devices. While the TAP space may be novel as an implantation site, TAP blocks are regional techniques for analgesia of the anterolateral abdominal wall guided by ultrasound. This technique has been used for over two decades for a variety of abdominal surgeries, such as caesarean section, hysterectomy, cholecystectomy, colectomy, prostatectomy, and hernia repair [425–432]. It is a highly vascularised region supplied by the superior epigastric, inferior epigastric and circumflex iliac arteries [431]. This dense vascular network could permit rapid development and distribution of neovascularisation adjacent to the macroencapsulation device surface thus ensuring that macroencapsulated cells would receive adequate oxygen and nutrient supply for survival and function [20]. This site meets the requirements for being easily accessible, can facilitate longitudinal monitoring of transplants and can provide nutritive support for islet cell survival. Morphometric analysis on the size of the TAP site (*Figure 5.6*) demonstrate that this 10 mL upscaled device of approximately 8527 mm² would fit comfortably into the area of the human TAP site measuring approximately 10,000 mm². This device was designed to have a maximum device thickness of 1mm to limit hypoxia and/or necrosis of islets, equating to a potential maximum volume of 8527 mm³. Given that the volume of a distended TAP site can reach approximately 360,000 mm³, it would provide ample space to accommodate this multiscale porosity macroencapsulation device. Furthermore, due to the bilateral nature of this site, it ensures optimal and efficient patient specific dosing, permitting the implantation of two devices if necessary.

In the porcine study we describe a 21-day safety and efficacy study which consisted of human-scaled multiscale porous macroencapsulation devices and a smaller cohort of smooth TPU devices for comparative means, implanted within the novel TAP site in an STZ-induced diabetic pig model. In this study it was imperative to confirm whether this site could facilitate an appropriate level of vascularisation and integration surrounding the multiscale porous devices to ensure viability and long-term efficacy of future macroencapsulated cells.

The inclusion of a smooth surfaced TPU device, not only permitted comparative analysis on the effects of textured versus smooth surfaces, but also on the biomaterial used to produce the device. TPU has excellent biocompatibility and safety records with over 30 years for use in medical applications such as balloon catheters, artificial heart valves and elastic hernia mesh implants [400–405]. However, none of these medical devices exclusively require the development of a highly interconnected vascularised network, and to the same extent, enhanced tissue integration for optimal functionality. Throughout this study, both device designs demonstrate comparable fibrous capsule thicknesses and area measurements, myofibroblast abundances and macrophage activation (*Figure 5.11-5.12, 5.15*). For macroencapsulation devices where diffusion in and out is necessary, micro vessel proliferation within the surrounding fibrous capsule is essential. Without sufficient vascularisation, cellular function and device efficacy cannot be maintained [309–311]. Upon analysis of the angiogenic response, the potential for angiogenic development was analogous surrounding the macroencapsulation devices (*Figure 5.13-5.14*). However, devices possessing micro- and macropore structures demonstrated an enhanced propensity to encourage tissue attachment when compared to smooth TPU devices. The imprints of the multiscale porous devices surface features in the immediate surrounding tissue were strikingly apparent in the cross-sectional views of MicroCT, SEM and histological images indicating an increased affinity for tissue integration around the rope-coils (*Figure 5.10-5.11*). Cross-sectional images of the smooth device showed little tissue attachment or integration with the surrounding tissue. When fibrous tissue does not adhere to the polymer, it can result in sliding and friction between the tissue and implant. This lack of tissue integration and resulting friction could promote the accumulation of serous fluid and inflammatory cells at the interface [252,253]. Increasing integration would also reduce the distance between the macroencapsulated cells and surrounding blood vessels, which is essential for device function and cell survival. Pull-off testing used to quantify the maximum tangential adhesion force or integration of the device into the surrounding tissue, confirmed that a substantially higher maximum force in the multiscale porous device compared to smooth silicone controls (*Figure 5.9*). These data indicate that the external texture allows excellent tissue integration when implanted in the submuscular TAP space of a pig.

Multiscale porous devices induced a consistently disorganised fibrous capsule composition which enveloped around the rope-coil structures at the device surface, resulting in improved integration. In contrast, the fibrous capsule surrounding the smooth device appeared distinctively layered. Due to the absence of any distinct surface features, the

formation of the fibrous capsule was unimpeded, which possibly contributed to its striking concentric layered organisation. DTI tractography analysis, further confirmed this highly concentric, uniform organisation of fibrous capsule architecture surrounding smooth surfaced devices (*Figure 5.8*). The analysis of tractography pathways, demonstrated a highly unorganised, multidirectional composition fibrous capsule surrounding multiscale porosity devices. This observation was accompanied by a significantly decreased FA (**** $P < 0.0001$), indicative of a more heterogeneous capsule architecture with a significantly increased MD (**** $P < 0.0001$), indicative of the affinity for multidirectional diffusion of water molecules [408,412–416]. These results demonstrate that multiscale porous macroencapsulation devices can promote a more heterogenous fibrous capsule development, greater tissue integration and greater diffusion properties when compared to smooth devices. *Flamini et al* previously suggested that DTI imaging and analysis are beneficial to the field of bioengineering for tissue characterisation, medical device design, and preclinical testing [412]. By obtaining realistic numerical models of tissue integrity, one can use these models to aid in preclinical testing of novel medical devices [434]. By providing a direct measure of capsule heterogeneity through FA analysis, and diffusional potential through MD analysis, DTI also has the potential to provide useful insights into water soluble macromolecule diffusion from a macroencapsulation device to the surrounding vasculature. The results of the DTI analysis surrounding multiscale porosity devices may be indicative for the tissues affinity for unimpeded diffusion of insulin after 21 days.

The primary goal of islet macroencapsulation is the re-establishment of glucose homeostasis maintained by adequate insulin production and secretion by macroencapsulated cells. Insulin can be induced by a multitude of hormones and neurotransmitters however, predominant secretagogue is glucose [22]. The normal physiological secretion of insulin is pulsatile [435,436] in nature however, maintenance of this delicate regulation from within a macroencapsulation device, remains one of the greatest challenges in the field. The kinetics of insulin through a macroencapsulation system are subject to numerous biological and physio-chemical factors [190,437]. The composition of the macroencapsulation device, and the resultant pericapsular fibrotic overgrowth can hugely influence insulin kinetics. This collagenous overgrowth can be attributed to an immune response against the device polymer or to antigen shedding through membrane pores from macroencapsulated islet tissue [438]. The surrounding deposition of collagenous fibrous tissue elevates mass-transfer resistance of the tissue, ultimately resulting in the impedance of analyte diffusion between the device and the surrounding vasculature

[439,440]. The configuration of the Beta O₂ device is a prime example of positive insulin kinetics, unhindered by the disruption of diffusion [229,230]. Although the relatively large surface-to-volume ratio of macroencapsulation devices can disrupt optimal exchange of macromolecules, thus compromising metabolic homeostasis. In the case of the multiscale porous device utilised in this study, the bioavailability of insulin through the device is equivalent to conventional insulin delivery subcutaneously (*Figure 5.7*). The purpose of this experiment was to create a reference measure, to analyse the devices capacity to release insulin produced by future encapsulated islet cells. This measure was previously used by Abramson *et al* [406], who developed an oral biologic delivery system that autonomously positions itself to engage with gastrointestinal tissue to achieve systemic drug uptake. Similar to Abramson *et al* [406] who used insulin as a model drug, the multiscale porous device demonstrated comparable if not equivalent results, when demonstrating the devices ability to deliver insulin compared to gold standard subcutaneous administration. The insulin delivery efficacy achieved with the multiscale porosity device suggests that this method could replace subcutaneous injections for insulin and justifies further chronic large animal studies with islets encapsulated within.

In conclusion, the implantation of an up-scaled multiscale porous macroencapsulation device within the novel TAP site, can facilitate the development of a highly vascularised, integrated, heterogeneously organised fibrous capsule with an affinity for unimpeded diffusion of insulin after 21 days. These findings prove that the properties of the surface multiscale texturing could be used to facilitate physiological diffusion necessary for efficacious islet macroencapsulation. This site met the requirements for being easily accessible and can facilitate longitudinal monitoring of devices. By choosing a site with abundant endogenous vasculature with the possibility for proangiogenic manipulation, it could enable the development of a highly interconnected vascularised network surrounding macroencapsulation devices, providing adequate oxygenation and nutrient supply for active and sustained engraftment of cells in future studies.

Chapter 6

Thesis Discussion

6.1 Overview

DM is a chronic metabolic disease characterised by the dysregulation of glucose metabolism. DM is a major health problem that has reached alarming levels across the globe. T1D is characterised by β -cell auto-immunity and the subsequent destruction of the insulin producing cells in the pancreas. Although T1D is the less prevalent of the two primary types of DM, the morbidity and mortality associated with T1D, combined with the substantial economic cost have made it a major public health issue that has attracted a great deal of interest for research into the treatment and prevention of the disease. As a consequence, many investigations in this field have pursued the development of a system known as the bioartificial pancreas. This three-part system would consist of donor human islets or insulin producing cells, a biocompatible ECM to house them, and a semi-permeable immunoisolating shell to prevent graft rejection without the need for systemic immunosuppression.

Over the course of this thesis, extensive efforts have been focused on investigating the most superior biocompatible approach, including surface modification techniques, implant site, configuration of device, and methods to improve vascularisation for the purpose of islet cell macroencapsulation. *In vivo* rodent experimentation demonstrated that a combination of complex micro- and macrotecture were optimal surface topographies, providing a scaffold for blood vessel development, tissue attachment and integration in the absence of a heightened macrophage response. In addition, *in vivo* data indicated that the addition of VEGF microspheres combined with a multiscale porosity device had a statistically increased angiogenic response by promoting increased vessel stability, maturity and vessel size within a 4-week time period. This demonstrated the potential to resolve the diffusion limitations of newly seeded/transplanted islet cells and ultimately reduce the time of cellular reconnection to host vasculature, improving potential islet survival within our macroencapsulation device. Moreover, a study of therapeutic efficacy proved that macroencapsulated islets have the potential to maintain glucose responsiveness and function for 8 weeks within the multiscale porosity device. Finally, the utility of this manufacturing approach to create clinical scale devices with efficacious insulin delivery was demonstrated through a 14-day porcine device delivery and safety study. As a surrogate for cells producing insulin in the device, we compared insulin infusion through the device to subcutaneous delivery as a direct comparison to current insulin delivery regimens. Bioavailability was equal when the same dose of insulin was delivered via the device vs subcutaneous injection in a diabetic pig model.

The results demonstrated clinical scalability, surgical delivery and functionality of textured devices. These experiments demonstrate significant progress made accumulating the extensive pre-clinical data required for translation of this project from the bench to bedside, but ultimately will inform all future work related to the clinical translation of the multiscale porosity macroencapsulation device as part of the DRIVE bioartificial pancreas.

6.2 Thesis results summary

6.2.1 Determining an optimal surface topography

It has been well established that a successful islet macroencapsulation device must facilitate; normal insulin and glucose kinetics for the maintenance of normoglycemia, optimal nutrient and waste exchange, all while maintaining the viability of macroencapsulated cells. The foreign body response (FBR) to synthetic materials is an enormous impediment to the development and efficacy of immunoprotective islet-macroencapsulation devices [180]. This FBR is often heightened when a polymeric device features a smooth external surface [246,247]. Fibrous tissue does not generally adhere to the polymer, and instead allows sliding and friction between the surrounding tissue and the device. Subsequent fibrotic encapsulation by dense impermeable avascular layers of collagen, impairs tissue integration and a lack of vascularisation severely affects the pharmacokinetics of mass transport in the peri-device tissue [254] and can limit nutrient and oxygen diffusion and cell viability and response. Promoting tissue integration and blood vessel formation surrounding macroencapsulation devices is imperative to ensure positional fixation within the host tissue and thus prevent adverse effects [256]. Thus, when determining an optimal surface topography for this thesis, we aimed to improve the devices ability to harness the desired degree of tissue integration and vascularisation for potential islet cell macroencapsulation.

To achieve this aim, novel additive manufacturing techniques were utilised to create a series of five 12 mm disk shaped implants, fabricated from medical grade silicone. Each subsequent implant in the series was progressively more complex than the previous, which was achieved by increasing the quantity of both rope-coil-derived macro-pores, and salt spray derived micro-pores. Previous studies have demonstrated that micro-range surface texture can modify cellular responses in the surrounding tissue, dampen chronic inflammation and promote angiogenesis, resulting in improved device integration [279,280]. These surface modifications were intended to encourage cellular attachment, while reducing macrophage and oriented fibroblasts aggregations, thus promoting tissue in-growth and vascularisation in proximity to the immunomodulatory membrane of the implant.

In the 14-day rodent study, it was demonstrated that implants possessing micro- and macropore structures showed an excellent propensity to encourage tissue attachment when compared to smooth implants. Increased tissue integration correlated with a thicker capsule due to its more tortuous development and increased affinity for tissue integration around the rope coil groups. Macrophage activity surrounding the implants was assessed as a measure of the FBR [280] which demonstrated that increasingly complex topographies do not evoke a significantly enhanced macrophage response. The formation of new vessels is imperative for the mass-diffusion of nutrients, waste, and oxygen to encapsulated cells. Without sufficient vascularisation, cellular function and device efficacy cannot be maintained. In order to supply sufficient oxygen to islet cell mitochondria, the maximum radial diffusion distance between an islet cell and a capillary must not exceed 200 μm [298,299]. The results of this study indicated that vascular beds surround all implants which could potentially facilitate macroencapsulated islet survival and subsequent insulin diffusion. However, this analysis proved that significant increases in vascular density correlate with increased complexity of implant surface topography. Crucially, the most complex implants, were also associated with a reduction in radial diffusion distance ($<30 \mu\text{m}$), suggesting the presence of optimally vascularised tissue to facilitate the survival of macroencapsulated cells [168].

Islet isolation procedures can often destroy the native islet vascular networks causing prolonged hypoxic stress contributing to a loss of 60% of transplanted islets during the first 48 h post-transplantation [227,228]. In order to supply sufficient oxygen to islet cell mitochondria, the maximum radial diffusion distance between an islet cell and a capillary must not exceed 200 μm [298,299]. For these reasons, the development and distribution of neovascularisation adjacent to macroencapsulation device surface as well as the spatial arrangement of the encapsulated cells is essential to promote survival of macroencapsulated islets and is a primary limiting factor in long-term device success.

6.2.2 VEGF releasing microspheres as a vascularisation strategy

Having established that multiscale porosity on the surface of soft tissue implants can enhance tissue integration and vascularity, a multiscale porosity macroencapsulation device was fabricated. However, islet survival and functional capacity are usually determined in the first three days post-transplantation, at which time the surrounding graft is largely avascular [130]. It has been established that rapid development of a highly interconnected vascularised network has the potential to resolve the diffusion limitations of newly seeded/transplanted islet cells and ultimately reduce the time of cellular reconnection to host vasculature and improve islet survival within the macroencapsulation device [309–311]. Rapid vascularisation in the vicinity of devices can also be promoted by the inclusion of growth factors such as VEGF to facilitate the controlled release of angiogenic cues [192,259,304,305]. Therefore, we wanted to determine whether encapsulating VEGF microspheres within multiscale porosity devices, could promote and enhance the formation of a substantial vascular network at the device surface.

Data from this study indicated that the addition of VEGF microspheres combined with a multiscale porosity device had a statistically increased angiogenic response by promoting increased vessel stability, maturity and vessel size within a 4-week time period. The successful development of a highly interconnected vascularised network demonstrated in this study, could have the potential to resolve the diffusion limitations of newly seeded/transplanted islet cells and ultimately reduce the time of cellular reconnection to host vasculature, improving potential islet survival within our macroencapsulation device.

6.2.3 Determining the therapeutic efficacy of the multiscale porosity macroencapsulation device

To develop an efficacious islet macroencapsulation system, one must recognise the complex relationship between, device design, islet quality, implantation site and integration into the host site. In this study, we described the optimisation of intra-peritoneal transplant methodology to achieve adequate angiogenic and tissue integration for increased viability and long-term efficacy of macroencapsulated syngeneic islets in an STZ induced T1D model.

Optimisation of the implantation procedure by suturing the macroencapsulation device internally to the pre-peritoneal site resulted in improved viability and efficacy of macroencapsulated cells. As devices maintained their configuration and position throughout the implantation period, the potential for tissue integration and vascularisation increased. Over a period of 8 weeks, over half of implanted rodents achieved graft-derived insulin levels, sufficient to prevent STZ-induced hyperglycemia.

This combination of an optimised intra-peritoneal implantation procedure and a multiscale porosity macroencapsulation device can facilitate efficacious islets and the maintenance of normoglycemia in diabetic rodents for up to 8 weeks. By choosing a site with abundant endogenous vasculature with the possibility for proangiogenic manipulation, it can enable the development of a highly interconnected vascularised network surrounding the macroencapsulation device to provide adequate oxygenation and nutrient supply for active and sustained engraftment.

6.2.4 Clinical translation study

Promising approaches for islet cell encapsulation are translated through large animal models that ultimately pave the way to proceed to Phase I and II clinical trials in human subjects. In the final study we aimed to detail the first steps in translating a rodent sized multi-scale porous device to a large scale, functional macroencapsulation device implanted in a diabetic porcine model.

To fully appreciate the benefits of islet macroencapsulation, a more appropriate implant site had to be identified. For this study, three potential sites within the Anterior Abdominal Wall were identified due to their ability to accommodate a macroencapsulation device. The TAP is a potential space between the transversus abdominus and the internal oblique muscles of the abdomen, and is routinely accessed by anaesthesiologists with ultrasound guidance to provide analgesia for abdominal surgery via a TAP block [389]. This site was chosen due to its dense vascular network which could permit rapid development and distribution of neovascularisation adjacent to macroencapsulation device surface thus ensuring that encapsulated cells would receive adequate oxygen and nutrient supply for survival and function [20]. This also site met the requirements for being easily accessible, can facilitate longitudinal monitoring of transplants and can provide nutritive support for islet cell survival.

Findings of this study demonstrated that implantation of an up-scaled multiscale porous macroencapsulation device within the novel TAP site, could facilitate the development of a highly vascularised, integrated, heterogeneously organised fibrous capsule with an affinity for unimpeded diffusion of insulin after 21 days. These findings prove that the properties of the surface multiscale texturing could be used to facilitate physiological diffusion necessary for efficacious islet macroencapsulation. This site met the requirements for being easily accessible and can facilitate longitudinal monitoring of devices.

The inclusion of a smooth surfaced TPU device in this study, not only permitted comparative analysis on the effects of textured versus smooth surfaces, but also on the biomaterial used to produce the device. Throughout this study, both device designs demonstrate comparable fibrous capsule thicknesses and area measurements, angiogenesis, myofibroblast abundances and macrophage activation. However, devices possessing micro- and macropore structures demonstrated an enhanced affinity for tissue integration around the rope-coils when compared to smooth TPU devices. When fibrous tissue does not adhere to the polymer, it can result in sliding and friction between the tissue and implant. This lack of tissue integration and resulting friction could promote the accumulation of serous fluid and inflammatory cells at the interface [252,253], which could in fact be the future following long term implantation of the TPU device however this would need to be tested further. Increasing integration would also reduce the distance between the macroencapsulated cells and surrounding blood vessels, which is essential for device function and cell survival. While histological analysis was similar across both device configurations, multiscale porous macroencapsulation devices can promote a more heterogenous fibrous capsule development, greater tissue integration and greater diffusion properties which may give it the edge for enhanced efficacy over both smooth surface silicone devices and smooth TPU macroencapsulation devices.

By choosing a site with abundant endogenous vasculature with the possibility for proangiogenic manipulation, it could enable the development of a highly interconnected vascularised network surrounding macroencapsulation devices, providing adequate oxygenation and nutrient supply for active and sustained engraftment of cells in future studies

6.3 Clinical relevance

6.3.1 Putting a positive spin on fibrous capsule development

The implantable medical device industry is plagued by the Foreign Body Response (FBR) which ultimately limits long-term performance and therapeutic efficacy. Medical devices that rely on integration with native tissue such as neural probes [441,442], indwelling catheters [443], mammary implants [444], pacemakers [445], glucose biosensors [446–448], and drug and cell delivery devices [446,449,450], are predominantly susceptible and impair functionality. Implantable medical devices have various failure rates that can be attributed to fibrosis and can be as high as 30 to 50% for implantable pacemakers [445] and 30% for mammoplasty prosthetics [444]. The FBR involves deposition of an avascular, collagen-rich

capsule around the implant by myofibroblasts that can result in significant impairment in device functionality. This dense fibrosis can lead to the implant being walled off thus preventing the device from functioning or integrating as intended [254]. Fibrous tissue does not generally adhere to the polymer, and instead allows sliding and friction between the tissue and implant. This lack of tissue integration and resulting friction can promote the accumulation of serous fluid and inflammatory cells at the interface [255]. Poor tissue integration of prostheses is associated with increased rates of infection in multiple types of soft tissue, including vascular and breast tissue [451]. The foreign body response to synthetic materials is an enormous impediment to the development and efficacy of immunoprotective cellular-encapsulation devices [180].

However, the additive manufacturing method used to create multiscale porosity topography is a fast, effective method of coating medical implants of diverse curved topologies, modulating the host immune response and guiding the foreign body response via surface topology. The patterning techniques described here offers tunability of fibrous capsule formation and angiogenesis through surface modification enabling increase or decrease of tissue integration, increase or decrease of fibrous capsule formation and increase or decrease of angiogenesis.

The methodology used to create micro- and macrotecture surface modifications is a simple, inexpensive method for the surface functionalisation of implantable biomaterials and has demonstrated the potential of being applied to various implantable devices to ameliorate the FBR to biomaterials.

6.3.2 DRIVE technology as a treatment for T1D

The primary objective of this thesis was focused on investigating the most superior biocompatible approach, including surface modification techniques, implant site, configuration of device, and methods to improve vascularisation for the purpose of islet cell encapsulation.

Ultimately, the primary objective of the DRIVE project was to develop an extravascular macroencapsulation device to act as a bioartificial pancreas. In the field of extravascular macroencapsulation, there are currently 3 main leaders in the field: Encaptra®, β Air, and the Sernova Cell Pouch System™. All three companies have been in development longer, and all three have already started first-in-human trials. This raises an important question: is there room in the market for another extravascular macroencapsulation bioartificial pancreas? The preliminary *in vivo* results from the DRIVE project are promising,

but can the technology compete with the existing technologies? See *Table 6.1* for comprehensive overview on how the DRIVE approach compares with other technologies.

The Encaptra Drug Delivery system, or the VC-01 product, utilises the PEC-01 cell line, which mature into glucose-responsive insulin-secreting beta-like cells, used to overcome the issue of donor pancreatic islet shortages, an issue that presented significant challenges to DRIVE [218,219]. However, the DRIVE product is flexible, and in the future when iPSC derived β -cells are available, the DRIVE product would be able to utilise those cells. Additionally, the VC-01 product is an immunoisolating device however, the company ViaCyte is also investigating the PEC-Direct and PEC-QT or VC-02 encapsulation systems. These are highly porous to allow blood vessel penetration and infiltration of the encapsulated cells at the cost of the immunoisolation, requiring immunosuppressive therapies in order to protect the implanted cells from immune rejection. If the DRIVE product can maintain its immunoisolating capacity, while also addressing vascularisation, it would be in a position to be able to compete with the VC-02 product. Similarly, this is also the competitive advantage of the DRIVE product over the Sernova Cell Pouch System which also prioritises vascularisation by compromising on an immunomodulatory barrier, thus immunosuppression is necessary to prevent rejection of implanted islets.

The β Air macroencapsulation device was developed by Beta-O₂ Technologies. β Air employs a novel strategy by providing continuous oxygenation of cells from the moment of encapsulation. This approach could potentially negate prolonged hypoxic stress which typically contributes to the loss of 60% of transplanted islets during the first 48 hours post-transplantation [227,228] and prolong the survival of encapsulated islets. This is not a strategy that the DRIVE product can compete with. However, if the DRIVE product can achieve the same degree of long-term efficacy as the β Air device, it will surpass the β Air device as it will not require daily refills of the O₂ reservoir [298].

While the bioartificial pancreas represents an exciting frontier in diabetes treatment, in reality the next step in medical devices for the treatment of diabetes may not require endogenous insulin production at all. Currently, open loop systems remain the main approach for managing DM but a shift towards more automated, interconnected systems in the future is expected. The concept of the artificial pancreas, the use of an insulin pump, a CGM device, and an insulin dosing algorithm may be the biggest competition to all macroencapsulation devices. Nevertheless, despite promising results the artificial pancreas still has many obstacles to overcome before the successful development of commercially viable artificial pancreas device. Artificial pancreas products are in early stages, but show

greatly improved blood glucose control [96]. However, the functional components of the artificial pancreas must be maintained; sensors of the CGM must be replaced every 2-7 days and require frequency calibration [452], the device must be recharged regularly and insulin pumps refilled every 3 days [453]. The insertion of CGM subcutaneously is an invasive procedure and thus results in an inflammatory response at the insertion site that may produce inaccurate CGM data [452] whilst catheter blockage may prevent insulin delivery. Secondly, changes in insulin sensitivity can occur based on concurrent illness, unusual levels of physical activity and medication taken by the patient [454]. Another significant obstacle is the suboptimal accuracy and reliability of commercially available CGM systems, which can give a relative absolute difference between sensor and reference glucose measurements of up to 15% [454,455]. Such a persistent deviation may cause insulin over-delivery and so increased risk of hypoglycemia, posing the greatest challenge to closed-loop insulin delivery. Additional technical problems include the challenge of integrating CGMs, insulin pumps and system algorithms from different commercial entities [454,456]. Although an artificial pancreas device will always need to have insulin reservoirs changed, many patients may find this to be an acceptable price to pay to avoid undergoing surgery for the same, if not increased levels of glucose control.

Islet transplantation offers the greatest potential to restore endogenous control over blood glucose levels in individuals with T1DM. Currently islet transplantation is approved in Canada, Australia, United Kingdom, and some European countries for use in patients with brittle T1DM – meaning the costs of islet transplantation are covered by national health systems or reimbursed by insurance companies.

In the United States, the FDA is reviewing a Biological License Application to approve islet transplantation, which would be of great significance [457]. The establishment of a replenishable stem cell source (for instance PEC-01 cells) will potentially address the issue of donor scarcity while the macroencapsulation devices will protect the transplanted islets from the recipients' aberrant immune response (removing the need for immunosuppressants) [458], potentially paving the way towards a cure for T1D

Table 6.1: Comparing current islet macroencapsulation systems with the DRIVE approach.

Company	Immunoprotection	Integration Strategy	Angiogenic Strategy	Oxygenation Strategy
DRIVE: β-Shell	Yes: Devices composed of medical grade silicone with selectively permeable membrane - pore size of ~ 5 μm.	Yes: Microporous with multi-layered macro structure externally to provide scaffold for surrounding tissue integration and microvasculature.	Yes: Incorporation of VEGF microspheres. Microporous with multi-layered macro structure externally.	Yes: Native HA/Perfluorodecalin oxygenated emulgel.
Viacyte: Encaptra	Yes: Devices composed of ePTFE with selectively permeable membrane - pore size of 0.45 μm.	No	No	No
Viacyte: PEC-QT & PEC-Direct	No. Immunosuppression required: Devices composed of ePTFE with large diameter pores.	No	Yes: Highly porous devices to allow blood vessel penetration and infiltration of the encapsulated cells.	No
Sernova: Cell Pouch	Partial, Immunosuppression required: Pouch composed of a polypropylene based matrix with large diameter pores. Sertolin technology: Microencapsulation of cells within a polymer sphere preventing immune cell attack.	Yes: Pouch to be implanted subcutaneously for 30-40 days to promote the development of surrounding tissue integration and microvasculature.	Yes: Pouch to be implanted subcutaneously for 30-40 days. Its interior is filled with an array of rods, or a single rod to act as plugs during the prevascularisation process.	No
Beta-O₂ Technologies: βAir	Yes: Devices possess PTFE membranes impregnated with high viscosity mannuronic acid alginate.	No	No	Yes: Incorporated oxygen gas reservoir to be replenished daily via an external port.
Defymed: MailPan	Yes: Devices composed of selectively permeable polycarbonate membrane.	No	No	No

6.4 Future work

The preclinical data obtained throughout the course of this PhD have established that the multiscale porosity macroencapsulation device has significant potential as a component of a bioartificial pancreas. The ideal configuration of the DRIVE technology would include prevascularisation period of two-four weeks prior to the introduction of a cell cargo. This prevascularisation period would involve implantation of the macroencapsulation device containing VEGF releasing microspheres suspended within a HA gel. This prevascularisation period would enable time for tissue integration and the development and distribution of neovascularisation adjacent to encapsulation device surface which would in turn promote survival of future encapsulated islets. Following this prevascularisation period, the device would be emptied of its contents and subsequently islets encapsulated within an oxygenated hydrogel would be injected into the device. This approach would negate the hypoxic implantation period that is often a primary limiting factor in device efficacy. By combining functional biomaterials developed and optimised within the DRIVE consortium for long-term clinical efficacy of transplanted islets, future studies must endeavour to reach key milestone objectives in translating this novel device by completing chronic studies in small and large animals to prepare for a Phase 1 clinical trial of the technology using human islets as the insulin producing cell source. The overall aim of the proposed future studies is to demonstrate human islet cell viability and long-term efficacy when encapsulated within a multiscale porosity macroencapsulation device. This will be achieved through four aims, with sub-tasks as follows.

1. Examine the ability of the multiscale porosity device to provide long-term in vivo immunoprotection to allogeneic islets in an immunocompetent rat model of T1D
 - i. **Induction of diabetes in rats using streptozotocin:** Adult recipient rats [Female Lewis (LEW/SsNHsd, haplotype RT1^l) 160 g] will receive an intra-venous injection of 60 mg/kg dose of Streptozotocin (STZ) to induce diabetes [354,355]. Blood glucose will be monitored and rats exhibiting a repeating basal circulating BG level of greater than 300 mg/dL will be considered diabetic.
 - ii. **Implant rodent-sized multiscale porosity devices in STZ-induced diabetic rats:** Rats will be anesthetized by isoflurane and 1 rodent-sized device will be implanted per rat submuscularly in the dorsum. This site will mimic the future submuscular implantation site in the anterior abdominal wall.

Each device will contain 2000 IEQ of allogenic rat islets [Male Wistar Furth (WF/NHsd, haplotype RT1^u) 200-250 g]. Intravenous Glucose Tolerance Test (IVGTT) will be carried out before STZ and 7d-28d after normal glycemia (<200 mg/dL) is achieved to compare glucose clearance AUC. Blood glucose will be monitored for a period >130 days allowing us to directly compare with the 2020 Bose *et al* study which examines a retrievable implant for the long-term encapsulation and survival of therapeutic xenogeneic cells [459].

2. Determine the pre-clinical efficacy of multiscale porosity device macroencapsulated human islets in an immunocompetent porcine model of T1D.
 - i. **Induction of diabetes in pigs using Streptozotocin:** To induce diabetes, 20-30 kg Landrace pigs will receive a single dose of STZ 150 mg/kg administered intravenously while under general anaesthesia. Blood glucose will be recorded using CGMS to improve the management of hyperglycemia and hypoglycemia before transplantation and their welfare after transplantation.
 - ii. **Implant pig-sized multiscale porosity macroencapsulation devices in STZ-induced diabetic pigs:** Diabetic pigs will be treated with insulin glargine (0.3–0.8 U/kg; Lantus; Sanofi-Aventis) once daily for glucose control, and the daily treatment will be stopped 36h before implantation to minimise the impact of remaining insulin glargine [460]. IVGTT will be carried out with 0.5 mg glucose/kg and blood sampling over subsequent 180 minutes. ELISA assay will measure Serum C-peptide and insulin (*on IVGTT blood samples - <0.4 ng/mL c-peptide = diabetic*). On day 7 after induction of diabetes, animals will undergo general anaesthesia and receive surgical implantation of porcine-sized devices into transversus abdominis plane (TAP). Devices will contain 1800-4600 IEQ/kg body weight[233] of human islets, supplied by islet expert Dr Federico Bertuzzi. Interstitial glucose concentration (IGC) will be monitored using CGMS (Dexcom G6) and two daily meals will be provided during the experiment for a period >60 days [459] including assessment of stimulated c-peptide/insulin production (post-IVGTT) and reduction in insulin requirements.
3. *Ex vivo* assessment of islet cell viability and function
 - i. **Explant device, assess fibrotic capsule and vascularisation surrounding rodent and porcine devices:** Masson's Trichrome stain and microCT analysis will be used to quantify the area of fibrotic encapsulation using previously established

techniques [461]. Immunohistochemistry will be used to assess vascularisation (CD31 staining) and macrophage response (CD68;pan-macrophage, CCR7; M1 macrophages, CD163; M2 macrophages) using previously established techniques within the NUIG lab [461].

- ii. **Explant device, assess viability and morphology of encapsulated islets within rodent and porcine devices:** Histological analysis of islet morphology will be performed using hematoxylin and eosin staining. Immunohistochemistry will be used to assess the presence of insulin and glucagon within islet cells and immunophenotyping intragraft immune cells using previously established techniques within the NUIG lab.

4. Clinical Translation

- i. **Device Manufacture:** GMP-like device manufacture will be carried out and will include development control of relevant manufacturing steps and control of critical steps and intermediates.
- ii. **Sterility:** Components of macroencapsulation system were previously assessed for sterilisation options using the decision tree for the selection of sterilisation methods (CPMP/QWP/054/98) with suitable studies performed to evaluate the optimal method in each case. Based on these outcomes, steam sterilisation was deemed optimal and a protocol of the macroencapsulation device will be established.
- iii. **Preparation for Phase I clinical trial:** Results of the studies performed in 1-4 will be compiled to accelerate progression to a future Phase I safety and efficacy clinical trial (based on the trial conducted by beta-O2 Technologies[233]). Multiscale porosity macroencapsulation devices containing isolated allogenic islets will be implanted in the TAP of 4 patients with T1D. Devices will be removed 180 days post-transplantation, with a safety follow-up for an additional 6 months.

6.5 Final conclusion

Over the course of this project it has been demonstrated that additive manufactured multiscale porous coatings on macroencapsulation devices can encourage and increase tissue integration and the formation of significantly larger, more stable, mature vascular network without heightening the foreign body response. Moreover, macroencapsulated syngeneic islets can maintain glucose responsiveness and function for up to 8 weeks. These findings demonstrate scalability and functionality with the possibility of resolving diffusion limitations of current macroencapsulation devices at clinical scale. Although, the device has yielded promising results in both small and large animal studies, a great deal of future work will be required to translate these results from animal models to first-in-man trials.

Bibliography

- [1] R. Drake, A.W. Vogl, A.W.M. Mitchel, *Gray's Anatomy for Students*, 3rd ed., Elsevier Health Sciences, London, United Kingdom, 2014.
- [2] R. Chandra, R.A. Liddle, Neural and hormonal regulation of pancreatic secretion, *Curr. Opin. Gastroenterol.* 25 (2009) 441–446. <https://doi.org/10.1097/MOG.0b013e32832e9c41>.
- [3] A.D. Cherrington, Glucagon Physiology, *Can. J. Diabetes.* 34 (2010) 187–188. [https://doi.org/10.1016/s1499-2671\(10\)43015-4](https://doi.org/10.1016/s1499-2671(10)43015-4).
- [4] A.E. Kitabchi, Proinsulin and C-peptide: A review, *Metabolism.* 26 (1977) 547–587. [https://doi.org/10.1016/0026-0495\(77\)90099-3](https://doi.org/10.1016/0026-0495(77)90099-3).
- [5] J. Wahren, Å. Kallas, A.A.F. Sima, The clinical potential of C-peptide replacement in type 1 diabetes, *Diabetes.* 61 (2012) 761–772. <https://doi.org/10.2337/db11-1423>.
- [6] R. Bilous, R. Donnelly, Normal Physiology of Insulin Secretion and Action, in: *Handb. Diabetes*, 4th ed., 2014. <http://www.diabetesincontrol.com/handbook-of-diabetes-4th-edition-excerpt-4-normal-physiology-of-insulin-secretion-and-action/> (accessed April 24, 2020).
- [7] A.C. Hauge-Evans, A.J. King, D. Carmignac, C.C. Richardson, I.C.A.F. Robinson, M.J. Low, M.R. Christie, S.J. Persaud, P.M. Jones, Somatostatin secreted by islet δ -cells fulfills multipleRoles as a paracrine regulator of islet function, *Diabetes.* 58 (2009) 403–411. <https://doi.org/10.2337/db08-0792>.
- [8] R.L. Batterham, C.W. Le Roux, M.A. Cohen, A.J. Park, S.M. Ellis, M. Patterson, G.S. Frost, M.A. Ghatei, S.R. Bloom, Pancreatic polypeptide reduces appetite and food intake in humans, *J. Clin. Endocrinol. Metab.* 88 (2003) 3989–3992. <https://doi.org/10.1210/jc.2003-030630>.
- [9] G. Katsuura, A. Asakawa, A. Inui, Roles of pancreatic polypeptide in regulation of food intake, *Peptides.* 23 (2002) 323–329. [https://doi.org/10.1016/S0196-9781\(01\)00604-0](https://doi.org/10.1016/S0196-9781(01)00604-0).
- [10] G. Pradhan, S.L. Samson, Y. Sun, Ghrelin: Much more than a hunger hormone, *Curr. Opin. Clin. Nutr. Metab. Care.* 16 (2013) 619–624. <https://doi.org/10.1097/MCO.0b013e328365b9be>.
- [11] M.J. Taylor, S.C. Baicu, Nonenzymatic Cryogenic Isolation of Therapeutic Cells: Novel Approach for Enzyme-Free Isolation of Pancreatic Islets Using In Situ Cryopreservation of Islets and Concurrent Selective Freeze Destruction of Acinar Tissue, *Cell Transplant.* 23 (2014) 1365–1379. <https://doi.org/10.3727/096368913X672055>.
- [12] O. Cabrera, D.M. Berman, N.S. Kenyon, C. Ricordi, P.O. Berggren, A. Caicedo, The unique cytoarchitecture of human pancreatic islets has implications for islet cell function, *Proc. Natl. Acad. Sci. U. S. A.* 103 (2006) 2334–2339. <https://doi.org/10.1073/pnas.0510790103>.
- [13] D.J. Steiner, A. Kim, K. Miller, M. Hara, Pancreatic islet plasticity: Interspecies comparison of islet architecture and composition, *Islets.* 2 (2010). <https://doi.org/10.4161/isl.2.3.11815>.
- [14] R. Arrojo e Drigo, Y. Ali, J. Diez, D.K. Srinivasan, P.O. Berggren, B.O. Boehm, New insights into the architecture of the islet of Langerhans: a focused cross-species assessment, *Diabetologia.* 58 (2015) 2218–2228. <https://doi.org/10.1007/s00125->

015-3699-0.

- [15] N. Trivedi, G.M. Steil, C.K. Colton, S. Bonner-Weir, G.C. Weir, Improved Vascularization of Planar Membrane Diffusion Devices following Continuous Infusion of Vascular Endothelial Growth Factor, *Cell Transplant.* 9 (2000) 115–124. <https://doi.org/10.1177/096368970000900114>.
- [16] F. Homo-Delarche, C. Boitard, Autoimmune diabetes: the role of the islets of Langerhans., *Immunol. Today.* 17 (1996) 456–60. <http://www.ncbi.nlm.nih.gov/pubmed/8908809> (accessed October 9, 2019).
- [17] N. Ballian, F.C. Brunicardi, Islet Vasculature as a Regulator of Endocrine Pancreas Function, *World J. Surg.* 31 (2007) 705–714. <https://doi.org/10.1007/s00268-006-0719-8>.
- [18] T.M. Suszynski, E.S. Avgoustiniatos, K.K. Papas, Oxygenation of the Intraportally Transplanted Pancreatic Islet, *J. Diabetes Res.* 2016 (2016). <https://doi.org/10.1155/2016/7625947>.
- [19] S. Bonner-Weir, Morphological evidence for pancreatic polarity of β -cell within islets of Langerhans, *Diabetes.* 37 (1988) 616–621. <https://doi.org/10.2337/diab.37.5.616>.
- [20] K.E. Dionne, C.K. Colton, M.L. Yarmush, Effect of hypoxia on insulin secretion by isolated rat and canine islets of Langerhans., *Diabetes.* 42 (1993) 12–21. <https://doi.org/10.2337/diab.42.1.12>.
- [21] J.E. Gerich, S.D. Wittlin, C. Meyer, Normal Glucose Homeostasis, in: *Princ. Diabetes Mellit.*, Springer US, 2004: pp. 39–56. https://doi.org/10.1007/978-1-4757-6260-0_2.
- [22] J.C. Henquin, Triggering and amplifying pathways of regulation of insulin secretion by glucose, *Diabetes.* 49 (2000) 1751–1760. <https://doi.org/10.2337/diabetes.49.11.1751>.
- [23] D.L. Curry, L.L. Bennett, G.M. Grodsky, Dynamics of insulin secretion by the perfused rat pancreas., *Endocrinology.* 83 (1968) 572–584. <https://doi.org/10.1210/endo-83-3-572>.
- [24] D. Porte, A.A. Pupo, Insulin responses to glucose: evidence for a two pool system in man., *J. Clin. Invest.* 48 (1969) 2309–2319. <https://doi.org/10.1172/JCI106197>.
- [25] E. Cerasi, R. Luft, The plasma insulin response to glucose infusion in healthy subjects and in diabetes mellitus., *Acta Endocrinol. (Copenh).* 55 (1967) 278–304. <https://doi.org/10.1530/acta.0.0550278>.
- [26] P. De Meyts, The Insulin Receptor and Its Signal Transduction Network, MDText.com, Inc., 2000. <http://www.ncbi.nlm.nih.gov/pubmed/27512793> (accessed May 11, 2020).
- [27] P. Moszczyński, Z. Tabarowski, Meal Plans for Diabetics, in: *Nutr. Ther. Interv. Diabetes Metab. Syndr.*, Elsevier, 2018: pp. 403–427. <https://doi.org/10.1016/b978-0-12-812019-4.00032-5>.
- [28] J.W. Ryder, J. Yang, D. Galuska, J. Rincón, M. Björnholm, A. Krook, S. Lund, O. Pedersen, H. Wallberg-Henriksson, J.R. Zierath, G.D. Holman, Use of a novel impermeable biotinylated photolabeling reagent to assess insulin- and hypoxia-stimulated cell surface GLUT4 content in skeletal muscle from type 2 diabetic

- patients, *Diabetes*. 49 (2000) 647–654. <https://doi.org/10.2337/diabetes.49.4.647>.
- [29] R.T. Watson, J.E. Pessin, Intracellular organization of insulin signaling and GLUT4 translocation, *Recent Prog. Horm. Res.* 56 (2001) 175–193. <https://doi.org/10.1210/rp.56.1.175>.
- [30] D.A. Sandoval, D.A. D'Alessio, Physiology of proglucagon peptides: Role of glucagon and GLP-1 in health and disease, *Physiol. Rev.* 95 (2015) 513–548. <https://doi.org/10.1152/physrev.00013.2014>.
- [31] R.H. Unger, L. Orci, Glucagon and the α Cell: Physiology and Pathophysiology, *N. Engl. J. Med.* 304 (1981) 1518–1524. <https://doi.org/10.1056/NEJM198106183042504>.
- [32] S. Hædersdal, A. Lund, F.K. Knop, T. Vilsbøll, The Role of Glucagon in the Pathophysiology and Treatment of Type 2 Diabetes, *Mayo Clin. Proc.* 93 (2018) 217–239. <https://doi.org/10.1016/j.mayocp.2017.12.003>.
- [33] I. Quesada, E. Tudurí, C. Ripoll, Á. Nadal, Physiology of the pancreatic α -cell and glucagon secretion: Role in glucose homeostasis and diabetes, *J. Endocrinol.* 199 (2008) 5–19. <https://doi.org/10.1677/JOE-08-0290>.
- [34] B.E. Dunning, J.E. Foley, B. Ahrén, Alpha cell function in health and disease: Influence of glucagon-like peptide-1, *Diabetologia*. 48 (2005) 1700–1713. <https://doi.org/10.1007/s00125-005-1878-0>.
- [35] S. Barg, Mechanisms of exocytosis in insulin-secreting B-cells and glucagon-secreting A-cells, *Pharmacol. Toxicol.* 92 (2003) 3–13. <https://doi.org/10.1034/j.1600-0773.2003.920102.x>.
- [36] T.D. Müller, B. Finan, C. Clemmensen, R.D. Di Marchi, M.H. Tschöp, The new biology and pharmacology of glucagon, *Physiol. Rev.* 97 (2017) 721–766. <https://doi.org/10.1152/physrev.00025.2016>.
- [37] M.J. Charron, P.M. Vuguin, Lack of glucagon receptor signaling and its implications beyond glucose homeostasis, *J. Endocrinol.* 224 (2015) R123–R130. <https://doi.org/10.1530/JOE-14-0614>.
- [38] F. Von Meyenn, T. Porstmann, E. Gasser, N. Selevsek, A. Schmidt, R. Aebersold, M. Stoffel, Glucagon-induced acetylation of Foxa2 regulates hepatic lipid metabolism, *Cell Metab.* 17 (2013) 436–447. <https://doi.org/10.1016/j.cmet.2013.01.014>.
- [39] International Diabetes Federation, *IDF Diabetes Atlas: Ninth edition 2019*, 2019.
- [40] *Diagnosis and Classification of Diabetes Mellitus*, (2010). <https://doi.org/10.2337/dc10-S062>.
- [41] D.M. Nathan, *Diabetes: Advances in diagnosis and treatment*, *JAMA - J. Am. Med. Assoc.* 314 (2015) 1052–1062. <https://doi.org/10.1001/jama.2015.9536>.
- [42] S.A. White, J.A. Shaw, D.E. Sutherland, Pancreas transplantation, *Lancet*. 373 (2009) 1808–1817. [https://doi.org/10.1016/S0140-6736\(09\)60609-7](https://doi.org/10.1016/S0140-6736(09)60609-7).
- [43] A.D. Association, *Diagnosis and classification of diabetes mellitus*, *Diabetes Care*. 37 (2014) S81–S90. <https://doi.org/10.2337/dc14-S081>.
- [44] *Diagnostic criteria for diabetes* | Diabetes UK, (n.d.). <https://www.diabetes.org.uk/professionals/position-statements-reports/diagnosis->

- ongoing-management-monitoring/new_diagnostic_criteria_for_diabetes (accessed May 18, 2020).
- [45] Diabetes, (n.d.). <https://www.who.int/en/news-room/fact-sheets/detail/diabetes> (accessed May 18, 2020).
- [46] C.H. Courtney, J.M. Olefsky, Insulin resistance, in: *Mech. Insul. Action Med. Intell. Unit*, Springer New York, 2007: pp. 185–209. https://doi.org/10.1007/978-0-387-72204-7_10.
- [47] S. Melmed, K.S. Polonsky, P.R. Larsen, H.M. Kronenberg, Williams textbook of endocrinology, in: Elsevier/Saunders (Ed.), 12th ed., Philadelphia, 2011: pp. 1371–1435.
- [48] O. Aouacheri, S. Saka, M. Krim, A. Messaadia, I. Maldi, The Investigation of the Oxidative Stress-Related Parameters in Type2 Diabetes Mellitus, *Can. J. Diabetes*. 39 (2015) 44–49. <https://doi.org/10.1016/j.jcjd.2014.03.002>.
- [49] Y.C. Shi, T.M. Pan, Red mold, diabetes, and oxidative stress: A review, *Appl. Microbiol. Biotechnol.* 94 (2012) 47–55. <https://doi.org/10.1007/s00253-012-3957-8>.
- [50] Y.M. Khazrai, G. Defeudis, P. Pozzilli, Effect of diet on type 2 diabetes mellitus: A review, *Diabetes. Metab. Res. Rev.* 30 (2014) 24–33. <https://doi.org/10.1002/dmrr.2515>.
- [51] N.M. Maruthur, E. Tseng, S. Hutfless, L.M. Wilson, C. Suarez-Cuervo, Z. Berger, Y. Chu, E. Iyoha, J.B. Segal, S. Bolen, Diabetes medications as monotherapy or metformin-based combination therapy for type 2 diabetes: A systematic review and meta-analysis, *Ann. Intern. Med.* 164 (2016) 740–751. <https://doi.org/10.7326/M15-2650>.
- [52] K. Zhou, H.K. Pedersen, A.Y. Dawed, E.R. Pearson, Pharmacogenomics in diabetes mellitus: Insights into drug action and drug discovery, *Nat. Rev. Endocrinol.* 12 (2016) 337–346. <https://doi.org/10.1038/nrendo.2016.51>.
- [53] C. Li, E.S. Ford, G. Zhao, J. Tsai, L.S. Balluz, W.H. Giles, Trends of insulin use among US adults with type 2 diabetes: The Behavioral Risk Factor Surveillance System, 1995-2007, *J. Diabetes Complications*. 26 (2012) 17–22. <https://doi.org/10.1016/j.jdiacomp.2011.11.005>.
- [54] S. Canivell, R. Gomis, Diagnosis and classification of autoimmune diabetes mellitus, *Autoimmun. Rev.* 13 (2014) 403–407. <https://doi.org/10.1016/j.autrev.2014.01.020>.
- [55] S.A. Paschou, N. Papadopoulou-Marketou, G.P. Chrousos, C. Kanaka-Gantenbein, On type 1 diabetes mellitus pathogenesis, *Endocr. Connect.* 7 (2018) R38–R46. <https://doi.org/10.1530/EC-17-0347>.
- [56] G.L.L. Xin, Y.P. Khee, T.Y. Ying, J. Chellian, G. Gupta, A.P. Kunnath, S. Nammi, T. Collet, P.M. Hansbro, K. Dua, D.K. Chellappan, Current Status on Immunological Therapies for Type 1 Diabetes Mellitus, *Curr. Diab. Rep.* 19 (2019) 22. <https://doi.org/10.1007/s11892-019-1144-3>.
- [57] A. Michels, L. Zhang, A. Khadra, J.A. Kushner, M.J. Redondo, M. Pietropaolo, Prediction and prevention of type 1 diabetes: Update on success of prediction and struggles at prevention, *Pediatr. Diabetes*. 16 (2015) 465–484. <https://doi.org/10.1111/pedi.12299>.

- [58] A.L. Peters, A.J. Ahmann, T. Battelino, A. Evert, I.B. Hirsch, M.H. Murad, W.E. Winter, H. Wolpert, Diabetes technology-continuous subcutaneous insulin infusion therapy and continuous glucose monitoring in adults: An endocrine society clinical practice guideline, *J. Clin. Endocrinol. Metab.* 101 (2016) 3922–3937. <https://doi.org/10.1210/jc.2016-2534>.
- [59] J.E. Yardley, K.E. Iscoe, R.J. Sigal, G.P. Kenny, B.A. Perkins, M.C. Riddell, Insulin Pump Therapy is associated with Less Post-Exercise Hyperglycemia than multiple daily injections: An observational study of physically active type 1 diabetes patients, *Diabetes Technol. Ther.* 15 (2013) 84–88. <https://doi.org/10.1089/dia.2012.0168>.
- [60] S. Little, T. Chadwick, P. Choudhary, C. Brennand, J. Stickland, S. Barendse, T. Olateju, L. Leelarathna, E. Walkinshaw, H.K. Tan, S.M. Marshall, R.M. Thomas, S. Heller, M. Evans, D. Kerr, D. Flanagan, J. Speight, J.A.M. Shaw, Comparison of Optimised MDI versus Pumps with or without Sensors in Severe Hypoglycaemia (the Hypo COMPaSS trial), *BMC Endocr. Disord.* 12 (2012) 33. <https://doi.org/10.1186/1472-6823-12-33>.
- [61] S.H. Golden, T. Sapir, Methods for insulin delivery and glucose monitoring in diabetes: summary of a comparative effectiveness review., *J. Manag. Care Pharm.* 18 (2012). <https://doi.org/10.18553/jmcp.2012.18.s6-a.1>.
- [62] M. Evans, P.M. Schumm-Draeger, J. Vora, A.B. King, A review of modern insulin analogue pharmacokinetic and pharmacodynamic profiles in type 2 diabetes: Improvements and limitations, *Diabetes, Obes. Metab.* 13 (2011) 677–684. <https://doi.org/10.1111/j.1463-1326.2011.01395.x>.
- [63] S. Garg, E. Moser, M.P. Dain, A. Rodionova, Clinical experience with insulin glargine in type 1 diabetes, *Diabetes Technol. Ther.* 12 (2010) 835–846. <https://doi.org/10.1089/dia.2010.0135>.
- [64] R. Coppolino, S. Coppolino, V. Villari, Study of the aggregation of insulin glargine by light scattering, *J. Pharm. Sci.* 95 (2006) 1029–1034. <https://doi.org/10.1002/jps.20609>.
- [65] F. Holleman, J.B.L. Hoekstra, Insulin lispro, *N. Engl. J. Med.* 337 (1997) 176–183. <https://doi.org/10.1056/NEJM199707173370307>.
- [66] A.R. Segal, T. Vootla, R.S. Beaser, Insulin: Making Sense of Current Options, *Endocrinol. Metab. Clin. North Am.* 45 (2016) 845–874. <https://doi.org/10.1016/j.ecl.2016.06.009>.
- [67] P.E. Cryer, Hypoglycaemia: The limiting factor in the glycaemic management of Type I and Type II diabetes, in: *Diabetologia*, 2002: pp. 937–948. <https://doi.org/10.1007/s00125-002-0822-9>.
- [68] C. V. Desouza, G.B. Bolli, V. Fonseca, Hypoglycemia, diabetes, and cardiovascular events, *Diabetes Care.* 33 (2010) 1389–1394. <https://doi.org/10.2337/dc09-2082>.
- [69] N.E. Kittah, A. Vella, Pathogenesis and management of hypoglycemia, *Eur. J. Endocrinol.* 177 (2017) R37–R47. <https://doi.org/10.1530/EJE-16-1062>.
- [70] J.M. Guettier, P. Gorden, Hypoglycemia, *Endocrinol. Metab. Clin. North Am.* 35 (2006) 753–766. <https://doi.org/10.1016/j.ecl.2006.09.005>.
- [71] I. Martín-Timón, Mechanisms of hypoglycemia unawareness and implications in diabetic patients, *World J. Diabetes.* 6 (2015) 912.

- <https://doi.org/10.4239/wjd.v6.i7.912>.
- [72] Pancreas Islet Transplantation for Patients With Type 1 Diabetes Mellitus: A Clinical Evidence Review, *Ont. Health Technol. Assess. Ser.* 15 (2015) 1–84.
- [73] A.M. James Shapiro, Islet transplantation in type 1 diabetes: Ongoing challenges, refined procedures, and long-term outcome, *Rev. Diabet. Stud.* 9 (2012) 385–406. <https://doi.org/10.1900/RDS.2012.9.385>.
- [74] S.F. Clarke, J.R. Foster, A history of blood glucose meters and their role in self-monitoring of diabetes mellitus, *Br. J. Biomed. Sci.* 69 (2012) 83–93. <https://doi.org/10.1080/09674845.2012.12002443>.
- [75] S.R. Patton, M.A. Clements, Continuous Glucose Monitoring Versus Self-monitoring of Blood Glucose in Children with Type 1 Diabetes- Are there Pros and Cons for Both?, *US Endocrinol.* 8 (2012) 27.
- [76] D. Rodbard, T. Bailey, L. Jovanovic, H. Zisser, R. Kaplan, S.K. Garg, Improved quality of glycemic control and reduced glycemic variability with use of continuous glucose monitoring, *Diabetes Technol. Ther.* 11 (2009) 717–723. <https://doi.org/10.1089/dia.2009.0077>.
- [77] M. Lu, Y. Zuo, J. Guo, X. Wen, Y. Kang, Continuous glucose monitoring system can improve the quality of glucose control and glucose variability compared with point-of-care measurement in critically ill patients: A randomized controlled trial, *Med. (United States)*. 97 (2018). <https://doi.org/10.1097/MD.00000000000012138>.
- [78] T.L. Pearson, Practical aspects of insulin pen devices, in: *J. Diabetes Sci. Technol.*, SAGE Publications Inc., 2010: pp. 522–531. <https://doi.org/10.1177/193229681000400304>.
- [79] E.K. McCoy, B.M. Wright, A review of insulin pen devices, *Postgrad. Med.* 122 (2010) 81–88. <https://doi.org/10.3810/pgm.2010.05.2145>.
- [80] D. Bruttomesso, S. Costa, A. Baritussio, Continuous subcutaneous insulin infusion (CSII) 30 years later: Still the best option for insulin therapy, *Diabetes. Metab. Res. Rev.* 25 (2009) 99–111. <https://doi.org/10.1002/dmrr.931>.
- [81] K. Kamoi, M. Miyakoshi, R. Maruyama, A quality-of-life assessment of intensive insulin therapy using insulin lispro switched from short-acting insulin and measured by an ITR-QOL questionnaire: A prospective comparison of multiple daily insulin injections and continuous subcutaneous insulin infusion, in: *Diabetes Res. Clin. Pract.*, Elsevier Ireland Ltd, 2004: pp. 19–25. <https://doi.org/10.1016/j.diabres.2003.10.005>.
- [82] D.A. Ignaut, S.L. Schwartz, S. Sarwat, H.L. Murphy, Comparative device assessments: Humalog KwikPen compared with vial and syringe and FlexPen, *Diabetes Educ.* 35 (2009) 789–798. <https://doi.org/10.1177/0145721709340056>.
- [83] A. Penfornis, K. Horvat, Dose accuracy comparison between SoloSTAR and FlexPen at three different dose levels, *Diabetes Technol. Ther.* 10 (2008) 359–362. <https://doi.org/10.1089/dia.2008.0082>.
- [84] A. Penfornis, Performance of a new reusable insulin pen, *Diabetes Technol. Ther.* 13 (2011) 373–379. <https://doi.org/10.1089/dia.2010.0174>.
- [85] R.W. Beck, T.D. Riddlesworth, K.J. Ruedy, C. Kollman, A.J. Ahmann, R.M. Bergenstal,

- A. Bhargava, B.W. Bode, S. Haller, D.F. Kruger, J.B. McGill, W. Polonsky, D. Price, E. Toschi, E. Toschi, H. Wolpert, A. Atakov-Castillo, E. Markovic, S. Aronoff, S. Brooks, G. Martinez, A. Mendez, T. Dunnam, A. Bhargava, K. Fitzgerald, D. Wright, T. Khoo, P. Theuma, T. Herrold, D. Thomsen, R. Bergenstal, K. McCann, A. Monk, C. Ashanti, D. Liljenquist, H. Judge, J. Halford, D. Kruger, S. Levy, A. Bhan, T. Cushman, L. Dawson, H. Remtema, F. Wolf, J. Neifing, J. Murdoch, S. Staat, T. Mayfield, A. Ahmann, B. Klopfenstein, F. Joarder, K. Hanavan, J. Castle, D. Aby-Daniel, V. Morimoto, D. DeFrang, B. Wollam, J. McGill, O. Jordan, C. Recklein, M. Kipnes, S. Haller, T. Ryan, B. Bode, J. Boyd, N. Rastogi, K. Lindmark, W. Biggs, L. Sandoval, R. Eifert, B. Cota, Q. Nguyen, A. Martinez, C. Duran, S. Segel, D. Sutton, M. Roura, R. Rosenwasser, J. McElveen, E. Knisely, A. Johnson, A.O. Odugbesan, K. Wardell, C. Paulus, J. Wahlen, J. Winkfield, H. Wahlen, E. Hepworth, D. Winkfield, S. Owens, S. Leichter, E. Evans, S. Konigsberg, J. Rahman, L. Gaudiani, N. Woods, J. Cardozo, K. Wheeler, J. Kane, T. Eubanks, K. Ruedy, R.W. Beck, C. Kollman, T. Riddlesworth, T. Mouse, D. Price, E. Casal, C. Graham, W. Polonsky, Effect of initiating use of an insulin pump in adults with type 1 diabetes using multiple daily insulin injections and continuous glucose monitoring (DIAMOND): a multicentre, randomised controlled trial, *Lancet Diabetes Endocrinol.* 5 (2017) 700–708. [https://doi.org/10.1016/S2213-8587\(17\)30217-6](https://doi.org/10.1016/S2213-8587(17)30217-6).
- [86] M. Sasaki, T. Mogi, Y. Wada, I. Hirose, A. Koizumi, An endemic condition of biochemical hypoglycemia among male volunteers, *Ind. Health.* 34 (1996) 323–333. <https://doi.org/10.2486/indhealth.34.323>.
- [87] B.H. Ginsberg, Patch Pumps for Insulin, *J. Diabetes Sci. Technol.* 13 (2019) 27–33. <https://doi.org/10.1177/1932296818786513>.
- [88] B. McAdams, A. Rizvi, An Overview of Insulin Pumps and Glucose Sensors for the Generalist, *J. Clin. Med.* 5 (2016) 5. <https://doi.org/10.3390/jcm5010005>.
- [89] The Omnipod® System | Omnipod® Insulin Management, (n.d.). <https://www.myomnipod.com/Omnipod-system> (accessed May 22, 2020).
- [90] Debiotech, (n.d.). https://www.debiotech.com/page/index.php?page=product_01&id=1&id_prod=40 (accessed May 22, 2020).
- [91] Solo | Accu-Chek.co.uk, (n.d.). <https://www.accu-chek.co.uk/insulin-pumps/solo> (accessed May 22, 2020).
- [92] BD Libertas™ Wearable Autoinjector - BD, (n.d.). <https://drugdeliversystems.bd.com/products/self-injection-systems/libertas-wearable-autoinjector> (accessed May 22, 2020).
- [93] MiniMed 670G Insulin Pump System | Medtronic Diabetes, (n.d.). <https://www.medtronicdiabetes.com/products/minimed-670g-insulin-pump-system> (accessed May 22, 2020).
- [94] A. Penforinis, E. Personeni, S. Borot, Evolution of devices in diabetes management., *Diabetes Technol. Ther.* 13 Suppl 1 (2011). <https://doi.org/10.1089/dia.2011.0058>.
- [95] L. Hinshaw, C.D. Man, D.K. Nandy, A. Saad, A.E. Bharucha, J.A. Levine, R.A. Rizza, R. Basu, R.E. Carter, C. Cobelli, Y.C. Kudva, A. Basu, Diurnal pattern of insulin action in type 1 diabetes implications for a closed-Loop system, *Diabetes.* 62 (2013) 2223–2229. <https://doi.org/10.2337/db12-1759>.

- [96] Jones RW, Gianni F, Despotou G, Katzis K, The Artificial Pancreas: Reducing Safety Risk via Intra-Peritoneal Insulin Delivery. - PubMed - NCBI, *Stud Heal. Technol Inform.* 238 (2017) 56–59. <https://www.ncbi.nlm.nih.gov/pubmed/28679886> (accessed May 18, 2020).
- [97] L. Heinemann, A. Stuhr, Self-measurement of Blood Glucose and Continuous Glucose Monitoring – Is There Only One Future?, *Eur. Endocrinol.* 14 (2018) 24. <https://doi.org/10.17925/ee.2018.14.2.24>.
- [98] A. Weisman, J.W. Bai, M. Cardinez, C.K. Kramer, B.A. Perkins, Effect of artificial pancreas systems on glycaemic control in patients with type 1 diabetes: a systematic review and meta-analysis of outpatient randomised controlled trials, *Lancet Diabetes Endocrinol.* 5 (2017) 501–512. [https://doi.org/10.1016/S2213-8587\(17\)30167-5](https://doi.org/10.1016/S2213-8587(17)30167-5).
- [99] Artificial Pancreas Device System Market Worth \$2000 Million by 2025 Exclusive Report by Infinium Global Research | Medgadget, (n.d.). <https://www.medgadget.com/2019/07/artificial-pancreas-device-system-market-worth-2000-million-by-2025-exclusive-report-by-infinium-global-research.html> (accessed May 26, 2020).
- [100] C. Cobelli, E. Renard, B. Kovatchev, Artificial pancreas: Past, present, future, *Diabetes.* 60 (2011) 2672–2682. <https://doi.org/10.2337/db11-0654>.
- [101] Pancreas and islet transplantation in type 1 diabetes, *Diabetes Care.* 29 (2006) 935. <https://doi.org/10.2337/diacare.29.04.06.dc06-9908>.
- [102] D.C. Hsu, C.H. Katelaris, Long-term management of patients taking immunosuppressive drugs, *Aust. Prescr.* 32 (2009) 68–71. <https://doi.org/10.18773/austprescr.2009.035>.
- [103] C.D. Holt, Overview of Immunosuppressive Therapy in Solid Organ Transplantation, *Anesthesiol. Clin.* 35 (2017) 365–380. <https://doi.org/10.1016/j.anclin.2017.04.001>.
- [104] N.M. Blondet, P.J. Healey, E. Hsu, Immunosuppression in the pediatric transplant recipient, *Semin. Pediatr. Surg.* 26 (2017) 193–198. <https://doi.org/10.1053/j.sempedsurg.2017.07.009>.
- [105] M.P. Gallagher, P.J. Kelly, M. Jardine, V. Perkovic, A. Cass, J.C. Craig, J. Eris, A.C. Webster, Long-term cancer risk of immunosuppressive regimens after kidney transplantation, *J. Am. Soc. Nephrol.* 21 (2010) 852–858. <https://doi.org/10.1681/ASN.2009101043>.
- [106] P.G. Dean, A. Kukla, M.D. Stegall, Y.C. Kudva, Pancreas transplantation, *BMJ.* 357 (2017). <https://doi.org/10.1136/bmj.j1321>.
- [107] S.S. Kim, J.H. Kim, I.J. Kim, Current challenges in diabetic nephropathy: Early diagnosis and ways to improve Outcomes, *Endocrinol. Metab.* 31 (2016) 245–253. <https://doi.org/10.3803/EnM.2016.31.2.245>.
- [108] R. Kandaswamy, P.G. Stock, S.K. Gustafson, M.A. Skeans, R. Urban, A. Fox, A.K. Israni, J.J. Snyder, B.L. Kasiske, OPTN/SRTR 2018 Annual Data Report: Pancreas, *Am. J. Transplant.* 20 (2020) 131–192. <https://doi.org/10.1111/ajt.15673>.
- [109] W.F. Ballinger, P.E. Lacy, Transplantation of intact pancreatic islets in rats, *Surgery.* 72 (1972) 175–186. <https://doi.org/10.5555/uri:pii:0039606072903315>.

- [110] C. Barker, C. Reckard, M. Ziegler, A. Naji, Liver as an immunologically privileged site for rat pancreatic-islet allografts., *Diabetes*. 2 (1975) 418. https://books.google.ie/books?id=UJPuBwAAQBAJ&pg=PA221&lpg=PA221&dq=barker+the+Liver+as+an+immunologically+privileged+site+for+rat+pancreatic-islet+allografts.&source=bl&ots=hERXO0NuGY&sig=ACfU3U3FFicRF1pPzaljtBkctm0xfKvV_w&hl=en&sa=X&ved=2ahUKewiRsf-Uy-XpAhWOT8AKHVZFASQQ6AEwAHoECACQAQ#v=onepage&q=barker+the+Liver+as+an+immunologically+privileged+site+for+rat+pancreatic-islet+allografts.&f=false (accessed June 3, 2020).
- [111] G.J. Kretschmer, D.R. Sutherland, A.J. Matas, W.D. Payne, J.S. Najarian, Autotransplantation of pancreatic fragments to the portal vein and spleen of totally pancreatectomized dogs: a comparative evaluation., *Ann. Surg.* 187 (1978) 79–86. <https://doi.org/10.1097/00000658-197801000-00015>.
- [112] J.S. Najarian, D.E.R. Sutherland, D. Baumgartner, B. Burke, J.J. Rynasiewicz, A.J. Matas, F.C. Goetz, Total or near total pancreatectomy and islet autotransplantation for treatment of chronic pancreatitis, *Ann. Surg.* 192 (1980) 526–542. <https://doi.org/10.1097/00000658-198010000-00011>.
- [113] M.R. Rickels, R.P. Robertson, Pancreatic Islet Transplantation in Humans: Recent Progress and Future Directions, *Endocr. Rev.* 40 (2019) 631–668. <https://doi.org/10.1210/er.2018-00154>.
- [114] D.W.R. Gray, P. McShane, A. Grant, P.J. Morris, A method for isolation of islets of Langerhans from the human pancreas, *Diabetes*. 33 (1984) 1055–1061. <https://doi.org/10.2337/diab.33.11.1055>.
- [115] G.L. Warnock, D. Ellis, R. V. Rajotte, I. Dawidson, S. Baekkeskov, J. Egebjerg, Studies of the isolation and viability of human islets of langerhans, *Transplantation*. 45 (1988) 957–963. <https://doi.org/10.1097/00007890-198805000-00024>.
- [116] C. Ricordi, P.E. Lacy, E.H. Finke, B.J. Olack, D.W. Scharp, Automated method for isolation of human pancreatic islets, *Diabetes*. 37 (1988) 413–420. <https://doi.org/10.2337/diab.37.4.413>.
- [117] M. Qi, B. Barbaro, S. Wang, Y. Wang, M. Hansen, J. Oberholzer, Human pancreatic islet isolation: Part I: Digestion and collection of pancreatic tissue, *J. Vis. Exp.* (2009). <https://doi.org/10.3791/1125>.
- [118] G. Bötticher, D. Sturm, F. Ehehalt, K.P. Knoch, S. Kersting, R. Grützmann, G.B. Baretton, M. Solimena, H.D. Saeger, Isolation of human islets from partially pancreatectomized patients, *J. Vis. Exp.* (2011). <https://doi.org/10.3791/2962>.
- [119] D.W. Scharp, P.E. Lacy, J. V. Santiago, C.S. McCullough, L.G. Weide, L. Falqui, P. Marchetti, R.L. Gingerich, A.S. Jaffe, P.E. Cryer, C.B. Anderson, M.W. Flye, Insulin independence after islet transplantation into type I diabetic patient, *Diabetes*. 39 (1990) 515–518. <https://doi.org/10.2337/diab.39.4.515>.
- [120] C. Ricordi, D.W.R. Gray, B.J. Hering, D.B. Kaufman, G.L. Warnock, N.M. Kneteman, S.P. Lake, N.J.M. London, C. Socci, R. Alejandro, Y. Zeng, D.W. Scharp, G. Viviani, L. Falqui, A. Tzakis, R.G. Bretzel, K. Federlin, G. Pozza, R.F.L. James, R. V. Rajotte, V. Di Carlo, P.J. Morris, D.E.R. Sutherland, T.E. Starzl, D.H. Mintz, P.E. Lacy, Islet isolation assessment in man and large animals, *Acta Diabetol. Lat.* 27 (1990) 185–195. <https://doi.org/10.1007/BF02581331>.

- [121] H.H. Huang, S. Harrington, L. Stehno-Bittel, The Flaws and Future of Islet Volume Measurements, *Cell Transplant.* 27 (2018) 1017–1026. <https://doi.org/10.1177/0963689718779898>.
- [122] A.J. Ahearn, J.R. Parekh, A.M. Posselt, Islet transplantation for Type 1 diabetes: Where are we now?, *Expert Rev. Clin. Immunol.* 11 (2014) 59–68. <https://doi.org/10.1586/1744666X.2015.978291>.
- [123] A.M.J. Shapiro, J.R.T. Lakey, E.A. Ryan, G.S. Korbutt, E. Toth, G.L. Warnock, N.M. Kneteman, R. V. Rajotte, Islet Transplantation in Seven Patients with Type 1 Diabetes Mellitus Using a Glucocorticoid-Free Immunosuppressive Regimen, *N. Engl. J. Med.* 343 (2000) 230–238. <https://doi.org/10.1056/NEJM200007273430401>.
- [124] C.B. Kemp, M.J. Knight, D.W. Scharp, P.E. Lacy, W.F. Ballinger, Transplantation of isolated pancreatic islets into the portal vein of diabetic Rats, *Nature.* 244 (1973) 447. <https://doi.org/10.1038/244447a0>.
- [125] A. Agarwal, K.L. Brayman, Update on islet cell transplantation for type 1 diabetes, *Semin. Intervent. Radiol.* 29 (2012) 90–98. <https://doi.org/10.1055/s-0032-1312569>.
- [126] Y. Zeng, C. Ricordi, J. Lendoire, P.B. Carroll, R. Alejandro, D.R. Bereiter, A. Tzakis, T.E. Starzl, The effect of prednisone on pancreatic islet autografts in dogs, *Surgery.* 113 (1993) 98–102. <https://doi.org/10.5555/uri:pii:003960609390150C>.
- [127] E.A. Ryan, D. Bigam, A.M.J. Shapiro, Current indications for pancreas or islet transplant, *Diabetes, Obes. Metab.* 8 (2006) 1–7. <https://doi.org/10.1111/j.1463-1326.2004.00460.x>.
- [128] A.A. Chentoufi, V. Geenen, N. Giannokakis, A. Amrani, Type 1 Diabetes Immunological Tolerance and Immunotherapy, *Clin. Dev. Immunol.* 2011 (2011). <https://doi.org/10.1155/2011/103738>.
- [129] S. Merani, C. Toso, J. Emamaullee, A.M.J. Shapiro, Optimal implantation site for pancreatic islet transplantation, *Br. J. Surg.* 95 (2008) 1449–1461. <https://doi.org/10.1002/bjs.6391>.
- [130] A.R. Pepper, B. Gala-Lopez, O. Ziff, A.M.J. Shapiro, Revascularization of transplanted pancreatic islets and role of the transplantation site., *Clin. Dev. Immunol.* 2013 (2013) 352315. <https://doi.org/10.1155/2013/352315>.
- [131] P.T.J. Hwang, D.K. Shah, J.A. Garcia, C.Y. Bae, D.-J. Lim, R.C. Huiszoon, G.C. Alexander, H.-W. Jun, Progress and challenges of the bioartificial pancreas, *Nano Converg.* 3 (2016). <https://doi.org/10.1186/s40580-016-0088-4>.
- [132] J.S. Kaddis, J.S. Danobeitia, J.C. Niland, T. Stiller, L.A. Fernandez, Multicenter analysis of novel and established variables associated with successful human islet isolation outcomes, *Am. J. Transplant.* 10 (2010) 646–656. <https://doi.org/10.1111/j.1600-6143.2009.02962.x>.
- [133] Z. Berkova, F. Saudek, P. Girman, K. Zacharovova, J. Kriz, E. Fabryova, I. Leontovyc, T. Koblas, L. Kosinova, T. Neskudla, E. Vavrova, D. Habart, S. Loukotova, M. Zahradnicka, K. Lipar, L. Voska, J. Skibova, Combining Donor Characteristics with Immunohistological Data Improves the Prediction of Islet Isolation Success, *J. Diabetes Res.* 2016 (2016). <https://doi.org/10.1155/2016/4214328>.
- [134] Organ Donation Transplant Ireland (ODTI) Publishes Annual Report 2018 - HSE.ie, (n.d.). <https://www.hse.ie/eng/services/news/media/pressrel/organ-donation->

- transplant-ireland-odti-publishes-annual-report-2018.html (accessed June 4, 2020).
- [135] M. Dhanasekaran, J.J. George, G. Loganaan, S. Narayanan, M.G. Hughes, S.K. Williams, A.N. Balamurugan, Pig islet xenotransplantation, *Curr. Opin. Organ Transplant.* 22 (2017) 452–462. <https://doi.org/10.1097/MOT.0000000000000455>.
- [136] C.G. Groth, A. Tibell, J. Tollemar, J. Bolinder, J. Östman, E. Möller, F.P. Reinholt, O. Korsgren, C. Hellerström, A. Andersson, Transplantation of porcine fetal pancreas to diabetic patients, *Lancet.* 344 (1994) 1402–1404. [https://doi.org/10.1016/S0140-6736\(94\)90570-3](https://doi.org/10.1016/S0140-6736(94)90570-3).
- [137] B. Richter, G. Neises, “Human” insulin versus animal insulin in people with diabetes mellitus, *Cochrane Database Syst. Rev.* (2005). <https://doi.org/10.1002/14651858.cd003816.pub2>.
- [138] A. Kim, K. Miller, J. Jo, G. Kilimnik, P. Wojcik, M. Hara, Islet architecture: A comparative study., *Islets.* 1 (2009) 129–136. <https://doi.org/10.4161/isl.1.2.9480>.
- [139] B.J. Hering, M. Wijkstrom, M.L. Graham, M. Hårdstedt, T.C. Aasheim, T. Jie, J.D. Ansite, M. Nakano, J. Cheng, W. Li, K. Moran, U. Christians, C. Finnegan, C.D. Mills, D.E. Sutherland, P. Bansal-Pakala, M.P. Murtaugh, N. Kirchof, H.J. Schuurman, Prolonged diabetes reversal after intraportal xenotransplantation of wild-type porcine islets in immunosuppressed nonhuman primates, *Nat. Med.* 12 (2006) 301–303. <https://doi.org/10.1038/nm1369>.
- [140] K. Cardona, G.S. Korbitt, Z. Milas, J. Lyon, J. Cano, W. Jiang, H. Bello-Laborn, B. Hacquoil, E. Strobert, S. Gangappa, C.J. Weber, T.C. Pearson, R. V. Rajotte, C.P. Larsen, Long-term survival of neonatal porcine islets in nonhuman primates by targeting costimulation pathways, *Nat. Med.* 12 (2006) 304–306. <https://doi.org/10.1038/nm1375>.
- [141] D.J. Van Der Windt, R. Bottino, A. Casu, N. Campanile, C. Smetanka, J. He, N. Murase, H. Hara, S. Ball, B.E. Loveland, D. Ayares, F.G. Lakkis, D.K.C. Cooper, M. Trucco, Long-term controlled normoglycemia in diabetic non-human primates after transplantation with hCD46 transgenic porcine islets, *Am. J. Transplant.* 9 (2009) 2716–2726. <https://doi.org/10.1111/j.1600-6143.2009.02850.x>.
- [142] J. Denner, Paving the path toward porcine organs for transplantation, *N. Engl. J. Med.* 377 (2017) 1891–1893. <https://doi.org/10.1056/NEJMcibr1710853>.
- [143] Z. Liu, W. Hu, T. He, Y. Dai, H. Hara, R. Bottino, D.K.C. Cooper, Z. Cai, L. Mou, Pig-to-primate islet xenotransplantation: Past, present, and future, *Cell Transplant.* 26 (2017) 925–947. <https://doi.org/10.3727/096368917X694859>.
- [144] E. Kemter, J. Denner, E. Wolf, Will Genetic Engineering Carry Xenotransplantation of Pig Islets to the Clinic?, *Curr. Diab. Rep.* 18 (2018). <https://doi.org/10.1007/s11892-018-1074-5>.
- [145] J.R. Millman, F.W. Pagliuca, Autologous pluripotent stem cell-derived β -like cells for diabetes cellular therapy, *Diabetes.* 66 (2017) 1111–1120. <https://doi.org/10.2337/db16-1406>.
- [146] J.R. Millman, C. Xie, A. Van Dervort, M. Gürtler, F.W. Pagliuca, D.A. Melton, Generation of stem cell-derived β -cells from patients with type 1 diabetes, *Nat. Commun.* 7 (2016). <https://doi.org/10.1038/ncomms11463>.
- [147] H.M. Shahjalal, A. Abdal Dayem, K.M. Lim, T. Il Jeon, S.G. Cho, Generation of

- pancreatic β cells for treatment of diabetes: Advances and challenges, *Stem Cell Res. Ther.* 9 (2018). <https://doi.org/10.1186/s13287-018-1099-3>.
- [148] K. Cierpka-Kmiec, A. Wronska, Z. Kmiec, In vitro generation of pancreatic β -cells for diabetes treatment. I. β -like cells derived from human pluripotent stem cells, *Folia Histochem. Cytobiol.* 57 (2019) 1–14. <https://doi.org/10.5603/FHC.a2019.0001>.
- [149] K.G. Maxwell, P. Augsornworawat, L. Velazco-Cruz, M.H. Kim, R. Asada, N.J. Hoglebe, S. Morikawa, F. Urano, J.R. Millman, Gene-edited human stem cell–derived β cells from a patient with monogenic diabetes reverse preexisting diabetes in mice, *Sci. Transl. Med.* 12 (2020). <https://doi.org/10.1126/scitranslmed.aax9106>.
- [150] Top Companies Developing Cell Therapy Treatments For Diabetes, (n.d.).
- [151] SERAXIS Inc . publishes clinical trial considerations for a type 1 diabetes stem cell–derived therapy, (2018).
- [152] S. Therapeutics, Semma Therapeutics Announces Pre-Clinical Proof-Of-Concept In Two Lead Programs In Type 1 Diabetes, (2019).
- [153] E. Cairns, Vertex spends nearly \$ 1bn on Semma ' s unproven diabetes cell tech, (2019) 2018–2019.
- [154] E. Bender, Biotechs Race to Develop Stem Cell Treatments for Diabetes, (2019) 1–6.
- [155] M. Qi, Transplantation of Encapsulated Pancreatic Islets as a Treatment for Patients with Type 1 Diabetes Mellitus, *Adv. Med.* 2014 (2014). <https://doi.org/10.1155/2014/429710>.
- [156] R.T. Prehn, J.M. Weaver, G.H. Algire, Diffusion-Chamber Technique Applied to a Study of the Nature of Homograft Resistance | *JNCI: Journal of the National Cancer Institute* | Oxford Academic, *J. Natl. Cancer Inst.* 15 (1954) 509–517. <https://academic.oup.com/jnci/article-abstract/15/3/509/1265406?redirectedFrom=PDF> (accessed June 8, 2020).
- [157] Koo J, Chang T M, Secretion of Erythropoietin From Microencapsulated Rat Kidney Cells: Preliminary Results - PubMed, *Int. J. Artif. Organs.* 16 (1993) 557–560. <https://pubmed.ncbi.nlm.nih.gov/8370612/> (accessed June 8, 2020).
- [158] T.M.S. Chang, Semipermeable microcapsules, *Science* (80-.). 146 (1964) 524–525. <https://doi.org/10.1126/science.146.3643.524>.
- [159] D.A. Cieslinski, H. David Humes, Tissue engineering of a bioartificial kidney, *Biotechnol. Bioeng.* 43 (1994) 678–681. <https://doi.org/10.1002/bit.260430718>.
- [160] H. Wong, T.M. Chang, Bioartificial Liver: Implanted Artificial Cells Microencapsulated Living Hepatocytes Increases Survival of Liver Failure Rats - PubMed, *Int. J. Artif. Organs.* 9 (1986) 335–336. <https://pubmed.ncbi.nlm.nih.gov/3781665/> (accessed June 8, 2020).
- [161] P. Aebischer, M. Goddard, A.P. Signore, R.L. Timpson, Functional recovery in hemiparkinsonian primates transplanted with polymer-encapsulated PC12 cells, *Exp. Neurol.* 126 (1994) 151–158. <https://doi.org/10.1006/exnr.1994.1053>.
- [162] J.L. Foster, G. Williams, L.J. Williams, B.E. Tuch, Differentiation of transplanted microencapsulated fetal pancreatic cells, *Transplantation.* 83 (2007) 1440–1448. <https://doi.org/10.1097/01.tp.0000264555.46417.7d>.

- [163] T. Meyer, B. Höcht, K. Ulrichs, Xenogeneic islet transplantation of microencapsulated porcine islets for therapy of type I diabetes: Long-term normoglycemia in STZ-diabetic rats without immunosuppression, in: *Pediatr. Surg. Int.*, *Pediatr Surg Int*, 2008: pp. 1375–1378. <https://doi.org/10.1007/s00383-008-2267-9>.
- [164] A.G. Abalovich, M.C. Bacqué, D. Grana, J. Milei, Pig Pancreatic Islet Transplantation Into Spontaneously Diabetic Dogs, *Transplant. Proc.* 41 (2009) 328–330. <https://doi.org/10.1016/j.transproceed.2008.08.159>.
- [165] T. Wang, J. Adcock, W. Kühtreiber, D. Qiang, K.J. Salleng, I. Trenary, P. Williams, Successful allotransplantation of encapsulated islets in pancreatectomized canines for diabetic management without the use of immunosuppression, *Transplantation.* 85 (2008) 331–337. <https://doi.org/10.1097/TP.0b013e3181629c25>.
- [166] R.B. Elliott, L. Escobar, R. Calafiore, G. Basta, O. Garkavenko, A. Vasconcellos, C. Bambra, Transplantation of micro- and macroencapsulated piglet islets into mice and monkeys, in: *Transplant. Proc.*, Elsevier USA, 2005: pp. 466–469. <https://doi.org/10.1016/j.transproceed.2004.12.198>.
- [167] D. Dufrane, R.M. Goebbels, A. Saliez, Y. Guiot, P. Gianello, Six-month survival of microencapsulated pig islets and alginate biocompatibility in primates: Proof of concept, *Transplantation.* 81 (2006) 1345–1353. <https://doi.org/10.1097/01.tp.0000208610.75997.20>.
- [168] T. Desai, L.D. Shea, Advances in islet encapsulation technologies., *Nat. Rev. Drug Discov.* 16 (2017) 338–350. <https://doi.org/10.1038/nrd.2016.232>.
- [169] G. Langlois, J. Dusseault, S. Bilodeau, S.K. Tam, D. Magassouba, J.P. Hallé, Direct effect of alginate purification on the survival of islets immobilized in alginate-based microcapsules, *Acta Biomater.* 5 (2009) 3433–3440. <https://doi.org/10.1016/j.actbio.2009.05.029>.
- [170] H. Iwata, H. Amemiya, T. Matsuda, H. Takano, R. Hayashi, T. Akutsu, Evaluation of microencapsulated islets in agarose gel as bioartificial pancreas by studies of hormone secretion in culture and by xenotransplantation, *Diabetes.* 38 (1989) 224–225. <https://doi.org/10.2337/diab.38.1.s224>.
- [171] B. A. Zielinski, P. Aebischer, Chitosan as a matrix for mammalian cell encapsulation, *Biomaterials.* 15 (1994) 1049–1056. [https://doi.org/10.1016/0142-9612\(94\)90090-6](https://doi.org/10.1016/0142-9612(94)90090-6).
- [172] G.M. Cruise, O.D. Hegre, F. V Lamberti, S.R. Hager, R. Hill, D.S. Scharp, J.A. Hubbell, In vitro and in vivo performance of porcine islets encapsulated in interfacially photopolymerized poly(ethylene glycol) diacrylate membranes., *Cell Transplant.* 8 (1999) 293–306. <https://doi.org/10.1177/096368979900800310>.
- [173] F. Lim, A.M. Sun, Microencapsulated islets as bioartificial endocrine pancreas, *Science (80-).* 210 (1980) 908–910. <https://doi.org/10.1126/science.6776628>.
- [174] R. Calafiore, G. Basta, Clinical application of microencapsulated islets: Actual perspectives on progress and challenges, *Adv. Drug Deliv. Rev.* 67–68 (2014) 84–92. <https://doi.org/10.1016/j.addr.2013.09.020>.
- [175] B.E. Tuch, G.W. Keogh, L.J. Williams, W. Wu, J.L. Foster, V. Vaithilingam, R. Philips, Safety and viability of microencapsulated human islets transplanted into diabetic

- humans, *Diabetes Care*. 32 (2009) 1887–1889. <https://doi.org/10.2337/dc09-0744>.
- [176] G.D. Prestwich, Engineering a clinically-useful matrix for cell therapy, *Organogenesis*. 4 (2008) 42–47. <https://doi.org/10.4161/org.6152>.
- [177] J.A. Burdick, G.D. Prestwich, Hyaluronic acid hydrogels for biomedical applications, *Adv. Mater.* 23 (2011). <https://doi.org/10.1002/adma.201003963>.
- [178] C.F. Gotfredsen, M.G. Stewart, G.M. O’Shea, J.R. Vose, T. Horn, A.J. Moody, The Fate of Transplanted Encapsulated Islets in Spontaneously Diabetic BB/Wor Rats - PubMed, *Diabetes Res.* 15 (1990) 157–163. <https://pubmed.ncbi.nlm.nih.gov/2132404/> (accessed June 8, 2020).
- [179] A.L. Hillberg, K. Kathirgamanathan, J.B. Lam, L.Y. Law, O. Garkavenko, R.B. Elliott, Improving alginate-poly-L-ornithine-alginate capsule biocompatibility through genipin crosslinking, *J. Biomed. Mater. Res. - Part B Appl. Biomater.* 101 B (2013) 258–268. <https://doi.org/10.1002/jbm.b.32835>.
- [180] J.H. Brauker, V.E. Carr-Brendel, L.A. Martinson, J. Crudele, W.D. Johnston, R.C. Johnson, Neovascularization of synthetic membranes directed by membrane microarchitecture, *J. Biomed. Mater. Res.* 29 (1995) 1517–1524. <https://doi.org/10.1002/jbm.820291208>.
- [181] P. Tolekis, Sernova’s Diabetes Cell Therapy Platform Technologies, 2010.
- [182] A.R. Pepper, R. Pawlick, B. Gala-Lopez, A. MacGillivray, D.M. Mazzuca, D.J.G. White, P.M. Toleikis, A.M. James Shapiro, Diabetes is reversed in a murine model by marginal mass syngeneic islet transplantation using a subcutaneous cell pouch device, *Transplantation*. 99 (2015) 2294–2300. <https://doi.org/10.1097/TP.0000000000000864>.
- [183] P.E. Lacy, O.D. Hegre, A. Gerasimidi-Vazeou, F.T. Gentile, K.E. Dionne, Maintenance of normoglycemia in diabetic mice by subcutaneous xenografts of encapsulated islets., *Science*. 254 (1991) 1782–4.
- [184] A.P. Monaco, T. Maki, H. Ozato, M. Carretta, S.J. Sullivan, K.M. Borland, M.D. Mahoney, W.L. Chick, T.E. Muller, J. Wolfrum, Transplantation of islet allografts and xenografts in totally pancreatectomized diabetic dogs using the hybrid artificial pancreas., *Ann. Surg.* 214 (1991) 339–60; discussion 361-2.
- [185] R. Storrs, R. Dorian, S.R. King, J. Lakey, H. Rilo, Preclinical development of the Islet Sheet., *Ann. N. Y. Acad. Sci.* 944 (2001) 252–66.
- [186] J.C. Stendahl, D.B. Kaufman, S.I. Stupp, Extracellular matrix in pancreatic islets: relevance to scaffold design and transplantation., *Cell Transplant.* 18 (2009) 1–12.
- [187] D.W. Scharp, N.S. Mason, R.E. Sparks, Islet immuno-isolation: The use of hybrid artificial organs to prevent islet tissue rejection, *World J. Surg.* 8 (1984) 221–229. <https://doi.org/10.1007/BF01655139>.
- [188] H. Ohgawara, S. Hirotani, J.I. Miyazaki, S. Teraoka, Membrane immunoisolation of a diffusion chamber for a bioartificial pancreas, *Artif. Organs*. 22 (1998) 788–794. <https://doi.org/10.1046/j.1525-1594.1998.06185.x>.
- [189] S. Song, G. Faleo, R. Yeung, R. Kant, A.M. Posselt, T.A. Desai, Q. Tang, S. Roy, Silicon nanopore membrane (SNM) for islet encapsulation and immunoisolation under convective transport, *Sci. Rep.* 6 (2016) 1–9. <https://doi.org/10.1038/srep23679>.

- [190] E.S. O'Sullivan, A. Vegas, D.G. Anderson, G.C. Weir, Islets transplanted in immunoisolation devices: A review of the progress and the challenges that remain, *Endocr. Rev.* 32 (2011) 827–844. <https://doi.org/10.1210/er.2010-0026>.
- [191] C.K. Colton, Oxygen supply to encapsulated therapeutic cells, *Adv. Drug Deliv. Rev.* 67–68 (2014) 93–110. <https://doi.org/10.1016/J.ADDR.2014.02.007>.
- [192] R. Krishnan, M. Alexander, L. Robles, C.E. Foster, J.R.T. Lakey, Islet and stem cell encapsulation for clinical transplantation., *Rev. Diabet. Stud.* 11 (2014) 84–101. <https://doi.org/10.1900/RDS.2014.11.84>.
- [193] D.M. Berman, J.J. O'Neil, L.C.K. Coffey, P.C.J. Chaffanjon, N.M. Kenyon, P. Ruiz, A. Pileggi, C. Ricordi, N.S. Kenyon, Long-term survival of nonhuman primate islets implanted in an omental pouch on a biodegradable scaffold, *Am. J. Transplant.* 9 (2009) 91–104. <https://doi.org/10.1111/j.1600-6143.2008.02489.x>.
- [194] P. De Vos, A.F. Hamel, K. Tatarkiewicz, Considerations for successful transplantation of encapsulated pancreatic islets, in: *Diabetologia*, *Diabetologia*, 2002: pp. 159–173. <https://doi.org/10.1007/s00125-001-0729-x>.
- [195] E. Polykandriotis, A. Arkudas, S. Euler, J.P. Beier, R.E. Horch, U. Kneser, Prävascularisationsstrategien im tissue engineering, *Handchirurgie Mikrochirurgie Plast. Chir.* 38 (2006) 217–223. <https://doi.org/10.1055/s-2006-924419>.
- [196] D.W. Scharp, P. Marchetti, Encapsulated islets for diabetes therapy: History, current progress, and critical issues requiring solution, *Adv. Drug Deliv. Rev.* 67–68 (2014) 35–73. <https://doi.org/10.1016/j.addr.2013.07.018>.
- [197] C.K. Colton, Oxygen supply to encapsulated therapeutic cells, *Adv. Drug Deliv. Rev.* 67–68 (2014) 93–110. <https://doi.org/10.1016/j.addr.2014.02.007>.
- [198] J.M. Anderson, Inflammatory response to implants., *ASAIO Trans.* 34 (n.d.) 101–7.
- [199] J.M. Anderson, Chapter 4 Mechanisms of inflammation and infection with implanted devices, *Cardiovasc. Pathol.* 2 (1993) 33–41. [https://doi.org/10.1016/1054-8807\(93\)90045-4](https://doi.org/10.1016/1054-8807(93)90045-4).
- [200] R.. Cotran, V. Kumar, S.. Robbins, Inflammation and repair, in: *Pathol. Basis Dis.*, 4th ed., W.B. Saunders, Philadelphia, 1989: pp. 33–86.
- [201] J. Gallin, I. Goldstein, R. Snyderman, *Inflammation: Basic Principles and Clinical Correlates*, Raven Press, New York, 1988.
- [202] L. Vroman, A.L. Adams, G.C. Fischer, P.C. Munoz, Interaction of high molecular weight kininogen, factor XII, and fibrinogen in plasma at interfaces., *Blood.* 55 (1980) 156–9.
- [203] A.J. Vegas, O. Veiseh, J.C. Doloff, M. Ma, H.H. Tam, K. Bratlie, J. Li, A.R. Bader, E. Langan, K. Olejnik, P. Fenton, J.W. Kang, J. Hollister-Locke, M.A. Bochenek, A. Chiu, S. Siebert, K. Tang, S. Jhunhunwala, S. Aresta-Dasilva, N. Dholakia, R. Thakrar, T. Vietti, M. Chen, J. Cohen, K. Siniakowicz, M. Qi, J. McGarrigle, S. Lyle, D.M. Harlan, D.L. Greiner, J. Oberholzer, G.C. Weir, R. Langer, D.G. Anderson, Combinatorial hydrogel library enables identification of materials that mitigate the foreign body response in primates, *Nat. Biotechnol.* 34 (2016) 345–352. <https://doi.org/10.1038/nbt.3462>.
- [204] J.C. Doloff, O. Veiseh, A.J. Vegas, H.H. Tam, S. Farah, M. Ma, J. Li, A. Bader, A. Chiu,

- A. Sadraei, S. Aresta-Dasilva, M. Griffin, S. Jhunjunwala, M. Webber, S. Siebert, K. Tang, M. Chen, E. Langan, N. Dholokia, R. Thakrar, M. Qi, J. Oberholzer, D.L. Greiner, R. Langer, D.G. Anderson, Colony stimulating factor-1 receptor is a central component of the foreign body response to biomaterial implants in rodents and non-human primates., *Nat. Mater.* 16 (2017) 671–680.
<https://doi.org/10.1038/nmat4866>.
- [205] T.T. Dang, A. V. Thai, J. Cohen, J.E. Slosberg, K. Siniakowicz, J.C. Doloff, M. Ma, J. Hollister-Lock, K.M. Tang, Z. Gu, H. Cheng, G.C. Weir, R. Langer, D.G. Anderson, Enhanced function of immuno-isolated islets in diabetes therapy by co-encapsulation with an anti-inflammatory drug, *Biomaterials.* 34 (2013) 5792–5801.
<https://doi.org/10.1016/j.biomaterials.2013.04.016>.
- [206] B. Rolfe, J. Mooney, B. Zhang, S. Jahnke, S.-J. Le, Y.-Q. Chau, Q. Huang, H. Wang, G. Campbell, J. Campbell, The Fibrotic Response to Implanted Biomaterials: Implications for Tissue Engineering, in: *Regen. Med. Tissue Eng. - Cells Biomater.*, InTech, 2011. <https://doi.org/10.5772/21790>.
- [207] O. Veiseh, J.C. Doloff, M. Ma, A.J. Vegas, H.H. Tam, A.R. Bader, J. Li, E. Langan, J. Wyckoff, W.S. Loo, S. Jhunjunwala, A. Chiu, S. Siebert, K. Tang, J. Hollister-Lock, S. Aresta-Dasilva, M. Bochenek, J. Mendoza-Elias, Y. Wang, M. Qi, D.M. Lavin, M. Chen, N. Dholakia, R. Thakrar, I. Lacić, G.C. Weir, J. Oberholzer, D.L. Greiner, R. Langer, D.G. Anderson, Size- and shape-dependent foreign body immune response to materials implanted in rodents and non-human primates, *Nat. Mater.* 14 (2015) 643–651. <https://doi.org/10.1038/nmat4290>.
- [208] A.J. Ryan, H.S. O’Neill, G.P. Duffy, F.J. O’Brien, Advances in polymeric islet cell encapsulation technologies to limit the foreign body response and provide immunoisolation, *Curr. Opin. Pharmacol.* 36 (2017) 66–71.
<https://doi.org/10.1016/j.coph.2017.07.013>.
- [209] S.F. Josephs, T. Loudovaris, A. Dixit, S.K. Young, R.C. Johnson, In vivo delivery of recombinant human growth hormone from genetically engineered human fibroblasts implanted within Baxter immunoisolation devices, in: *J. Mol. Med.*, Springer Verlag, 1999: pp. 211–214. <https://doi.org/10.1007/s001090050338>.
- [210] TheraCyte, (n.d.). <https://theracyte.com/> (accessed April 11, 2020).
- [211] M. Ratner, Shire punts on bioscaffolds for cell-based regenerative medicine., *Nat. Biotechnol.* 30 (2012) 727–728. <https://doi.org/10.1038/nbt0812-727>.
- [212] E.D. O’Cearbhaill, K.S. Ng, J.M. Karp, Emerging medical devices for minimally invasive cell therapy, *Mayo Clin. Proc.* 89 (2014) 259–273.
<https://doi.org/10.1016/j.mayocp.2013.10.020>.
- [213] A.K. Sörenby, M. Kumagai-Braesch, A. Sharma, K.R. Hultenby, A.M. Wernerson, A.B. Tibell, Preimplantation of an immunoprotective device can lower the curative dose of islets to that of free islet transplantation-studies in a rodent model, *Transplantation.* 86 (2008) 364–366.
<https://doi.org/10.1097/TP.0b013e31817efc78>.
- [214] M. Kumagai-Braesch, S. Jacobson, H. Mori, X. Jia, T. Takahashi, A. Wernerson, M. Flodström-Tullberg, A. Tibell, The TheraCyte™ device protects against islet allograft rejection in immunized hosts., *Cell Transplant.* 22 (2013) 1137–46.
<https://doi.org/10.3727/096368912X657486>.

- [215] T. Boettler, D. Schneider, Y. Cheng, K. Kadoya, E.P. Brandon, L. Martinson, M. Von Herrath, Pancreatic tissue transplanted in theracyte™ encapsulation devices is protected and prevents hyperglycemia in a mouse model of immune-mediated diabetes, *Cell Transplant.* 25 (2016) 609–614. <https://doi.org/10.3727/096368915X688939>.
- [216] Z. Yang, M. Chen, L.B. Fialkow, J.D. Ellett, R. Wu, J.L. Nadler, Survival of pancreatic islet xenografts in NOD mice with the theracyte device., *Transplant. Proc.* 34 (2002) 3349–50. [https://doi.org/10.1016/s0041-1345\(02\)03685-0](https://doi.org/10.1016/s0041-1345(02)03685-0).
- [217] M.M. Gabr, M.M. Zakaria, A.F. Refaie, A.M. Ismail, S.M. Khater, S.A. Ashamallah, M.M. Azzam, M.A. Ghoneim, Insulin-producing Cells from Adult Human Bone Marrow Mesenchymal Stromal Cells Could Control Chemically Induced Diabetes in Dogs: A Preliminary Study, *Cell Transplant.* 27 (2018) 937–947. <https://doi.org/10.1177/0963689718759913>.
- [218] A.D. Agulnick, D.M. Ambruzs, M.A. Moorman, A. Bhoumik, R.M. Cesario, J.K. Payne, J.R. Kelly, C. Haakmeester, R. Srijemac, A.Z. Wilson, J. Kerr, M.A. Frazier, E.J. Kroon, K.A. D'Amour, Insulin-Producing Endocrine Cells Differentiated In Vitro From Human Embryonic Stem Cells Function in Macroencapsulation Devices In Vivo, *Stem Cells Transl. Med.* 4 (2015) 1214–1222. <https://doi.org/10.5966/sctm.2015-0079>.
- [219] T.C. Schulz, Concise Review: Manufacturing of Pancreatic Endoderm Cells for Clinical Trials in Type 1 Diabetes, *Stem Cells Transl. Med.* 4 (2015) 927–931. <https://doi.org/10.5966/sctm.2015-0058>.
- [220] A Safety, Tolerability, and Efficacy Study of VC-01™ Combination Product in Subjects with Type I Diabetes Mellitus, (ClinicalTrials. Gov Identifier NCT02239354). (n.d.).
- [221] One-Year Follow-up Safety Study in Subjects Previously Implanted with VC-01™, (ClinicalTrials.Gov Identifier: NCT02939118). (n.d.).
- [222] A Safety and Tolerability Study of VC-02™ Combination Product in Subjects with Type 1 Diabetes Mellitus, (ClinicalTrials.Gov Identifier: NCT03162926). (n.d.).
- [223] A Safety, Tolerability, and Efficacy Study of VC-02™ Combination Product in Subjects with Type 1 Diabetes Mellitus and Hypoglycemia Unawareness, (ClinicalTrials.Gov Identifier: NCT03163511). (n.d.).
- [224] ViaCyte to Present Preliminary PEC-Direct Clinical Data at Cell & Gene Meeting on the Mesa - ViaCyte, (n.d.). <https://viacyte.com/press-releases/viacyte-to-present-preliminary-pec-direct-clinical-data-at-cell-gene-meeting-on-the-mesa/> (accessed July 7, 2020).
- [225] Center for Beta Cell Therapy in Diabetes and ViaCyte Announce Start of European Clinical Trial of Human Stem Cell-derived Implants in Type 1 Diabetes Patients - ViaCyte, (n.d.). <https://viacyte.com/press-releases/center-for-beta-cell-therapy-in-diabetes-and-viacyte-announce-start-of-european-clinical-trial-of-human-stem-cell-derived-implants-in-type-1-diabetes-patients/> (accessed July 7, 2020).
- [226] News & Events - ViaCyte, (n.d.). <https://viacyte.com/news-events/> (accessed July 7, 2020).
- [227] D.M. Harlan, N.S. Kenyon, O. Korsgren, B.O. Roep, for the I. of D. Immunology of Diabetes Society, Current advances and travails in islet transplantation., *Diabetes.* 58 (2009) 2175–84. <https://doi.org/10.2337/db09-0476>.

- [228] E. Pedraza, M.M. Coronel, C.A. Fraker, C. Ricordi, C.L. Stabler, Preventing hypoxia-induced cell death in beta cells and islets via hydrolytically activated, oxygen-generating biomaterials., *Proc. Natl. Acad. Sci. U. S. A.* 109 (2012) 4245–50. <https://doi.org/10.1073/pnas.1113560109>.
- [229] U. Barkai, G.C. Weir, C.K. Colton, B. Ludwig, S.R. Bornstein, M.D. Brendel, T. Neufeld, C. Bremer, A. Leon, Y. Evron, K. Yavriyants, D. Azarov, B. Zimermann, S. Maimon, N. Shabtay, M. Balyura, T. Rozenshtein, P. Vardi, K. Bloch, P. De Vos, A. Rotem, Enhanced oxygen supply improves islet viability in a new bioartificial pancreas, *Cell Transplant.* 22 (2013) 1463–1476. <https://doi.org/10.3727/096368912X657341>.
- [230] T. Neufeld, B. Ludwig, U. Barkai, G.C. Weir, C.K. Colton, Y. Evron, M. Balyura, K. Yavriyants, B. Zimermann, D. Azarov, S. Maimon, N. Shabtay, T. Rozenshtein, D. Lorber, A. Steffen, U. Willenz, K. Bloch, P. Vardi, R. Taube, P. de Vos, E.C. Lewis, S.R. Bornstein, A. Rotem, The Efficacy of an Immunoisolating Membrane System for Islet Xenotransplantation in Minipigs, *PLoS One.* 8 (2013) e70150. <https://doi.org/10.1371/journal.pone.0070150>.
- [231] B. Ludwig, A. Reichel, A. Steffen, B. Zimerman, A. V. Schally, N.L. Block, C.K. Colton, S. Ludwig, S. Kersting, E. Bonifacio, M. Solimena, Z. Gendler, A. Rotem, U. Barkai, S.R. Bornstein, Transplantation of human islets without immunosuppression, *Proc. Natl. Acad. Sci. U. S. A.* 110 (2013) 19054–19058. <https://doi.org/10.1073/pnas.1317561110>.
- [232] An Open Label, Pilot Investigation, to Assess the Safety and Efficacy of Transplantation of Macro-Encapsulated Human Islets within the Bioartificial Pancreas Beta-Air in Patients with Type 1 Diabetes Mellitus, (ClinicalTrials.Gov Identifier: NCT02064309). (n.d.).
- [233] P.O. Carlsson, D. Espes, A. Sedigh, A. Rotem, B. Zimerman, H. Grinberg, T. Goldman, U. Barkai, Y. Avni, G.T. Westermark, L. Carlbom, H. Ahlström, O. Eriksson, J. Olerud, O. Korsgren, Transplantation of macroencapsulated human islets within the bioartificial pancreas β Air to patients with type 1 diabetes mellitus, *Am. J. Transplant.* 18 (2018) 1735–1744. <https://doi.org/10.1111/ajt.14642>.
- [234] J. Kriz, G. Vilk, D.M. Mazzuca, P.M. Toleikis, P.J. Foster, D.J.G. White, A novel technique for the transplantation of pancreatic islets within a vascularized device into the greater omentum to achieve insulin independence, *Am. J. Surg.* 203 (2012) 793–797. <https://doi.org/10.1016/j.amjsurg.2011.02.009>.
- [235] B.L. Gala-Lopez, A.R. Pepper, P. Dinyari, A.J. Malcolm, T. Kin, L.R. Pawlick, P.A. Senior, A.M.J. Shapiro, Subcutaneous clinical islet transplantation in a prevascularized subcutaneous pouch – preliminary experience, 2016.
- [236] A Phase I/II Study of the Safety and Efficacy of Sernova’s Cell Pouch™ for Therapeutic Islet Transplantation, (ClinicalTrials.Gov Identifier: NCT01652911). (n.d.).
- [237] A Safety, Tolerability and Efficacy Study of Sernova’s Cell Pouch™ for Clinical Islet Transplantation, (ClinicalTrials.Gov Identifier: NCT03513939). (n.d.).
- [238] M. Thomas, K. Moriyama, I. Ledebø, AN69: Evolution of the world’s first high permeability membrane, *Contrib. Nephrol.* 173 (2011) 119–129. <https://doi.org/10.1159/000328961>.
- [239] A. Rodriguez-Brotons, Improvement of pancreatic islets viability in the bioartificial

- pancreas, n.d. <https://tel.archives-ouvertes.fr/tel-01402074> (accessed April 9, 2020).
- [240] L. Kessler, M. Aprahamian, M. Keipes, C. Damgé, M. Pinget, D. Poinot, Diffusion properties of an artificial membrane used for Langerhans islets encapsulation: an in vitro test, *Biomaterials*. 13 (1992) 44–49. [https://doi.org/10.1016/0142-9612\(92\)90094-5](https://doi.org/10.1016/0142-9612(92)90094-5).
- [241] L. Kessler, C. Jesser, Y. Lombard, V. Karsten, A. Belcourt, M. Pinget, P. Poindron, Cytotoxicity of peritoneal murine macrophages against encapsulated pancreatic rat islets: In vivo and in vitro studies, *J. Leukoc. Biol.* 60 (1996) 729–736. <https://doi.org/10.1002/jlb.60.6.729>.
- [242] L. Kessler, G. Legeay, A. Coudreuse, P. Bertrand, C. Poleunus, X. Vanden Eynde, K. Mandes, P. Marchetti, M. Pinget, A. Belcourt, Surface treatment of polycarbonate films aimed at biomedical application, *J. Biomater. Sci. Polym. Ed.* 14 (2003) 1135–1153. <https://doi.org/10.1163/156856203769231619>.
- [243] J. Magisson, A. Sassi, D. Xhema, A. Kobalyan, P. Gianello, B. Mourer, N. Tran, C.-T. Burcez, R. Bou Aoun, S. Sigrist, Safety and function of a new pre-vascularized bioartificial pancreas in an allogeneic rat model, *J. Tissue Eng.* 11 (2020) 204173142092481. <https://doi.org/10.1177/2041731420924818>.
- [244] M. Farina, J.F. Alexander, U. Thekkedath, M. Ferrari, A. Grattoni, Cell encapsulation: Overcoming barriers in cell transplantation in diabetes and beyond, *Adv. Drug Deliv. Rev.* 139 (2019) 92–115. <https://doi.org/10.1016/j.addr.2018.04.018>.
- [245] Defymed | Advanced therapies inspired for you, (n.d.). <https://www.defymed.com/> (accessed April 9, 2020).
- [246] C.E. Campbell, A.F. von Recum, Microtopography and soft tissue response., *J. Invest. Surg.* 2 (1989) 51–74. <http://www.ncbi.nlm.nih.gov/pubmed/2487399> (accessed June 23, 2019).
- [247] S.J. James, M. Pogribna, B.J. Miller, B. Bolon, L. Muskhelishvili, Characterization of cellular response to silicone implants in rats: implications for foreign-body carcinogenesis., *Biomaterials*. 18 (1997) 667–75. <http://www.ncbi.nlm.nih.gov/pubmed/9151998> (accessed June 23, 2019).
- [248] W. Siggelkow, A. Faridi, K. Spiritus, U. Klinge, W. Rath, B. Klosterhalfen, Histological analysis of silicone breast implant capsules and correlation with capsular contracture., *Biomaterials*. 24 (2003) 1101–9. <http://www.ncbi.nlm.nih.gov/pubmed/12504533> (accessed June 23, 2019).
- [249] N. Wisniewski, M. Reichert, Methods for reducing biosensor membrane biofouling, *Colloids Surfaces B Biointerfaces*. 18 (2000) 197–219. [https://doi.org/10.1016/S0927-7765\(99\)00148-4](https://doi.org/10.1016/S0927-7765(99)00148-4).
- [250] W.K. Ward, J.E. Troupe, Assessment of chronically implanted subcutaneous glucose sensors in dogs: the effect of surrounding fluid masses., *ASAIO J.* 45 (n.d.) 555–61. <http://www.ncbi.nlm.nih.gov/pubmed/10593686> (accessed June 23, 2019).
- [251] J.M. Anderson, A. Rodriguez, D.T. Chang, Foreign body reaction to biomaterials, *Semin. Immunol.* 20 (2008) 86–100. <https://doi.org/10.1016/j.smim.2007.11.004>.
- [252] A.F. Von Recum, T.G. Van Kooten, The influence of micro-topography on cellular response and the implications for silicone implants, *J. Biomater. Sci. Polym. Ed.*

- (1995). <https://doi.org/10.1163/156856295X00698>.
- [253] B. Pittet, D. Montandon, D. Pittet, Infection in breast implants, *Lancet Infect. Dis.* 5 (2005) 94–106. [https://doi.org/10.1016/S1473-3099\(05\)01281-8](https://doi.org/10.1016/S1473-3099(05)01281-8).
- [254] L. Zhang, Z. Cao, T. Bai, L. Carr, J.-R. Ella-Menye, C. Irvin, B.D. Ratner, S. Jiang, Zwitterionic hydrogels implanted in mice resist the foreign-body reaction, *Nat. Biotechnol.* 31 (2013) 553–556. <https://doi.org/10.1038/nbt.2580>.
- [255] E.M. Hetrick, H.L. Prichard, B. Klitzman, M.H. Schoenfish, Reduced foreign body response at nitric oxide-releasing subcutaneous implants, *Biomaterials.* 28 (2007) 4571. <https://doi.org/10.1016/J.BIOMATERIALS.2007.06.036>.
- [256] B. Ratner, A. Hoffman, S. F. J. Lemons, *Biomaterials Science; An introduction to materials in medicine*, 3rd Editio, Academic Press, 2012.
- [257] A. Uysal, O. Kayiran, ??nder Karaaslan, M.G. Ulusoy, U. Ko??er, F. ??z Atalay, H. ??st??n, Evaluation and Management of Exposed High-density Porous Polyethylene Implants, *J. Craniofac. Surg.* 17 (2006) 1129–1136. <https://doi.org/10.1097/01.scs.0000244913.75102.12>.
- [258] P. Lin, C.-W. Lin, R. Mansour, F. Gu, Improving biocompatibility by surface modification techniques on implantable bioelectronics, *Biosens. Bioelectron.* 47 (2013) 451–460. <https://doi.org/10.1016/j.bios.2013.01.071>.
- [259] J.D. Weaver, D.M. Headen, J. Aquart, C.T. Johnson, L.D. Shea, H. Shirwan, A.J. García, Vasculogenic hydrogel enhances islet survival, engraftment, and function in leading extrahepatic sites, *Sci. Adv.* 3 (2017) e1700184. <https://doi.org/10.1126/sciadv.1700184>.
- [260] M.G. Monaghan, M. Holeiter, E. Brauchle, S.L. Layland, Y. Lu, A. Deb, A. Pandit, A. Nsair, K. Schenke-Layland, Exogenous miR-29B Delivery Through a Hyaluronan-Based Injectable System Yields Functional Maintenance of the Infarcted Myocardium, *Tissue Eng. Part A.* 24 (2018) 57–67. <https://doi.org/10.1089/ten.tea.2016.0527>.
- [261] C.V. Howard, M. Reed, *Unbiased Stereology: Three-Dimensional Measurement in Microscopy*, 1st Editio, Garland science/BIOS Scientific Publisher, Oxford, 1998.
- [262] Y. GARCIA, B. WILKINS, R. COLLIGHAN, M. GRIFFIN, A. PANDIT, Towards development of a dermal rudiment for enhanced wound healing response, *Biomaterials.* 29 (2008) 857–868. <https://doi.org/10.1016/j.biomaterials.2007.10.053>.
- [263] P. Dockery, J. Fraher, The quantification of vascular beds: A stereological approach, *Exp. Mol. Pathol.* 82 (2007) 110–120. <https://doi.org/10.1016/j.yexmp.2006.12.011>.
- [264] H.J. Gundersen, E.B. Jensen, Stereological estimation of the volume-weighted mean volume of arbitrary particles observed on random sections., *J. Microsc.* 138 (1985) 127–42. <http://www.ncbi.nlm.nih.gov/pubmed/4020857> (accessed June 23, 2019).
- [265] E.M. Sweeney, P. Dockery, D.J. Crankshaw, Y.M. O’Brien, J.M. Walsh, J.J. Morrison, Human uterine lower segment myometrial cell and nuclear volume at term: influence of maternal age, *J. Anat.* 225 (2014) 625–633. <https://doi.org/10.1111/joa.12240>.
- [266] C. Howard, M. Reed, *Unbiased Stereology*, QTP Publications, United Kingdom, 2010.

- [267] J. Yin, M. Kukucka, J. Hoffmann, A. Sterner-Kock, J. Burhenne, W.E. Haefeli, H. Kuppe, W.M. Kuebler, Sildenafil Preserves Lung Endothelial Function and Prevents Pulmonary Vascular Remodeling in a Rat Model of Diastolic Heart Failure, *Circ. Hear. Fail.* 4 (2011) 198–206. <https://doi.org/10.1161/CIRCHEARTFAILURE.110.957050>.
- [268] J. NygenGaard, T. Bendtsen, R. Bjugn, A. Lokkegaard, Y. Tang, H.J. Gundersen, A Stereological Approach to Capillary Networks., in: S. AK (Ed.), *Morphometry - Appl. to Med. Sci.*, Macmillan India Ltd, New Delhi, 1996: pp. 217–228.
- [269] G. Bergers, S. Song, The role of pericytes in blood-vessel formation and maintenance, *Neuro. Oncol.* 7 (2005) 452–464. <https://doi.org/10.1215/S1152851705000232>.
- [270] W. Koh, A.N. Stratman, A. Sacharidou, G.E. Davis, Chapter 5 In Vitro Three Dimensional Collagen Matrix Models of Endothelial Lumen Formation During Vasculogenesis and Angiogenesis, in: *Methods Enzymol.*, 2008: pp. 83–101. [https://doi.org/10.1016/S0076-6879\(08\)02005-3](https://doi.org/10.1016/S0076-6879(08)02005-3).
- [271] P. Arun Gopinathan, G. Kokila, S. Siddeeqh, R. Prakash, P. L, Reexploring picosirius red: A review, *Indian J. Pathol. Oncol.* 7 (2020) 196–203. <https://doi.org/10.18231/j.ijpo.2020.038>.
- [272] R. Koren, E. Yaniv, D. Kristt, J. Shvero, V. Veltman, I. Grushko, R. Feinmesser, J. Sulkes, R. Gal, Capsular collagen staining of follicular thyroid neoplasms by picosirius red: Role in differential diagnosis, *Acta Histochem.* 103 (2001) 151–157. <https://doi.org/10.1078/0065-1281-00587>.
- [273] J.K. Roush, G.J. Breur, J.W. Wilson, Picosirius red staining of dental structures, *Biotech. Histochem.* 63 (1988) 363–367. <https://doi.org/10.3109/10520298809107612>.
- [274] L.C.U. Junqueira, G. Bignolas, R.R. Brentani, A simple and sensitive method for the quantitative estimation of collagen, *Anal. Biochem.* 94 (1979) 96–99. [https://doi.org/10.1016/0003-2697\(79\)90795-4](https://doi.org/10.1016/0003-2697(79)90795-4).
- [275] L.C.U. Junqueira, G. Bignolas, R.R. Brentani, Picosirius staining plus polarization microscopy, a specific method for collagen detection in tissue sections, *Histochem. J.* 11 (1979) 447–455. <https://doi.org/10.1007/BF01002772>.
- [276] M. Szendroi, G. Vajta, L. Kovacs, Z. Schaff, K. Lapis, Polarization colours of collagen fibres: a sign of collagen production activity in fibrotic processes, *Acta Morphol.Hung.* (1984).
- [277] S.Y. Yu, C.A. Tozzi, J. Babiarz, P.C. Leppert, Collagen changes in rat cervix in pregnancy--polarized light microscopic and electron microscopic studies., *Proc. Soc. Exp. Biol. Med.* (1995).
- [278] M. Wolman, F.H. Kasten, Polarized light microscopy in the study of the molecular structure of collagen and reticulin, *Histochemistry.* (1986). <https://doi.org/10.1007/BF00508652>.
- [279] J.M. Anderson, A.K. McNally, Biocompatibility of implants: lymphocyte/macrophage interactions., *Semin. Immunopathol.* 33 (2011) 221–33. <https://doi.org/10.1007/s00281-011-0244-1>.
- [280] R. Klopffleisch, F. Jung, The pathology of the foreign body reaction against biomaterials., *J. Biomed. Mater. Res. A.* 105 (2017) 927–940.

<https://doi.org/10.1002/jbm.a.35958>.

- [281] Z. Sheikh, P.J. Brooks, O. Barzilay, N. Fine, M. Glogauer, Macrophages, foreign body giant cells and their response to implantable biomaterials1. *Metchnikoff I, Prize N. Mini - review : Macrophage Polarization. Biorad.* 2015;2:1–8., *Materials (Basel)*. 8 (2015) 5671–5701. <https://doi.org/10.3390/ma8095269>.
- [282] J.R. Jackson, M.P. Seed, C.H. Kircher, D.A. Willoughby, J.D. Winkler, The codependence of angiogenesis and chronic inflammation., *FASEB J.* 11 (1997) 457–65. <http://www.ncbi.nlm.nih.gov/pubmed/9194526> (accessed October 7, 2019).
- [283] B.N. Brown, B.M. Sicari, S.F. Badylak, Rethinking regenerative medicine: A macrophage-centered approach, *Front. Immunol.* (2014). <https://doi.org/10.3389/fimmu.2014.00510>.
- [284] J.M. Anderson, A.K. McNally, Biocompatibility of implants: lymphocyte/macrophage interactions, *Semin. Immunopathol.* 33 (2011) 221–233. <https://doi.org/10.1007/s00281-011-0244-1>.
- [285] P. Italiani, D. Boraschi, From Monocytes to M1/M2 Macrophages: Phenotypical vs. Functional Differentiation, *Front. Immunol.* 5 (2014) 514. <https://doi.org/10.3389/fimmu.2014.00514>.
- [286] B.N. Brown, J.E. Valentin, A.M. Stewart-Akers, G.P. McCabe, S.F. Badylak, Macrophage phenotype and remodeling outcomes in response to biologic scaffolds with and without a cellular component, *Biomaterials.* 30 (2009) 1482–1491. <https://doi.org/10.1016/j.biomaterials.2008.11.040>.
- [287] S.F. Badylak, J.E. Valentin, A.K. Ravindra, G.P. McCabe, A.M. Stewart-Akers, Macrophage phenotype as a determinant of biologic scaffold remodeling., *Tissue Eng. Part A.* 14 (2008) 1835–42. <https://doi.org/10.1089/ten.tea.2007.0264>.
- [288] A.M. Danino, P. Basmacioglu, S. Saito, F. Rocher, C. Blanchet-Bardon, M. Revol, J.M. Servant, Comparison of the capsular response to the Biocell RTV and Mentor 1600 Siltex breast implant surface texturing: a scanning electron microscopic study., *Plast. Reconstr. Surg.* 108 (2001) 2047–52. <http://www.ncbi.nlm.nih.gov/pubmed/11743398> (accessed July 3, 2019).
- [289] A. Sood, E.Y. Xue, C. Sangiovanni, P.J. Therattil, E.S. Lee, Breast Massage, Implant Displacement, and Prevention of Capsular Contracture After Breast Augmentation With Implants: A Review of the Literature., *Eplasty.* 17 (2017) e41. <http://www.ncbi.nlm.nih.gov/pubmed/29348783> (accessed October 7, 2019).
- [290] B. Ludwig, S. Ludwig, A. Steffen, Y. Knauf, B. Zimmerman, S. Heinke, S. Lehmann, U. Schubert, J. Schmid, M. Bleyer, U. Schönmann, C.K. Colton, E. Bonifacio, M. Solimena, A. Reichel, A. V. Schally, A. Rotem, U. Barkai, H. Grinberg-Rashi, F.J. Kaup, Y. Avni, P. Jones, S.R. Bornstein, Favorable outcome of experimental islet xenotransplantation without immunosuppression in a nonhuman primate model of diabetes, *Proc. Natl. Acad. Sci. U. S. A.* 114 (2017) 11745–11750. <https://doi.org/10.1073/pnas.1708420114>.
- [291] J. Oberholzer, E. Langan, N. Dholakia, D.G. Anderson, R. Thakrar, M. Chen, H.H. Tam, J. Li, O. Veiseh, M. Qi, S. Jhunjunwala, S. Siebert, M. Ma, J. Wyckoff, R. Langer, Y. Wang, M. Bochenek, D.L. Greiner, G.C. Weir, J. Hollister-Lock, I. Lacik, S. Aresta-Dasilva, J.C. Doloff, D.M. Lavin, A.R. Bader, A. Chiu, W.S. Loo, A.J. Vegas, J. Mendoza-Elias, K. Tang, Size- and shape-dependent foreign body immune response to

- materials implanted in rodents and non-human primates, *Nat. Mater.* (2015). <https://doi.org/10.1038/nmat4290>.
- [292] U. Barkai, G.C. Weir, C.K. Colton, B. Ludwig, S.R. Bornstein, M.D. Brendel, T. Neufeld, C. Bremer, A. Leon, Y. Evron, K. Yavriyants, D. Azarov, B. Zimmermann, S. Maimon, N. Shabtay, M. Balyura, T. Rozenshtein, P. Vardi, K. Bloch, P. de Vos, A. Rotem, Enhanced oxygen supply improves islet viability in a new bioartificial pancreas., *Cell Transplant.* 22 (2013) 1463–76. <https://doi.org/10.3727/096368912X657341>.
- [293] J.D. Weaver, D.M. Headen, J. Aquart, C.T. Johnson, L.D. Shea, H. Shirwan, A.J. García, Vasculogenic hydrogel enhances islet survival, engraftment, and function in leading extrahepatic sites, *Sci. Adv.* (2017). <https://doi.org/10.1126/sciadv.1700184>.
- [294] E.A. Phelps, K.L. Templeman, P.M. Thulé, A.J. García, Engineered VEGF-releasing PEG-MAL hydrogel for pancreatic islet vascularization., *Drug Deliv. Transl. Res.* 5 (2015) 125–36. <https://doi.org/10.1007/s13346-013-0142-2>.
- [295] S. Perteghella, B. Vigani, L. Mastracci, F. Grillo, B. Antonioli, M. Galuzzi, M.C. Tosca, B. Crivelli, S. Preda, G. Tripodo, M. Marazzi, T. Chlapanidas, M.L. Torre, Stromal Vascular Fraction Loaded Silk Fibroin Mats Effectively Support the Survival of Diabetic Mice after Pancreatic Islet Transplantation., *Macromol. Biosci.* 17 (2017). <https://doi.org/10.1002/mabi.201700131>.
- [296] A.R. Pepper, B. Gala-Lopez, R. Pawlick, S. Merani, T. Kin, A.M.J. Shapiro, A prevascularized subcutaneous device-less site for islet and cellular transplantation., *Nat. Biotechnol.* 33 (2015) 518–23. <https://doi.org/10.1038/nbt.3211>.
- [297] K.C. Scheiner, F. Coulter, R.F. Maas-Bakker, G. Ghersi, T.T. Nguyen, R. Steendam, G.P. Duffy, W.E. Hennink, E.D. O’Cearbhaill, R.J. Kok, Vascular endothelial growth factor (VEGF)-releasing microspheres based on poly(ϵ -caprolactone-PEG- ϵ -caprolactone)-b-poly(L-lactide) multi-block copolymers incorporated in a 3D-printed poly(dimethylsiloxane) (PDMS) cell macroencapsulation device, *J. Pharm. Sci.* (2019). <https://doi.org/10.1016/j.xphs.2019.10.028>.
- [298] U. Barkai, A. Rotem, P. de Vos, Survival of encapsulated islets: More than a membrane story., *World J. Transplant.* 6 (2016) 69–90. <https://doi.org/10.5500/wjt.v6.i1.69>.
- [299] D.C. Chow, L.A. Wenning, W.M. Miller, E.T. Papoutsakis, Modeling pO₂ distributions in the bone marrow hematopoietic compartment. I. Krogh’s model, *Biophys. J.* 81 (2001) 675–684. [https://doi.org/10.1016/S0006-3495\(01\)75732-3](https://doi.org/10.1016/S0006-3495(01)75732-3).
- [300] R.F. Padera, C.K. Colton, Time course of membrane microarchitecture-driven neovascularization, *Biomaterials.* 17 (1996) 277–284. [https://doi.org/10.1016/0142-9612\(96\)85565-7](https://doi.org/10.1016/0142-9612(96)85565-7).
- [301] J.H. Brauker, V.E. Carr-Brendel, L.A. Martinson, J. Crudele, W.D. Johnston, R.C. Johnson, Neovascularization of synthetic membranes directed by membrane microarchitecture, *J. Biomed. Mater. Res.* 29 (1995) 1517–1524. <https://doi.org/10.1002/jbm.820291208>.
- [302] F.A. Auger, L. Gibot, D. Lacroix, The Pivotal Role of Vascularization in Tissue Engineering, *Annu. Rev. Biomed. Eng.* 15 (2013) 177–200. <https://doi.org/10.1146/annurev-bioeng-071812-152428>.
- [303] Y. Kawakami, H. Iwata, Y. Gu, M. Miyamoto, Y. Murakami, T. Yamasaki, W. Cui, Y.

- Ikada, M. Imamura, K. Inoue, Modified Subcutaneous Tissue with Neovascularization is Useful as the Site for Pancreatic Islet Transplantation, *Cell Transplant.* 9 (2000) 729–732. <https://doi.org/10.1177/096368970000900523>.
- [304] J.J. Vallbacka, M. V. Sefton, Vascularization and Improved *In Vivo* Survival of VEGF-Secreting Cells Microencapsulated in HEMA-MMA, *Tissue Eng.* 13 (2007) 2259–2269. <https://doi.org/10.1089/ten.2006.0284>.
- [305] H.K. Tilakaratne, S.K. Hunter, M.E. Andracki, J.A. Benda, V.G.J. Rodgers, Characterizing short-term release and neovascularization potential of multi-protein growth supplement delivered via alginate hollow fiber devices, *Biomaterials.* 28 (2007) 89–98. <https://doi.org/10.1016/j.biomaterials.2006.08.011>.
- [306] M. Najjar, V. Manzoli, M. Abreu, C. Villa, M.M. Martino, R.D. Molano, Y. Torrente, A. Pileggi, L. Inverardi, C. Ricordi, J.A. Hubbell, A.A. Tomei, Fibrin gels engineered with pro-angiogenic growth factors promote engraftment of pancreatic islets in extrahepatic sites in mice, *Biotechnol. Bioeng.* 112 (2015) 1916–1926. <https://doi.org/10.1002/bit.25589>.
- [307] K.C. Scheiner, R.F. Maas-Bakker, T.T. Nguyen, A.M. Duarte, G. Hendriks, L. Sequeira, G.P. Duffy, R. Steendam, W.E. Hennink, R.J. Kok, Sustained Release of Vascular Endothelial Growth Factor from Poly(ϵ -caprolactone-PEG- ϵ -caprolactone)-*b*-Poly(L-lactide) Multiblock Copolymer Microspheres, *ACS Omega.* 4 (2019) 11481–11492. <https://doi.org/10.1021/acsomega.9b01272>.
- [308] M.G. Monaghan, M. Holeiter, E. Brauchle, S.L. Layland, Y. Lu, A. Deb, A. Pandit, A. Nsair, K. Schenke-Layland, Exogenous miR-29B Delivery Through a Hyaluronan-Based Injectable System Yields Functional Maintenance of the Infarcted Myocardium, *Tissue Eng. Part A.* 24 (2018) 57. <https://doi.org/10.1089/TEN.TEA.2016.0527>.
- [309] A.N. Balamurugan, Y. Gu, Y. Tabata, M. Miyamoto, W. Cui, H. Hori, A. Satake, N. Nagata, W. Wang, K. Inoue, Bioartificial Pancreas Transplantation at Prevascularized Intermuscular Space: Effect of Angiogenesis Induction on Islet Survival, *Pancreas.* 26 (2003) 279–285. <https://doi.org/10.1097/00006676-200304000-00012>.
- [310] A. Pileggi, R.D. Molano, C. Ricordi, E. Zahr, J. Collins, R. Valdes, L. Inverardi, Reversal of Diabetes by Pancreatic Islet Transplantation into a Subcutaneous, Neovascularized Device, *Transplantation.* 81 (2006) 1318–1324. <https://doi.org/10.1097/01.tp.0000203858.41105.88>.
- [311] T. Sakurai, A. Satake, S. Sumi, K. Inoue, N. Nagata, Y. Tabata, J. Miyakoshi, The Efficient Prevascularization Induced by Fibroblast Growth Factor 2 With a Collagen-Coated Device Improves the Cell Survival of a Bioartificial Pancreas, *Pancreas.* 28 (2004) e70–e79. <https://doi.org/10.1097/00006676-200404000-00028>.
- [312] E.M. Conway, D. Collen, P. Carmeliet, Molecular mechanisms of blood vessel growth, *Cardiovasc. Res.* 49 (2001) 507–521. [https://doi.org/10.1016/S0008-6363\(00\)00281-9](https://doi.org/10.1016/S0008-6363(00)00281-9).
- [313] P. Carmeliet, Mechanisms of angiogenesis and arteriogenesis, *Nat. Med.* 6 (2000) 389–395. <https://doi.org/10.1038/74651>.
- [314] C.J. Drake, C.D. Little, VEGF and vascular fusion: Implications for normal and pathological vessels, *J. Histochem. Cytochem.* 47 (1999) 1351–1355. <https://doi.org/10.1177/002215549904701101>.

- [315] M. Kazemi, A. Carrer, S. Moimas, L. Zandonà, R. Bussani, B. Casagrande, S. Palmisano, P. Prelazzi, M. Giacca, L. Zentilin, N. De Manzini, M. Giacca, S. Zacchigna, VEGF121 and VEGF165 differentially promote vessel maturation and tumor growth in mice and humans, *Cancer Gene Ther.* 23 (2016) 125–132. <https://doi.org/10.1038/cgt.2016.12>.
- [316] M.N. Nakatsu, R.C.A. Sainson, S. Pérez-Del-Pulgar, J.N. Aoto, M. Aitkenhead, K.L. Taylor, P.M. Carpenter, C.C.W. Hughes, VEGF121 and VEGF165 Regulate Blood Vessel Diameter Through Vascular Endothelial Growth Factor Receptor 2 in an in Vitro Angiogenesis Model, *Lab. Invest.* 83 (2003) 1873–1885. <https://doi.org/10.1097/01.LAB.0000107160.81875.33>.
- [317] N. Ferrara, The Biology of Vascular Endothelial Growth Factor, *Endocr. Rev.* 18 (1997) 4–25. <https://doi.org/10.1210/er.18.1.4>.
- [318] J.A. Nagy, A.M. Dvorak, H.F. Dvorak, VEGF-A and the induction of pathological angiogenesis, *Annu. Rev. Pathol.* 2 (2007) 251–275. <https://doi.org/10.1146/annurev.pathol.2.010506.134925>.
- [319] A.K. Sörenby, M. Kumagai-Braesch, A. Sharma, K.R. Hultenby, A.M. Wernerson, A.B. Tibell, Preimplantation of an Immunoprotective Device Can Lower the Curative Dose of Islets to That of Free Islet Transplantation—Studies in a Rodent Model, *Transplantation.* 86 (2008) 364–366. <https://doi.org/10.1097/TP.0b013e31817efc78>.
- [320] S. Song, E.J. Kim, C.S. Bahney, T. Micalau, R. Marcucio, S. Roy, The synergistic effect of micro-topography and biochemical culture environment to promote angiogenesis and osteogenic differentiation of human mesenchymal stem cells, *Acta Biomater.* 18 (2015) 100–111. <https://doi.org/10.1016/j.actbio.2015.02.021>.
- [321] L. Krishnan, C.C. Chang, S.S. Nunes, S.K. Williams, J.A. Weiss, J.B. Hoying, Manipulating the microvasculature and its microenvironment., *Crit. Rev. Biomed. Eng.* 41 (2013) 91–123. <http://www.ncbi.nlm.nih.gov/pubmed/24580565> (accessed October 10, 2019).
- [322] A. Lathuilière, S. Cosson, M.P. Lutolf, B.L. Schneider, P. Aebischer, A high-capacity cell macroencapsulation system supporting the long-term survival of genetically engineered allogeneic cells, *Biomaterials.* 35 (2014) 779–791. <https://doi.org/10.1016/J.BIOMATERIALS.2013.09.071>.
- [323] A. Rosengren, N. Danielsen, L.M. Bjursten, Reactive capsule formation around soft-tissue implants is related to cell necrosis, *J. Biomed. Mater. Res.* 46 (1999) 458–464. [https://doi.org/10.1002/\(SICI\)1097-4636\(19990915\)46:4<458::AID-JBM3>3.0.CO;2-I](https://doi.org/10.1002/(SICI)1097-4636(19990915)46:4<458::AID-JBM3>3.0.CO;2-I).
- [324] N. Khosravi, A. Maeda, R.S. DaCosta, J.E. Davies, Nanosurfaces modulate the mechanism of peri-implant endosseous healing by regulating neovascular morphogenesis, *Commun. Biol.* 1 (2018) 72. <https://doi.org/10.1038/s42003-018-0074-y>.
- [325] A.K.J. Gradel, T. Porsgaard, J. Lykkesfeldt, T. Seested, S. Gram-Nielsen, N.R. Kristensen, H.H.F. Refsgaard, Factors Affecting the Absorption of Subcutaneously Administered Insulin: Effect on Variability, *J. Diabetes Res.* 2018 (2018). <https://doi.org/10.1155/2018/1205121>.
- [326] V. Valla, Therapeutics of diabetes mellitus: focus on insulin analogues and insulin pumps., *Exp. Diabetes Res.* 2010 (2010) 178372.

- <https://doi.org/10.1155/2010/178372>.
- [327] C. Schuetz, T. Anazawa, S.E. Cross, L. Labriola, R.P.H. Meier, R.R. Redfield, H. Scholz, P.G. Stock, N.W. Zammit, β Cell Replacement Therapy: The Next 10 Years, *Transplantation*. 102 (2018) 215–229. <https://doi.org/10.1097/TP.0000000000001937>.
- [328] N. Sakata, A. Tan, N. Chan, A. Obenaus, J. Mace, R. Peverini, L. Sowers, R. Chinnock, E. Hathout, Efficacy Comparison Between Intraportal and Subcapsular Islet Transplants in a Murine Diabetic Model, *Transplant. Proc.* 41 (2009) 346–349. <https://doi.org/10.1016/j.transproceed.2008.08.155>.
- [329] E.S. O’Sullivan, A. Vegas, D.G. Anderson, G.C. Weir, Islets transplanted in immunoisolation devices: A review of the progress and the challenges that remain, *Endocr. Rev.* 32 (2011) 827–844. <https://doi.org/10.1210/er.2010-0026>.
- [330] T. Kobayashi, Y. Aomatsu, H. Iwata, T. Kin, H. Kanehiro, M. Hisanaga, S. Ko, M. Nagao, Y. Nakajima, Indefinite islet protection from autoimmune destruction in nonobese diabetic mice by agarose microencapsulation without immunosuppression, *Transplantation*. 75 (2003) 619–625. <https://doi.org/10.1097/01.TP.0000053749.36365.7E>.
- [331] R.B. Elliott, L. Escobar, P.L.J. Tan, M. Muzina, S. Zwain, C. Buchanan, Live encapsulated porcine islets from a type 1 diabetic patient 9.5 yr after xenotransplantation, *Xenotransplantation*. 14 (2007) 157–161. <https://doi.org/10.1111/j.1399-3089.2007.00384.x>.
- [332] M.A. Bochenek, O. Veiseh, A.J. Vegas, J.J. McGarrigle, M. Qi, E. Marchese, M. Omami, J.C. Doloff, J. Mendoza-Elias, M. Nourmohammadzadeh, A. Khan, C.C. Yeh, Y. Xing, D. Isa, S. Ghani, J. Li, C. Landry, A.R. Bader, K. Olejnik, M. Chen, J. Hollister-Lock, Y. Wang, D.L. Greiner, G.C. Weir, B.L. Strand, A.M.A. Rokstad, I. Lacik, R. Langer, D.G. Anderson, J. Oberholzer, Alginate encapsulation as long-term immune protection of allogeneic pancreatic islet cells transplanted into the omental bursa of macaques, *Nat. Biomed. Eng.* 2 (2018) 810–821. <https://doi.org/10.1038/s41551-018-0275-1>.
- [333] C.K. Colton, Implantable biohybrid artificial organs, *Cell Transplant.* 4 (1995) 415–436. [https://doi.org/10.1016/0963-6897\(95\)00025-S](https://doi.org/10.1016/0963-6897(95)00025-S).
- [334] M. De Groot, T.A. Schuur, R. Van Schilfgaarde, Causes of limited survival of microencapsulated pancreatic islet grafts, *J. Surg. Res.* 121 (2004) 141–150. <https://doi.org/10.1016/j.jss.2004.02.018>.
- [335] M.M. Coronel, C.L. Stabler, Engineering a local microenvironment for pancreatic islet replacement, *Curr. Opin. Biotechnol.* 24 (2013) 900–908. <https://doi.org/10.1016/j.copbio.2013.05.004>.
- [336] J.D. Weaver, D.M. Headen, M.D. Hunckler, M.M. Coronel, C.L. Stabler, A.J. García, Design of a vascularized synthetic poly(ethylene glycol) macroencapsulation device for islet transplantation, *Biomaterials*. 172 (2018) 54–65. <https://doi.org/10.1016/j.biomaterials.2018.04.047>.
- [337] A.J. Hwa, G.C. Weir, Transplantation of Macroencapsulated Insulin-Producing Cells, *Curr. Diab. Rep.* 18 (2018) 50. <https://doi.org/10.1007/s11892-018-1028-y>.
- [338] D.J. Van Der Windt, G.J. Echeverri, J.N.M. Ijzermans, D.K.C. Cooper, The choice of

- anatomical site for islet transplantation, *Cell Transplant.* 17 (2008) 1005–1014. <https://doi.org/10.3727/096368908786991515>.
- [339] J.O.A.M. van Baal, K.K. Van de Vijver, R. Nieuwland, C.J.F. van Noorden, W.J. van Driel, A. Sturk, G.G. Kenter, L.G. Rikkert, C.A.R. Lok, The histophysiology and pathophysiology of the peritoneum, *Tissue Cell.* 49 (2017) 95–105. <https://doi.org/10.1016/j.tice.2016.11.004>.
- [340] P.R. Oskarsson, P.E. Lins, L. Backman, U.C. Adamson, Continuous intraperitoneal insulin infusion partly restores the glucagon response to hypoglycaemia in type 1 diabetic patients, *Diabetes Metab.* 26 (2000) 118–124.
- [341] C.K.N. Wan, A. Giacca, M. Matsuhisa, B. El-Bahrani, L. Lam, C. Rodgers, Z. Qing Shi, Increased responses of glucagon and glucose production to hypoglycemia with intraperitoneal versus subcutaneous insulin treatment, *Metabolism.* 49 (2000) 984–989. <https://doi.org/10.1053/meta.2000.7727>.
- [342] L. Bally, H. Thabit, R. Hovorka, Finding the right route for insulin delivery—an overview of implantable pump therapy, *Expert Opin. Drug Deliv.* 14 (2017) 1103–1111. <https://doi.org/10.1080/17425247.2017.1267138>.
- [343] G. Basta, P. Montanucci, G. Luca, C. Boselli, G. Noya, B. Barbaro, M. Qi, K.P. Kinzer, J. Oberholzer, R. Calafiore, Long-term metabolic and immunological follow-up of nonimmunosuppressed patients with type 1 diabetes treated with microencapsulated islet allografts: Four cases, *Diabetes Care.* 34 (2011) 2406–2409. <https://doi.org/10.2337/dc11-0731>.
- [344] R.B. Elliott, L. Escobar, P.L.J. Tan, O. Garkavenko, R. Calafiore, P. Basta, A. V. Vasconcellos, D.F. Emerich, C. Thanos, C. Bamba, Intraperitoneal alginate-encapsulated neonatal porcine islets in a placebo-controlled study with 16 diabetic cynomolgus primates, in: *Transplant. Proc.*, 2005: pp. 3505–3508. <https://doi.org/10.1016/j.transproceed.2005.09.038>.
- [345] P. Soon-Shiong, R.E. Heintz, N. Merideth, Q.X. Yao, Z. Yao, T. Zheng, M. Murphy, M.K. Moloney, M. Schmehl, M. Harris, R. Mendez, R. Mendez, P.A. Sandford, Insulin independence in a type 1 diabetic patient after encapsulated islet transplantation, *Lancet.* 343 (1994) 950–951. [https://doi.org/10.1016/S0140-6736\(94\)90067-1](https://doi.org/10.1016/S0140-6736(94)90067-1).
- [346] Y. Sun, X. Ma, D. Zhou, I. Vacek, A.M. Sun, Normalization of diabetes in spontaneously diabetic cynomolgus monkeys by xenografts of microencapsulated porcine islets without immunosuppression, *J. Clin. Invest.* 98 (1996) 1417–1422. <https://doi.org/10.1172/JCI118929>.
- [347] A. Omer, M. Keegan, E. Czismadia, P. De Vos, N. Van Rooijen, S. Bonner-Weir, G.C. Weir, Macrophage depletion improves survival of porcine neonatal pancreatic cell clusters contained in alginate macrocapsules transplanted into rats, *Xenotransplantation.* 10 (2003) 240–251. <https://doi.org/10.1034/j.1399-3089.2003.01150.x>.
- [348] E. Dassau, E. Renard, J. Place, A. Farret, M.J. Pelletier, J. Lee, L.M. Huyett, A. Chakrabarty, F.J. Doyle, H.C. Zisser, Intraperitoneal insulin delivery provides superior glycaemic regulation to subcutaneous insulin delivery in model predictive control-based fully-automated artificial pancreas in patients with type 1 diabetes: a pilot study, *Diabetes, Obes. Metab.* 19 (2017) 1698–1705. <https://doi.org/10.1111/dom.12999>.

- [349] D.M. Nathan, F.L. Dunn, J. Bruch, C. McKittrick, M. Larkin, C. Haggan, J. Lavin-Tompkins, D. Norman, D. Rogers, D. Simon, Postprandial insulin profiles with implantable pump therapy may explain decreased frequency of severe hypoglycemia, compared with intensive subcutaneous regimens, in insulin-dependent diabetes mellitus patients, *Am. J. Med.* 100 (1996) 412–417. [https://doi.org/10.1016/S0002-9343\(97\)89516-2](https://doi.org/10.1016/S0002-9343(97)89516-2).
- [350] J.L. Selam, R.N. Bergman, D. Raccah, N. Jean-Didier, J. Lozano, M.A. Charles, Determination of portal insulin absorption from peritoneum via novel nonisotopic method, *Diabetes*. 39 (1990) 1361–1365. <https://doi.org/10.2337/diab.39.11.1361>.
- [351] S. Fukuda, S.G. Yabe, J. Nishida, F. Takeda, K. Nashiro, H. Okochi, The intraperitoneal space is more favorable than the subcutaneous one for transplanting alginate fiber containing iPS-derived islet-like cells, *Regen. Ther.* 11 (2019) 65–72. <https://doi.org/10.1016/j.reth.2019.05.003>.
- [352] J.D. Carter, S.B. Dula, K.L. Corbin, R. Wu, C.S. Nunemaker, A practical guide to rodent islet isolation and assessment, *Biol. Proced. Online.* 11 (2009) 3–31. <https://doi.org/10.1007/s12575-009-9021-0>.
- [353] Home, (n.d.). <https://iidp.coh.org/> (accessed March 12, 2020).
- [354] M.C. Deeds, J.M. Anderson, A.S. Armstrong, D.A. Gastineau, H.J. Hiddinga, A. Jahangir, N.L. Eberhardt, Y.C. Kudva, Single dose streptozotocin-induced diabetes: Considerations for study design in islet transplantation models, *Lab. Anim.* 45 (2011) 131–140. <https://doi.org/10.1258/la.2010.010090>.
- [355] E.H. Karunanayake, D.J. Hearse, G. Mellows, The metabolic fate and elimination of streptozotocin, *Biochem. Soc. Trans.* 3 (1975) 410–414. <https://doi.org/10.1042/bst0030410>.
- [356] D.A. Rees, J.C. Alcolado, Animal models of diabetes mellitus, *Diabet. Med.* 22 (2005) 359–370. <https://doi.org/10.1111/j.1464-5491.2005.01499.x>.
- [357] D. Cheța, Animal models of type I (insulin-dependent) diabetes mellitus., *J. Pediatr. Endocrinol. Metab.* 11 (n.d.) 11–9. <https://doi.org/10.1515/jpem.1998.11.1.11>.
- [358] A. Al-Awar, K. Kupai, M. Veszelka, G. Sz4cs, Z. Attieh, Z. Murlasits, S. Török, A. Pósa, C. Varga, Experimental Diabetes Mellitus in Different Animal Models, (2016). <https://doi.org/10.1155/2016/9051426>.
- [359] E.H. Karunanayake, D.J. Hearse, G. Mellows, The synthesis of [14C]streptozotocin and its distribution and excretion in the rat, *Biochem. J.* 142 (1974) 673–683. <https://doi.org/10.1042/bj1420673>.
- [360] Y. Cheng, J.-L. Zhang, Y.-F. Liu, T.-M. Li, N. Zhao, Islet transplantation for diabetic rats through the spleen., *Hepatobiliary Pancreat. Dis. Int.* 4 (2005) 203–6. <http://www.ncbi.nlm.nih.gov/pubmed/15908316> (accessed April 8, 2020).
- [361] A. Rajab, J. Buss, E. Diakoff, G.A. Hadley, K. Osei, R.M. Ferguson, Comparison of the portal vein and kidney subcapsule as sites for primate islet autotransplantation, *Cell Transplant.* 17 (2008) 1015–1023. <https://doi.org/10.3727/096368908786991533>.
- [362] G. Christoffersson, J. Henriksnäs, L. Johansson, C. Rolny, H. Ahlström, J. Caballero-Corbalan, R. Segersvärd, J. Permert, O. Korsgren, P.O. Carlsson, M. Phillipson, Clinical and experimental pancreatic islet transplantation to striated muscle: Establishment of a vascular system similar to that in native islets, *Diabetes*. 59

- (2010) 2569–2578. <https://doi.org/10.2337/db10-0205>.
- [363] G.J. Echeverri, K. McGrath, R. Bottino, H. Hara, E.M. Dons, D.J. Van Der Windt, B. Ekser, A. Casu, S. Houser, M. Ezzelarab, R. Wagner, M. Trucco, F.G. Lakkis, D.K.C. Cooper, Endoscopic gastric submucosal transplantation of islets (ENDO-STI): Technique and initial results in diabetic pigs, *Am. J. Transplant.* 9 (2009) 2485–2496. <https://doi.org/10.1111/j.1600-6143.2009.02815.x>.
- [364] Z. Kakabadze, S. Gupta, A. Pileggi, R.D. Molano, C. Ricordi, G. Shatirishvili, G. Loladze, K. Mardaleishvili, M. Kakabadze, E. Berishvili, Correction of diabetes mellitus by transplanting minimal mass of syngeneic islets into vascularized small intestinal segment, *Am. J. Transplant.* 13 (2013) 2550–2557. <https://doi.org/10.1111/ajt.12412>.
- [365] Z. Kakabadze, K. Shanava, C. Ricordi, A.M.J. Shapiro, S. Gupta, E. Berishvili, An isolated venous sac as a novel site for cell therapy in diabetes mellitus, *Transplantation.* 94 (2012) 319–324. <https://doi.org/10.1097/TP.0b013e31825e4a83>.
- [366] P. Maffi, G. Balzano, M. Ponzoni, R. Nano, V. Sordi, R. Melzi, A. Mercalli, M. Scavini, A. Esposito, J. Peccatori, E. Cantarelli, C. Messina, M. Bernardi, A. Del Maschio, C. Staudacher, C. Doglioni, F. Ciceri, A. Secchi, L. Piemonti, Autologous pancreatic islet transplantation in human bone marrow, *Diabetes.* 62 (2013) 3523–3531. <https://doi.org/10.2337/db13-0465>.
- [367] B.E. Tuch, G.W. Keogh, L.J. Williams, W. Wu, J.L. Foster, V. Vaithilingam, R. Philips, Safety and viability of microencapsulated human islets transplanted into diabetic humans, *Diabetes Care.* 32 (2009) 1887–1889. <https://doi.org/10.2337/dc09-0744>.
- [368] D. Dufrane, M. Van Steenberghe, R.M. Goebbels, A. Saliez, Y. Guiot, P. Gianello, The influence of implantation site on the biocompatibility and survival of alginate encapsulated pig islets in rats, *Biomaterials.* 27 (2006) 3201–3208. <https://doi.org/10.1016/j.biomaterials.2006.01.028>.
- [369] V. Vaithilingam, C. Fung, S. Ratnapala, J. Foster, V. Vaghjiani, U. Manuelpillai, B.E. Tuch, Characterisation of the Xenogeneic Immune Response to Microencapsulated Fetal Pig Islet-Like Cell Clusters Transplanted into Immunocompetent C57BL/6 Mice, *PLoS One.* 8 (2013). <https://doi.org/10.1371/journal.pone.0059120>.
- [370] S.A. Safley, L.M. Kapp, C. Tucker-Burden, B. Hering, J.A. Kapp, C.J. Weber, Inhibition of cellular immune responses to encapsulated porcine islet xenografts by simultaneous blockade of two different costimulatory pathways., *Transplantation.* 79 (2005) 409–18. <https://doi.org/10.1097/01.tp.0000150021.06027.dc>.
- [371] J. Radziuk, S. Pye, D.E. Seigler, J.S. Skyler, R. Offord, G. Davies, Splanchnic and systemic absorption of intraperitoneal insulin using a new double-tracer method., *Am. J. Physiol.* 266 (1994) E750-9. <https://doi.org/10.1152/ajpendo.1994.266.5.E750>.
- [372] A. Giacca, A. Caumo, G. Galimberti, G. Petrella, M.C. Librenti, M. Scavini, G. Pozza, P. Micossi, Peritoneal and subcutaneous absorption of insulin in type I diabetic subjects, *J. Clin. Endocrinol. Metab.* 77 (1993) 738–742. <https://doi.org/10.1210/jcem.77.3.8370695>.
- [373] Long-term Function of Beta Cell Allografts in Non-uremic Type 1 Diabetic Patients - Full Text View - ClinicalTrials.gov, (n.d.).

- <https://clinicaltrials.gov/ct2/show/NCT00798785> (accessed February 4, 2020).
- [374] Open-label Investigation of the Safety and Effectiveness of DIABECCELL(R) in Patients With Type I Diabetes Mellitus - Full Text View - ClinicalTrials.gov, (n.d.). <https://clinicaltrials.gov/ct2/show/NCT00940173> (accessed February 4, 2020).
- [375] Open-label Investigation of the Safety and Effectiveness of DIABECCELL® in Patients With Type 1 Diabetes Mellitus - Full Text View - ClinicalTrials.gov, (n.d.). <https://clinicaltrials.gov/ct2/show/NCT01739829> (accessed February 4, 2020).
- [376] Bet Cell Therapy in Diabetes Type 1 - Full Text View - ClinicalTrials.gov, (n.d.). <https://clinicaltrials.gov/ct2/show/NCT01379729> (accessed February 4, 2020).
- [377] M.F. Flessner, The transport barrier in intraperitoneal therapy, *Am. J. Physiol. - Ren. Physiol.* 288 (2005) F433-42. <https://doi.org/10.1152/ajprenal.00313.2004>.
- [378] K. Suzuki, S. Bonner-Weir, N. Trivedi, K.H. Yoon, J. Hollister-Lock, C.K. Colton, G.C. Weir, Function and survival of macroencapsulated syngeneic islets transplanted into streptozocin-diabetic mice, *Transplantation.* 66 (1998) 21–28. <https://doi.org/10.1097/00007890-199807150-00004>.
- [379] S. Vériter, J. Mergen, R.-M. Goebbels, N. Aouassar, C. Grégoire, B. Jordan, P. Levêque, B. Gallez, P. Gianello, D. Dufrane, In vivo selection of biocompatible alginates for islet encapsulation and subcutaneous transplantation., *Tissue Eng. Part A.* 16 (2010) 1503–13. <https://doi.org/10.1089/ten.TEA.2009.0286>.
- [380] P.O. Carlsson, F. Palm, A. Andersson, P. Liss, Markedly decreased oxygen tension in transplanted rat pancreatic islets irrespective of the implantation site, *Diabetes.* 50 (2001) 489–495. <https://doi.org/10.2337/diabetes.50.3.489>.
- [381] Y. Sato, H. Endo, H. Okuyama, T. Takeda, H. Iwahashi, A. Imagawa, K. Yamagata, I. Shimomura, M. Inoue, Cellular hypoxia of pancreatic β -cells due to high levels of oxygen consumption for insulin secretion in vitro, *J. Biol. Chem.* 286 (2011) 12524–12532. <https://doi.org/10.1074/jbc.M110.194738>.
- [382] N. Sakata, T. Aoki, G. Yoshimatsu, H. Tsuchiya, T. Hata, Y. Katayose, S. Egawa, M. Unno, Strategy for clinical setting in intramuscular and subcutaneous islet transplantation, *Diabetes. Metab. Res. Rev.* 30 (2014) 1–10. <https://doi.org/10.1002/dmrr.2463>.
- [383] R.F. Nicosia, S.V. Nicosia, M. Smith, Vascular endothelial growth factor, platelet-derived growth factor, and insulin-like growth factor-1 promote rat aortic angiogenesis in vitro, *Am. J. Pathol.* 145 (1994) 1023–1029. [/pmc/articles/PMC1887435/?report=abstract](https://pubmed.ncbi.nlm.nih.gov/11887435/) (accessed July 24, 2020).
- [384] M. Zakrzewska, E. Marcinkowska, A. Wiedlocha, FGF-1: From biology through engineering to potential medical applications, *Crit. Rev. Clin. Lab. Sci.* 45 (2008) 91–135. <https://doi.org/10.1080/10408360701713120>.
- [385] O. Korsgren, Islet encapsulation: Physiological possibilities and limitations, *Diabetes.* 66 (2017) 1748–1754. <https://doi.org/10.2337/db17-0065>.
- [386] P.O. Carlsson, D. Espes, A. Sedigh, A. Rotem, B. Zimmerman, H. Grinberg, T. Goldman, U. Barkai, Y. Avni, G.T. Westermark, L. Carlbom, H. Ahlström, O. Eriksson, J. Olerud, O. Korsgren, O. Carlsson, D. Espes, | Amir Sedigh, A. Rotem, B. Zimmerman, H. Grinberg, T. Goldman, U. Barkai, Y. Avni, G.T. Westermark, L. Carlbom, | Håkan Ahlström, O. Eriksson, J. Olerud, O. Korsgren, Transplantation of macroencapsulated

- human islets within the bioartificial pancreas β Air to patients with type 1 diabetes mellitus, *Am. J. Transplant.* 18 (2018) 1735–1744. <https://doi.org/10.1111/ajt.14642>.
- [387] R.A. Stokes, K. Cheng, A. Lalwani, M.M. Swarbrick, H.E. Thomas, T. Loudovaris, T.W. Kay, W.J. Hawthorne, P.J. O'connell, J.E. Gunton, Transplantation sites for human and murine islets, (2017). <https://doi.org/10.1007/s00125-017-4362-8>.
- [388] A. Frontini, S. Cinti, Distribution and Development of Brown Adipocytes in the Murine and Human Adipose Organ, *Cell Metab.* 11 (2010) 253–256. <https://doi.org/10.1016/j.cmet.2010.03.004>.
- [389] M.J. Young, A.W. Gorlin, V.E. Modest, S.A. Quraishi, Clinical implications of the transversus abdominis plane block in adults, *Anesthesiol. Res. Pract.* 2012 (2012) 731645. <https://doi.org/10.1155/2012/731645>.
- [390] H. Willschke, A. Bösenberg, P. Marhofer, S. Johnston, S.C. Kettner, O. Wanzel, S. Kapral, Ultrasonography-guided rectus sheath block in paediatric anaesthesia - A new approach to an old technique, *Br. J. Anaesth.* 97 (2006) 244–249. <https://doi.org/10.1093/bja/ael143>.
- [391] E.L. Felix, C.A. Michas, M.H. Gonzalez, Laparoscopic hernioplasty - TAPP vs TEP, *Surg. Endosc.* 9 (1995) 984–989. <https://doi.org/10.1007/BF00188456>.
- [392] S.A. Waits, E.K. Kim, M.N. Terjimanian, L.M. Tishberg, C.M. Harbaugh, K.H. Sheetz, C.J. Sonnenday, J. Sullivan, S.C. Wang, M.J. Englesbe, Morphometric Age and Mortality After Liver Transplant, *JAMA Surg.* 149 (2014) 335. <https://doi.org/10.1001/jamasurg.2013.4823>.
- [393] V.M. Vaughn, D.C. Cron, M.N. Terjimanian, Z.S. Gala, S.C. Wang, G.L. Su, M.L. Volk, Analytic morphomics identifies predictors of new-onset diabetes after liver transplantation, *Clin. Transplant.* 29 (2015) 458–464. <https://doi.org/10.1111/ctr.12537>.
- [394] M.N. Terjimanian, C.M. Harbaugh, A. Hussain, K.O. Olugbade, S.A. Waits, S.C. Wang, C.J. Sonnenday, M.J. Englesbe, Abdominal adiposity, body composition and survival after liver transplantation, *Clin. Transplant.* 30 (2016) 289–294. <https://doi.org/10.1111/ctr.12688>.
- [395] M.J. Pienta, P. Zhang, B.A. Derstine, B. Enchakalody, W.B. Weir, T. Grenda, R. Goulson, R.M. Reddy, A.C. Chang, S.C. Wang, J. Lin, Analytic Morphomics Predict Outcomes After Lung Transplantation, *Ann. Thorac. Surg.* 105 (2018) 399–405. <https://doi.org/10.1016/j.athoracsur.2017.08.049>.
- [396] M.N. Terjimanian, P.W. Underwood, D.C. Cron, J.J. Augustine, K.A. Noon, D.A. Cote, S.C. Wang, M.J. Englesbe, K.J. Woodside, Morphometric age and survival following kidney transplantation, *Clin. Transplant.* 31 (2017) e13066. <https://doi.org/10.1111/ctr.13066>.
- [397] D.C. Cron, K.A. Noon, D.R. Cote, M.N. Terjimanian, J.J. Augustine, S.C. Wang, M.J. Englesbe, K.J. Woodside, Using analytic morphomics to describe body composition associated with post-kidney transplantation diabetes mellitus, *Clin. Transplant.* 31 (2017) e13040. <https://doi.org/10.1111/ctr.13040>.
- [398] K. Chughtai, Y. Song, P. Zhang, B. Derstine, E. Gatza, J. Friedman, L. Hully, C. Inglis, S. Goldstein, J. Magenau, A. Pawarode, P. Reddy, M. Riwes, G. Yanik, S.C. Wang, S.W.

- Choi, Analytic morphomics: A novel CT imaging approach to quantify adipose tissue and muscle composition in allogeneic hematopoietic cell transplantation, *Bone Marrow Transplant*. 51 (2016) 446–450. <https://doi.org/10.1038/bmt.2015.267>.
- [399] G.P. Duffy, S.T. Robinson, R. O'Connor, R. Wylie, C. Mauerhofer, G. Bellavia, S. Straino, F. Cianfarani, K. Mendez, R. Beatty, R. Levey, J. O'Sullivan, L. McDonough, H. Kelly, E.T. Roche, E.B. Dolan, Implantable Therapeutic Reservoir Systems for Diverse Clinical Applications in Large Animal Models, *Adv. Healthc. Mater.* (2020) 2000305. <https://doi.org/10.1002/adhm.202000305>.
- [400] P. Alves, R. Cardoso, T.R. Correia, B.P. Antunes, I.J. Correia, P. Ferreira, Surface modification of polyurethane films by plasma and ultraviolet light to improve haemocompatibility for artificial heart valves, *Colloids Surfaces B Biointerfaces*. 113 (2014) 25–32. <https://doi.org/10.1016/j.colsurfb.2013.08.039>.
- [401] G.N. Arjun, P. Ramesh, Structural characterization, mechanical properties, and in vitro cytocompatibility evaluation of fibrous polycarbonate urethane membranes for biomedical applications, *J. Biomed. Mater. Res. - Part A*. 100 A (2012) 3042–3050. <https://doi.org/10.1002/jbm.a.34255>.
- [402] R.Y. Kannan, H.J. Salacinski, P.E. Butler, G. Hamilton, A.M. Seifalian, Current status of prosthetic bypass grafts: A review, *J. Biomed. Mater. Res. - Part B Appl. Biomater.* 74 (2005) 570–581. <https://doi.org/10.1002/jbm.b.30247>.
- [403] R. Sonntag, J. Reinders, J.P. Kretzer, What's next? Alternative materials for articulation in total joint replacement, *Acta Biomater.* 8 (2012) 2434–2441. <https://doi.org/10.1016/j.actbio.2012.03.029>.
- [404] A. Lambertz, R.R.M. Vogels, D. Busch, P. Schuster, S.J. Övel, U.P. Neumann, U. Klinge, C.D. Klink, Laparotomy closure using an elastic suture: A promising approach, *J. Biomed. Mater. Res. - Part B Appl. Biomater.* 103 (2015) 417–423. <https://doi.org/10.1002/jbm.b.33222>.
- [405] A. Lambertz, R.R.M. Vogels, M. Binnebösel, D.S. Schöb, K. Kossel, U. Klinge, U.P. Neumann, C.D. Klink, Elastic mesh with thermoplastic polyurethane filaments preserves effective porosity of textile implants, *J. Biomed. Mater. Res. - Part A*. 103 (2015) 2654–2660. <https://doi.org/10.1002/jbm.a.35411>.
- [406] A. Abramson, E. Caffarel-Salvador, M. Khang, D. Dellal, D. Silverstein, Y. Gao, M.R. Frederiksen, A. Vegge, F. Hubálek, J.J. Water, A. V. Friderichsen, J. Fels, R.K. Kirk, C. Cleveland, J. Collins, S. Tamang, A. Hayward, T. Landh, S.T. Buckley, N. Roxhed, U. Rahbek, R. Langer, G. Traverso, An ingestible self-orienting system for oral delivery of macromolecules, *Science* (80-.). 363 (2019) 611–615. <https://doi.org/10.1126/science.aau2277>.
- [407] P.J. Basser, J. Mattiello, D. LeBihan, MR diffusion tensor spectroscopy and imaging, *Biophys. J.* 66 (1994) 259–267. [https://doi.org/10.1016/S0006-3495\(94\)80775-1](https://doi.org/10.1016/S0006-3495(94)80775-1).
- [408] P.J. Basser, C. Pierpaoli, Microstructural and physiological features of tissues elucidated by quantitative-diffusion-tensor MRI, *J. Magn. Reson. - Ser. B*. 111 (1996) 209–219. <https://doi.org/10.1006/jmrb.1996.0086>.
- [409] G.E. Uhlenbeck, L.S. Ornstein, On the theory of the Brownian motion, *Phys. Rev.* 36 (1930) 823–841. <https://doi.org/10.1103/PhysRev.36.823>.
- [410] T. Beppu, T. Inoue, Y. Shibata, A. Kurose, H. Arai, K. Ogasawara, A. Ogawa, S.

- Nakamura, H. Kabasawa, Measurement of fractional anisotropy using diffusion tensor MRI in supratentorial astrocytic tumors, *J. Neurooncol.* 63 (2003) 109–116. <https://doi.org/10.1023/A:1023977520909>.
- [411] D. Jones, *Diffusion MRI: Theory, Methods, and Applications.*, Oxford University Press, 2011. <https://doi.org/10.1360/zd-2013-43-6-1064>.
- [412] V. Flamini, A.P. Creane, C.M. Kerskens, C. Lally, Imaging and finite element analysis: A methodology for non-invasive characterization of aortic tissue, *Med. Eng. Phys.* 37 (2015) 48–54. <https://doi.org/10.1016/j.medengphy.2014.10.006>.
- [413] J.A. Brunberg, T.L. Chenevert, P.E. McKeever, D.A. Ross, L.R. Junck, K.M. Muraszko, R. Dauser, J.G. Pipe, A.T. Betley, In vivo MR determination of water diffusion coefficients and diffusion anisotropy: Correlation with structural alteration in gliomas of the cerebral hemispheres, *Am. J. Neuroradiol.* 16 (1995) 361–371.
- [414] B.P. Witwer, R. Moftakhar, K.M. Hasan, P. Deshmukh, V. Haughton, A. Field, K. Arfanakis, J. Noyes, C.H. Moritz, M.E. Meyerand, H.A. Rowley, A.L. Alexander, B. Badie, Diffusion-tensor imaging of white matter tracts in patients with cerebral neoplasm, *J. Neurosurg.* 97 (2002) 568–575. <https://doi.org/10.3171/jns.2002.97.3.0568>.
- [415] C. Mekkaoui, M.P. Jackowski, W.J. Kostis, C.T. Stoeck, A. Thiagalingam, T.G. Reese, V.Y. Reddy, J.N. Ruskin, S. Kozerke, D.E. Sosnovik, Myocardial scar delineation using diffusion tensor magnetic resonance tractography, *J. Am. Heart Assoc.* 7 (2018). <https://doi.org/10.1161/JAHA.117.007834>.
- [416] D.G. León, M. López-Yunta, J.M. Alfonso-Almazán, M. Marina-Breyse, J.G. Quintanilla, J. Sánchez-González, C. Galán-Arriola, F. Castro-Núñez, J.J. González-Ferrer, B. Ibáñez, J. Pérez-Villacastín, N. Pérez-Castellano, V. Fuster, J. Jalife, M. Vázquez, J. Aguado-Sierra, D. Filgueiras-Rama, Three-dimensional cardiac fibre disorganization as a novel parameter for ventricular arrhythmia stratification after myocardial infarction., *Europace.* 21 (2019) 822–832. <https://doi.org/10.1093/europace/euy306>.
- [417] D.M. Little, R.G. Holloway, Diffusion tensor imaging: Scientific advance, clinical tool, or just a pretty picture?, *Neurology.* 68 (2007) 9–10. <https://doi.org/10.1212/01.wnl.0000251193.41966.a8>.
- [418] H. Yoon, W.J. Moon, S.S. Nahm, J. Kim, K. Eom, Diffusion Tensor Imaging of Scarring, Necrosis, and Cavitation Based on Histopathological Findings in Dogs with Chronic Spinal Cord Injury: Evaluation of Multiple Diffusion Parameters and Their Correlations with Histopathological Findings, *J. Neurotrauma.* 35 (2018) 1387–1397. <https://doi.org/10.1089/neu.2017.5409>.
- [419] A.L. Alexander, J.E. Lee, M. Lazar, A.S. Field, *Diffusion Tensor Imaging of the Brain*, n.d.
- [420] J. Veraart, D.S. Novikov, D. Christiaens, B. Ades-aron, J. Sijbers, E. Fieremans, Denoising of diffusion MRI using random matrix theory, *Neuroimage.* 142 (2016) 394–406. <https://doi.org/10.1016/j.neuroimage.2016.08.016>.
- [421] E. Kellner, B. Dhital, V.G. Kiselev, M. Reisert, Gibbs-ringing artifact removal based on local subvoxel-shifts, *Magn. Reson. Med.* 76 (2016) 1574–1581. <https://doi.org/10.1002/mrm.26054>.

- [422] A. Leemans, B. Jeurissen, J. Sijbers, D.K. Jones, ExploreDTI: a graphical toolbox for processing, analyzing, and visualizing diffusion MR data, n.d. <http://www.exploredti.com>. (accessed April 14, 2020).
- [423] J.M. Juliana, I. Zanette, P.B. Noël, M.B. Cardoso, M.A. Kimm, F. Pfeiffer, Three-dimensional non-destructive soft-tissue visualization with X-ray staining microtomography, *Sci. Rep.* 5 (2015) 1–7. <https://doi.org/10.1038/srep14088>.
- [424] M.A. Horvath, C.E. Varela, E.B. Dolan, W. Whyte, D.S. Monahan, C.J. Payne, I.A. Wamala, N. V. Vasilyev, F.A. Pigula, D.J. Mooney, C.J. Walsh, G.P. Duffy, E.T. Roche, Towards Alternative Approaches for Coupling of a Soft Robotic Sleeve to the Heart, *Ann. Biomed. Eng.* 46 (2018) 1534–1547. <https://doi.org/10.1007/s10439-018-2046-2>.
- [425] A.N. Rafi, Abdominal field block: A new approach via the lumbar triangle, *Anaesthesia.* 56 (2001) 1024–1026. <https://doi.org/10.1046/j.1365-2044.2001.02279-40.x>.
- [426] N. Elkassabany, M. Ahmed, S.B. Malkowicz, D.F. Heitjan, J.A. Isserman, E.A. Ochroch, Comparison between the analgesic efficacy of transversus abdominis plane (TAP) block and placebo in open retropubic radical prostatectomy: A prospective, randomized, double-blinded study, *J. Clin. Anesth.* 25 (2013) 459–465. <https://doi.org/10.1016/j.jclinane.2013.04.009>.
- [427] N.T. Ventham, S. O'Neill, N. Johns, R.R. Brady, K.C.H. Fearon, Evaluation of novel local anesthetic wound infiltration techniques for postoperative pain following colorectal resection surgery: A meta-analysis, *Dis. Colon Rectum.* 57 (2014) 237–250. <https://doi.org/10.1097/DCR.0000000000000006>.
- [428] T. Gao, J.J. Zhang, F.C. Xi, J.L. Shi, Y. Lu, S.J. Tan, W.K. Yu, Evaluation of Transversus Abdominis Plane (TAP) block in hernia surgery, *Clin. J. Pain.* 33 (2017) 369–375. <https://doi.org/10.1097/AJP.0000000000000412>.
- [429] R. Champaneria, L. Shah, J. Geoghegan, J.K. Gupta, J.P. Daniels, Analgesic effectiveness of transversus abdominis plane blocks after hysterectomy: A meta-analysis, *Eur. J. Obstet. Gynecol. Reprod. Biol.* 166 (2013) 1–9. <https://doi.org/10.1016/j.ejogrb.2012.09.012>.
- [430] K. Peng, F.H. Ji, H.Y. Liu, S.R. Wu, Ultrasound-Guided Transversus Abdominis Plane Block for Analgesia in Laparoscopic Cholecystectomy: A Systematic Review and Meta-Analysis, *Med. Princ. Pract.* 25 (2016) 237–246. <https://doi.org/10.1159/000444688>.
- [431] H.-C. Tsai, T. Yoshida, T.-Y. Chuang, S.-F. Yang, C.-C. Chang, H.-Y. Yao, Y.-T. Tai, J.-A. Lin, K.-Y. Chen, Transversus Abdominis Plane Block: An Updated Review of Anatomy and Techniques, (2017). <https://doi.org/10.1155/2017/8284363>.
- [432] B.M. Mishriky, R.B. George, A.S. Habib, Transversus abdominis plane block for analgesia after Cesarean delivery: A systematic review and meta-analysis, *Can. J. Anesth.* 59 (2012) 766–778. <https://doi.org/10.1007/s12630-012-9729-1>.
- [433] P.B. Kingsley, Introduction to diffusion tensor imaging mathematics: Part I. Tensors, rotations, and eigenvectors, *Concepts Magn. Reson. Part A.* 28A (2006) 101–122. <https://doi.org/10.1002/cmr.a.20048>.
- [434] H. Zahedmanesh, D. John Kelly, C. Lally, Simulation of a balloon expandable stent in

- a realistic coronary artery-Determination of the optimum modelling strategy, *J. Biomech.* 43 (2010) 2126–2132. <https://doi.org/10.1016/j.jbiomech.2010.03.050>.
- [435] B. Hellman, E. Gylfe, P. Bergsten, E. Grapengiesser, P.E. Lund, A. Berts, A. Tengholm, D.G. Pipeleers, Z. Ling, Glucose induces oscillatory Ca²⁺ signalling and insulin release in human pancreatic beta cells., *Diabetologia.* 37 Suppl 2 (1994) S11-20. <https://doi.org/10.1007/bf00400821>.
- [436] P. Marchetti, D.W. Scharp, M. Mclear, R. Gingerich, E. Finke, B. Olack, C. Swanson, R. Giannarelli, R. Navalesi, P.E. Lacy, Pulsatile insulin secretion from isolated human pancreatic islets, *Diabetes.* 43 (1994) 827–830. <https://doi.org/10.2337/diab.43.6.827>.
- [437] P. Buchwald, S.R. Cechin, J.D. Weaver, C.L. Stabler, Experimental evaluation and computational modeling of the effects of encapsulation on the time-profile of glucose-stimulated insulin release of pancreatic islets, *Biomed. Eng. Online.* 14 (2015) 28. <https://doi.org/10.1186/s12938-015-0021-9>.
- [438] V. Vaithilingam, G. Kollarikova, M. Qi, I. Lacik, J. Oberholzer, G.J. Guillemin, B.E. Tuch, Effect of prolonged gelling time on the intrinsic properties of barium alginate microcapsules and its biocompatibility, *J. Microencapsul.* 28 (2011) 499–507. <https://doi.org/10.3109/02652048.2011.586067>.
- [439] R.C. Wood, E.L. LeCluyse, J.A. Fix, Assessment of a model for measuring drug diffusion through implant-generated fibrous capsule membranes., *Biomaterials.* 16 (1995) 957–9. [https://doi.org/10.1016/0142-9612\(95\)93122-t](https://doi.org/10.1016/0142-9612(95)93122-t).
- [440] J.M. Anderson, H. Niven, J. Pelagalli, L.S. Olanoff, R.D. Jones, The role of the fibrous capsule in the function of implanted drug-polymer sustained release systems, *J. Biomed. Mater. Res.* 15 (1981) 889–902. <https://doi.org/10.1002/jbm.820150613>.
- [441] F. Lotti, F. Ranieri, G. Vadalà, L. Zollo, G. Di Pino, Invasive intraneural interfaces: Foreign body reaction issues, *Front. Neurosci.* 11 (2017). <https://doi.org/10.3389/fnins.2017.00497>.
- [442] T.D.Y. Kozai, A.S. Jaquins-Gerstl, A.L. Vazquez, A.C. Michael, X.T. Cui, Brain tissue responses to neural implants impact signal sensitivity and intervention strategies, *ACS Chem. Neurosci.* 6 (2015) 48–67. <https://doi.org/10.1021/cn500256e>.
- [443] N. Cetin, N.M. Sav, E. Ciftci, B. Yildiz, Foreign Body Reaction to Dialysis Catheter and Peritoneal Fluid Eosinophilia in a Child on Continuous Ambulatory Peritoneal Dialysis, 2017. www.ijkd.org (accessed June 19, 2020).
- [444] X. Liu, L. Zhou, F. Pan, Y. Gao, X. Yuan, D. Fan, Comparison of the postoperative incidence rate of capsular contracture among different breast implants: A cumulative meta-analysis, *PLoS One.* 10 (2015). <https://doi.org/10.1371/journal.pone.0116071>.
- [445] K.G. Tarakji, C.R. Ellis, P. Defaye, C. Kennergren, Cardiac implantable electronic device infection in patients at risk, *Arrhythmia Electrophysiol. Rev.* 5 (2016) 65–71. <https://doi.org/10.15420/aer.2015.27.2>.
- [446] S. AA, K. B, T. GA, R. WM, Engineering the Tissue Which Encapsulates Subcutaneous Implants. II. Plasma-tissue Exchange Properties, *J. Biomed. Mater. Res.* 40 (1998). [https://doi.org/10.1002/\(SICI\)1097-4636\(19980615\)40:4<586::AID-JBM10>3.0.CO;2-E](https://doi.org/10.1002/(SICI)1097-4636(19980615)40:4<586::AID-JBM10>3.0.CO;2-E).

- [447] M.T. Novak, F. Yuan, W.M. Reichert, Modeling the relative impact of capsular tissue effects on implanted glucose sensor time lag and signal attenuation, *Anal. Bioanal. Chem.* 398 (2010) 1695–1705. <https://doi.org/10.1007/s00216-010-4097-6>.
- [448] V. Thome-Duret, M. Gangnerau, Y. Zhang, G. Wilson, G. Reach, Modification of the Sensitivity of Glucose Sensor Implanted Into Subcutaneous Tissue - PubMed, *Diabetes Metab.* 3 (1996) 174–178. <https://pubmed.ncbi.nlm.nih.gov/8697304/> (accessed June 19, 2020).
- [449] W.M. Fritschy, P. de Vos, H. Groen, F.A. Klatter, A. Pasma, G.H.J. Wolters, R. van Schilfgaarde, The capsular overgrowth on microencapsulated pancreatic islet grafts in streptozotocin and autoimmune diabetic rats, *Transpl. Int.* 7 (1994) 264–271. <https://doi.org/10.1007/BF00327154>.
- [450] P. Soon-Shiong, M. Otterlie, G. Skjak-Braek, O. Smidsrod, R. Heintz, R. Lanza, T. Espevik, An Immunologic Basis for the Fibrotic Reaction to Implanted Microcapsules - PubMed, *Transpl. Proc.* 23 (1991) 758–759. <https://pubmed.ncbi.nlm.nih.gov/1990681/> (accessed June 19, 2020).
- [451] S. Barr, E. Hill, A. Bayat, Current Implant Surface Technology: An Examination of Their Nanostructure and Their Influence on Fibroblast Alignment and Biocompatibility, *Eplasty.* 9 (2009). <https://www.ncbi.nlm.nih.gov/pmc/articles/PMC2698670/> (accessed July 8, 2019).
- [452] V.N. Shah, A. Shoskes, B. Tawfik, S.K. Garg, Closed-loop system in the management of diabetes: Past, present, and future, *Diabetes Technol. Ther.* 16 (2014) 477–490. <https://doi.org/10.1089/dia.2014.0193>.
- [453] L. Brown, E.R. Edelman, Optimal control of blood glucose: The diabetic patient or the machine?, *Sci. Transl. Med.* 2 (2010). <https://doi.org/10.1126/scitranslmed.3001083>.
- [454] K. Baker, D. Watson, Comparison of bioartificial and artificial pancreatic transplantation as promising therapies for Type I Diabetes Mellitus, *Biosci. Horizons Int. J. Student Res.* 9 (2016) 2016. <https://doi.org/10.1093/biohorizons/hzw002>.
- [455] H. Thabit, R. Hovorka, Closed-loop insulin delivery in type 1 diabetes, *Endocrinol. Metab. Clin. North Am.* 41 (2012) 105–117. <https://doi.org/10.1016/j.ecl.2011.12.003>.
- [456] T. Peyser, E. Dassau, M. Breton, J.S. Skyler, The artificial pancreas: current status and future prospects in the management of diabetes, *Ann. N. Y. Acad. Sci.* 1311 (2014) 102–123. <https://doi.org/10.1111/nyas.12431>.
- [457] A.M.J. Shapiro, M. Pokrywczynska, C. Ricordi, Clinical pancreatic islet transplantation, *Nat. Rev. Endocrinol.* 13 (2017) 268–277. <https://doi.org/10.1038/nrendo.2016.178>.
- [458] B. Cooper-Jones, C. Ford, Islet cell replacement therapy for insulin-dependent diabetes, *CADTH.* (2017).
- [459] S. Bose, L.R. Volpatti, D. Thiono, V. Yesilyurt, C. McGladrigan, Y. Tang, A. Facklam, A. Wang, S. Jhunhunwala, O. Veisheh, J. Hollister-Lock, C. Bhattacharya, G.C. Weir, D.L. Greiner, R. Langer, D.G. Anderson, A retrievable implant for the long-term encapsulation and survival of therapeutic xenogeneic cells, *Nat. Biomed. Eng.* (2020). <https://doi.org/10.1038/s41551-020-0538-5>.

- [460] J. Yu, J. Wang, Y. Zhang, G. Chen, W. Mao, Y. Ye, A.R. Kahkoska, J.B. Buse, R. Langer, Z. Gu, Glucose-responsive insulin patch for the regulation of blood glucose in mice and minipigs, *Nat. Biomed. Eng.* (2020) 1–8. <https://doi.org/10.1038/s41551-019-0508-y>.
- [461] E.B. Dolan, C.E. Varela, K. Mendez, W. Whyte, R.E. Levey, S.T. Robinson, E. Maye, J. O'Dwyer, R. Beatty, A. Rothman, Y. Fan, J. Hochstein, S.E. Rothenbucher, R. Wylie, J.R. Starr, M. Monaghan, P. Dockery, G.P. Duffy, E.T. Roche, An actuatable soft reservoir modulates host foreign body response, *Sci. Robot.* 4 (2019) eaax7043. <https://doi.org/10.1126/scirobotics.aax7043>.
- [462] The Pancreas – Earth's Lab, (n.d.). <https://www.earthslab.com/anatomy/pancreas/> (accessed April 24, 2020).
- [463] Introduction | Britannica.com, (n.d.). <https://www.britannica.com/science/pancreas> (accessed June 3, 2020).
- [464] F.R. Castiello, K. Heileman, M. Tabrizian, Microfluidic perfusion systems for secretion fingerprint analysis of pancreatic islets: Applications, challenges and opportunities, *Lab Chip.* 16 (2016) 409–431. <https://doi.org/10.1039/c5lc01046b>.
- [465] P. V. Röder, B. Wu, Y. Liu, W. Han, Pancreatic regulation of glucose homeostasis, *Exp. Mol. Med.* 48 (2016) e219. <https://doi.org/10.1038/emm.2016.6>.
- [466] A. Katsarou, S. Gudbjörnsdóttir, A. Rawshani, D. Dabelea, E. Bonifacio, B.J. Anderson, L.M. Jacobsen, D.A. Schatz, A. Lernmark, Type 1 diabetes mellitus, *Nat. Rev. Dis. Prim.* 3 (2017) 1–17. <https://doi.org/10.1038/nrdp.2017.16>.
- [467] Type 1 Diabetes Treatments - Learn about the different types of insulin for type 1 diabetes - Learn about the different types of insulin for type 1 diabetes and newer therapies to help you better manage your glucose better., (n.d.). <https://www.endocrineweb.com/conditions/type-1-diabetes/type-1-diabetes-treatments> (accessed June 9, 2020).
- [468] What Is Living With An Artificial Pancreas Like? - The Medical Futurist, (n.d.). <https://medicalfuturist.com/living-with-an-artificial-pancreas/> (accessed June 3, 2020).
- [469] J.M. Anderson, M.S. Shive, Biodegradation and biocompatibility of PLA and PLGA microspheres, *Adv. Drug Deliv. Rev.* 28 (1997) 5–24. [https://doi.org/10.1016/S0169-409X\(97\)00048-3](https://doi.org/10.1016/S0169-409X(97)00048-3).
- [470] R.L. GELLER, T. LOUDOVARIS, S. NEUENFELDT, R.C. JOHNSON, J.H. BRAUKER, Use of an Immunoisolation Device for Cell Transplantation and Tumor Immunotherapy, *Ann. N. Y. Acad. Sci.* 831 (2006) 438–451. <https://doi.org/10.1111/j.1749-6632.1997.tb52216.x>.
- [471] TheraCyte Implantable Cell Device | Surgical Instruments, Research Instruments, Laboratory Equipment | WPI, (n.d.). <https://www.wpiinc.com/var-505395-theracyte-implantable-cell-device> (accessed April 12, 2020).
- [472] Diabetes Device Engineering | Implanting Cell Replacement Therapies, (n.d.). <https://viacyte.com/device-engineering/> (accessed April 10, 2020).
- [473] B. Cooper-Jones, C. Ford, Islet Cell Replacement Therapy for Insulin-Dependent Diabetes, Canadian Agency for Drugs and Technologies in Health, 2016. <http://www.ncbi.nlm.nih.gov/pubmed/29369575> (accessed April 10, 2020).

- [474] type 1 diabetes treatment | bioartificial pancreas | Beta-O2 Technologies Ltd., (n.d.). <https://beta-o2.com/> (accessed April 9, 2020).
- [475] Open-label Investigation of the Safety and Effectiveness of DIABECCELL(R) in Patients With Type I Diabetes Mellitus (Identification No. NCT00940173), (n.d.).
- [476] Open-label Investigation of the Safety and Effectiveness of DIABECCELL® in Patients With Type 1 Diabetes Mellitus (Identification No. NCT01739829), (n.d.).
- [477] Open-label Investigation of the Safety and Efficacy of DIABECCELL in Patients With Type 1 Diabetes Mellitus (Identification No. NCT01736228), (n.d.).
- [478] Sernova Press, (n.d.).
- [479] One-Year Follow-up Safety Study in Subjects Previously Implanted With VC-01™ (Identification No. NCT02939118), (n.d.).
- [480] Safety and Efficacy Study of Encapsulated Human Islets Allotransplantation to Treat Type 1 Diabetes (Identification No. NCT00790257), (n.d.).
- [481] A.E. Vlahos, I. Talior-Volodarsky, S.M. Kinney, A scalable device-less biomaterial approach for subcutaneous islet transplantation 1 2, (n.d.). <https://doi.org/10.1101/2020.06.26.172148>.